博士論文

Research on optical depth-measurement of functional microstructures beyond the diffraction limit

(回折限界を超えた微細機能構造の
光学的深さ計測に関する研究)

指導教員　高橋　哲　教授

東京大学大学院工学系研究科 先端学際工学専攻

学籍番号 37-167334

叶　世蔚

Abstract

Functional microstructures, produced with a deterministic pattern of geometric features designed to give a specific function, have received significant scientific interest over the past years, mainly because it has played a decisive role in the development of many industrial fields, such as semiconductor industry, medical and biochemical applications, automotive industry and telecommunication area, etc. Furthermore, a trend towards miniaturization of functional microstructures can be observed, particularly at a micro- and nanometer scale. As critical dimensions are scaled down, the functional exploitation of several physical phenomena becomes more and more important, e.g. adhesive surfaces, super-hydrophobic surfaces, subwavelength structured surfaces, microfluidics system and solar cell surfaces, etc. On the surface of these functional microstructures, the microgroove structure, having an aperture size of a micro- and nanometer scale with high aspect ratio, is one of the essential micro-shape component and acts as the key functional element, such as micro U-shape cavities of optical sensors, nano hole arrays of solar cell surfaces, microchannels of microfluidics systems and hydrophobic microgroove structures, and so on. In order to reliably fabricate these functional microstructures, the quality control of microgroove based on dimensional metrology is gaining importance. Especially, the miniaturization process of functional microstructures and the rapid progress of manufacturing technologies are driving an imperious need of dimensional micro and nano metrology with high accuracy. Among the various quality control factors, this research focuses on the depth measurement of microgrooves, which is one of the most challenging tasks.

The conventional depth evaluation methods mainly include stylus profilometry, scanning probe microscopy (SPM), cross-section scanning electron microscopy (SEM), scatterometry, confocal laser scanning microscopy (CLSM) and optical interferometry. Although stylus profilometry and SPM are versatile and well established, there are limitations related to measurement speed and potential surface damage. Cross-section SEM has the advantages of relatively high throughput and the resolution with nanometers level, whereas the technology requires the vacuum condition for measurement and obviously destroys the sample. For all

optical metrologies, the non-contact nature and high potential of in-process measurement are clear merits. Scatterometry is a promising technology for quality control with fast speed and astonishing accuracy, however, this method only can be applied to overall evaluation for periodic gratings. Compared to scatterometry, CLSM and optical interferometry can output the depth information with respect to position. Furthermore, compared to CLSM, optical interferometry has the important property of higher sensitivity irrespective of magnification, not requiring a scanning process, and a better axial resolution for depth measurement. However, due to the significant errors of the measured depths, CLSM and optical interferometry cannot be applied to the depth measurement of microgrooves, width of which is fewer than the diffraction limit. In this PhD thesis, the microgroove with width fewer than the diffraction limit is named by diffraction-limited microgroove.

In order to solve these problems, the goal of this thesis is to develop a novel optical depth measurement method, which (1) enables the quantitative evaluation of the diffraction-limited microgrooves, having an aspect-ratio of 1, on different materials, with an accuracy of 10%, (2) is capable of the individual difference evaluation of each microgroove, and (3) has a depth measurement range optically greater than half of the incident wavelength, without the phase ambiguity problem.

The proposed method, called Far-field-based Near-field Reconstruction Depth Measurement (FNRDM), connects the depth information of diffraction-limited microgrooves with the near-field phase difference, which can be calculated from practical far-field optical observations rather than directly measured by specialized equipment, i.e., near-field scanning optical microscopy. By the FDTD method, the theoretical analysis was performed to demonstrate the validity and the detectable depth of FNRDM when measuring the diffraction-limited microgrooves. Furthermore, the practical applicabilities of FNRDM were discussed, including materials, internal shapes, noise conditions, grating structures and microhole structures. The simulation results show that: (1) the depth of a fine 200-nm-wide and 300-nm-deep microgroove can be measured by FNRDM, with an accuracy of 8 nm (3%) beyond the diffraction limit of 540 nm. (2) When the scattering light from the edges of microgrooves becomes the dominating contribution of the synthetically observed optical

wave, FNRDM cannot be applied to evaluate the depth. It is found that, by FNRDM, the measurable aspect-ratios are 5 for the 200-nm-wide microgroove, 3 for the 100-nm-wide microgroove and 1 for 50-nm-wide microgroove, beyond the diffraction limit, by using the wavelength of 488 nm. (3) As long as the optical wave from the bottom surface is radiated to the far-field, FNRDM has the potential to evaluate the depth information. (4) Under the noise condition, although the accuracy of depth measurement is greatly influenced by numerical aperture, both a 200-nm-wide microgroove with an aspect ratio of 1.5 and a 100-nm-wide microgroove with an aspect ratio of 2 can be quantitatively evaluated with less than 10% error by using imaging objective with numerical aperture of 0.95 and the wavelength of 488 nm (the Rayleigh criterion = 313 nm). (5) When using FNRDM to measure the depth of grating structure, a modified equation for calculating the amplitude of the top surface was proposed to ensure the measurement accuracy. Furthermore, it is found that when the pitch of the grating structure is much larger than the diffraction limit of applied imaging system, each microgroove of the grating can be regarded as an isolated element, and the depth can be measured as the case of an equally single microgroove. (6) When measuring microhole structure by FNRDM using linear polarization, the depth of a microhole with 200-nm in diameter and 300-nm in depth can be quantitatively evaluated, with an accuracy of 10 nm (3%), beyond the diffraction limit of 313 nm.

Then, a measurement system based on low-coherence illumination was developed to inspect the required far-field observations of the proposed FNRDM method. Besides the feature of low-coherence illumination, the designs of this measurement system also include an infinite corrected imaging system, a Linnik interferometer, an incident plane wave unit and an optical cage system. By comparing the height maps of a same flat surface on transparent polymer by a laser-based setup and the developed system based on low-coherence illumination, it is found that the spatial uniformity and accuracy of images by the low-coherence illumination are substantially better than the laser source. In addition, through the evaluations of temporally topography histogram of point measurement and spatial topography histogram of area measurement, it is demonstrated that the measurement system

allows for spatially sensitive optical path-length measurement (2.24 nm) and temporally sensitive optical path-length measurement (0.83nm).

Next, the nanochannels on a microfluidic sample (COC, nominal width = 300 nm, depth = 110 nm) were measured to verify the validity of FNRDM. Both a AFM and the developed measurement system were used to measure this sample. There are some experiment results: (1) the overall evaluation of measured depths of nanochannels in the same area are 67 nm by conventional optical interferometry, 107 nm by FNRDM and 114 nm by AFM measurement, respectively. (2) The same trend in depth variation of different nanochannels between FNRDM and AFM was confirmed. (3) The repeated experiments by FNRDM were performed, and the standard deviation is approximately 2 nm. According to the experiment results, our method has the advantages of greatly improved accuracy over conventional interferometry and enables the individual difference evaluation of each nanochannel, which is not possible with scatterometry. It is demonstrated that FNRDM and the developed measurement system can measure the depth of 300-nm-wide nanochannels beyond the diffraction limit (772 nm) with an accuracy of less than 10%.

However, similar to other optical depth measurement methods based on phase change, FNRDM using a single wavelength have the limitation: the measured depth which is optically greater than half of the incident wavelength subjects to the phase measurement ambiguity. In order to solve this problem, a noise-immune dual-wavelength interferometry was proposed. Using the noise-immune dual-wavelength interferometry, not only the depth measurement range can be extended, but also the noise level can be dramatically decreased to that in a single-wavelength phase map. Combined with the developed measurement system based on low-coherence illumination, a dual-wavelength interferometer unit (λ = 532 nm and 520 nm) was inserted to meet the requirements of practical measurements. Two experiments of measuring the gratings on different materials were performed. The experiment results showed that: (1) the 1000-nm-wide microgrooves, having an aspect-ratio of 1, with width less than the diffraction limit (1159 nm and 1132 nm) of develop measurement system on a silicon surface, can be quantitatively evaluated with an accuracy of less than 5% by the combination of FNRDM and the noise-immune dual-wavelength interferometry. (2) The

700-nm-wide microgrooves, having an aspect-ratio over 0.5, with width less than the diffraction limit (772 nm and 755 nm) of develop measurement system on transparent polymer surface, can be quantitatively evaluated with an accuracy of less than 10% by the combination of FNRDM and the noise-immune dual-wavelength interferometry. The combination also has a potential of measuring the depth of diffraction-limited and steep microgrooves with high accuracy.

Simultaneously, a novel method using a Fluorinert droplet was also presented to achieve the phase unwrapping. This method includes the generation and combination of two phase maps under an air condition and a droplet condition. When the two phase maps are combined, the measured depths are equivalent to those measured by a longer wavelength based on the refractive index difference. In order to achieve the droplet-based phase unwrapping method, a one-shot interferometry based on the Fourier Transform method, an auxiliary horizontal observation setup with high speed camera and a Fluorinert liquid with unique properties were presented. Based on the RCWA simulation, the numerical analysis was performed to verify the applicability of the droplet-based phase unwrapping method. In the case of diffraction-free microgrooves, the simulation results show that the droplet-based phase unwrapping method enables the depth evaluation of a 1000-nm-wide and 300-nm-deep microgroove with an accuracy of 16 nm (5%), without the phase ambiguity problem, using the wavelength of 488 nm. In the case of diffraction-limited microgrooves, the FNRDM method was combined to calculate the near-field phase difference. The simulation results suggest that by the droplet-based phase unwrapping method and FNRDM, the depth of a 300-nm-wide microgroove, with an aspect-ratio of 1, can be quantitatively evaluated with an accuracy of 24 nm (8%), without the phase ambiguity problem, beyond the diffraction limit of 540 nm, using numerical aperture of 0.55 and the wavelength of 488 nm. The proposed method enables the phase unwrapping by using only single-wavelength illumination, has a high temporal resolution and requires significantly less computational work than other least-squares integration technologies.

Overall, the highlights of our work lie in: (1) using only the far-field observations, the depth of diffraction-limited microgrooves can be quantitatively evaluated with an accuracy

of less than 10%, which is not possible by conventional optical depth measurement method based on phase change. (2) The proposed method is capable of the individual difference evaluation of each diffraction-limited microgroove, which is not possible with scatterometry. (3) The depth measurement range has been extended to optically greater than half of the incident wavelength without the phase ambiguity problem, which makes it possible to measure the depth of diffraction-limited and high aspect ratio microgrooves. (4) Not only the silicon surface, but also the transparent polymer surface can be measured. (5) Due to the clear merits of optical metrology and a dependence of only far-field observations, the proposed method has a high potential of in-process measurement. Therefore, our work brings a progress to optically three-dimensional imaging of diffraction-limited microstructures and motivate the studies in bio-inspired functional surfaces, precision engineering, medical and biochemical applications, etc. Furthermore, the results of this study have the potential to impact various industries where high-precision-microstructure mass production is crucial, such as semiconductors and microsystem techniques. We think these findings will be of great interest to researchers in dimensional micro and nano metrology, and particularly to researchers working on optically depth measurement and super-resolution technology.

Contents

List of Figures

List of Tables

List of Abbreviations

SPM	scanning probe microscopy
SEM	scanning electron microscopy
AFM	Atomic Force Microscopy
CLSM	confocal laser scanning microscopy
FNRDM	Far-field-based Near-field Reconstruction Depth Measurement
FDTD	finite-difference time-domain
TE	transverse electric
TM	transverse magnetic
PML	Perfectly Matched Layer
asf	Amplitude spread function
COC	cyclic olefin copolymer
CWL	center wavelength
FWHM (bandwidth)	Full width at half maximum
OPD	optical path difference
RCWA	Rigorous Coupled Wave Analysis

Chapter 1. Introduction

This chapter provides an introduction to the functional microstructures concerning the functional properties, the miniaturization trend and the applications. Especially, on the surface of these functional microstructures, the microgroove is one of the essential micro-shape component and acts as the key functional element. The great demand for and the miniaturization trend of functional microstructures are driving the need of depth measurement in micro and nano scale with high accuracy. Then, an overview of the current approaches used in depth measurement is given. For depth measurement of microgrooves, optical interferometry is a promising method due to its high throughput, noninvasiveness, feasibility in individual difference evaluation, high axial resolution and the potential of in-process measurement. However, when the width of microgrooves is fewer than the diffraction limit, optical interferometry cannot be exploited owing to the significant errors of the measured depths. These all motivated the developments made within the course of this work. Finally, the objectives and organization of this thesis are presented.

1.1 Functional microstructures

Functional microstructures, the surfaces of which are active interfaces between subjects and the environment, are produced with a deterministic pattern of usually high aspect ratio geometric features designed to give a specific function [1]. Because the most important physical phenomena involving exchange of energy and signal transmission take place on surfaces, the structured surfaces play a decisive role in the behavior of functional properties.

1.1.1 Functional properties and their applications

The functional properties of engineered microstructures include improved adhesion, super-hydrophobicity, special optical properties, generation and preservation of energy, hydrodynamic properties, hard and tough surfaces, efficient heat transfer, and antibiofouling etc. Some of these functional properties and their applications have been introduced in the following.

1.1.1.1 Adhesion

Adhesion is the tendency of dissimilar particles or surfaces to cling to one another. An adhesive surface is one of bio-inspired functional microstructures and mimics the surface of geckos' foot. It is found that geckos have the ability to move across ceilings and even smooth vertical walls due to their foot attachment pads [2].

Figure 1.1 is one example of manufactured adhesive surfaces developed by Greiner et al [3]. Adhesive surfaces have tremendous applications in biomedical materials and devices, labeling and for fixing household items. For example, the gecko tape can act as a bonding agent for surgical applications. Researchers in collaboration with two Boston hospitals developed a stretchable and biodegradable tape to replace conventional surgical staples and sutures [4]. As the adhesive features of geckos are directional, they stick only when applied in a particular direction, and the adhesive force is directly proportional to the tangential force [5]. Hence, these adhesive surfaces also have some applications for part handling in manufacturing and as aids for human and robot climbing for reconnaissance missions and space exploration [6].
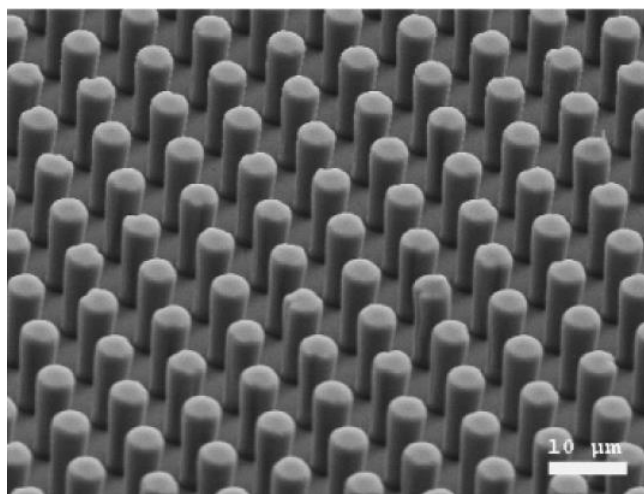
Figure 1. 1 PDMS microfibrils formed by soft molding on SU-8 photolithographic templates developed by Greiner. [3]

1.1.1.2 Super-hydrophobicity

Super-hydrophobic surfaces characterized by a contact angle greater than $150\,°$ are extremely difficult to wet. Wetting is the ability of a liquid to maintain contact with a solid surface, resulting from intermolecular interactions when the two are brought together. The degree of wetting is given in terms of the contact angle, which is the angle between the liquid-vapor interface and the solid–liquid interface. A hydrophobic surface has a contact angle greater than or equal to $90\,°$, whereas hydrophilic surfaces have lower contact angles. Wenzel [7] predicated that hydrophobicity is enhanced by surface roughness. As shown in Fig. 1.2, hydrophobicity and sliding behavior of water droplets were investigated on various hydrophobic pillarlike and microgroove structures on a silicon wafer by Yoshimitsu [8].
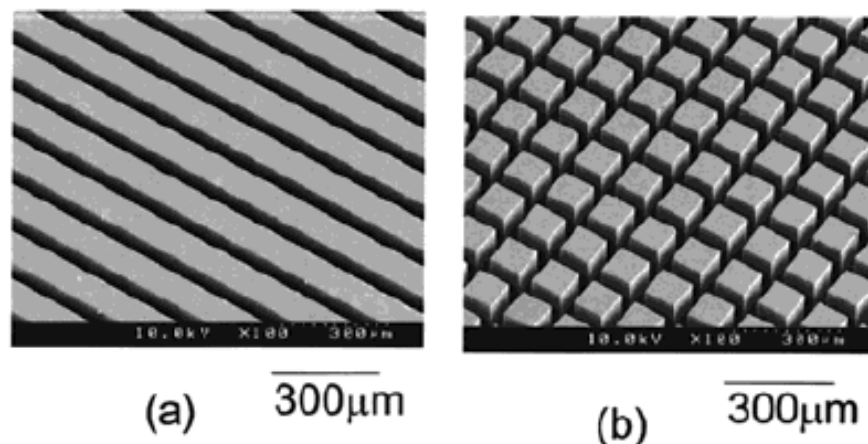
Figure 1. 2 Hydrophobic pillarlike and microgroove structures on a silicon wafer. [8]

Super-hydrophobic surfaces are used in textiles, glassware, architecture, optical windows for electronic devices, and windows in automobiles [9]. Investigations have been developed to obtain the super-hydrophobic poly-lactic acid fabrics by ultraviolet photo-grafting of hydrophobic silica particles functionalized with vinyl groups over silica [10]. This approach can be extended to other materials and provide a robust technique to fabricate water and dust-repellent fabrics. In addition, super-hydrophobic coatings show the ability to minimize fluid drag for objects in water [11]. Silicon surfaces with super-hydrophobic coatings are used as electrodes of a battery [12].

1.1.1.3 Optical properties

Subwavelength structured surfaces are attractive for new optical elements, and many products with these functional structured surfaces have been developed. The subwavelength structure has the following optical features: artificial refractive index, form birefringence, resonance and band-gap effects.

Moth-eye structures have been an area of interest due to their excellent broadband anti-reflective properties and the related product applications [13]. The antireflective properties of moth eyes are due to a periodic arrangement of sub wavelength structures on their facet lenses [14]. Similar features that lead to anti-reflective functionality were observed on various species of butterflies as well as cicada and termite wings [15]. The engineered antireflective structure can be applied to optical view windows, infrared optical elements and solar cells. A non-symmetric structure resulting in optically anisotropy is called form birefringence. Achromatic quarter-wave plates of subwavelength gratings have been designed by Kikuta, *et al* [16]. When the pitch of the grating structure is smaller than the wavelength of the incident light, the structure is considered to be an optically anisotropic medium. Applications based on the resonance and band-gap effects are narrow-band grating filters and polarization beam splitters [17]. Figure 1.3 is an example of the fabricated polarization multiplexed computer-generated holograms when applying subwavelength structured surfaces to high efficiency diffractive optical elements [18].
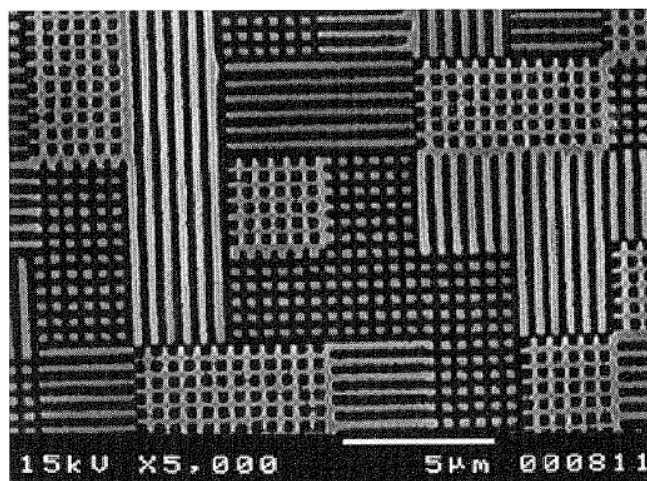
Figure 1. 3 Scanning electron micrograph of a part of the fabricated polarization multiplexed computer-generated holograms pattern. [18]

1.1.1.4 Energy scavenging

Solar cells, typically manufactured using semiconducting silicon and having 24% efficiency in converting solar energy to electrical energy, are regarded as a promising approach to green, renewable energy. Despite its advantages and continuing advances, this technology remains non-cost-competitive against traditional fossil fuels and thus has not yet been massively deployed. Recent researches have been focused on developing new solar cell systems that incorporate optically active nanostructures, such as quantum dots [19], nanotubes [20], nanohole arrays, which offer substantial potential for new device structures. As shown in Fig. 1.4, Peng, *et al.* has reported the fabrication of a silicon nanohole solar cell which show a good mechanical robustness and a superior optical absorption ability [21].
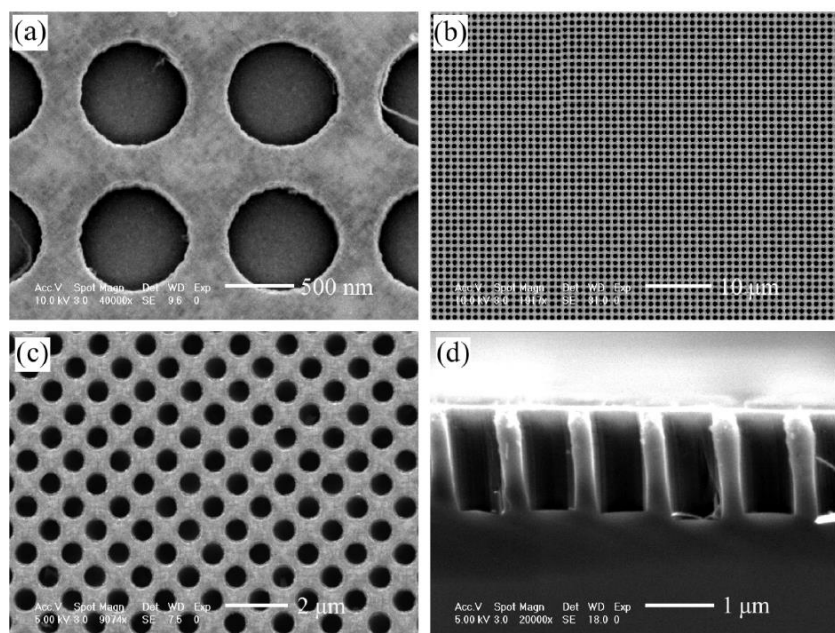
Figure 1. 4 SEM images of silicon nanoholes by Peng. [21]

1.1.1.5 Hydrodynamic properties

Hydrodynamic properties have a great influence on the applications of structured surfaces. At small scales (channel diameters of around 100 nm to several hundred micrometers), the impact factors for surface forces, such as surface tension, energy dissipation, and fluidic

resistance, govern the system [22]. Hence the fluid flow at the micro-scale acts differently from that in the macroscopic scale.

Microfluidics deals with the behavior, precise control and manipulation of fluids that are geometrically constrained to the small scales. These so-called lab-on-a-chip components are manufactured in silicon and polymer material. Key application areas of microfluidics range from biology to energy. The most successful commercial application of microfluidics is the inkjet printhead [23]. Additionally, advances in microfluidics technology are revolutionizing molecular biology procedures for enzymatic analysis, DNA analysis and proteomics. Furthermore, the basic idea of microfluidic biochips is to integrate assay operations such as detection, as well as sample pre-treatment and sample preparation on one chip [24]. An emerging application area for biochips is clinical pathology. In clinical pathology, the use of a small volume of liquid is highly desirable, because it minimizes the amount of sample necessary and allows for early stage detection of diseases. Figure 1.5 shows a complete micro/nano fluidic system with 30 nm channels by direct nanoimprint lithography [25].
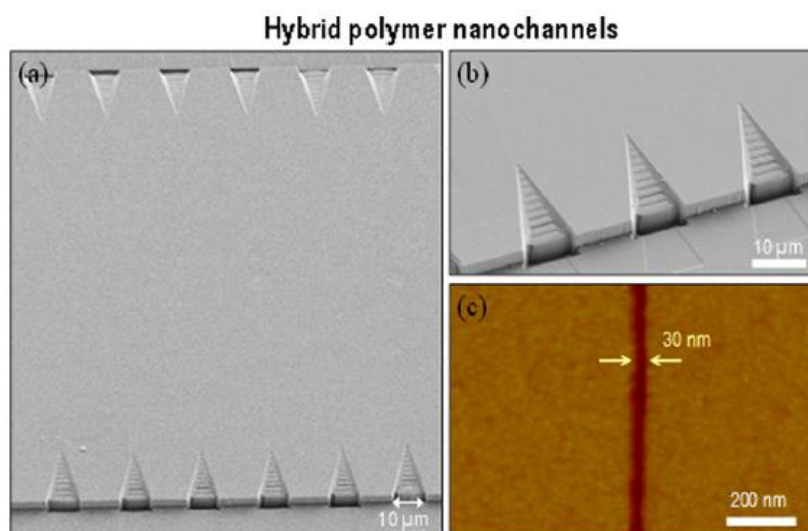
Figure 1.5 Images of the final device made by UV-NIL on a transparent inorganic-organic polymer. (a) shows a general view of a device. (b) shows details of the 3D tapered inlets and (c) shows an AFM image of a channel, 30 nm wide. [25]

1.1.2 Miniaturization of functional microstructures

An obvious characteristic of functional microstructures is their micro- and nanometer dimensional scale, and a rush towards miniaturization can be observed in the past decades. Miniaturization of functional microstructures has some advantages: (a) the micro- and nanometer scale are the key factor for functional properties. For example, the pitch of a form birefringence wave-plate is fewer than the wavelength of the incident light. And as the dimension reduces, different surface phenomena can be applied to the same application. For example, adhesion is controlled by surface wettability, roughness and its interlocking properties [26]. (b) In the semiconductor industry, miniaturization makes integrated circuits smaller, faster and cheaper. (c) As instrumentation, such as microfluidics, reduces in overall size, so do fluid volumes used in the analyses, which subsequently offers scientists several ancillary advantages: sample size reduction, reagent volume reduction, faster analysis time and lowered operational cost. (d) Miniaturization makes it easier to move the analysis equipment from laboratory to laboratory, which reduces the risk of sample contamination or loss through mishandling.

Miniaturization has been one of the driving forces of technology in the past decades. As predicted by Taniguchi in 1983, nanometer accuracy is achievable for precision machining processes [27]. Figure 1.6 illustrates Taniguchi's prediction. This development has been made very clear in the semiconductor industry, where the number of transistors in a dense integrated circuit doubles each 18 months approximately. This phenomenon is usually referred to Moore's law. Currently, the transistor gate widths are on the order of 7 nm wide. Furthermore, functional microstructures at the micro- and nanometer scale have already been manufactured in other fields. Irene, *et al.* has proposed a method to fabricate 30 nm channels of a complete micro/nano fluidic system by direct nanoimprint lithography [25]. Peng, *et al.* has reported the fabrication of a silicon nanohole solar cell which show a good mechanical robustness and a superior optical absorption ability [21]. Research by Tanu, *et al.* show that the hierarchical polymeric microfibrils (10-μm-wide and 70-μm-long) with nanofibril arrays (60-nm-wide and 500-nm-long) were obtained as an adhesive surface by using bonded porous alumina templates [28].

7
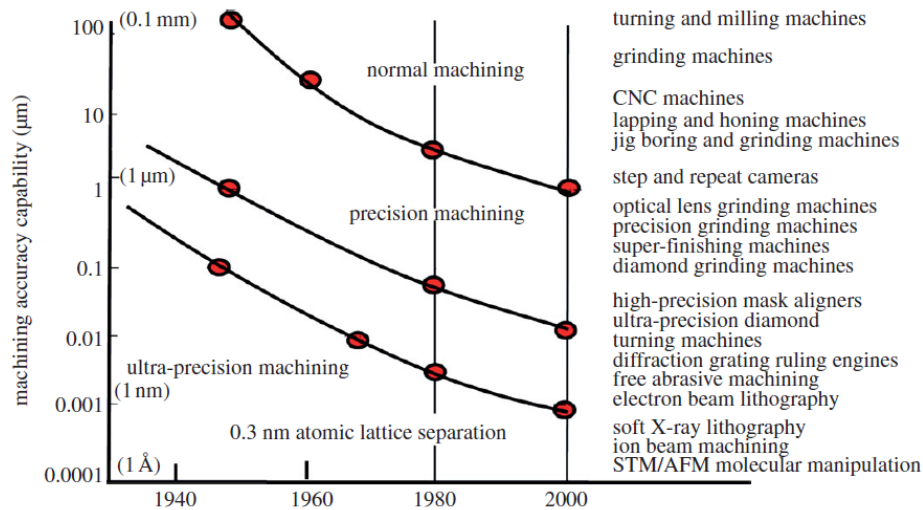
Figure 1.6: The development of achievable machining accuracy by Taniguchi. [27]

1.1.3 Materials for functional microstructures

In general, engineering materials are grouped into four basic classifications: metals, ceramics, polymers, and semiconductor materials. It is well known that the origin of micro technology is the microelectronics area. Therefore, the preferred materials are the semiconductor materials, among which silicon is the clear favourite. Significantly, the semiconductor materials form the foundation for integrated circuits, which make up the over $200 billion semiconductor industry. These integrated circuits, in turn, fuel the nearly $1 trillion worldwide electronics market. The market pull of the IT-sector has driven the development of both materials and technologies related to semiconductors in general and to silicon in particular. Other applications of the semiconductor materials include the solar cells, the microelectromechanical systems, chemical sensors, and infrared detectors.

On the other hand, there is an increasing trend of fabricating functional microstructures with the more traditional materials, such as polymers, metals and glasses. Especially, the microfluidics and some bio-inspired functional surfaces are mainly manufactured by the polymer materials [29][30]. Polymer products have many advantages of reduced cost and simplified manufacturing procedures, particularly when compared to glass and silicon. And the extremely attractive benefit of polymer materials is that they are available in a wide range of types to meet the needs of the manufacturers.

1.1.4 Microgrooves

On the surface of these functional microstructures, microgroove structure, having an aperture size of micro- or nanometer scale, with high aspect ratio, is one of the essential micro-shape component and acts as the key functional element, such as micro U-shape cavities for optical sensors [31], nano hole arrays for solar cell systems [21], microchannels of microfluidics systems for DNA analysis [25], and so on. Hence, as a fundamental element of various microstructures, the microgroove is the main research subject of this work.

1.2 Depth measurement

In general, metrology is regarded as a key discipline in making engineered products possible. Dimensional metrology, which covers measurement of dimensions and geometries based on distance measurements, is an integral part of all quality assurance systems to achieve the proper fit, performance and life time of engineered products. The miniaturization process of functional microstructures and the rapid progress of manufacturing technologies are driving the need of dimensional micro and nano metrology with high accuracy. For a microgroove, the following dimensional measurement tasks can be distinguished [32][33]:

- Width as defined by the distance between two opposing surfaces. Example: width of grating lines in a Mollusk Shell [34] or subwavelength structured surfaces.
- Depth. Example: depth of channels on the microfluidic surfaces.
- Pitch (or periodicity) defined as the average distance between features oriented in the same direction. Example: the grating distance on the Mollusk Shell surface.
- Texture and roughness.
- Aspect ratio as defined by the depth of a structure divided by its width.

Among the various quality control factors, this research focuses on the depth measurement of microgrooves, which is one of the most challenging tasks. The conventional depth evaluation methods mainly include stylus profilometry, scanning probe microscopy (SPM), cross-section scanning electron microscopy (SEM), optical metrologies.

1.2.1 Stylus profilometry

For stylus profilometry, a diamond tip is brought into direct contact with the surface, with calibrated contact force, in order to acquire the surface height. As the tip moves across the surface, the motion of the tip is amplified, filtered, and detected. The lateral resolution of stylus profilometry is sub-μm level and limited by its tip geometry and actual surface slopes [35]. Care must be exercised to prevent indentations of the surface by the tip, depending on materials and forces used.

1.2.2 Scanning Probe Microscopy (SPM)

SPM [36][37] is a branch of microscopy that forms images of surfaces using a physical probe that scans the specimen. Commonly a feedback loop is used to regulate the gap distance between the sample and the probe. The data are typically obtained as height coordinates on a two-dimensional grid of data points and displayed as a computer image. Atomic Force Microscopy (AFM), one type of SPM, employs the tip at the end of a micro-fabricated cantilever with a low spring constant to measure the tip-sample forces, as the tip presses against the sample. Forces between the tip and the sample surface cause the cantilever to bend or deflect, as the tip is scanned over the sample. The cantilever deflection is measured, and the measurements generate a map of surface topography. The resolution of AFM is on the order of nanometers. However, because of the slow scanning speed, the measurement time of AFM can be rather long and the applications are commonly restricted to two-dimensional (2D) measurement, i.e. the height along a single line.

1.2.3 Cross-section SEM

Scanning electron microscopy (SEM) [38] is a type of electron microscope that produces images of a sample by scanning the surface with a focused beam of electrons. The electrons interact with atoms in the sample, producing various signals that contain information about the surface topography and composition of the sample. SEM has some unique properties, such as high magnification levels, extremely high resolution (a few nanometers level), large depth of field, elemental analysis capability and minimum diffraction effects. SEM can be operated in cross-section mode to achieve depth measurement of microgrooves [39]. However, SEM requires vacuum condition for measurement and the distortions introduced

in cross-section SEM can cause large systematic errors. Furthermore, cross-section SEM obviously destroys the sample, a drawback that rules this technique out for widespread applications.

1.2.4 Optical metrologies

Over the past few decades, there has been extensive development of optical metrologies to supplement depth measurement at micro- and nano scale. These techniques include scatterometry, confocal laser scanning microscopy (CLSM) and optical interferometry.

1.2.4.1 Scatterometry

Recently scatterometry [40][41][42][43] has been introduced as a novel tool in nano metrology. It is based on white light diffraction, where both the direct beam (0th order) and all orders of scattered light are analyzed. With no moving parts and based on optical signal processing, it offers a fast optical method for a variety of optical gratings with an astonishing accuracy. The principle is as follows: (a) the sample is irradiated by the white light to collect the scattered light as well as the 0th order beam; (b) the spectra are analyzed by simulating the model gratings and fitting the model parameters to the observed spectra. Because scatterometry can provide nanometer accuracy at the desired resolution, this method is widely used for quality control of gratings in semiconductor industry. However, the challenge of scatterometry is parameter cross-correlations. In addition, this technology only can be applied to periodic gratings, and the results are estimated values of overall measurement.

1.2.4.2 CLSM

Based on the focus detection principle, confocal laser scanning microscopy (CLSM) [44][45][46] is a three-dimensional (3D) optical imaging technique by means of using a spatial pinhole to block out-of-focus light in image formation. Capturing multiple 2D images at different depths in a sample enables the reconstruction of 3D structures, which is similar to computer tomography. As only one point in the sample is illuminated at a time, 2D or 3D imaging requires scanning over a regular raster in the specimen. There are some advantages of CLSM: (a) compared to stylus profilometry and SPM, CLSM has the advantage of not

requiring a probe to be suspended nanometers from the surface. The working distance of CLSM is typically comparable to that of a conventional optical microscope. (b) Compared to scatterometry, CLSM provides quantitative depth information with respect to lateral position. (c) The lateral resolution of CLSM can be improved by eliminating higher orders of the diffraction pattern. For example, if pinhole diameter is smaller than Airy disk produced by a point object, then only the first order of the diffraction pattern can be collected in the detector while the higher orders are blocked. The improved lateral resolution is theoretically $\sqrt{2}$ times than the diffraction limit. The diffraction limit is given

$$d = \frac{0.61 \times \lambda}{NA} \tag{1.1}$$

with d the lateral resolution, λ the wavelength and NA the numerical aperture of the objectives. However, the axial resolution of CLSM is 2-3 times worse than the lateral resolution and approximately 500 nm [47][48], which is insufficient for depth measurement of microgrooves. In additional, the measurement noise of CLSM is highly sensitive to its magnification power. As illustrated in Fig. 1.7, Peter showed the trend of surface topography repeatability as a function of objective numerical aperture (NA) for CLSM [49].
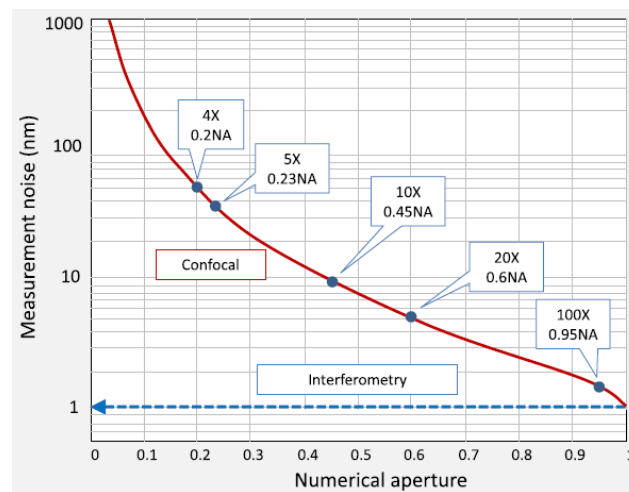
Figure 1.7 Qualitative comparison of surface topography repeatability as a function of objective NA for interference and confocal microscopes. [49]

1.2.4.3 Optical interferometry

In optical interferometry [50][51][52][53][54][55][56][57][58][59][60], light from a single source is divided into two beams that travel unequal paths, then combined again to produce interference. This interference appears as a pattern of light and dark bands called interference fringes, which give information about the difference in optical path lengths.

As shown in Fig. 1.7, optical interferometry has the important property of higher sensitivity irrespective of magnification compared to CLSM [49]. For objectives higher than 0.75 NA, the noise in a confocal system approaches 1 nm, rivaling interferometric techniques. For interferometry, there is in principle no direct dependence on the objective NA, although the secondary effects of air turbulence or reduced signal to noise may increase at lower magnifications.

However, the lateral resolution of optical interferometry is limited by diffraction. A schematic of measuring a microgroove structure by conventional optical interferometry based on phase change is illustrated in Fig. 1.8. A microgroove structure is illuminated by an incident plane wave, and the depth of microgroove is proportional to the reflected far-field phase difference (θ) between the top surface and the bottom surface, based on Eq. (1.2).

$$depth = \frac{\lambda}{2} \times \left(\frac{\theta}{2\pi} + k \right) \tag{1.2}$$

(a) Incident   (b) Reflection
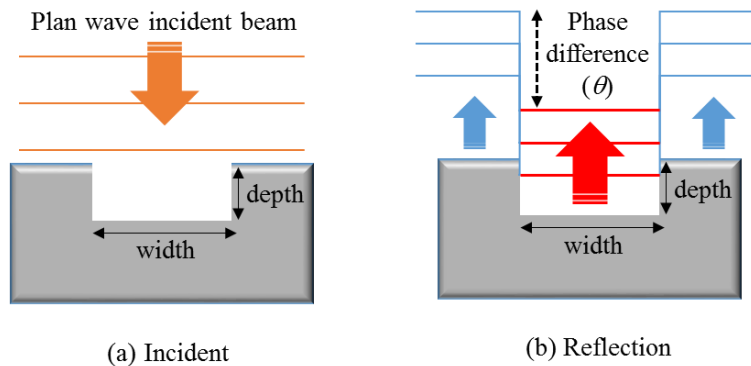
Figure 1.8 Schematic of measuring a microgroove by conventional optical interferometry

Where k is an unknown integer caused by phase wrapping problem. Optical interferometry can offer a sub-nanometer vertical resolution for depth measurement, but cannot be applied to the microgrooves, width of which are fewer than the diffraction limit [61][62]. Figure 1.9 shows an example of general limitation in depth measurement by the conventional optical

interferometry based on phase change. In Fig. 1.9, we plot a variation trend of measured depths calculated by the far-field phase differences as a function of widths. The simulation conditions include a 488-nm wavelength, a 0.55 NA, and the corresponding 540-nm diffraction limit. It is clearly found that as the simulated depth increases, the measured depths of the 1000-nm-wide microgroove are almost coincident with the theoretical values, but only a minute change in measured depths can be observed in the case of the 200-nm-wide microgrooves. Hence, the depths of a 200-nm-wide microgroove cannot be evaluated while the depth of a 1000-nm-wide microgroove can be measured with a numerical aperture of imaging system of 0.55 and a wavelength of 488 nm.

In this PhD thesis, the microgroove with width far larger than the diffraction limit is named as diffraction-free microgroove, while the microgroove with width fewer than the diffraction limit is named by diffraction-limited microgroove. When applying conventional optical interferometry into depth measurement of diffraction-limited microgrooves, there is a great discrepancy between the measured depth and true value.
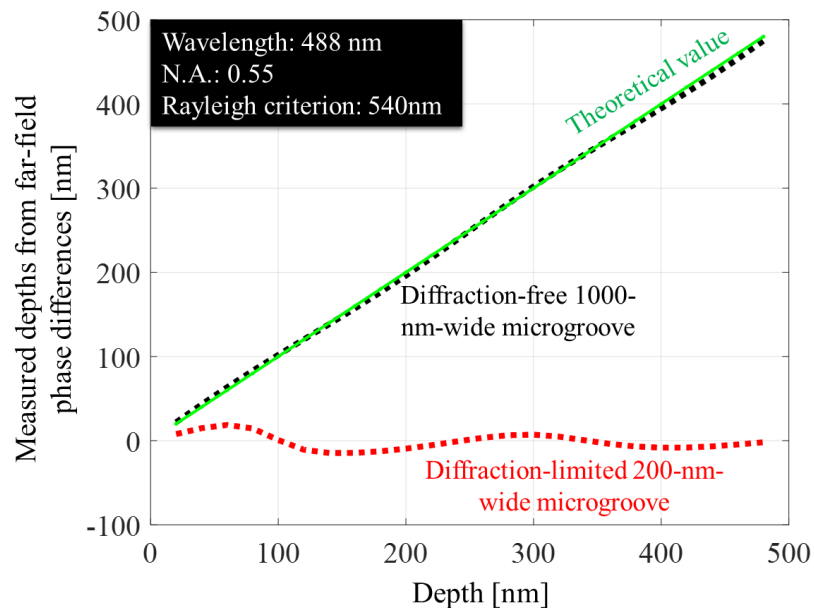
Figure 1.9 Limitation of depth measurement by the conventional optical interferometry based on phase change.

1.2.5 Summary

General considerations about measurement capabilities of these types of instruments can be summarized in Table 1.1. In Table 1.1, ○, △ and ×indicate excellent performance, medium level and poor performance, respectively. Although stylus profilometry and APM are versatile and well established, there are limitations related to measurement speed and potential surface damage. Even very light pressure leaves detectable traces on plastics, glass, and even metals. Reduced contact pressure can minimize the damage, at the expense of measurement speed and fidelity. Cross-section SEM has the advantages of relatively high throughput and the resolution with nanometers level, whereas the technology requires the vacuum condition for measurement and obviously destroys the sample. For all optical metrologies, the non-contact nature and high potential of in-process measurement are clear merits. Scatterometry is a promising technology for quality control with fast speed and astonishing accuracy, however, this method only can be applied to overall evaluation for periodic gratings. Compared to scatterometry, CLSM and optical interferometry, based on acquisition of topography data from point by point scans, can output the quantitative depth information with respect to position. Furthermore, compared to CLSM, optical interferometry has the important property of higher sensitivity irrespective of magnification, not requiring a scanning process, and a better axial resolution for depth measurement. However, due to the significant errors of the measured depths, optical interferometry cannot be applied to depth measurement of diffraction-limited microgrooves.

Table 1.1 Conventional depth evaluation methods.

	Stylus profilometry	AFM	Cross-section SEM	Scatterometry	CLSM	optical interferometry
Throughput (not requiring a scanning process)	×	×	△	○	×	○
Noninvasiveness	×	△	×	○	○	○
Individual difference evaluation	○	○	○	× (overall evaluation for periodic gratings)	○	○
Lateral resolution	△ (sub-μm)	○ (nm)	○ (nm)	○ (nm)	△ (sub-μm)	× (sub-μm)
Axial resolution	○ (sub-nm)	○ (sub-nm)	○ (nm)	○ (nm)	× (sub-μm)	○ (sub-nm)
Accuracy in depth measurement of diffraction-limited microgrooves	○	○	○	○	×	×

1.3 Objectives

All of current depth measurement methods of microgrooves shown in previous research have some disadvantages. The optical interferometry based on phase change is a promising method due to its high throughput, noninvasiveness, feasibility in individual difference evaluation, high axial resolution and the potential of in-process measurement. However, because of the significant errors of the measured depths, the optical interferometry cannot be applied to depth measurement of diffraction-limited microgrooves. Hence, the focus of this research is to develop a novel optical depth measurement method, which (1) enables the

quantitative evaluation of the diffraction-limited microgrooves, having an aspect-ratio of 1, on different materials, with an accuracy of 10%, (2) is capable of the individual difference evaluation of each microgroove, and (3) has a depth measurement range optically greater than half of the incident wavelength, without the phase ambiguity problem. The contributions of this Ph.D. thesis can be divided into the following areas:

1.3.1 Far-field-based Near-field Reconstruction Depth Measurement(FNRDM)

As described in previous sections, due to the significant errors of the measured depths (see Fig. 1.9), the conventional optical interferometry based on phase change cannot be applied to depth measurement of diffraction-limited microgrooves. In order to overcome this problem, we proposed a novel technology, called Far-field-based Near-field Reconstruction Depth Measurement(FNRDM). FNRDM connects the depth information of diffraction-limited microgrooves with the near-field phase difference, which can be calculated from practical far-field optical observations rather than directly measured by specialized equipment, i.e., near-field scanning optical microscopy. Both the numerical analysis based on the FDTD method and some practical experiments are performed to demonstrate the validity of FNRDM. Further, the maximal measureable depth and the practical applicability of FNRDM are theoretically discussed.

1.3.2 A measurement system based on low-coherence illumination

In order to measure all the required far-field observations of the proposed FNRDM method, the designs of an infinite corrected imaging system, a Linnik interferometer and an incident plane wave unit are presented. Then, considering the spatially background noise caused by the laser speckle and the multiple interference from a transparent surface, the low-coherence illumination is used, achieved by a LED source and a carefully selected bandpass filter. Finally, an optical cage system is also exploited to achieve the spatially sensitive optical path-length measurement and temporally sensitive optical path-length measurement.

1.3.3 Noise-immune dual-wavelength interferometry

Since the phase of light is 2π periodic, the depths of microgrooves which are optically larger than half of the incident wavelength subject to the phase measurement ambiguity. In order to achieve the depth measurement of deep microgrooves, a noise-immune dual-wavelength interferometry was proposed. Using the noise-immune dual-wavelength interferometry, not only the depth measurement range can be extended, but also the noise level can be dramatically decreased to that in a single-wavelength phase map. Two experiments of measuring the diffraction-limited gratings on a silicon surface and a transparent polymer surface are implemented, to show that a combination of the proposed FNRDM method and the noise-immune dual-wavelength interferometry enables the quantitative depth evaluation of the diffraction limited and deep microgrooves with an accuracy of less than 10%. The combination also provides a potential of measuring the depth of diffraction-limited and steep microgrooves with high accuracy.

1.3.4 A novel phase unwrapping method using a Fluorinert liquid

A droplet-based phase unwrapping method using a Fluorinert liquid is also proposed to solve the phase ambiguity problem. This method includes the generation and combination of two phase maps under an air condition and a droplet condition. When the two phase maps are combined, the synthetic depth is equivalent to the depth measured by a longer wavelength based on the refractive index difference. In this method, a one-shot interferometry based on the Fourier Transform method, an auxiliary horizontal observation setup with high speed camera and a Fluorinert liquid with unique properties are presented. The proposed method enables the phase unwrapping by using only single-wavelength illumination, has a high temporal resolution and requires significantly less computational work than other least-squares integration technologies.

1.3.5 Discussion of the practical applicability of FNRDM

A further discussion about the practical applicability of FNRDM is demonstrated. The practical applicabilities to be investigated include versatile microgrooves with different internal conditions, grating structure and microhole structure. As long as the optical wave from the bottom surface is radiated to the far-field, FNRDM has the potential to evaluate the

depth. One of the important measurement characteristics of FNRDM is that we do not need a priori knowledge about the reflection efficiency from the bottom surface of microgrooves, which can be solved as an unknown information. Furthermore, when fully considering the contribution of top surface for grating structure and the polarization of incident beam for microhole structure, FNRDM also enables the quantitative depth evaluation with an accuracy of 10% beyond the diffraction limit. The discussion indicates that the proposed FNRDM method not only can be applied to depth measurement of fine microgrooves, but also has a potential to evaluate the depth of kinds of diffraction-limited microstructures.

1.4 Organization

This section is a summary of the research performed within the scope of this Ph.D. thesis, and the organization is shown in Fig. 1.10.

This chapter, **Chapter 1**, provides an introduction to the research background, concerning the functional microstructures and the state-of-the-art technology of depth measurement, and the research objectives.

Chapter 2 gives a brief introduction about the theory of diffraction, Fourier Optics, near-field optics and the FDTD method. Then, the near-field and far-field optical waves reflected from microgrooves based on the FDTD simulations are analyzed. The reason why the significant errors of depth measurement exist by optical interferometry based on phase change is elaborated. Finally, a novel optical depth measurement method was proposed, called Far-field-based Near-field Reconstruction Depth Measurement (FNRDM). FNRDM connects the depth information of diffraction-limited microgrooves with the near-field phase difference, which can be calculated from practical far-field optical observations rather than directly measured by specialized equipment, i.e., near-field scanning optical microscopy.

Chapter 3 presents a theoretical analysis to demonstrate the validity of FNRDM, when measuring the diffraction-limited microgrooves. Further, the detectable depth of FNRDM and the applicability under the noise condition are discussed.

Chapter 4 focuses on the development of the measurement system. A measurement system based on low-coherence illumination is developed to inspect the required far-field

observations of the proposed FNRDM method. Besides the feature of low-coherence illumination, the designs of this measurement system also include an infinite corrected imaging system, a Linnik interferometer, an incident plane wave unit and an optical cage system. Two experiments are performed to demonstrate that the developed measurement system not only provides speckle-free images, but also allows for spatially sensitive optical path-length measurement and temporally sensitive optical path-length measurement.

Chapter 5 describes an experiment to verify the validity of the proposed FNRDM method. The depth of 300-nm-wide nanochannels on a microfluidic sample are measured by both a AFM and the developed measurement system. By comparing the results between the two methods, it is clearly found that the measured depth by FNRDM has an accuracy of less than 10% beyond the diffraction limit (772 nm) of the measurement system. The experiment results suggest that FNRDM has the advantages of greatly improved accuracy over conventional interferometry and enables the individual difference evaluation of each nanochannel, which is not possible with scatterometry.

Chapter 6 gives a brief introduction about the phase wrapped problem and the conventional dual-wavelength interferometry. Then, a noise-immune phase unwrapping method was presented to extend the depth measurement range and make the noise level dramatically decreased to that in a single-wavelength phase map. By the FDTD method, the feasibility of the noise-immune phase unwrapping method is numerically analyzed. Next, two experiments are performed to demonstrate the validity of a combination of the proposed FNRDM method and the noise-immune dual-wavelength interferometry, when measuring the diffraction-limited and deep microgrooves. The experiment results suggest that the proposed method enables the quantitative depth evaluation of the diffraction-limited and deep microgrooves, on both silicon surface and the transparent polymer surface, with an accuracy of less than 10%, without the phase ambiguity problem. The combination also has a potential of measuring the depth of diffraction-limited and steep microgrooves with high accuracy.

Chapter 7 shows a novel phase unwrapping method using a Fluorinert liquid. This method includes the generation and combination of two phase maps under an air condition

and a droplet condition. When the two phase maps are combined, the synthetic depth is equivalent to the depth measured by a longer wavelength based on the refractive index difference. In order to achieve the droplet-based phase unwrapping method, a one-shot interferometry based on the Fourier Transform method, an auxiliary horizontal observation setup with high speed camera and a Fluorinert liquid with unique properties are presented. Based on the RCWA simulation, the numerical analysis for both the diffraction-free and diffraction-limited microgrooves are performed to verify the applicability of the droplet-based phase unwrapping method using a Fluorinert liquid.

Chapter 8 discusses the practical applicability of FNRDM. The practical applicabilities to be investigated include versatile microgrooves with different internal conditions, grating structure and microhole structure. The simulations based on the FDTD method are performed to demonstrate the validity of measuring the mentioned diffraction-limited microstructures by FNRDM.

Chapter 9 is conclusions and future work.

Background and objectives

Chapter 1 Introduction

- Functional microstructures
- State-of-the-art technology of quantitative depth measurement
- Objectives

Proposal of optical depth measurement method

Chapter 2 Proposal for optical depth measurement of diffraction-limited microgrooves

- Theory of diffraction, Fourier Optics and near-field optics
- The FDTD method
- Numerical analysis of far-field imaging forming of diffraction-limited microgrooves
- Proposal: Far-filed-based Near-field Reconstruction Depth Measurement (FNRDM)

Experiment verification of FNRDM

Chapter 4 Measurement system based on low-coherence illumination

- Designs of the measurement system
- Low-coherence illumination
- Speckle-free imaging
- Temporal and spatial sensitivies of measurement system

Theoretical verification of FNRDM

Chapter 3 Numerical analysis of the proposed FRNDM method

- Numerical analysis of the feasibility of FNRDM
- Detectable depth of FNRDM
- Applicabilities under noise condition

Chapter 5 Experiment verification of FNRDM beyond the diffraction limit

- A transparent microfluidic sample with nanochannels
- AFM measurement
- Measurement by the developed setup and FNRDM

The phase unwrapping methods

Chapter 6 Phase unwrapping based on dual-wavelength interferometry

- A noise-immune phase unwrapping method
- Numerical analysis by the FDTD method
- A combination of FNRDM and the noise-immune dual-wavelength interferometry
- Two experiments

Chapter 7 Numerical analysis of a novel phase unwrapping method using a Fluorinert droplet

- Droplet-based phase unwrapping method
- A Fluorinert liquid
- One-shot interferometry
- Analysis based on RCWA simulations

Practical applicabilities of FRNDM

Chapter 8 Numerical analysis of the practical applicability of FNRDM

- Diffraction-limited microgrooves with versatile conditions: tapered structure, micro roughness, coating conditions, PMMA material, etc.
- Diffraction-limited grating structures
- Diffraction-limited microhole

Summary

Chapter 9 Conclusions and future work

Figure 1.10 Structure of organization of this thesis

Chapter 2. Proposal for optical depth measurement of diffraction-limited microgrooves

This chapter gives a brief introduction about the theory of diffraction, Fourier Optics, near-field optics, to develop an understanding of the way optical systems process light to form images. Then, the finite-difference time-domain (FDTD) method is presented, which is a numerical tool for modeling computational electrodynamics and extremely useful in analyzing the electromagnetic fields in both near-field and the far-field. Next, both the near-field and far-field optical waves reflected from microgrooves are analyzed by the FDTD method. The results showed the far-field optical response forming mechanism of diffraction-limited microgrooves and explained why the significant errors exist in depth measurement by optical interferometry based on phase change, descried in Chapter 1. Finally, according to this analysis, we proposed a novel optical depth measurement method which enables the quantitative depth evaluation of diffraction-limited microgrooves with high accuracy. The proposed method is called Far-field-based Near-field Reconstruction Depth Measurement (FNRDM). FNRDM connects the depth information of diffraction-limited microgrooves with the near-field phase difference, which can be calculated from practical far-field optical observations rather than directly measured by specialized equipment, i.e., near-field scanning optical microscopy.

2.1 Optical image formation

In any optical imaging system, light must propagate from the source to the object, where it is absorbed or scattered or reflected etc., and then from the object to the recorder. The theory of diffraction [63][64][65], covering both free-space propagation and propagation through apertures, and Fourier optics [66] are important for the understanding of optical image formation.

2.1.1 Theory of diffraction [63]

Suppose that we have an aperture in a screen illuminated from behind by a point light source, and we want to determine the field at an observation plane with a distance from the aperture. The key idea is the Huygens-Fresnel principle, which is a superposition concept. The field at any point in the observation plane is the superposition of the contributions from each point in the aperture plane, where we can think of each such point as a point source emitting a spherical wave. As illustrated in Fig. 2.1, $E_1(x_1, y_1)$ and $E_2(x_2, y_2)$ denote the complex amplitudes of electrical fields at an arbitrary point (x_1, y_1) in the aperture plane and an arbitrary point (x_2, y_2) in the observation plane, respectively. r is the propagating distance between E_1 and E_2. z is the distance between aperture plane and observation plane. According to Huygens-Fresnel Principle, point (x_1, y_1) within the aperture may be envisioned as being covered with coherent secondary point sources. Thus, $E_2(x_2, y_2)$ can be obtained by adding all optical waves that radiate from the aperture plane. This addition can also be written as a so-called superposition integral, given by Eq. (2.1).
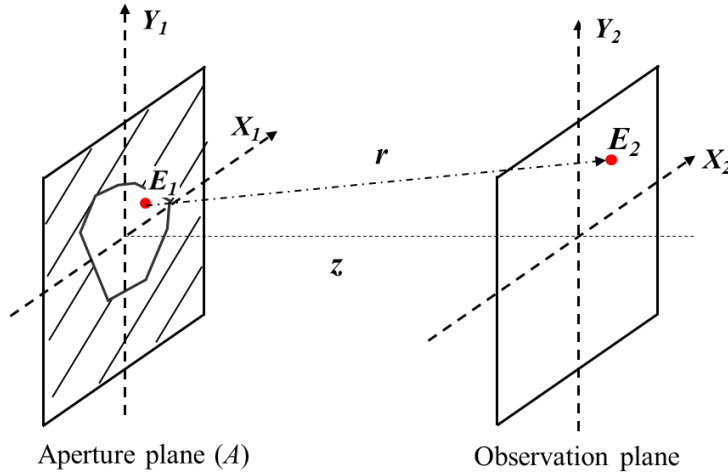
Figure 2.1 Diffraction from an arbitrary aperture.

$$E_2 = \frac{1}{i\lambda} \int_A \frac{E_1}{r} \exp(ikr) K(\chi) dA \qquad (2.1)$$

Where k is the wave vector and equal with $2\pi/\lambda$, $K(\chi)$ is the obliquity factor, χ is the diffraction angle. If the point light source is far away from the aperture plane and the incident beam irradiating on the aperture plane can be regarded as the plane wave illumination, Kirchhoff gave the following expression for $K(\chi)$:

$$K(\chi) = \frac{1 + \cos \chi}{2} \tag{2.2}$$

Then, if the distance (z) between aperture plane and observation plane is much larger than Fresnel distance (R_F), given by Eq. (2.3), the relation between $E_1(x_1, y_1)$ and $E_2(x_2, y_2)$ can be written as Eq. (2.4), which is the so-called Fraunhofer diffraction regime.

$$R_F = \frac{(x_1^2 + y_1^2)_{max}}{\lambda} \tag{2.3}$$

$$E_2(x_2, y_2) = \frac{\exp(ikz)}{i\lambda z} \exp(\frac{ik}{2z}(x_2^2 + y_2^2)) \iint E_1(x_1, y_1) \exp(-ik\frac{x_1 x_2 + y_1 y_2}{z}) dx_1 dy_1 \tag{2.4}$$

For a sufficiently large z and sufficiently small x_2 and y_2, the relation between them satisfies Eq. (2.5). Under that condition, the relation between $E_1(x_1, y_1)$ and $E_2(x_2, y_2)$ becomes a pure Fourier transform, shown in Eq. (2.6). In other words, the field distribution in the Fraunhofer diffraction pattern is the Fourier transform of the field distribution across the aperture.

$$\frac{x_2^2 + y_2^2}{z} << 1 \tag{2.5}$$

$$E_2(x_2, y_2) = \frac{\exp(ikz)}{i\lambda z} \iint E_1(x_1, y_1) \exp(-ik\frac{x_1 x_2 + y_1 y_2}{z}) dx_1 dy_1 \tag{2.6}$$

As depicted in Fig. 2.2, a monochromatic plane wave propagating is incident on the circular aperture with a radius of a. Assume that ε_A is the source strength per unit area in the aperture plane and ε_A is constant over the entire aperture. For a circular opening, polar coordinates are suggested in mathematical calculation. In the observation plane, q denotes the polar radius for an arbitrary point M on the observation plane. Then, the irradiance at point M is given by Eq. (2.7).
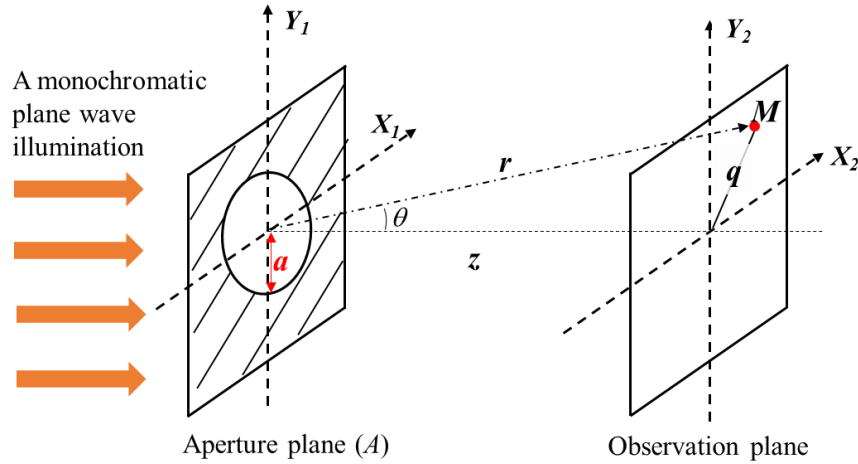
Fig. 2.2 Fraunhofer diffraction at a circular aperture.

$$I(M) = \frac{2\varepsilon_A^2(\pi a^2)^2}{r^2}\left[\frac{J_1(kaq/r)}{kaq/r}\right]^2 \tag{2.7}$$

The irradiance $I(0)$ at the center of the pattern on the observation plane is

$$I(0) = \frac{\varepsilon_A^2(\pi a^2)^2}{2r^2} \tag{2.8}$$

If r is assumed to be essentially constant over the pattern, we can write

$$I(\theta) = I(0)\left[\frac{2J_1(ka\sin\theta)}{ka\sin\theta}\right]^2 \tag{2.9}$$

Where $\sin\theta = q/r$. Such a pattern is plotted in Fig. 2.3. Because of the axial symmetry, the towering central maximum corresponds to a high-irradiance circular spot known as the Airy disk. The central disk is surrounded by a dark ring that corresponds to the first zero of the function $J_1(u)$. It is known that $J_1(u) = 0$ when $u = 3.83$, that is, $kaq/r = 3.83$. The radius q_1 drawn to the center of this first dark ring can be thought of as the extent of the Airy disk. It is given by

$$q_1 = 1.22\frac{r\lambda}{2a} \tag{2.10}$$
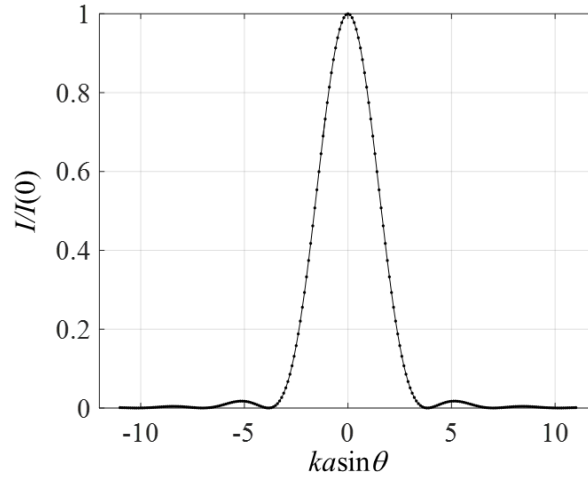
Fig. 2.3 The Airy pattern.

For a lens focused on the observation plane, the focal length $f \approx r$, so

$$q_1 = 1.22 \frac{f\lambda}{D} \qquad (2.11)$$

Where D is the aperture diameter. According to the Rayleigh Criterion, two points are said to be just resolved when the center of one Airy disk falls on the first minimum of another Airy pattern. For a microscopy, the diffraction limit is given

$$d = \frac{0.61 \times \lambda}{NA} \qquad (2.12)$$

with d the lateral resolution, λ the wavelength and NA the numerical aperture of the objectives.

2.1.2 Fourier optics [63-65]

In any optical imaging system, the light propagates both free space and lenses. A lens can also perform a Fourier transform. As shown in Fig. 2.4, if the electric field in the front focal plane of a lens is $E_1(x_1, y_1)$, then the electric field $E_2(x_2, y_2)$ in the back focal plane is:

27
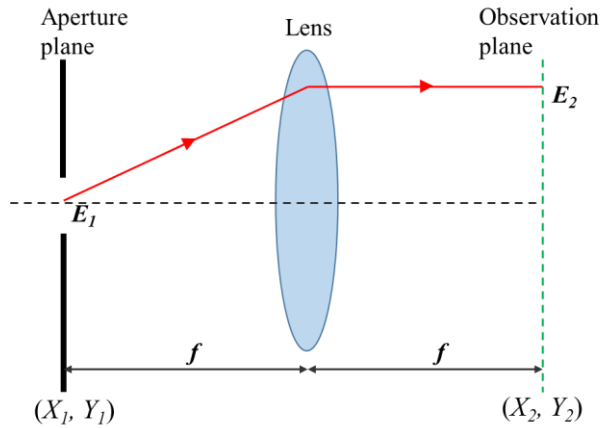
Fig. 2.4 A lens performing a Fourier transform.

$$E_2(x_2, y_2) = \frac{\exp(ikf)}{i\lambda f} \iint E_1(x_1, y_1) \exp(-ik \frac{x_1 x_2 + y_1 y_2}{f}) dx_1 dy_1 \qquad (2.13)$$

Where f is the focal length of the lens. It is found that Eq. (2.13) is the same with Eq. (2.6) by substituting distance z with the focal length f. Therefore, we can bring the observation plane in close to the aperture without changing the Fraunhofer diffraction pattern by using a focusing lens.

Fourier techniques give a framework to describe how to form images. The imaging system is linear and space invariant. Consider the self-luminous and incoherent source depicted in Fig. 2.5. We can imagine that each point on the object plane (S_o) emits light that is processed by the optical system. The scattering light emerges to form a spot on the image plane (S_i). In addition, assume that the magnification between object and image planes is 1. If $dudv$ is a differential element located at (u, v) on the object plane, then the element will emit a radiant flux of $I_0(u, v)dudv$. Because of diffraction (and the possible presence of aberrations), this light is smeared out into some sort of blur spot over a finite area on the image plane rather than focused to a point. According to the sifting property of the delta function, the irradiance distribution $I_0(x, y)$ on the object plane can be written as

$$I_o(x, y) = \iint I_o(u, v) \delta(x - u, y - v) dudv \qquad (2.14)$$
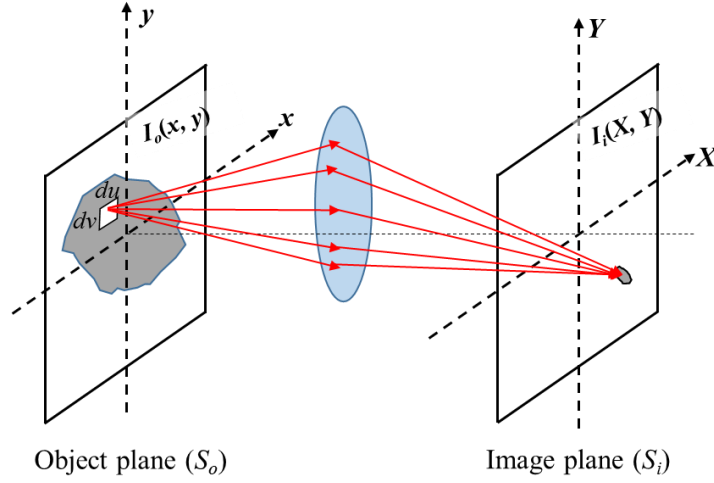
Fig. 2.5 A lens system forming an image.

$I_0(x, y)$ can be regarded as a linear combination of elementary delta functions, each weighted by a number $I_0(u, v)$. Therefore, the irradiance distribution $I_i(X, Y)$ on the image plane is the superposition of the images formed by each delta function, which is expressed in Eq. (2.15).

$$I_i(X,Y) = \iint I_o(x, y)h(X - x, Y - y)dxdy \qquad (2.15)$$

Where function h is the so-called impulse response, which is the response of the system to a delta function. And in optics, function h is the point spread function (*PSF*). In a well-corrected system, *PSF* is the Airy irradiance function (Eq. (2.9)) centered on the Gaussian image point, given by Eq. (2.16).

$$psf = \left[\frac{2J_1(ka\sin\theta)}{ka\sin\theta} \right]^2 \qquad (2.16)$$

From Eq. (2.15), $I_i(X, Y)$ is a superposition over weighted *PSF*s in the image plane using the same weighting function as in the object plane. This equation is also the so-called convolution integral in two dimensions. Therefore, under the circumstance of incoherent illumination, the irradiance distribution on the image plane is the convolution of the irradiance distribution on the object plane and point spread function, given by Eq. (2.17).

$$I_i(X,Y) = I_o(x, y) \otimes psf \qquad (2.17)$$

If the light source is coherent light, then analysis of optical imaging will be based on complex amplitudes of electric fields. Once more the resulting image would be described by a spread function, although it would be an amplitude spread function (*asf*). Shown in Eq. (2.18), the complex amplitude $E_i(X, Y)$ on the image plane is the convolution of the complex amplitude $E_o(x, y)$ on the object plane and amplitude spread function.

$$E_i(X,Y) = E_o(x,y) \otimes asf \qquad (2.18)$$

2.2 Near-field optics and the FDTD method

2.2.1 Near-field optics

In optics, the near-field and far-field are regions of the electric field around an object. As an object scatters incident illumination, there are two types of waves: (a) the propagating wave and (b) non-propagating wave or evanescent wave. Near-field optical waves [67][68], composed of both propagating components and non-propagating waves, are localized to the source region of optical radiation or to the surfaces of materials interacting with free radiation, i.e. the electric field on the object plane in section 2.1.2. While far-field optical waves are at greater distances away from the object, i.e. the electric field on the image plane in section 2.1.2. Generally, the near-field region is characterized by the region in space where the evanescent waves cannot be neglected. Because of its exponential distance dependence, the evanescent wave cannot exist in free-space and is restricted to material boundaries, making it impossible to decouple the evanescent wave from its source. Consequently, an evanescent wave cannot exist in the absence of other waves in space.

In many situations, near-field optical waves are explored for their ability to localize optical energy to length scales smaller than the diffraction limit. This localization is being explored for ultrasensitive detection and for high-resolution optical microscopy and spectroscopy. Compared with far-field optical waves, the physical properties of near-field optical waves are drastically different, such as spatial and temporal coherence, the polarization state and thermal energy density.

2.2.2 The FDTD method

Although near-field optical waves contain high spatial frequency information that defines smaller features, they are confined in the near-filed region of test structures and cannot be observed without specialized equipment, i.e., near-field scanning optical microscopy [69][70][71]. The finite-difference time-domain (FDTD) method is a very useful technique to analyze the electromagnetic fields in both the near-field and the far-field scattered from a complex geometrical object [72][73][74].

The FDTD method has been widely used to solve Maxwell's Equations in the electromagnetic interactions between different objects. The basic mathematical and physics formalism behind the FDTD algorithm is discussed as an indispensable background in this section [75].

The simplest statement of Maxwell's Equations applies to the behavior of the electric and magnetic fields in free space with no charges and no currents. In that instance,

$$\begin{aligned} \nabla \cdot E &= 0 \\ \nabla \cdot B &= 0 \\ \nabla \times E &= -\frac{\partial B}{\partial t} \\ \nabla \times H &= \frac{\partial D}{\partial t} \end{aligned}$$
(2.19)

Where D, E, B and H are electric flux density, electric field, magnetic flux density and magnetic field, respectively. $\nabla\cdot$ and $\nabla\times$ symbols denote the divergence operator and the curl operator. Consider the general environment as a liner, homogeneous and isotropic medium, which is physically at rest, the constitutive relations are:

$$\begin{aligned} D &= \varepsilon E \\ B &= \mu H \end{aligned}$$
(2.20)

Where ε and μ are dielectric constant and magnetic permeability, respectively. In three dimensions, Maxwell Equations have six electromagnetic field components. With the assumption that the structure is infinite in the z dimension and that the fields are independent of z, the Maxwell's equations are split into two independent groups of equations (Eq. (2.21) and (2.22)) that can be solved in the xy plane only, which results in the transverse electric

(TE) and transverse magnetic (TM) equations. Then, we can use the components of E_x, E_y, and H_z to solve TE equations and those of H_x, H_y, and E_z to solve TM equations.

$$\frac{\partial E_z}{\partial y} - \frac{\partial E_y}{\partial z} = -\mu \frac{\partial H_x}{t}$$

$$\frac{\partial E_x}{\partial z} - \frac{\partial E_z}{\partial x} = -\mu \frac{\partial H_y}{t} \tag{2.21}$$

$$\frac{\partial E_y}{\partial x} - \frac{\partial E_x}{\partial y} = -\mu \frac{\partial H_z}{t}$$

$$\frac{\partial H_z}{\partial y} - \frac{\partial H_y}{\partial z} = \varepsilon \frac{\partial E_x}{t}$$

$$\frac{\partial H_x}{\partial z} - \frac{\partial H_z}{\partial x} = \varepsilon \frac{\partial E_y}{t} \tag{2.22}$$

$$\frac{\partial H_y}{\partial x} - \frac{\partial H_x}{\partial y} = \varepsilon \frac{\partial E_z}{t}$$

A schematic of three-dimensional Yee Cell in the FDTD method is shown in Fig. 2.6. It contains six electromagnetic field components: electric fields of E_x, E_y, E_z and magnetic fields of H_x, H_y, H_z. The use of the FDTD method is based on the discretization of the whole area into numbers of cells. As shown in Fig. 2.6, determined spatial distributions of electromagnetic field components are assigned in certain points of the area (x, y, z), taking into account discrete and finite step size $(\Delta x, \Delta y, \Delta z)$.
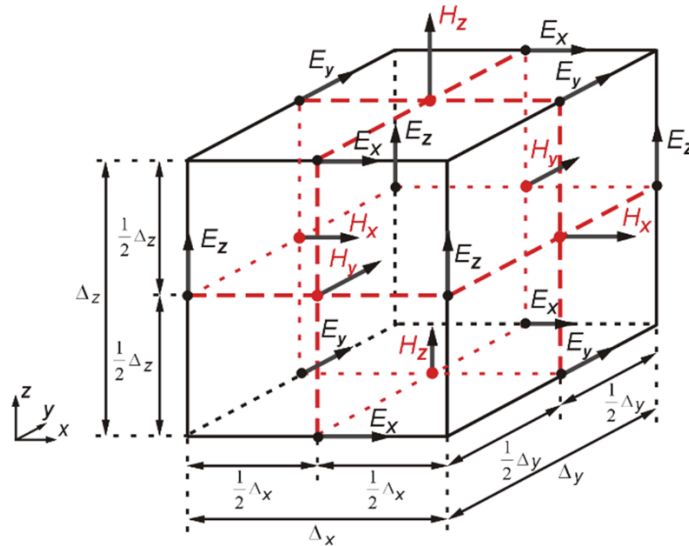
Figure 2.6 Schematic of Yee Cell in the FDTD method.

32

Yee's scheme also consists in considering electric field and magnetic field shifted in space by half a cell and in time by half a time step via the central difference approximation. Considering that the function $f(x,y,z,t)$ denotes the electric or magnetic field in the coordinate system, it can be discretized as

$$
\begin{aligned}
\frac{\partial f(x,y,z,t)}{\partial x}\Big|_{x=i\Delta x} &= \frac{f^n(i+0.5, j, k) - f^n(i+0.5, j, k)}{\Delta x} \\
\frac{\partial f(x,y,z,t)}{\partial y}\Big|_{y=j\Delta y} &= \frac{f^n(i, j+0.5, k) - f^n(i, j-0.5, k)}{\Delta y} \\
\frac{\partial f(x,y,z,t)}{\partial x}\Big|_{z=k\Delta z} &= \frac{f^n(i, j, k+0.5) - f^n(i, j, k-0.5)}{\Delta z} \\
\frac{\partial f(x,y,z,t)}{\partial t}\Big|_{t=n\Delta t} &= \frac{f^{n+0.5}(i, j, k) - f^{n-0.5}(i, j, k)}{\Delta t}
\end{aligned}
\tag{2.23}
$$

Where Δx, Δy and Δz are the spatial offset between sample points, and Δt is the temporal offset. The index i, j and k correspond to the spatial steps (effectively the spatial location), while the index n corresponds to the temporal step. By substituting Eq. (2.23) to Eq. (2.21) and (2.22), we can obtain the update equation for both electric field and magnetic field.

$$
\begin{aligned}
E_x^n(i,j,k) &= E_x^{n-1}(i,j,k) + \\
\frac{\Delta t}{\varepsilon}\Big(& \frac{H_z^{n+0.5}(i, j+0.5, k) - H_z^{n+0.5}(i, j-0.5, k)}{\Delta y} - \frac{H_y^{n+0.5}(i, j, k+0.5) - H_y^{n+0.5}(i, j, k-0.5)}{\Delta z}\Big) \\
E_y^n(i,j,k) &= E_y^{n-1}(i,j,k) + \\
\frac{\Delta t}{\varepsilon}\Big(& \frac{H_x^{n+0.5}(i, j, k+0.5) - H_x^{n+0.5}(i, j, k-0.5)}{\Delta z} - \frac{H_z^{n+0.5}(i+0.5, j, k) - H_z^{n+0.5}(i-0.5, j, k)}{\Delta x}\Big) \\
E_z^n(i,j,k) &= E_z^{n-1}(i,j,k) + \\
\frac{\Delta t}{\varepsilon}\Big(& \frac{H_y^{n+0.5}(i+0.5, j, k) - H_y^{n+0.5}(i-0.5, j, k)}{\Delta x} - \frac{H_x^{n+0.5}(i, j+0.5, k) - H_x^{n+0.5}(i, j-0.5, k)}{\Delta y}\Big)
\end{aligned}
\tag{2.24}
$$

$$H_x^n(i,j,k) = H_x^{n-1}(i,j,k) -$$
$$\frac{\Delta t}{\mu}(\frac{E_z^{n+0.5}(i,j+0.5,k) - E_z^{n+0.5}(i,j-0.5,k)}{\Delta y} - \frac{E_y^{n+0.5}(i,j,k+0.5) - E_y^{n+0.5}(i,j,k-0.5)}{\Delta z})$$
$$H_y^n(i,j,k) = H_y^{n-1}(i,j,k) -$$
$$\frac{\Delta t}{\mu}(\frac{E_x^{n+0.5}(i,j,k+0.5) - E_x^{n+0.5}(i,j,k-0.5)}{\Delta z} - \frac{E_z^{n+0.5}(i+0.5,j,k) - E_z^{n+0.5}(i-0.5,j,k)}{\Delta x})$$
$$H_z^n(i,j,k) = H_z^{n-1}(i,j,k) -$$
$$\frac{\Delta t}{\mu}(\frac{E_y^{n+0.5}(i+0.5,j,k) - E_y^{n+0.5}(i-0.5,j,k)}{\Delta x} - \frac{E_x^{n+0.5}(i,j+0.5,k) - E_x^{n+0.5}(i,j-0.5,k)}{\Delta y}) \tag{2.25}$$

Eq. (2.24) and (2.25) are generic equations which can be applied to any magnetic-field node. It is found that the future value of electric field (or magnetic field) depends on only its previous value and the neighboring magnetic fields (or electric fields).

It has been verified that at least 10 cells per wavelength are necessary to ensure an adequate representation. The wavelength to consider is the smallest wavelength in the simulation. Once the cell size has been chosen, the time step is also chosen according to stability considerations. The time increment (Δt) has to obey the following bound, known as Courant-Freidrichs-Lewy (CFL) stability criterion [76], is given as

$$\Delta t \leq \frac{1}{c\sqrt{(\Delta x)^2 + (\Delta y)^2 + (\Delta z)^2}} \tag{2.26}$$

Where c is propagation speed of the light. Although the FDTD method has a high requirement of memory and simulation time, the advantages of the FDTD method include the incorporation of the effects of reflection and emission, modeling wave propagation in complex media, etc.

2.3 Numerical analysis of near-field and far-field optical responses from microgrooves

2.3.1 Simulation setup

Figure 2.7 shows both the far-field and near-field optical waves when optical methods based on phase change are applied in depth measurement of microgrooves. A microgroove

structure is illuminated by an incident plane wave, and the depth of the microgroove structure is proportional to the practically detected far-field phase difference (θ) between the top surface and bottom surface, according to conventional optical methods based on phase change.
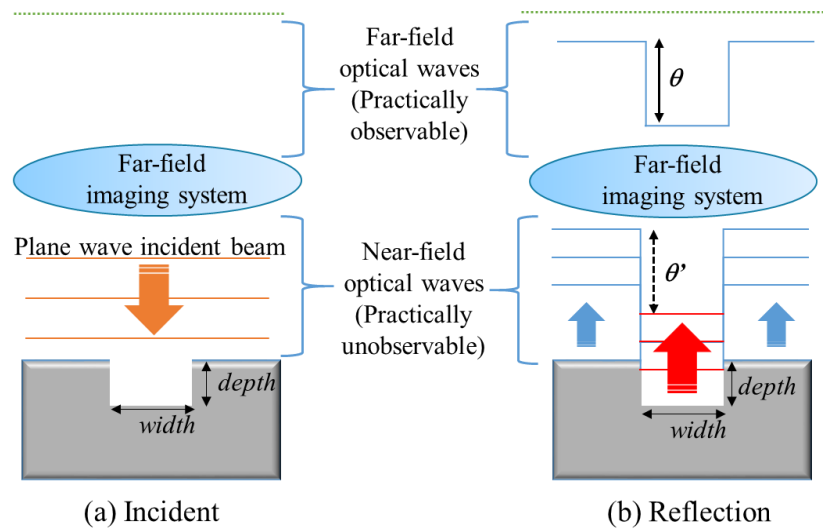
Figure 2.7 Far-field and near-field optical waves of microgrooves

The FDTD method is applied to analyze both the near-field and far-field optical waves from the microgroove. In this PhD thesis, we use a commercial software (Rsoft) to implement the FDTD method. In this Chapter, the details of the simulation setup of the FDTD method were concluded as follows.

(a) Define the physical structures and a light source. As illustrated in Fig. 2.8, it is the schematic of the microgroove model, where a silicon microgroove structure is illuminated by a plane wave with a wavelength of 488 nm. The incident beam propagates along the z direction, and the distance between the light source and the top surface of the microgroove is 1 μm.
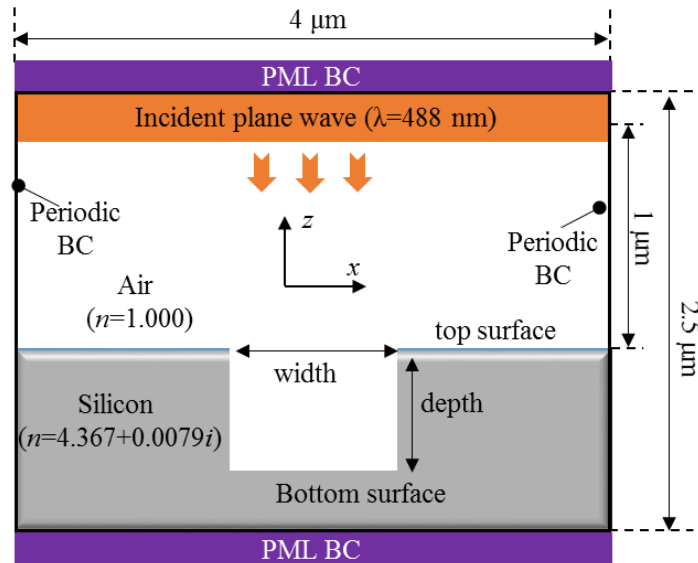
Figure 2.8 The FDTD simulation of a silicon microgroove structure

(b) Define a simulation region and boundary conditions. Both the reliable results and the requirements of memory and simulation time should be taken into account. The width and height of the simulation region in Fig. 2.8 are 4 μm and 2.5 μm, respectively. Setting reasonable mesh size is crucial. Here, the mesh size is set as 5 nm. In addition to the mesh size, we need to define how the electromagnetic fields behave at the boundaries of the simulation region. By default, Rsoft uses Perfectly Matched Layer (PML) boundary conditions (BC) [77][78]. A PML boundary consists of several grid points added to the edge of the domain and is designed to act as a highly lossy material that absorbs all incident energy without producing reflections. This allows field energy which is incident on the boundary to effectively leave the region. A periodic boundary stipulates that any field which leaves the boundary on one side of the domain should reenter the domain on the opposite side. Hence, as shown in Fig. 2.8, PML boundary conditions are set at the upside and downside of the simulation region, while periodic boundary conditions are used at the left and right sides of the simulation region.

(c) Define monitors to record data for analysis. The complex amplitudes of electric field in *xz* plane are recorded by using frequency analysis.

2.3.2 Influence of polarization

Before the phase analysis for depth measurement, the polarization state of incident beam is discussed when measuring the microgroove structure.1000-nm-wide and 200-nm-wide microgrooves are simulated in the same settings (described model in Fig. 2.8), with a same depth (300 nm), under P polarization and S polarization, respectively. Figure 2.9 depicts the near-field amplitude distribution resulting from the interaction of the incident light with a 1000-nm-wide microgroove under different polarizations, while the results of 200-nm-wide microgroove are shown in Fig. 2.10. In Fig. 2.9 and 2.10, the grey layers are inserted to hide the electric fields inside the silicon material, and the displayed amplitudes are normalized. It is found that the near-field amplitude distribution resulting from the interaction of the incident light and the microgroove is affected by the applied polarization. And the microgroove with a width greater than half of the wavelength is less affected by the polarization state. It is concluded that a polarized incident wave of perpendicular to the inner wall (P polarization) is useful to deliver light energy to the bottom surface of the microgroove, even for a width less than half of the wavelength. Hence, P polarization is used in the following two-dimensional simulation models for the phase analysis.
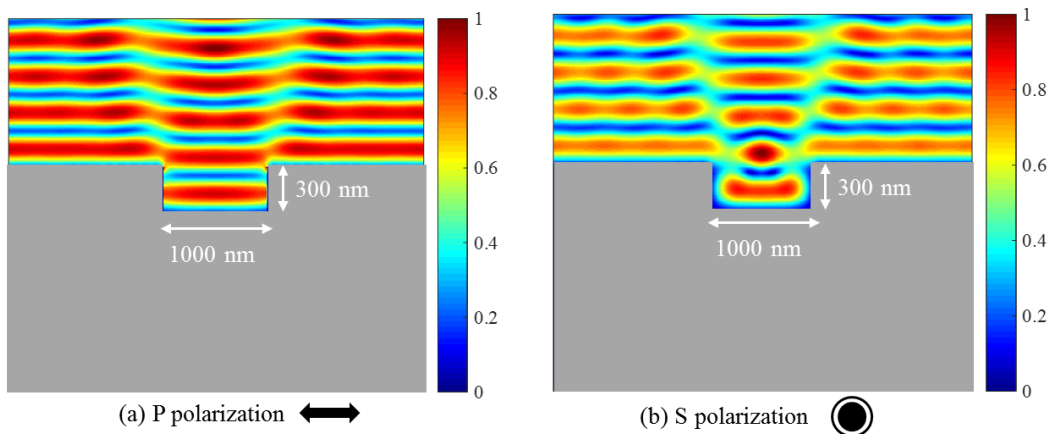
Figure 2.9 The near-field amplitude distribution resulting from the interaction of the incident light with a 1000-nm-wide microgroove under different polarizations: (a) P polarization and (b) S polarization.

(a) P polarization ⟷ (b) S polarization ⊙
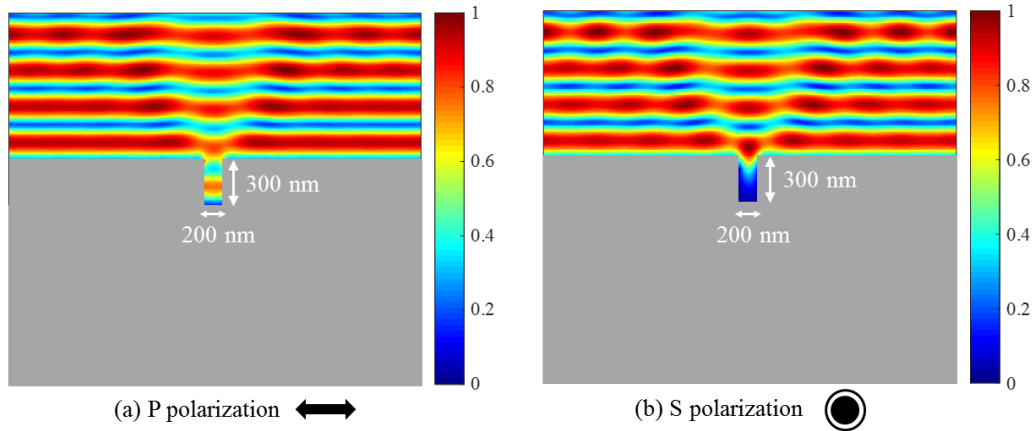
Figure 2.10 The near-field amplitude distribution resulting from the interaction of the incident light with a 200-nm-wide microgroove under different polarizations: (a) P polarization and (b) S polarization.

2.3.3 Phases analysis of diffraction-free and diffraction-limited microgrooves

In this research, the phase information of reflected optical waves is the component of interest. The FDTD method can simulate reflections but cannot distinguish between a forward and backward traveling field. As shown in Fig. 2.11(a), the same but simplified version of the microgroove model (Fig. 2.8), the recorded complex amplitude in a grid includes both the incident beam (E_i) and the reflected beam (E_r). In order to extract only the reflected component, we simulated another model, named as air model illustrated in Fig. 2.11(b), where only the silicon microgroove is deleted but other settings are kept the same with the microgroove model. The recorded data in the air model contains only the incident electric field (E_i) which has the same value with the microgroove model. Through a subtraction process of the data between the two simulation models, the reflected electric field can be obtained for further post-processing.
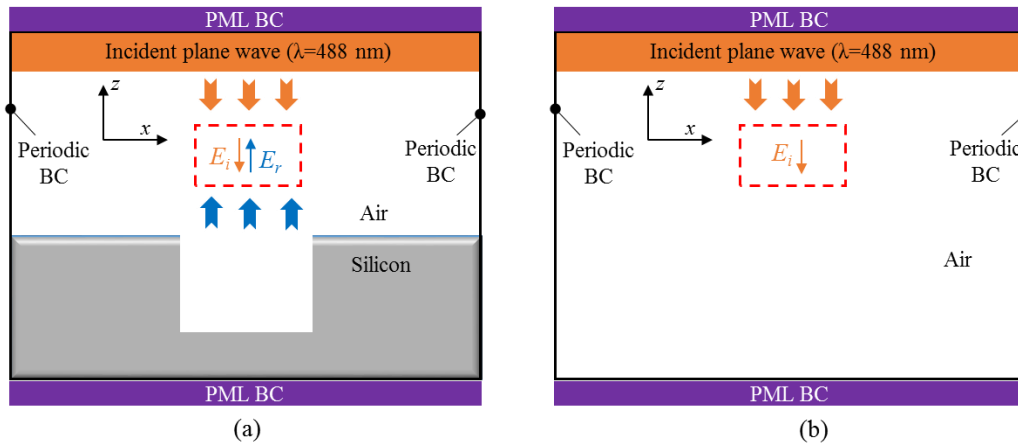
Fig. 2.11 Schematic of the recorded data in a grid size of (a) the microgroove model and (b) the air model.

Figure 2.12 plots a schematic of analyzing the reflected phase information from the microgrooves by the FDTD method. The basic settings are the same with Fig. 2.8 and the applied polarization is P polarization. Two types of microgrooves with different widths (1000 nm and 200 nm) and same depth (300 nm) are simulated. The NN' plane is the near-field recording plane, which is 20 nm above the top surface of microgrooves, while FF' plane is the far-field imaging plane with the *NA* of 0.55. The diffraction limit of the imaging system is 540 nm. Figure 2.13 shows the near-field phase distributions for 1000-nm-wide and 200-nm-wide microgrooves, while the corresponding far-field phase distributions are plotted in Fig. 2.14 according to the theory of optical image formation. It is found that the near-field phase distributions are extremely similar between the diffraction-free 1000-nm-wide microgroove (Fig. 2.13(a)) and the diffraction-limited 200-nm-wide microgroove (Fig. 2.13(b)). However, such a similarity cannot be found in the far-field plane. For the diffraction-free microgroove, the obvious phase difference between the top surface and the bottom surface can be observed, and the far-filed and near-field phase differences are almost the same, which indicates the feasibility of depth evaluation of diffraction-free microgrooves by conventional optical interferometry. However, in the case of diffraction-limited 200-nm-wide microgroove, only a minute far-field phase difference can be observed (Fig. 2.14(b)).

(a)   (b)
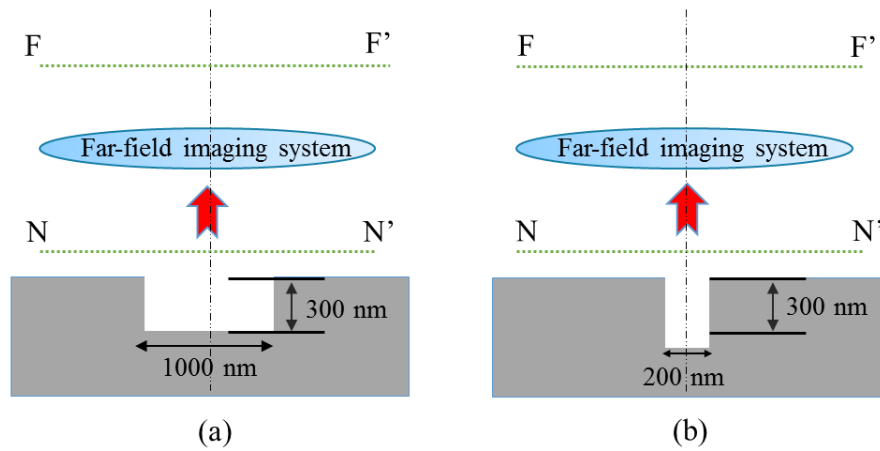
Figure 2.12 A schematic of analyzing the reflected phase information from the microgrooves by the FDTD method: (a) a diffraction-free microgroove and (b) a diffraction-limited microgroove

(a) Width = 1000 nm   (b) Width = 200 nm
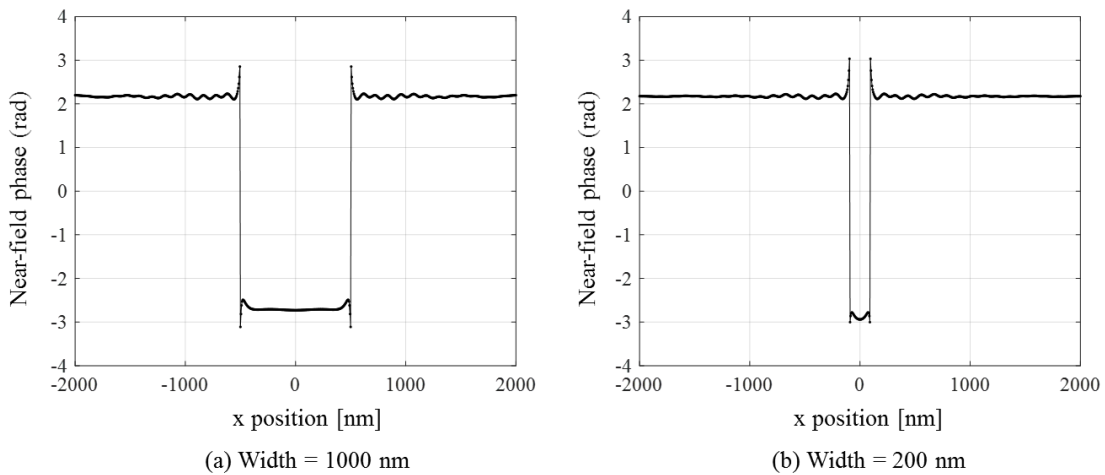
Figure 2.13 The near-field phase distributions reflected from: (a) a diffraction-free microgroove and (b) a diffraction-limited microgroove
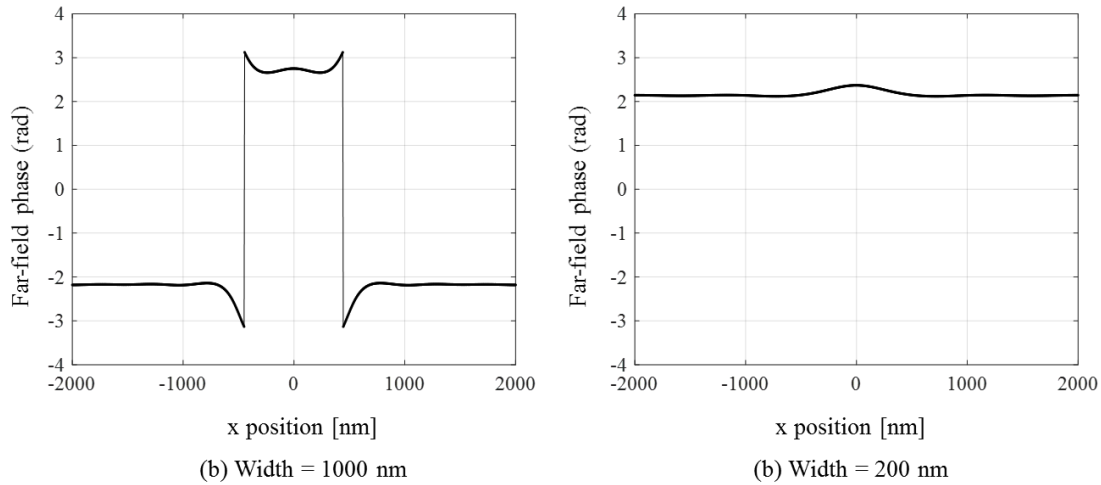
Figure 2.14 The far-field phase distributions reflected from: (a) a diffraction-free microgroove and (b) a diffraction-limited microgroove

For a further understanding, we simulated the performance of phase distribution when the depths of both the diffraction-free and diffraction-limited microgrooves vary. The phase at the central position of the microgroove is used to calculate the phase difference and the corresponding depth information by Eq. (1.2). Figure 2.15 plots the measured depths from near-field phase differences as a function of simulated depths, while the results from far-field phase differences are illustrated in Fig. 2.16, which is the same with Fig. 1.9. As the simulated depths increase, both far-field and near-field phase differences can be applied in depth evaluation with high accuracy for the diffraction-free microgrooves. However, for the diffraction-limited microgroove, the measured depths cannot accurately reflect the depth information by using far-field phase differences, but the results by near-field phase differences are almost coincident with the theoretical values, similar to the results of diffraction-free microgroove.
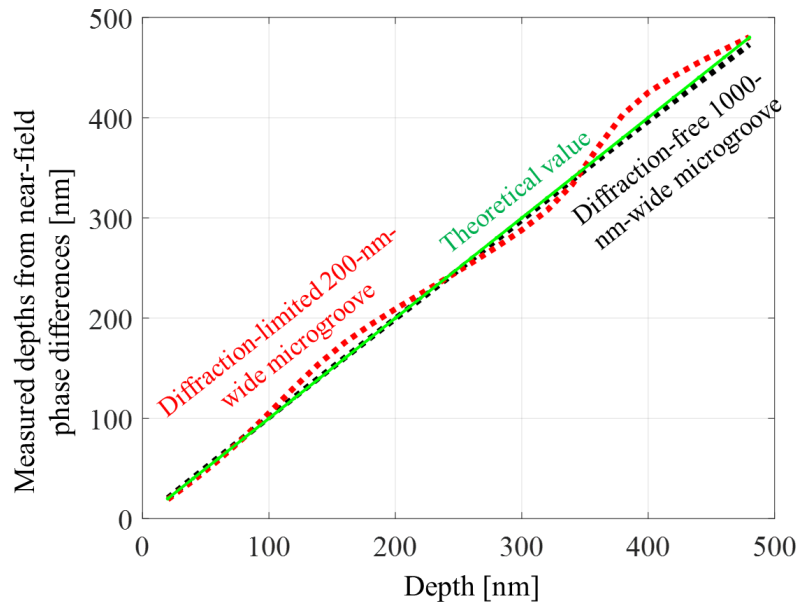
Figure 2.15 Measured depths using near-field phase differences.
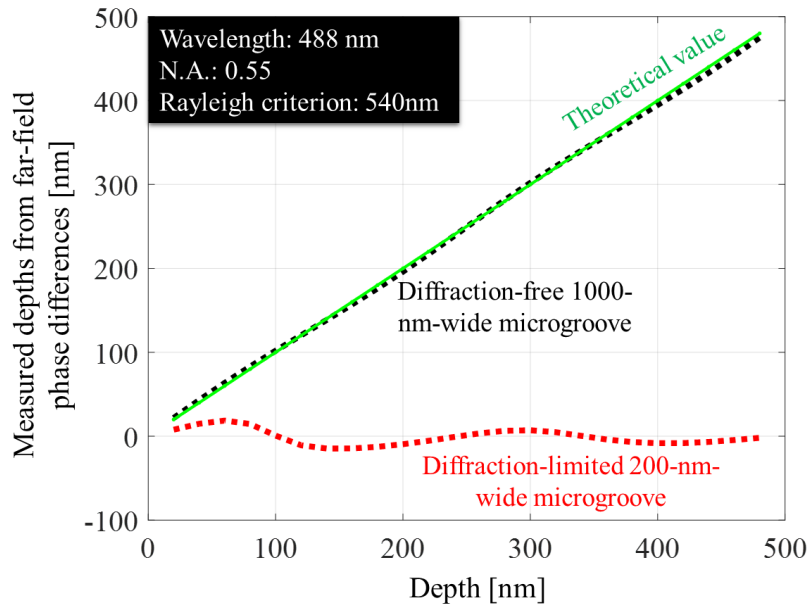
Figure 2.16 Measured depths using far-field phase differences.

The discrepancy of measured depths between near-field phase difference and far-field phase difference for the diffraction limited microgroove can be explained by Fig. 2.17. According to the theory of optical imaging formation, a far-field image is formed by the

convolution of the complex amplitude of the near-field optical wave from the target surface and the amplitude spread function of the employed imaging system. In the case of the diffraction-free microgroove (Fig. 2.17(a)), the far-field optical wave at the opening position of the microgroove totally originates from the bottom surface, and the far-field phase difference (θ_f) is equal to the near-field phase difference (θ_n) resulting in the original depth information. Nevertheless, for the diffraction-limited microgrooves (Fig. 2.17(b)), at the opening position of the microgroove on the far-field imaging plane, there are contributions of the top surface reflection due to the spread of *asf*. As a result, θ_f is decreased than θ_n and cannot accurately reflect the original depth information.
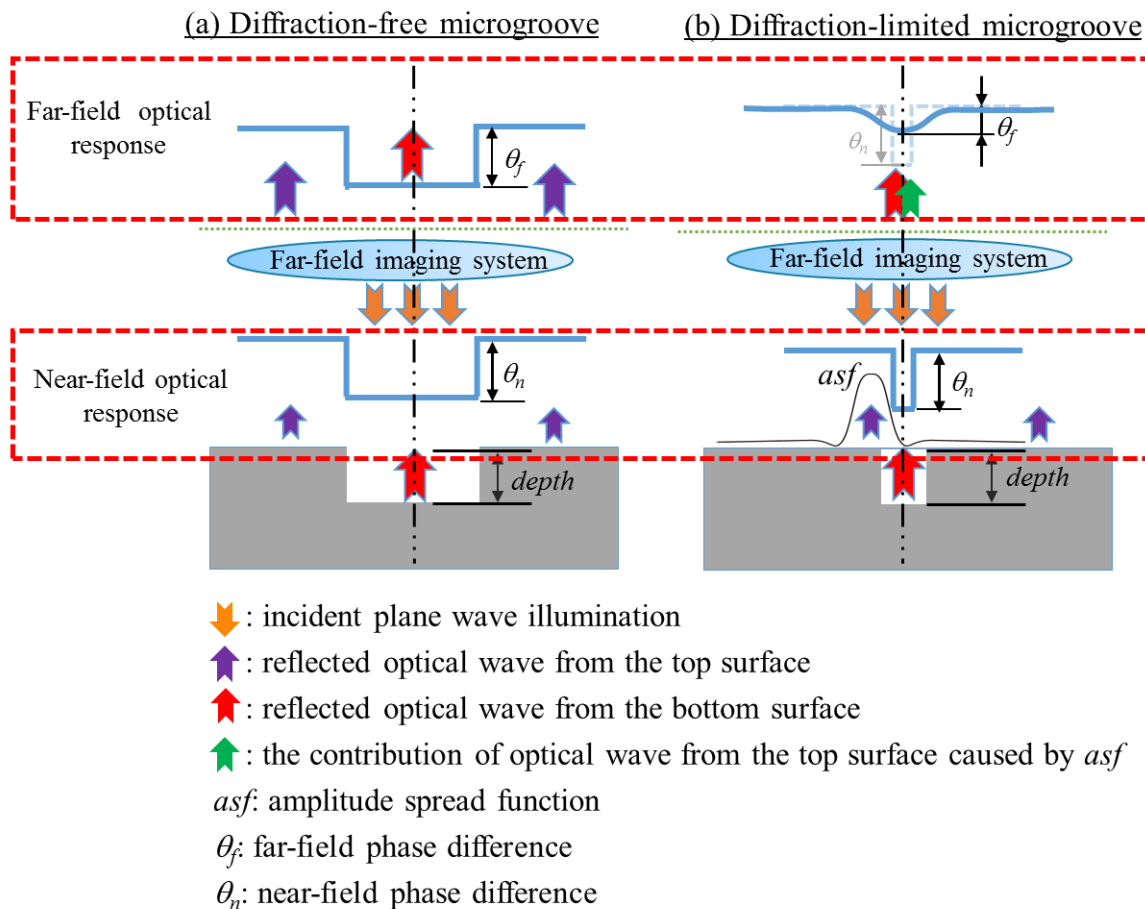
Figure 2.17 Schematic of far-field optical wave forming mechanism for (a) diffraction-free microgrooves and (b) diffraction-limited microgrooves.

2.4 Far-field-based Near-field Reconstruction Depth Measurement (FNRDM)

Based on the analysis of far-field optical wave forming mechanism of diffraction-limited microgrooves, a novel optical method was proposed to achieve the depth measurement with high accuracy. The proposed method is called Far-field-based Near-field Reconstruction Depth Measurement (FNRDM) [61][62]. FNRDM connects the depth information of diffraction-limited microgrooves with the near-field phase difference, which can be calculated from practical far-field optical observations rather than directly measured by specialized equipment, i.e., near-field scanning optical microscopy [79][80][81][82]. Figure 2.18 shows a model on a complex plane diagram reflecting the examined physical characteristics. The blue, red and green arrow denote far-field observed wave at the opening position of microgroove, reflected optical waves from the bottom surface and the top surface, respectively. A_f, A_b and A_t are the corresponding complex amplitudes of the mentioned optical waves. In the case of diffraction-free microgrooves, A_f is almost the same with A_b, resulting in that the observable phase coincides with the original depth information (Fig. 2.18(a)). On the other hand, for diffraction-limited microgrooves, A_f is not equal to A_b, but a vector sum of A_b and the contribution of A_t generated by the amplitude spread function on the complex plane (Fig. 2.18(b)). Apparently, when measuring the diffraction-limited microgrooves, A_f, A_b and A_t obey the cosine law, with which near-field phase difference (θ_n) and the corresponding depth information can be calculated.

(a)

(b)
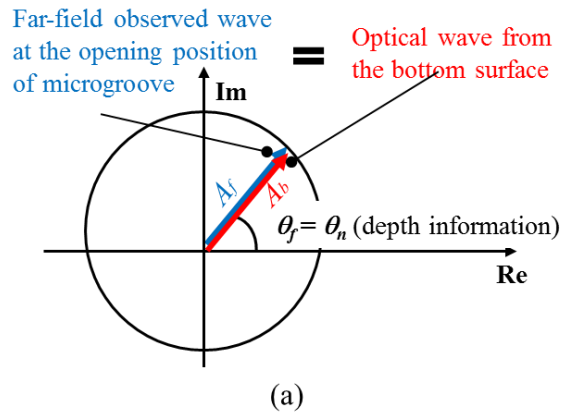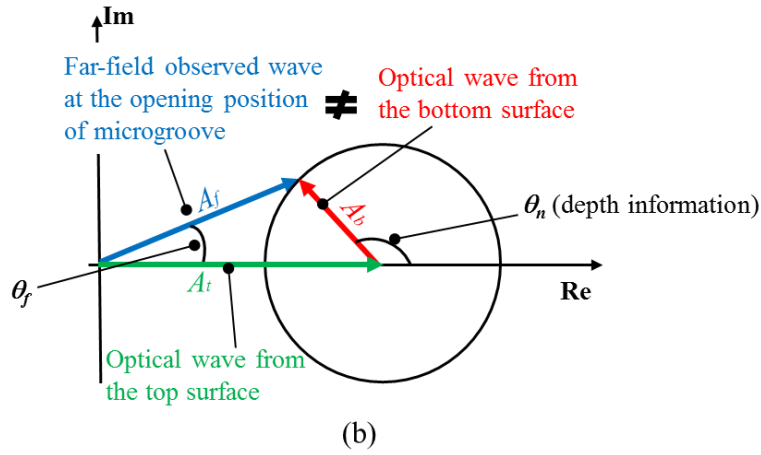
Figure 2.18 Schematic of the proposed FNRDM method on a complex plane: (a) diffraction-free microgrooves and (b) diffraction-limited microgrooves.

A_f and θ_f are far-filed parameters and can be obtained by practical measurements, e.g. optical imaging system and conventional optical interferometry. Therefore, if the contribution of the top surface reflection is given, the complex vector of the optical wave only from the bottom surface with the depth information can be derived. The calculation process for A_t is interpreted in Fig. 2.19. Assuming an arbitrary point i on the top surface of microgroove (the point number is n). Then on the far-field imaging plane, the reflected amplitude ($A_{t,\,i}$) from i can be given

$$A_{t,i} = \delta_i \otimes asf(i) = A_\delta \times asf(i), i = 1, 2, 3...n \tag{2.27}$$
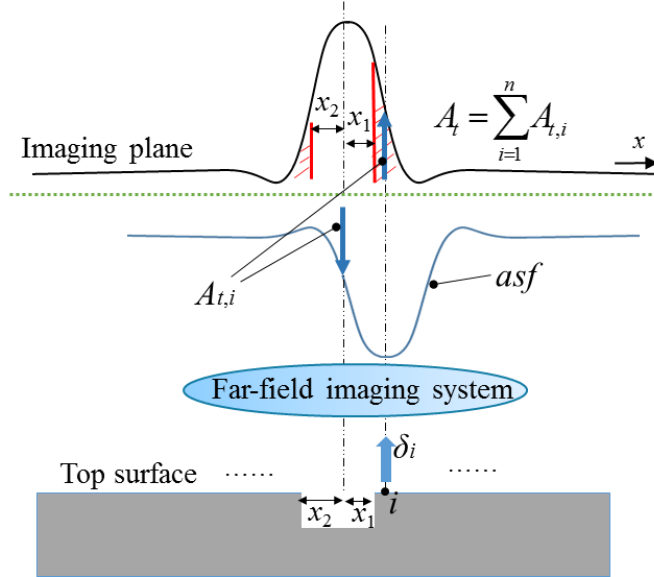
Figure 2.19 Schematic of calculating the amplitude from the top surface (A_t).

Where δ_i and A_δ are the δ-pulse signal reflected from point i in the near-field and its amplitude. For δ_i from each point, A_δ can be assumed the same due to the homogenous material. Then, A_t can be regarded as the summary of $A_{t,i}$, and determined by the lateral distance between the detection position and the edges of microgroove (x_1 and x_2 in Fig. 3.2, the width of microgroove= $x_1 + x_2$) and *asf* through Eq. (2.28).

$$A_t = \sum_{i=1}^{n} A_{t,i} = A_\delta \times \left[\int_{x_1}^{+\infty} asf(x)dx + \int_{x_2}^{+\infty} asf(x)dx \right] \tag{2.28}$$

Because the amplitude of the δ-pulse signal (A_δ) in the near-field is unknown, another model of a uniform surface without the microgroove area is introduced for further calculation, illustrated in Fig. 2.20. The amplitude (A_u) from the uniform surface in the far-field imaging plane is given

$$A_u = \sum_{i=1}^{n} A_{u,i} = A_\delta \times \int_{-\infty}^{+\infty} asf(x)dx \tag{2.29}$$
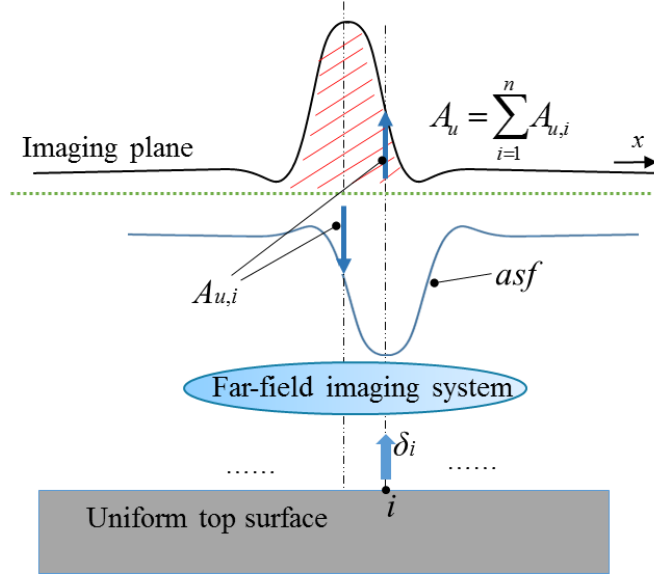
Figure 2.20 Amplitude reflected from a uniform surface without the microgroove area.

By dividing Eq. (2.28) by Eq. (2.29), the unknown A_δ can be eliminated and we can obtain

$$A_t(x_1) = \frac{A_u \times \left[\int_{x_1}^{+\infty} asf(x)dx + \int_{w-x_1}^{+\infty} asf(x)dx \right]}{\int_{-\infty}^{+\infty} asf(x)dx} \qquad (2.30)$$

Where w is the width of the microgroove. A_u is also a far-filed parameter and can be obtained by illuminating the uniform flat surface with the same material.

The retrieval algorithm for calculating the reflected near-field phase difference (θ_n) and the corresponding depth information is shown in Eq. (2.31) based on three far-field measurement parameters (A_f, A_u and θ_f).

$$\begin{cases} A_b = \sqrt{A_f^2 + A_t^2 + 2A_f A_t \cos\theta_f} \\ \theta_n = \pi - \arcsin\dfrac{A_f \sin\theta_f}{A_b} + 2\pi k, k = 0, 1, 2... \\ depth = \dfrac{\lambda}{2} \times \left(\dfrac{\theta_n}{2\pi} + k \right) \end{cases} \qquad (2.31)$$

Hence, by using the proposed FNRDM method to measure the depth of the diffraction-limited microgrooves on different materials, the applicable conditions include:

(a) The amplitude at the opening position of the microgroove can be directly measured.

(b) The amplitude from the top surface can be calculated by using the measurable amplitude from the uniform surface.

(c) The phase information can be measured by phase shift interferometry.

(d) When measuring the transparent sample, the coherence length of the measurement system should be shorter than the thickness of the sample and longer than the depth of microgrooves.

2.5 Analysis of influence of the scattering light from the edges

In this thesis, the phase difference by using FNRDM is defined by subtracting the phase at the central position of microgroove by the phase at the top surface. In other words, by FNRDM, we evaluate the depths of diffraction-limited microgroove by an effective depth at the central position of microgroove, rather than the depth distribution along the overall opening positions. There are two reasons: (1) Figure 2.21 plots the near-field phase distribution from a 200-nm-wide and 300-nm-deep microgroove, which is the same with Fig. 2.13(b). In the magnified blue dashed box, we found that the near-field phases are nonuniform from the uniform bottom surface, which means a theoretical difficulty in measuring the depth distribution even by near-field optical response. The possible reason of the nonuniform near-field phase distribution is the scattering light from the edges of microgroove [83], shown in Fig. 2.22. In the opening position of the microgroove, besides the contributions of the optical waves from the top surface and bottom surface, the scattering light from the edges of the microgroove is a main source of the theoretical error of FNRDM. (2) Using FNRDM to measure the depth distribution of diffraction-limited microgrooves has a higher requirement of lateral resolution, when measuring the required far-field amplitude distributions (A_f and A_u) and phase distribution (θ_f) by optical imaging system and conventional optical interferometry. Hence, in order to ensure the accuracy of depth measurement, the phase difference at the central position of microgroove is exploited for evaluating the depth of the diffraction-limited microgroove due to the least influence of the scattering light from the edges. Although the depth distribution along the overall opening

positions of diffraction-limited microgrooves cannot be accurately evaluated, an effective depth measurement at the central position of microgroove by FNRDM is of great significance and brings a tremendous progress to optically three-dimensional imaging of diffraction-limited microstructures.
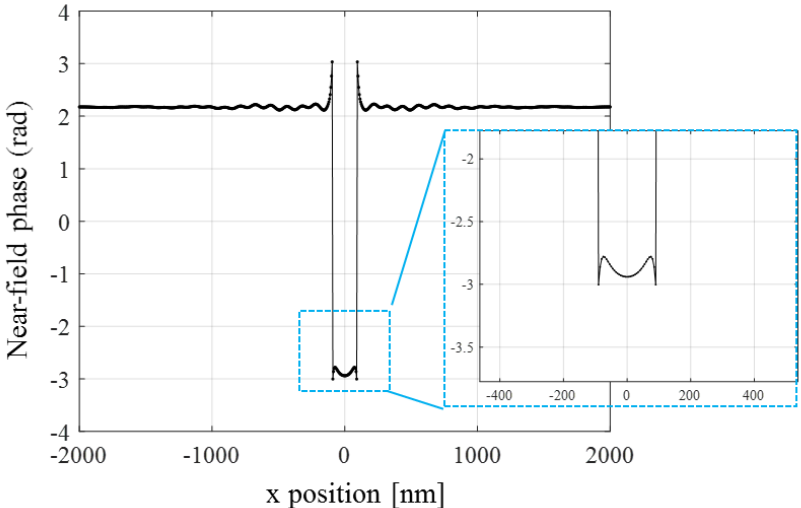
Figure 2.21 The nonuniform near-field phase distribution from the uniform bottom surface of a 200-nm-wide and 300-nm-deep microgroove.
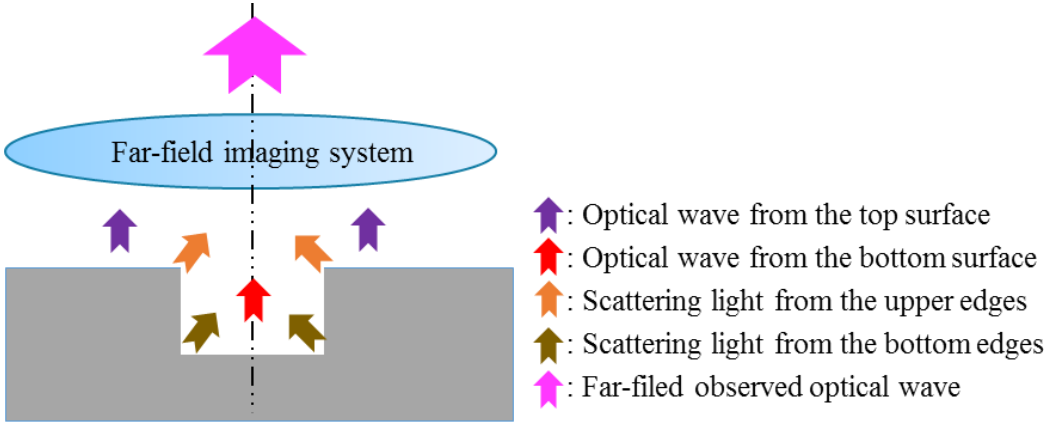
Figure 2.22 The influence of scattering light from the edges of microgrooves

In order to further analyze the influence of scattering light from edges, two discussions based on FDTD simulations were performed.

(1) As the depth increase, the influence of scattering light from upper edges. When considering the contribution from the upper edges, the schematic of calculating depth information is plotted in Fig. 2.23. θ_s denotes the phase information caused by scattering light from the upper edges. As shown in Fig. 2.24, θ_s can be calculated by the infinite model, where the depth of the microgroove model is set as infinite in the FDTD simulation. Because there isn't reflection from the bottom surface in the infinite model. Then substituting θ_s into the microgroove model, the depth of information with considering the scattering light from the upper edges can be calculated.
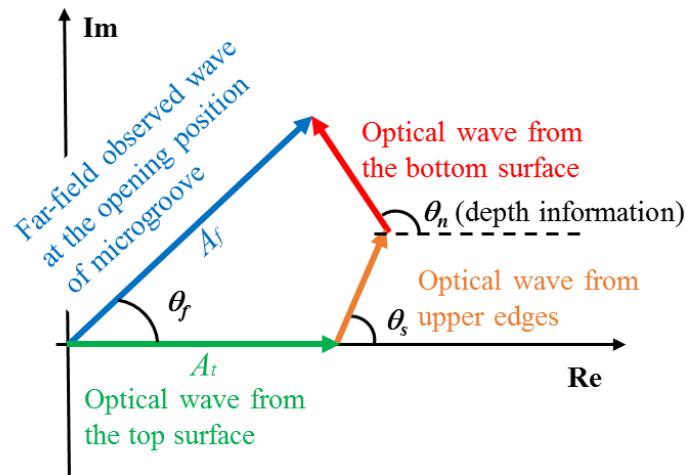
Fig. 2.23 Schematic of calculating depth information when considering the scattering light from the upper edges
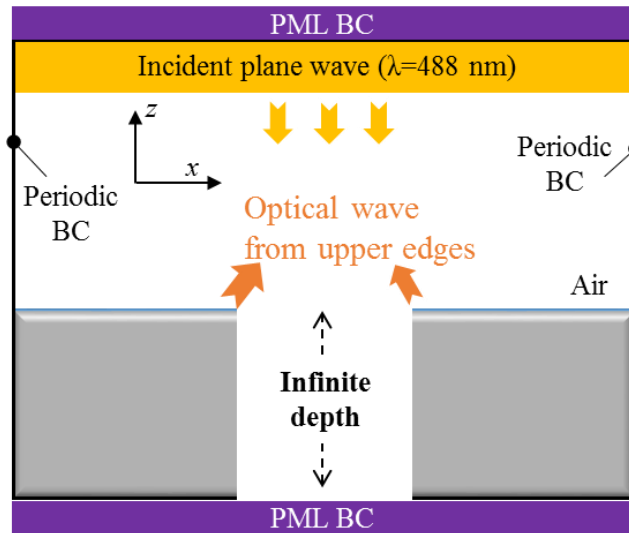
Fig. 2.24 The finite model for calculating θ_s

Figure 2.25 shows the results with and without considering the scattering light from the upper edges. The simulation parameters are as followings: 488-nm-wavelength, NA = 0.55, the diffraction limit = 540 nm, silicon 100-nm-wide microgroove. It is found that: (1) when eliminating the scattering light from the upper edges, the measured depth (red dotted line) by FNRDM is much close to theoretical values, compared to the model without considering the scattering light (black dotted line). (2) As simulated depth increases, the measured depths without considering the scattering light tend to be a stable value, while this threshold has been broken with considering the scattering light. Obviously, as the simulated depth increases, the optical wave from the bottom surface becomes weaker while the scattering light from the upper edges is almost the same. When the simulated depth is sufficiently large, the scattering light is much stronger than the optical waves from the bottom surface and becomes the dominating contribution of the synthetically observed optical wave, the measured depth tends to be a stable value and FNRDM cannot be applied to evaluate the depth with high accuracy. (3) The measured depths with considering the scattering light from the upper edges are always larger than the theoretical values. The increasing trend in the measured depths may be explained by the influence of the scattering light from the bottom edges. As the simulated depth increases, the scattering light from the bottom edges is also variable.
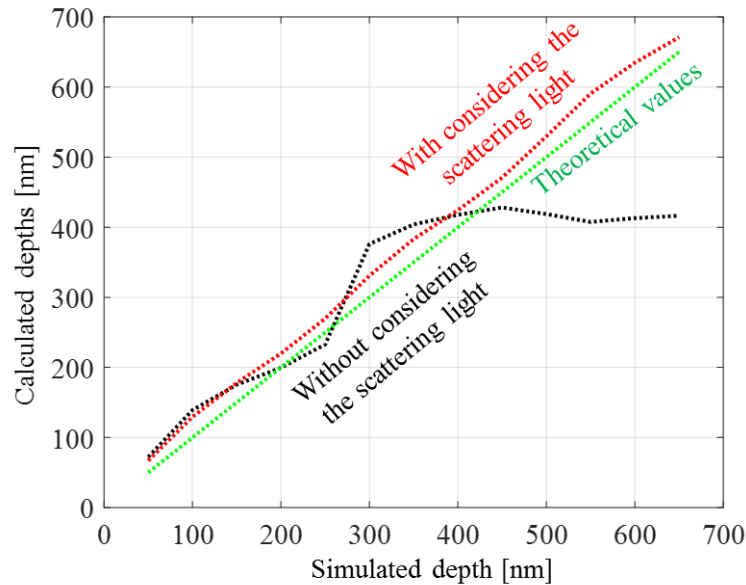
Fig. 2.25 Measured depths of the 100-nm-wide microgrooves with and without considering the scattering light from the upper edges

(2) The influence of different types of upper edges. Figure 2.26 shows the schematic of typical two examples of microgrooves with different upper edges. The simulation parameters are as followings: 488-nm-wavelength, NA = 0.55, the diffraction limit = 540 nm, 200-nm-wide and 300-nm-deep standard microgroove. And the results are summarized in Table 2.1. It is found that the observed far-field amplitude from the microgroove (A_f) changes depending on the shape of upper edges. However, for all those structures, the measured depths by the proposed FNRDM method have an accuracy of less than 10% error, no matter whether there are defections of the upper edges.

(a) Triangular edges   (b) Round edges
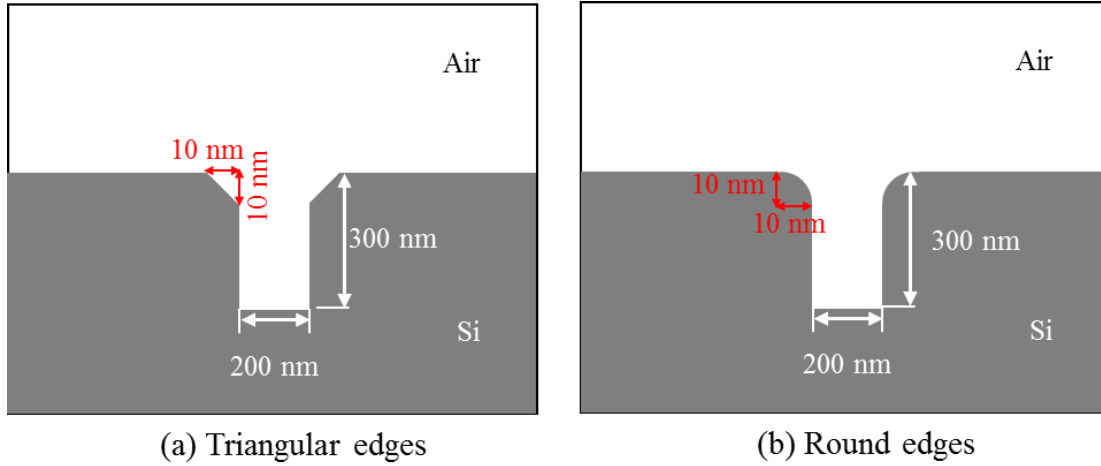
Fig. 2.26 Schematic of typical two examples of microgrooves with different upper edges

Table 2.1 The measurement results for the examined structures in the Fig. 2.26.

Types	Standard microgroove	Triangular edges	Round edges
Observed far-field amplitude from the microgroove (A_f) [a.u.]	150.5	148.2	148.7
Calculated far-field phase difference by 4-step phase shift method (θ_f) [rad]	0.23	0.22	0.23
Calculated far-field amplitude from the top surface (A_t) [a.u.]	149.3	149.3	149.3
Measured depths by FNRDM [nm]	308.0	310.6	310.4

Although it is known that the accuracy of depth measurement can be improved by eliminating the scattering light from the edges, it is still difficult to eliminate or decrease the scattering light in the practical measurement, which is also our important future work.

2.6 Conclusions

In this Chapter, a brief introduction about the theory of diffraction and Fourier Optics was given to develop an understanding of the way optical systems process light to form images. According to the optical imaging theory, the far-field optical image is formed by the convolution of the complex amplitude of the near-field optical wave from the structure and the point spread function. Then, the near-field optics, which can break the diffraction limit, was introduced.

Next, the finite-difference time-domain (FDTD) method was presented, which is a numerical tool for modeling computational electrodynamics and extremely useful in analyzing the electromagnetic fields in both near-field and the far-field.

Both the near-field and far-field phase information reflected from diffraction-free and diffraction-limited microgrooves were analyzed by the FDTD method. It is found that, for the diffraction-limited microgroove, the measured depths cannot accurately reflect the depth information by using far-field phase differences, but the results by near-field phase differences are almost coincident with the theoretical values, similar to the results of diffraction-free microgroove. Based on the far-field optical response forming mechanism of diffraction-limited microgrooves, we explained the limitation of depth measurement by the conventional optical interferometry based on phase change.

Finally, a novel optical depth measurement method (FNRDM) was proposed to achieve the depth evaluation of diffraction-limited microgrooves with high accuracy. FNRDM connects the depth information of diffraction-limited microgrooves with the near-field phase difference, which can be calculated from practical far-field optical observations rather than directly measured by specialized equipment, i.e., near-field scanning optical microscopy. The practical far-field observations include the amplitude from the microgroove structure (A_f), phase difference between the top surface and the bottom surface (θ_f) and the amplitude from a uniform surface without microgroove area (A_u). By FNRDM, we evaluate the depths of the diffraction-limited microgroove by an effective depth at the central position of microgroove, rather than the depth distribution along the overall opening positions, because of the scattering light from the edges of microgroove. When the depth to be measured is sufficiently large, the scattering light is much stronger than the optical waves from the bottom surface

and becomes the dominating contribution of the synthetically observed optical wave, the measured depth tends to be a stable value and FNRDM cannot be applied to evaluate the depth.

Chapter 3. Numerical analysis of the proposed FNRDM method

In Chapter 2, we proposed a novel optical depth measurement method (FNRDM) which enables the depth evaluation of diffraction-limited microgrooves with high accuracy. FNRDM connects the depth information of diffraction-limited microgrooves with the near-field phase difference, which can be calculated from practical far-field optical observations rather than directly measured by specialized equipment, i.e., near-field scanning optical microscopy. In this chapter, the numerical analysis based on the FDTD simulations is performed to demonstrate the validation of the measurement principle. Further, the detectable depth of FNRDM and the applicability under the noise condition are discussed.

3.1 Verification by numerical analysis

In this section, we attempted to verify the basic validity of FNRDM by the combination of Rsoft simulation and Matlab processing. The processes of obtaining the far-field parameters (A_f, A_u and θ_f) required in FNRDM in the simulation analysis are as followings.

3.1.1 Far-field amplitudes

By the FDTD method, the complex amplitude of electric field of interest can be recorded. Figure 3.1 illustrates a schematic of the simulated microgroove model, and the basic parameters of the microgroove model and the settings for optical imaging system are listed in Tab. 3.1. Figure 3.2 plots the far-field amplitude distribution of reflected optical wave, and A_f at the central position is 150.5.
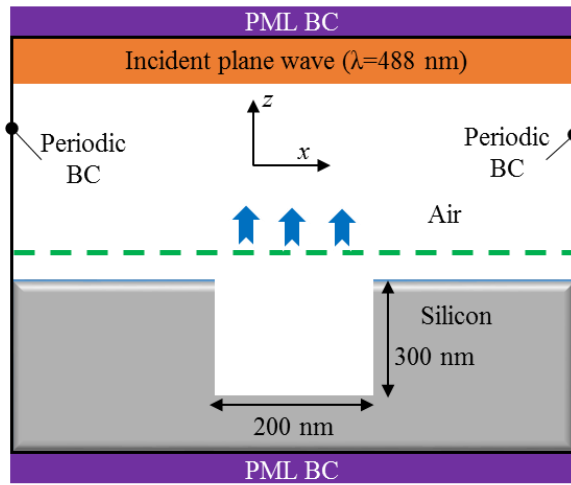
Figure 3.1 The simulation model of a microgroove structure for the verification of FNRDM

Table 3.1 Basic simulation settings for the verification of FNRDM

Parameters	
Wavelength of incident beam	488 nm
Grid size	5 nm (x) × 5 nm (z)
Simulation region	4 μm (width) × 2.5 μm (height)
Near-field recording plane	20 nm above the top surface of microgroove
NA	0.55
The diffraction limit	540 nm

Figure 3.2 The far-field amplitude distribution reflected from the microgroove.

In order to obtain A_u, another model of the uniform surface under the same conditions of Table 3.1 is simulated, shown in Fig. 3.3. Also, the far-field amplitude distribution reflected from uniform surface can be plotted in Fig. 3.4. Substituting A_u (229.2) to Eq. 2.30, A_t at the central position of microgroove is calculated as 149.3.
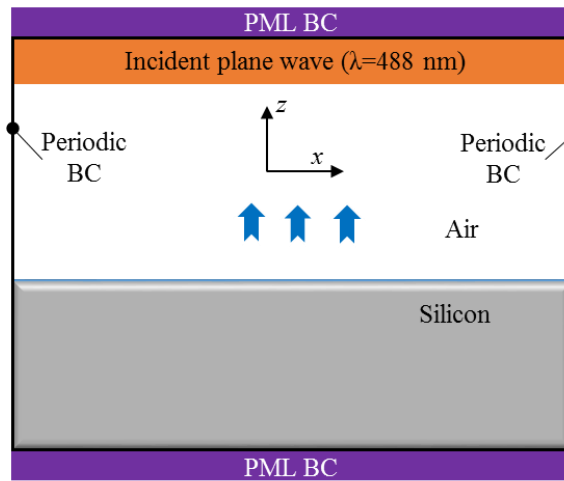
Figure 3.3 The simulation model of the uniform surface for the verification of FNRDM
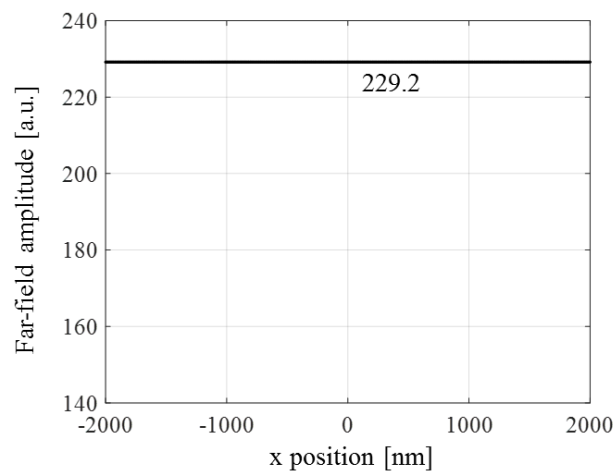
Figure 3.4 The far-field amplitude distribution reflected from the uniform surface

3.1.2 Far-field phase

3.1.2.1 Four-step phase shift method

In consideration of the practical application, the phase shift method [84][85][86][87] is used to extract the phase information from the observed intensities in the simulation analysis. Phase shifting interferometry is a powerful means of analyzing interferograms to recover the phase information by recording multiple interferograms. In the two-beam phase shift interferometer, the intensity distribution of kth interferogram can be expressed by

$$I_k(x, y) = I_s(x, y) + I_r(x, y) + 2\sqrt{I_s(x, y)I_r(x, y)} \cos(\varphi(x, y) + \alpha_k) \tag{3.1}$$

Where $I_s(x, y)$ and $I_r(x, y)$ are the intensity distributions from the sample and the reference, respectively. $\varphi(x, y)$ is the phase distribution to be measured. α_k is the relative reference phase for kth interferogram. Equation (3.1) shows that there are three unknowns in one interferogram irradiance pattern: $I_s(x, y)$, $I_r(x, y)$ and $\varphi(x, y)$. The latter unknown is of primary interest since it encodes the depth information of interest. With three unknowns, at least three measurements with different values of α are needed to recover $\varphi(x, y)$. Although the three-step algorithm gives an exact result, it is sensitive to errors in the value of $\varphi(x, y)$ and measurement noise. The four-step algorithm, providing superior performance over the three-step algorithm, is used in our work.

In the four-step phase shifting interferometry, α_1, α_2, α_3 and α_4 are 0, $\pi/2$, π and $3\pi/2$, respectively. Then, the intensity distributions of the four interferograms are

$$
\begin{aligned}
I_1 &= I_s + I_r + 2\sqrt{I_s I_r} \cos(\varphi) \\
I_2 &= I_s + I_r + 2\sqrt{I_s I_r} \cos(\varphi + \frac{\pi}{2}) = I_s + I_r - 2\sqrt{I_s I_r} \sin(\varphi) \\
I_3 &= I_s + I_r + 2\sqrt{I_s I_r} \cos(\varphi + \pi) = I_s + I_r - 2\sqrt{I_s I_r} \cos(\varphi) \\
I_4 &= I_s + I_r + 2\sqrt{I_s I_r} \cos(\varphi + \frac{3\pi}{2}) = I_s + I_r + 2\sqrt{I_s I_r} \sin(\varphi)
\end{aligned}
\tag{3.2}
$$

Where the (x, y) dependence is omitted. Solving for the phase gives

$$\varphi = \arctan \frac{I_4 - I_2}{I_1 - I_3} \tag{3.3}$$

3.1.2.2 Simulation analysis for far-field phase

As depicted in Fig. 3.5, it is a schematic of simulating the four-step phase shift measurement. Four simulations, called step 1-4, are needed to obtain the complex amplitudes of the reference optical waves. In the step 1, the height of the reference surface is kept the same as the microgroove model to set $\alpha_1=0$. Then, in the step 2, the height of the reference surface is reduced by $\lambda/8$ to set $\alpha_2=\pi/2$. Analogously, the height decrements of the step 3 and 4 are $\lambda/4$ and $3\lambda/8$, respectively. Then, according to the superposition of coherent beams, the complex amplitudes of the optical waves from the microgroove structure and the four reference surfaces are added in the complex plane to obtain the relative interferograms, shown in Fig. 3.6.
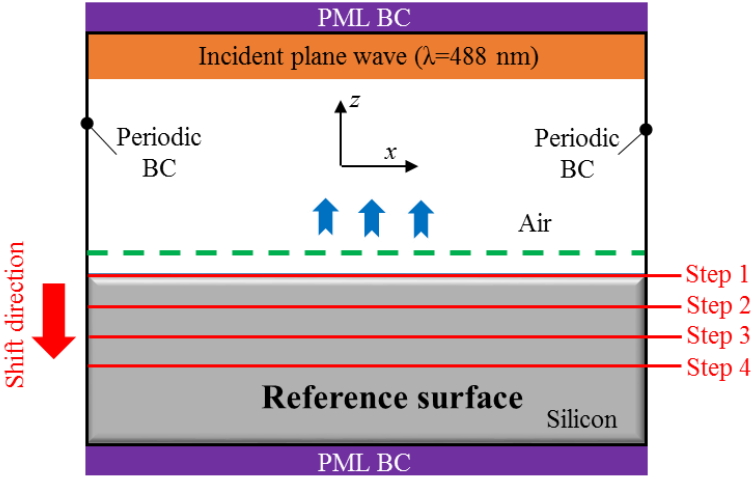
Figure 3.5 Schematic of simulating the four-step phase shift measurement.
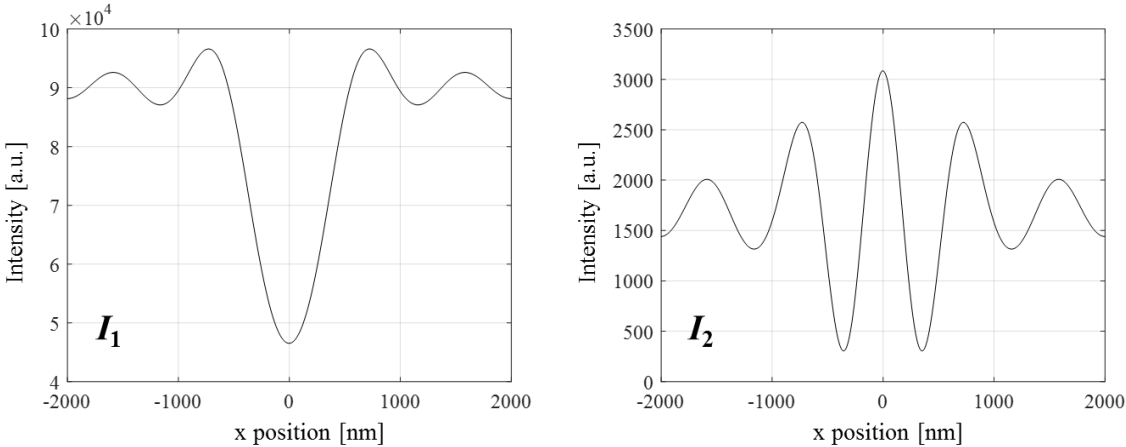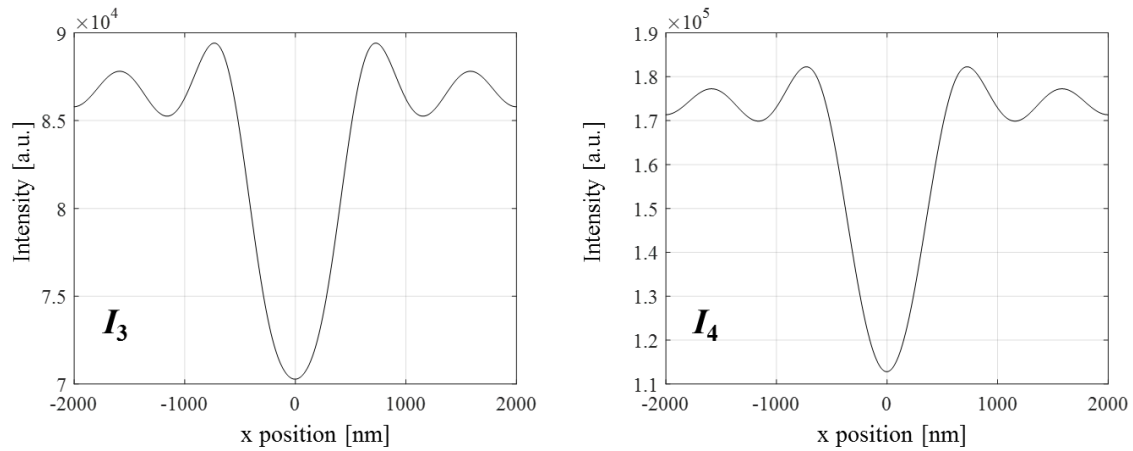
Figure 3.6 The obtained interferograms by four-step phase shift method

By the four-step phase shift method, the far-filed phase distribution is depicted in Fig. 3.7(a). As a contrast, we also plotted the far-filed phase distribution from only the microgroove structure by the FDTD method (Fig. 3.7(b)). The consistency between the two far-field phase distributions is confirmed, which indicates the feasibility of the four-step phase shift method. θ_f at the central position of the microgroove is 0.23 rad.

(a) By the four-step phase shift method   (b) By the FDTD method
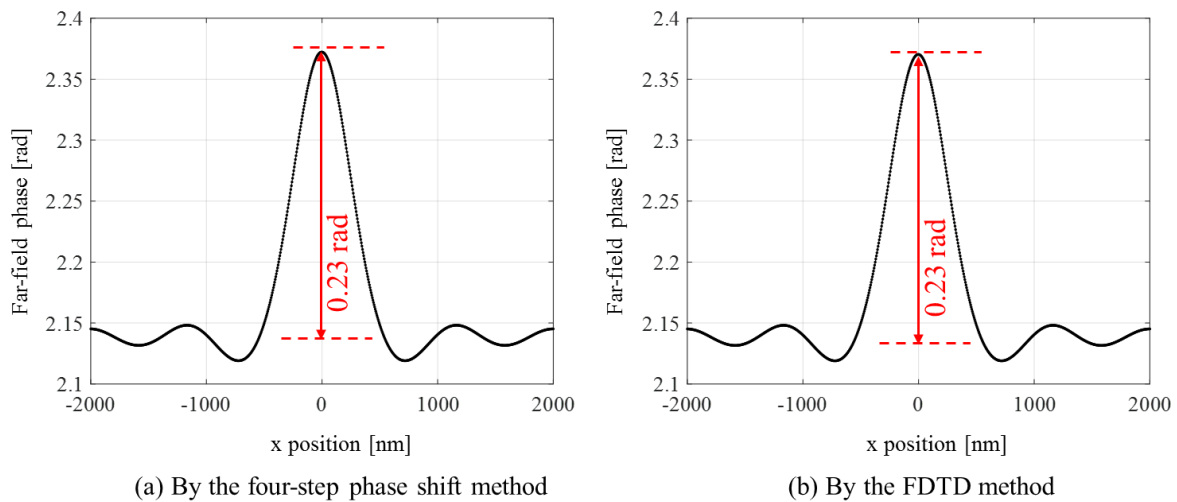
Figure 3.7 Far-field phase distribution of simulated microgroove by: (a) four-step phase shift method and (b) recorded data in the FDTD method

3.1.3 Measured depth by FNRDM

By using the relation of three values as complex vectors as shown in Fig. 3.8, the near-field phase difference (θ_n) at the central position of the microgroove can be calculated as 1.65 rad. Then, according to Eq. (2.31), we can get the depth value of 308 nm (the integer $k = 1$ due to the phase wrapping problem) for the 300-nm-depth microgroove. The phase unwrapping problem will be discussed in Chapters 7 and 8. The simulation results suggest that by FNRDM the depth of a 200-nm-wide and 300-nm-deep microgroove can be measured with an accuracy of 8 nm (2%) beyond the diffraction limit (540 nm).
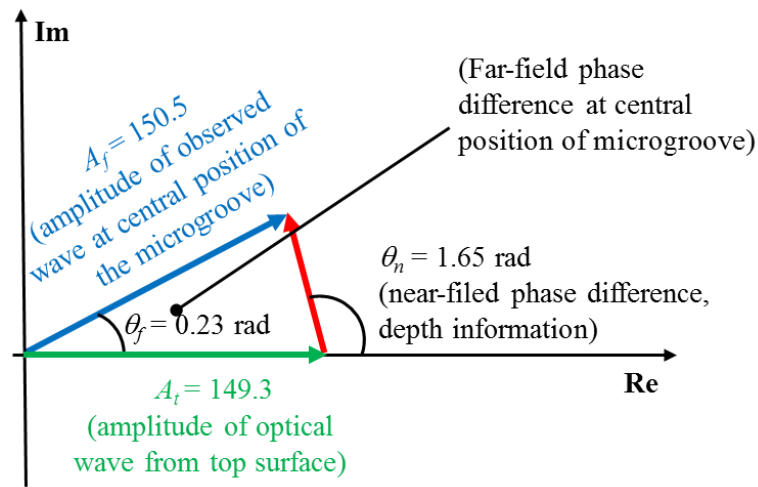
Figure 3.8 Depth calculation by proposed FNRDM method in the simulated 200-nm-wide and 300-nm-deep microgroove.

3.2 The detectable depth by FNRDM

In this section, the detectable depth by FNRDM will be discussed under the circumstance of different *NA*s and widths of diffraction-limited microgrooves. Firstly, for 200-nm-wide microgrooves under the same simulation conditions with Tab. 3.1, the simulated depths vary from 20 nm to 1500 nm. Figure 3.9(a) shows the depth measurement characteristics of FNRDM, while the measured depths using near-field phases are plotted in Fig. 3.9(b). From Fig. 3.9(a), it is clear to see that the maximal detectable depth by FNRDM is almost 1 μm, which means a relatively high aspect ratio of 5.0. The error is defined as dividing the differences between the measured depths of FNRDM and the simulated depths by the simulated depths, and the evaluation is carried out by computing the mean value of the errors.

When the measurement range is 20-1000 nm, the average errors are 4.0%, 3.8% and 3.3% for NA=0.2, 0.55 and 0.95, respectively. However, the conventional method of using only far-field phase difference (θ_f) cannot measure the depth even with NA= 0.95. On the other hand, through the comparison with the results by using near-field phases (Fig. 3.9(b)), a similar trend in measured depths according to the depth variation can be observed, which suggests that it is feasible to calculate the near-field phase and the corresponding depth information by proposed FNRDM. Furthermore, in the case of 200-nm-wide microgrooves, the maximal detectable depth (1000 nm) by FNRDM is slightly greater than that (~800 nm) of near-field phase. This phenomenon may be explained by the filtering effect of the scattering light from the edges generated by the optical imaging system.
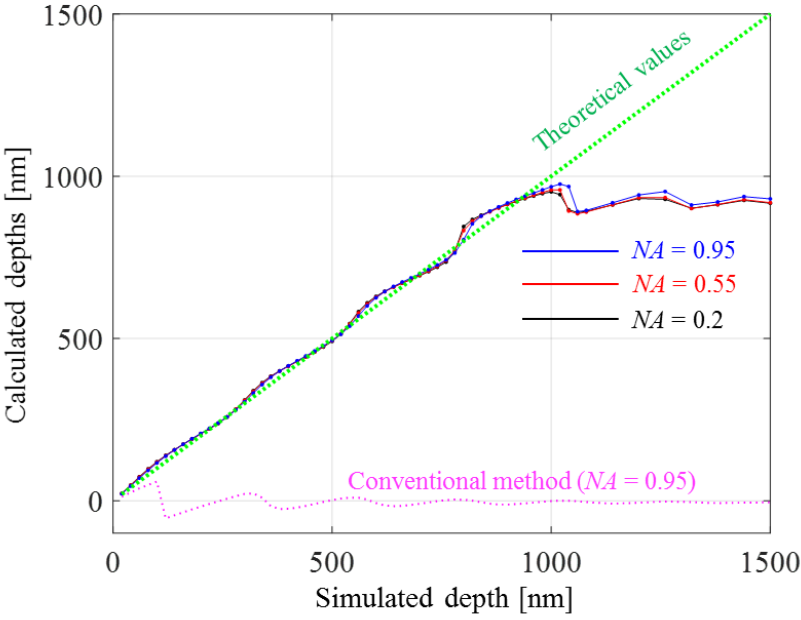
(a) By FNRDM
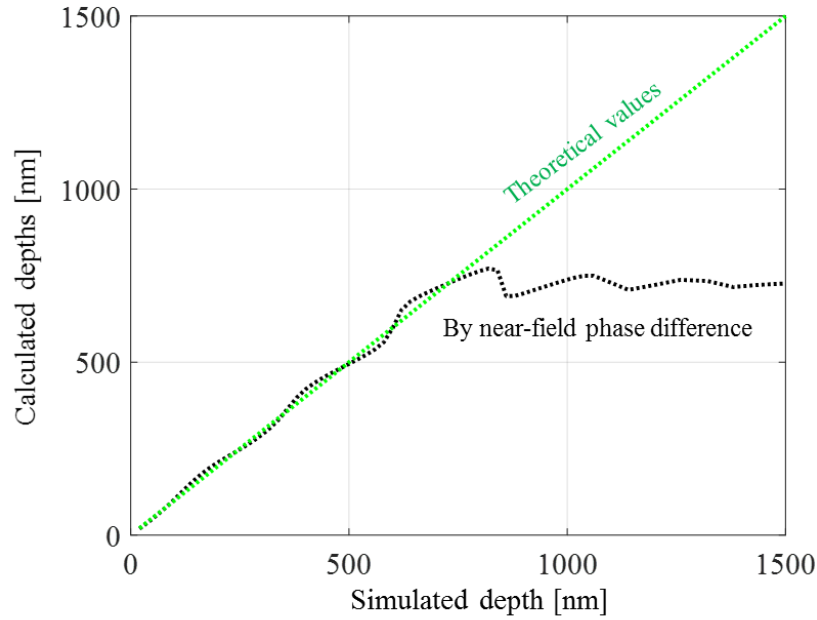
(b) By near-field phase of the FDTD method

Figure 3.9 Measured depths of the 200-nm-wide microgrooves by: (a) the proposed FNRDM method and (b) direct near-filed phase of the FDTD method

Secondly, under the same simulation conditions with the case of 200-nm-wide microgroove, 100-nm-wide and 50-nm-wide microgrooves are analyzed. The simulated depth ranges are 20-600 nm and 20-360 nm, respectively. Figures 3.10 and 3.11 plot the measurement results of two types of microgrooves with *NA*=0.2, 0.55 and 0.95 by FNRDM and near-field phases. For both the two types of microgrooves, the similar trends in measured depths according to the depth variation between FNRDM and using near-field phases can be observed. In addition, the detectable depth ranges between FNRDM and using near-field phases for the two types of microgrooves are almost the same. The expansion of detectable depth range by FNRDM cannot be observed as the case of 200-nm-wide microgrooves. By FNRDM, some observations are as followings: (a) for the 100-nm-wide microgroove, the maximal detectable depths of FNRDM is approximately 300 nm and the corresponding aspect-ratio is 3. During this depth range, the average errors are 17.7%, 17.4% and 16.3% for *NA*=0.2, 0.55 and 0.95, respectively. (b) For the 50-nm-wide microgroove, although the measured depths by FNRDM are much closer to the simulated depths than the results by

64

conventional method, the average errors are relatively large, which are 35.3%, 34.7% and 33.3% for *NA*=0.2, 0.55 and 0.95, when the measured depth range is below 50 nm. Obviously, when the width of the measured microgroove becomes smaller, the optical wave from the bottom surface becomes weaker while the scattering light from the upper edges becomes stronger, which will result in a greater measurement error in depth evaluation. When the simulated depth is sufficiently large, the scattering light is much stronger than the optical waves from the bottom surface and becomes the dominating contribution of the synthetically observed optical wave, FNRDM cannot be applied to evaluate the depth with high accuracy. As shown in Figures 3.9(a), 3.10(a) and 3.11(a), when the simulated depths exceed the maximal detectable depths for the corresponding microgrooves with certain widths, the measured depths of FNRDM tend to be stable values. By FNRDM, the measurable aspect-ratios under the mentioned simulation conditions are 5 for the 200-nm-wide microgroove, 3 for the 100-nm-wide microgroove and 1 for 50-nm-wide microgroove.
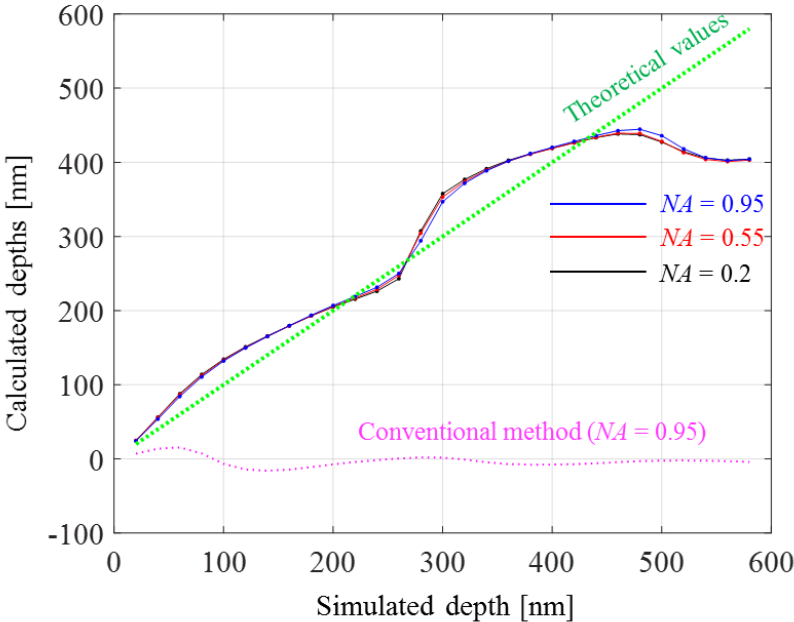
(a) By FNRDM
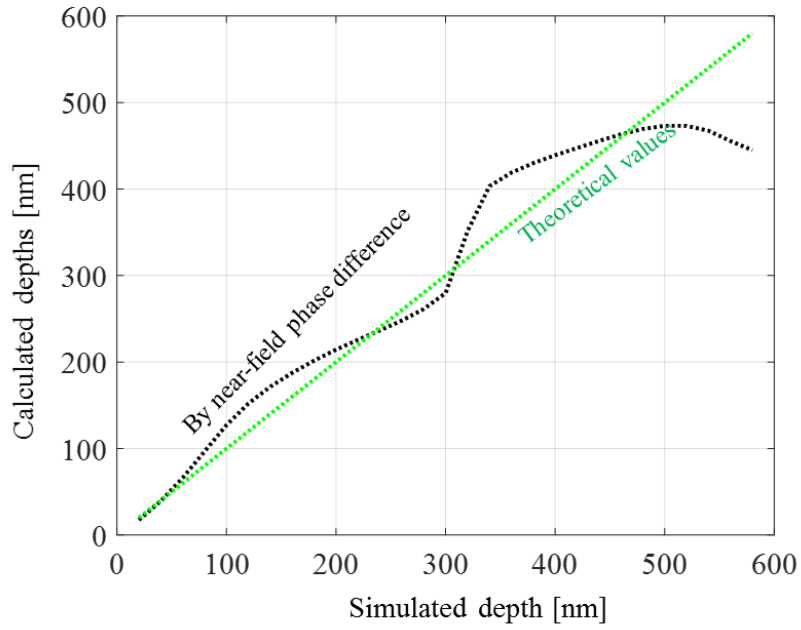
(b) By near-field phase of the FDTD method

Figure 3.10 Measured depths of the 100-nm-wide microgrooves by: (a) the proposed FNRDM method and (b) direct near-filed phase of the FDTD method
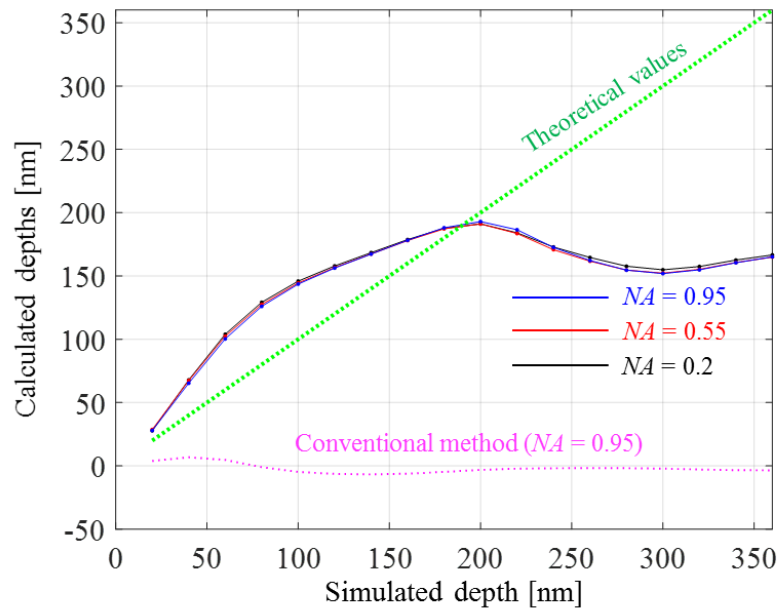
(a) By FNRDM
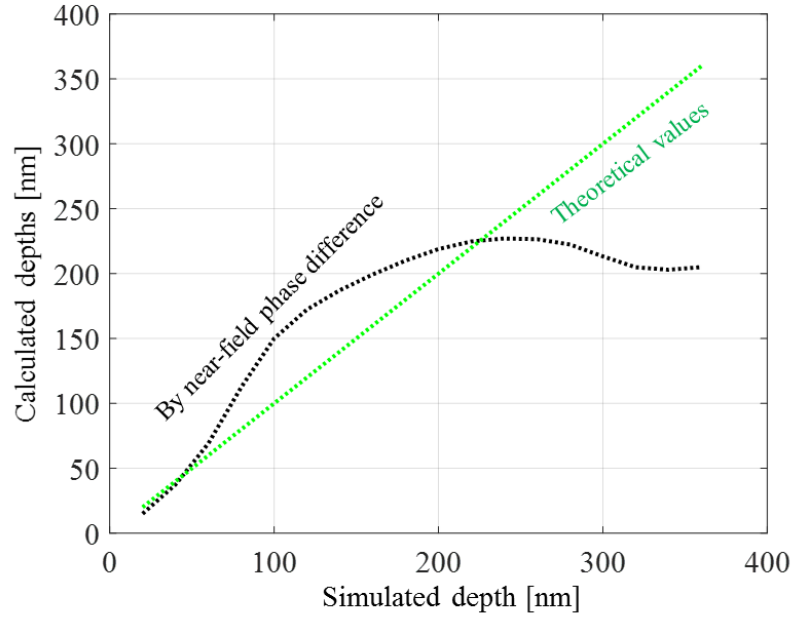
(b) By near-field phase of the FDTD method

Figure 3.11 Measured depths of the 100-nm-wide microgrooves by: (a) the proposed FNRDM method and (b) direct near-filed phase of the FDTD method

From Figures 3.9, 3.10 and 3.11, it is also found that the depth of the diffraction-limited microgroove can be measured by FNRDM even with a small *NA*, while a tiny improvement in measurement accuracy with high *NA* can be observed. In the practical application, the sensitivity of measuring the far-field phase should be considered under different *NA*s. Figure 3.12 plots the far-field phase difference (θ_f) at the central position of the microgroove as a function of the simulated depths with *NA*=0.2, 0.55 and 0.95, respectively. The simulation results show that for all the microgrooves with different widths, the measured far-field phase difference is larger when the applied *NA* is higher, which indicates a high sensitivity of using high *NA* for far-field phase detection. In the practical experiments, the setup with high *NA* should be considered to improve the system robustness and reduce the influence of the measurement noises, which will be introduced next section.

(a) 200-nm-wide microgrooves

(b) 100-nm-wide microgrooves

(c) 50-nm-wide microgrooves
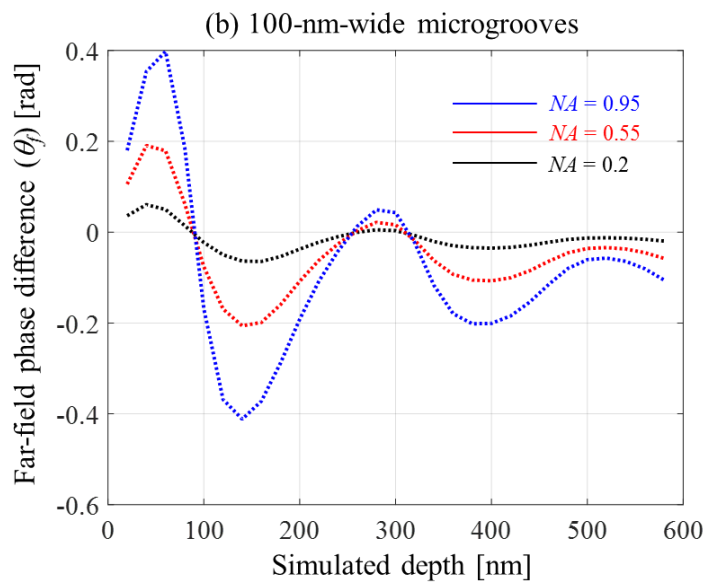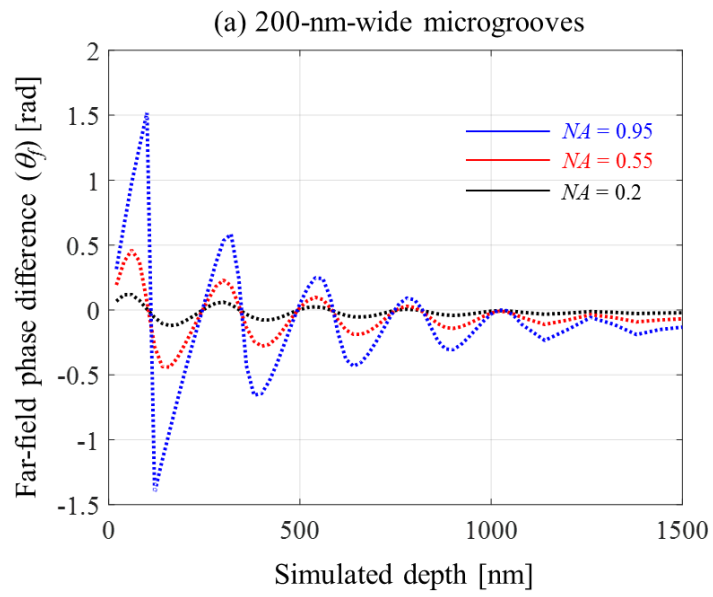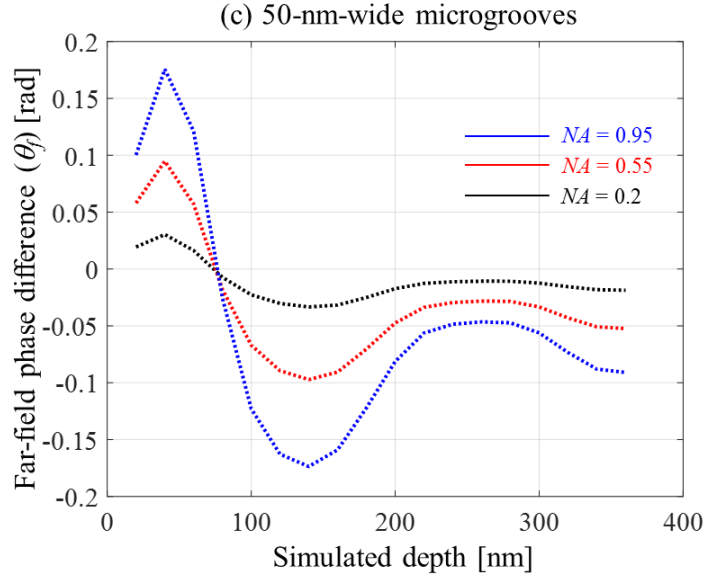
Figure 3.12 The far-field phase difference (θ_f) at the central position of the microgroove as a function of the simulated depths with different *NA*: (a) 200-nm-wide microgrooves, (b) 100-nm-wide microgrooves and (c) 50-nm-wide microgrooves.

3.3 Applicability of FNRDM under practical noise conditions

In order to apply the proposed FNRDM method to the production site, the diffraction-limited microgrooves under environmental noise condition were analyzed in this section. Ideally, various sources of the measurement uncertainty should be considered, such as vibration, stray light, fluctuation of air, stability of light source, refractive index fluctuation due to atmospheric pressure and temperature change, shot noise of optical detector, and so on. But, as the first step of the uncertainty estimation of the proposed method, only the uncertainty of the observed intensity distributions (A_f, A_u and the interferograms used for calculating the far-filed phase) are analyzed in this section. Therefore, a statistical analysis adding Gaussian noise with sigma $2\sigma = 3\%$ to the observed intensity distributions is performed. It is believed that the fluctuation value (Gaussian noise with sigma $2\sigma = 3\%$) of the observed intensity distributions is close to the practical noise condition, including the mentioned uncertainty sources, and the noise level can be thought as almost a standard level at the general production site for micro-manufacturing.

The 200-nm-wide and 300-nm-deep microgroove under the simulation condition of Tab. 3.1 was analyzed. The analysis processes are as followings. (a) Adding the Gaussian noise with sigma $2\sigma = 3\%$ to each of the interferograms in the four-step phase shift method. Figure 3.13 plots an example of the extracted far-field phase distribution from the set of four phase shifted intensity distributions under above noise condition. And the maximal error of the two phase distributions (black and red lines in Fig.3.13) is calculated for further processing. (b) Considering the worst situations by using $\pm 3\%$ noise to the observed amplitudes from the microgroove and the uniform surface (A_f and A_u) combined with plus or minus the maximal error of far-field phase difference (θ_f). According to the proposed FNRDM with the noisy detection data, we can get the statistical results estimating systematic error in Fig. 3.14. It is found that, under the noise condition, the standard deviations (Std.de) of measurement errors are 26 nm, 8 nm and 3 nm with $NA = 0.2$, 0.55 and 0.95, respectively. The results suggest that numerical aperture directly affects the measurement accuracy, as analyzed in Section 3.2 (Fig. 3.12). Under the mentioned noise condition, the 200-nm-width microgrooves with an aspect ratio of 1.5, can be quantitatively evaluated with less than 5% error by using imaging objective with numerical aperture of 0.95 and the wavelength of 488 nm (the Rayleigh criterion = 313 nm).
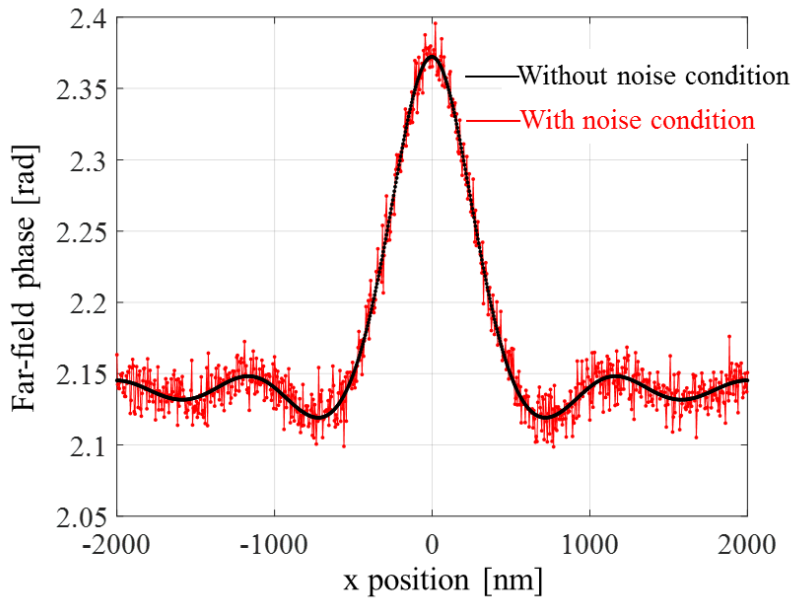
Figure 3.13 An example of the extracted far-field phase distribution from the set of four phase shifted intensity distributions under the noise condition.
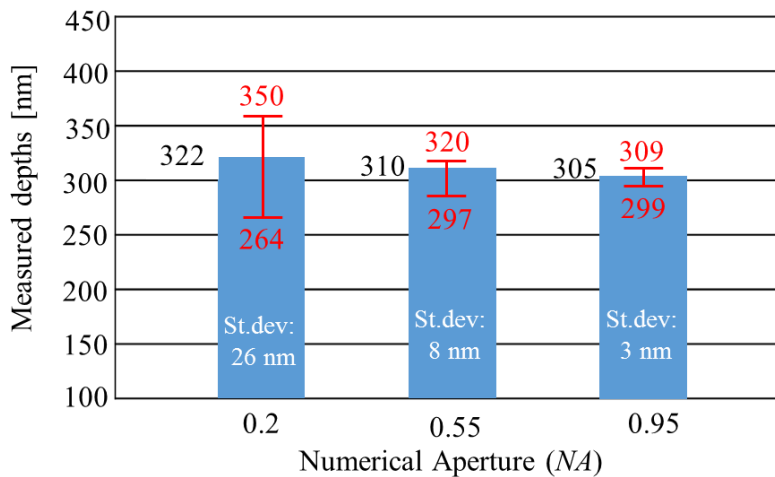
Figure 3.14 Estimation of systematic error under the practical noise environment for the 200-nm-wide and 300-nm-deep microgroove (R.C. = 313 nm for 0.95 NA, 541 nm for 0.55 NA, and 1488 nm for 0.20 NA; λ = 488 nm).

In addition, another type of microgroove (100-nm-wide, 200-nm-deep, aspect-ratio of 2) was analyzed under the same noise condition. The statistical results are shown in Fig. 3.15.

Under noise condition, the standard deviations (Std.de) of measurement errors are 38 nm, 11 nm and 6 nm with NA = 0.2, 0.55 and 0.95, respectively. The coincidence of the influence by NA with the case of 200-nm-wide microgrooves can be observed. With NA of 0.95 and the wavelength of 488.0 nm (the Rayleigh criterion = 313 nm), the measurement accuracy is less than 10% by the proposed FNRDM method in the case of 100-nm-width microgroove under the Gaussian noise with sigma 2σ = 3%.
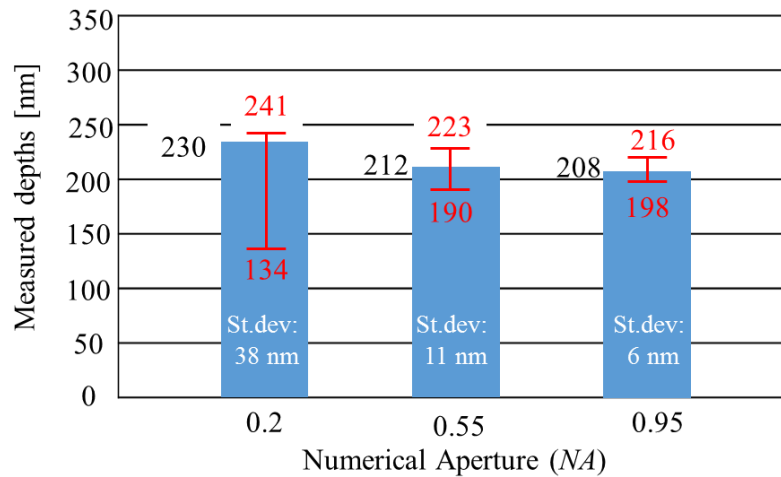
Figure 3.15 Estimation of systematic error under the practical noise environment for the 100-nm-wide and 200-nm-deep microgroove (R.C. = 313 nm for 0.95 NA, 541 nm for 0.55 NA, and 1488 nm for 0.20 NA; λ = 488 nm).

3.4 Conclusions

In this chapter, the numerical analysis based on the FDTD method was implemented to demonstrate both the validity and the detectable depth of FNRDM. Firstly, a simulation analysis for a fine 200-nm-wide and 300-nm-deep microgroove was performed to validate the feasibility of FNRDM with a wavelength of incident beam of 488 nm and a numerical aperture of 0.55. The results showed that FNRDM can measure the depth of the 200-nm-wide microgroove with an accuracy of 8 nm (3%) beyond the diffraction limit of 540 nm, which cannot be evaluated by the conventional interferometry based on phase change.

Then, the detectable depths of FNRDM for microgrooves with different widths were discussed by the FDTD simulation. Obviously, the scattering light from the edges of

microgrooves has an impact on the resultant optical wave at the opening position, resulting in a theoretical error in the observed phase. As the simulated depth increases, the optical wave from the bottom becomes weaker while the scattering light is almost the same. When the simulated depth is sufficiently large, the scattering light is much stronger than the optical waves from the bottom surface and becomes the dominating contribution of the synthetically observed optical wave, FNRDM cannot be applied to evaluate the depth. It is found that, by FNRDM, the measurable aspect-ratios are 5 for the 200-nm-wide microgroove, 3 for the 100-nm-wide microgroove and 1 for 50-nm-wide microgroove by using the wavelength of 488 nm, beyond the diffraction limit of applied imaging system.

Finally, we analyzed the practical applicability of the proposed FNRDM method under the noise condition. Two types of diffraction-limited microgrooves under environmental noise condition were analyzed. The results suggest that under the noise condition, (1) numerical aperture directly affects the measurement accuracy; (2) both a 200-nm-wide microgroove with an aspect ratio of 1.5 and a 100-nm-wide microgroove with an aspect ratio of 2 can be quantitatively evaluated with less than 10% error by using imaging objective with numerical aperture of 0.95 and the wavelength of 488 nm (the Rayleigh criterion = 313 nm).

Chapter 4. Measurement system based on low-coherence illumination

In chapter 2, a novel optical depth measurement method (FNRDM) was proposed to achieve the depth evaluation of diffraction-limited microgrooves with high accuracy. Not only validation of the measurement principle but also a feasibility study for its practical applicability were demonstrated. In the proposed FNRDM method, there are three required far-field observations: the amplitude from the microgroove structure (A_f), phase difference between the top surface and the bottom surface (θ_f), and the amplitude from a uniform surface without microgroove area (A_u). In this section, a measurement system based on low-coherence illumination and Linnik interferometry was developed to measure the three far-filed observations.

4.1 Fundamental design of the measurement system

According to the far-field observations to be measured, the measurement system can be separated into two parts: (a) one part for amplitude detection and (b) another part for phase measurement. Considering the micro and nano scale of the microgroove, the magnification power of the measurement system is extremely important.

4.1.1   Infinity-corrected optical system

As shown in Fig. (a), in a finite correction optical system [88][89][90], the objective lens forms an intermediate image by itself. While in an infinity-corrected optical system, a light beam emitted from a specimen passes through the objective lens which does not form an image and enters as an infinity parallel beam in the tube lens which forms an intermediate image, as depicted in Fig. 4.1 (b). Because of the flexible space between objective and tube lens, termed the infinity space, an infinity-corrected optical system basically has the following advantages: (1) a magnification does not change even if the distance between the objective lens and tube lens is changed. (2) Even if a parallel flat plate is inserted between

the objective lens and tube lens, the parfocal point remains unchanged and no image shifting occurs. Hence, the infinity corrected optical system are commonly used in microscope systems to offer high quality imaging.

(a)

(b)
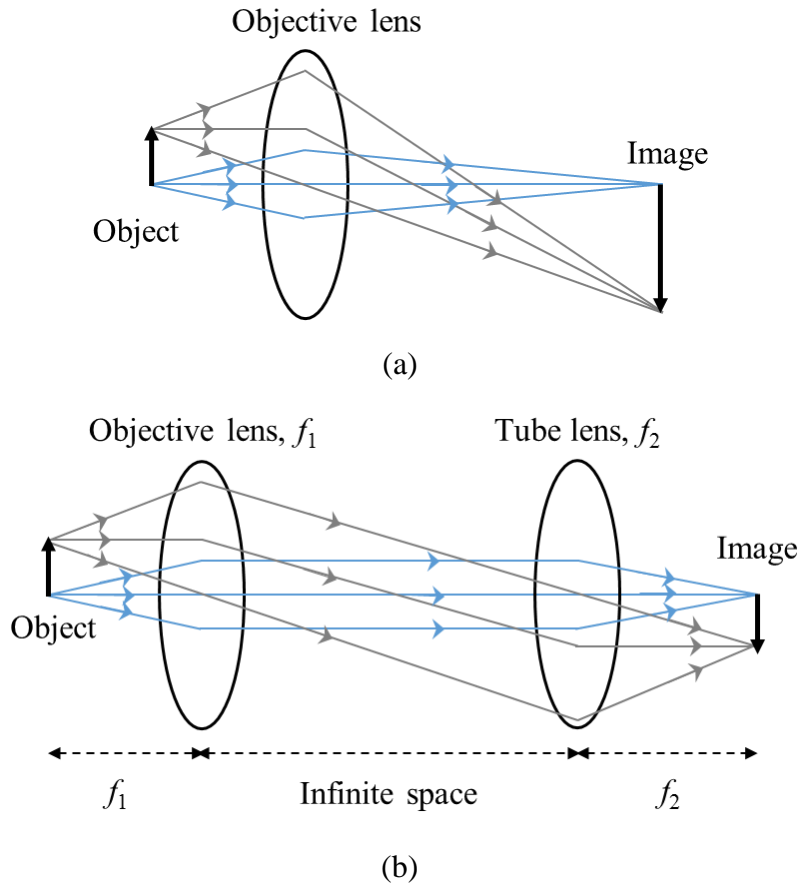
Figure 4.1 Schematics of (a) a finite correction optical system and (b) an infinity-corrected optical system.

4.1.2 Linnik interferometer

Interference microscopy is widely used to measure the far-field phase by detecting the optical path difference between two beams that have been split. Figure 4.2 shows the schematics of three common interferometers. Interferometers with low magnification from 1× to 5× are usually realized in the Michelson interferometer [91][92][93], as shown in Fig. 4.2(a). In this setup, a light source is split into two arms by a beamsplitter. The two beams are reflected back toward the beamsplitter, then are combined. The resulting interference

pattern that is not directed back toward the source is typically directed to some type of photoelectric detector or camera. In this setup, the reference mirror is placed outside the imaging path. At these low magnifications, the aperture angle is rather small and the field of view is quite big. So, in a Michelson interferometer, the mirror inside the imaging path would block too much light coming from the object. Figure 4.2(b) shows the schematic of a Mirau interferometer [94][95][96]. Here, two plane parallel glass plates are placed in front of the objective lens. The difference between the Mirau interferometer and the Michelson is in the physical location of the reference arm. The reference arm of a Mirau interferometer is located within a microscope objective assembly. Hence, due to its space saving and robust against mechanical influences, the Mirau interferometer is widely used in white light interferometers. As shown in Fig. 4.2(c), the basic configuration of a Linnik interferometer [97][98][99][100] is the same with a Michelson interferometer. In the Linnik interferometer, no components in front of the objective lens in the measurement arm are needed. In order to achieve an equal optical path length in the reference path and reduce aberrations, the objective lens in the measurement arm is duplicated in the reference arm. Due to the more complex design, a Linnik setup is quite expensive. Another reason why it is rarely used is the demanding adjustment and its sensitivity to mechanical and thermal influences. However, compared to the Michelson interferometer and Mirau interferometer, the Linnik type provides the highest numerical aperture and magnification, and preserves the whole working distance.

(a)

(b)

(c)
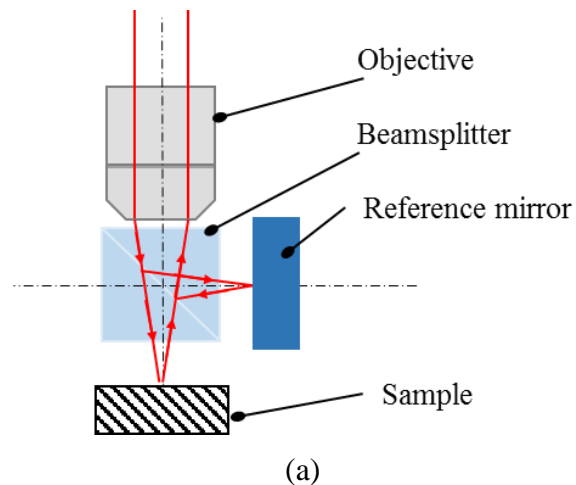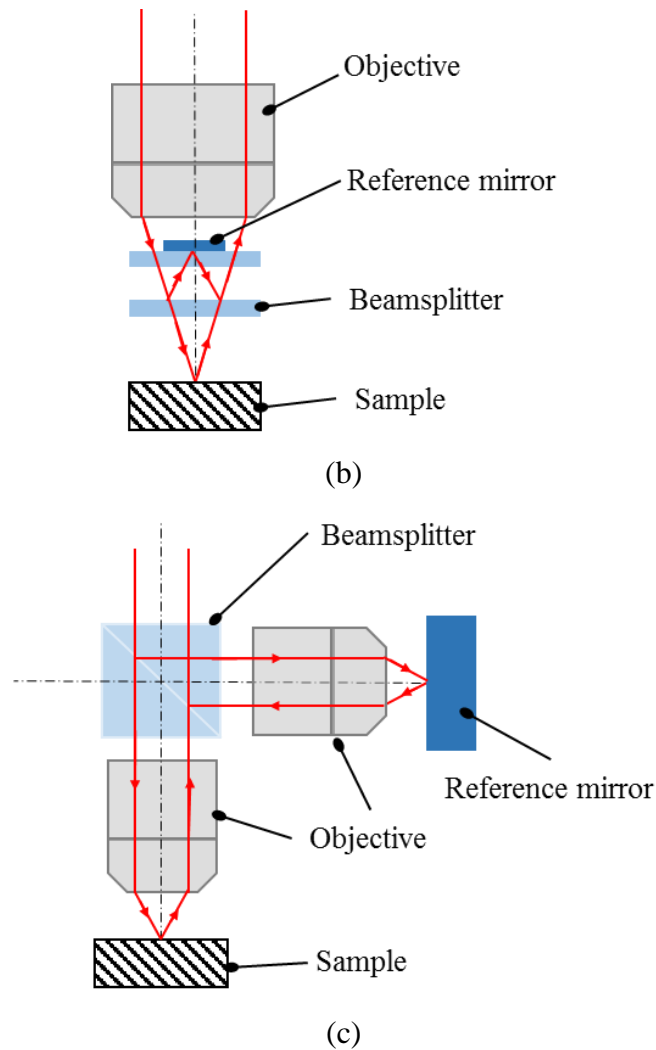
Figure 4.2 Schematics of three common interferometers: (a) a Michelson interferometer; (b) a Mirau interferometer and (c) a Linnik interferometer

Considering both the measurement accuracy and the miniaturization of the microgroove to be measured, the interference microscopy with higher magnification and higher lateral resolution is more advantageous. Hence, in this research, a design of Linnik interferometer was adopted for the far-field phase detection.

4.2 A plane wave incident unit

As mentioned measurement principle in Fig. 1.8, a plane wave incident illumination is crucial in depth measurement phase on change. Otherwise, e.g. in the case of Gaussian type illumination, the phase difference between the bottom surface and the top surface is not only caused by the depth of microgroove, but also the wavefront difference during the propagation. As we can see from Fig. 4.2(c), the light passing through the objective lens in conventional Linnik interferometer is a focused beam, which results in theoretical wavefront errors in the depth evaluation. Hence, a modified Linnik microscopic interferometer system based on three identical objective lenses and the optical path reversibility principle were designed to achieve plane wave illumination, as shown in Fig. 4.3.
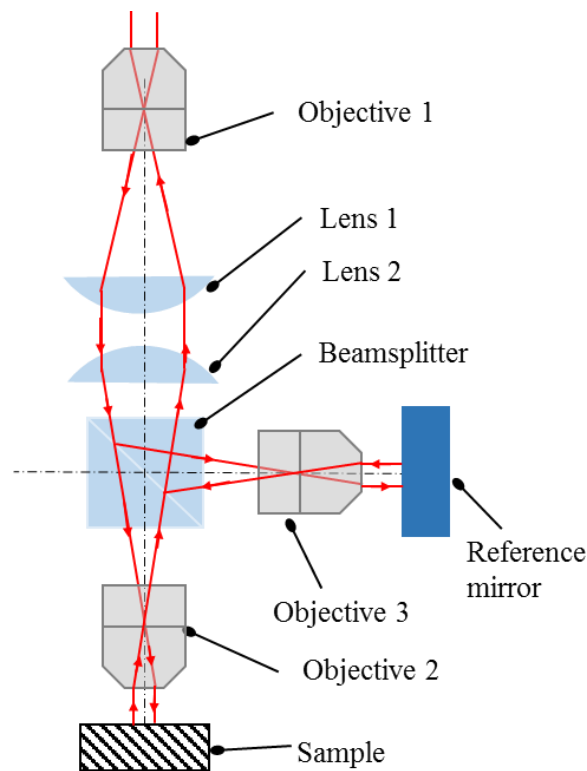
Figure 4.3 A modified Linnik interferometer to achieve a plane wave incident illumination.

In this modified Linnik setup, a collimated beam passes through the objective 1 and two identical convex-plane lenses set in opposite directions (lens 1 and 2). Then, a beamsplitter is used to divide the incident beam into two arms of equal intensity. One beam passes through

the object 2 and illuminates the sample. The other passes through the objective 3 and radiates the reference mirror. All the applied objectives are identical. The key factor is to ensure the distance between the objective 1 and lens 1 is equal to the distance between lens 2 and the objective 2 or objective 3, for obtaining plane wave illumination in measurement arm and reference arm.

In order to verify the plane wave illumination by the proposed design of the modified Linnik interferometer, a shearing plate (Shearing Interferometers SI035P, Thorlabs) was used to determine if the light after objective 2 or objective 3 is collimated. Figures 4.4 and 4.5 are the cross-section of this shearing plate and the instructional patterns by different beams, which are both provided by the homepage of Thorlabs (https://www.thorlabs.com). The shearing plate consists of a wedged optical flat mounted at 45 ° and a diffuser plate with a ruled reference line in the middle. A diffuser plate is used to view the interference fringes created by Fresnel reflections from the front and back surfaces of the optical flat. If the beam is collimated, the resulting fringe pattern will be parallel to the central ruled reference line, however, the fringe pattern by a converging or diverging beam is oblique with the central ruled reference line, as suggested in Fig. 4.4.
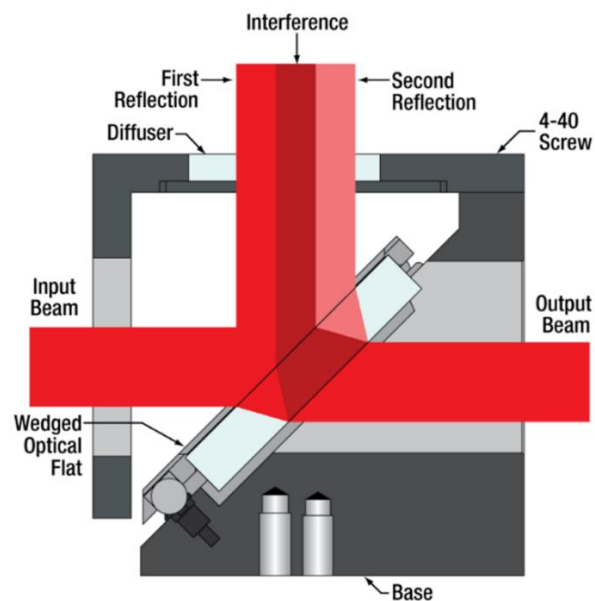
Figure 4.4 Schematic of cross-section of the shearing plate provided by Thorlabs.

Collimated   Converging or diverging
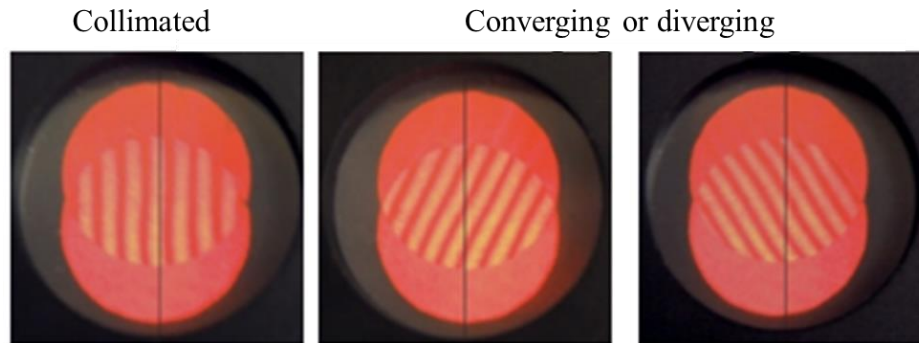
Figure 4.5 The instructional patterns by different beams provided by Thorlabs.

Figure 4.6 shows the observed patterns on the diffuser plate by the designs of conventional Linnik interferometer and modified Linnik interferometer, respectively. The incident beam is a collimated beam from a He–Ne laser source (632.8 nm, 15 mW). The applied three objective lenses (Mitutoyo Plan Apo Infinity Corrected Objective) have a focal length of 20 mm, while the focal length of the two identical lens is 150 mm. It is clearly found that the observed fringes in the modified Linnik interferometer are parallel to the central ruled reference line, similar to the collimated pattern in Fig. 4.5, while there are slanted fringes in the conventional Linnik interferometer. This observation is a strong indicator of incident plane wave illumination by the modified Linnik microscope interferometer.

(a) The pattern by conventional Linnik interferometer   (b) The pattern by modified Linnik interferometer

Figure 4.6 The practically observed patters by (a) a conventional Linnik interferometer and (b) the modified Linnik interferometer

4.3 A measurement system with laser illumination

Due to highly spatial and temporal coherence and high irradiance, the laser source is widely applied in micro and nano measurement [101][102][103][104]. Figure 4.7 is the design of a laser-based measurement system constituted by an infinite corrected imaging system and the modified Linnik interferometer. The light source is a linearly polarized laser, which is connected to a polarization maintaining single model optical fiber. Then the point light source passes through a collimating lens and an aperture. Next, it is the part of modified Linnik interferometer, where a shutter is mounted before objective 3 in the reference path. When the shutter is closed, this measurement system is just an imaging system and only the reflected beam from sample is collected by the CCD camera. When the shutter is opened, two beams reflected from the sample and the reference are combined at the beamsplitter and create interferograms and are finally captured by the CCD. The sample is mounted on a three-axis stage, and the reference mirror is mounted on a PZT actuator to achieve phase shifting control. A computer manipulates the CCD sampling and the PZT actuator for nanoscale shift and sample motion. The parameters of the laser source, the CCD camera, the PZT and other elements are listed in Tables 4.1 - 4.5, respectively. Figure 4.8 is a photography of the developed laser-based measurement system. The red line denotes the incident beam, while the reflected beams are indicated as the blue line.
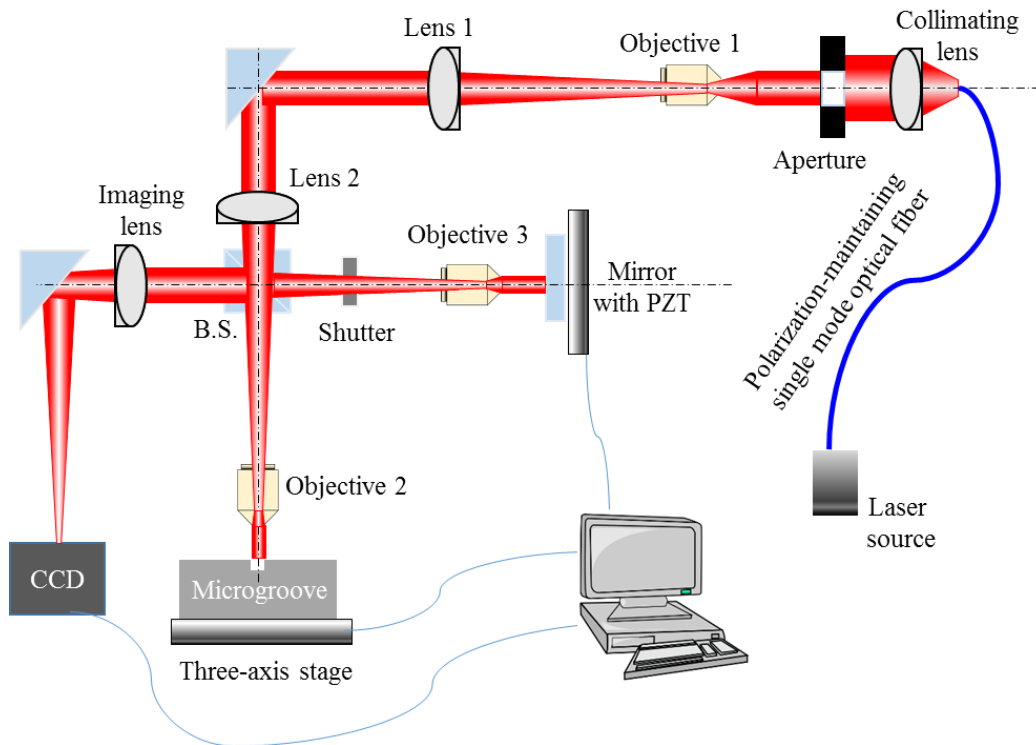
Figure 4.7 The design of a laser-based measurement system

Table 4.1 Parameters of the laser source

	Parameters
Manufacture company	Melles Griot
Type	He–Ne laser
Series number	05 LHP 151
Power	5 mW
Wavelength	632.8 nm
Polarization	Linear polarization
Beam diameter	0.8 mm

Table 4.2 Parameters of the CCD camera

	Parameters
Manufacture company	Basler
Model number	acA3800-14μm
Resolution (H × V)	3840 pixel × 2748 pixel
Resolution	10 MP
Pixel Size (H × V)	1.67 μm × 1.67 μm
Frame Rate	14 fps
Pixel Bit Depth	8 bits

Table 4.3 Parameters of the PZT actuator

	Parameters
Manufacture company	PI (Physik Instrumente)
Series number	P-753.21C
Closed-loop travel	25 μm
Resolution	0.1 nm
Linearity error (closed-loop)	0.03%
Repeatability	± 2 nm
Pitch / yaw	± 7 μrad

Table 4.4 Parameters of the PZT controller

	Parameters
Manufacture company	PI (Physik Instrumente)
Series number	E-710.4CL
Type	Closed loop
Channels	4
Sampling rates	50 μs (sensor); 200 μs (servo loop, 4 channels)
Effective Resolution, DAC	20 bits

Table 4.5 Parameters of other elements in the laser-based setup

	Parameters
Beamsplitter	A splitting ratio of 50:50
Objective lens	Mitutoyo Plan Apo Infinity Corrected Objective; $NA = 0.28$; Focal length = 20 mm
Imaging lens	Focal length = 400 mm
Magnification power of the system	20×
The diffraction limit	1379 nm
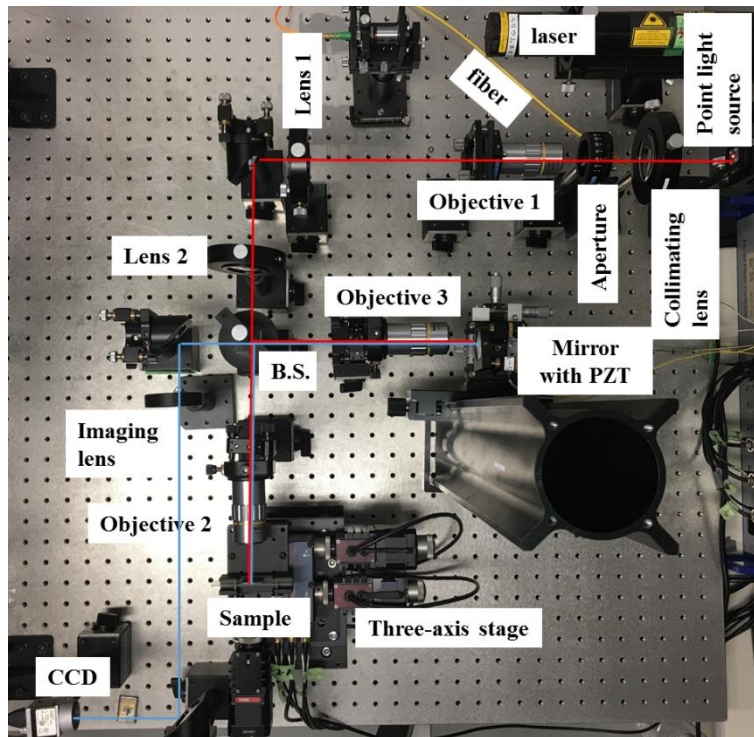
Figure 4.8 A photography of the laser-based measurement system

Figure 4.9 shows an observation for a flat silicon surface by the developed laser-based measurement system. The spatially background noise was found, which is called speckle noise [105][106][107]. The speckle noise is a random intensity pattern when fairly coherent light is reflected from a rough surface. Such patterns are clearly visible to the observer when

highly coherent laser source is used, even in polymer materials. Undoubtedly, the speckle noise is source of the measurement accuracy in depth measurement when highly coherent laser is used for illumination.
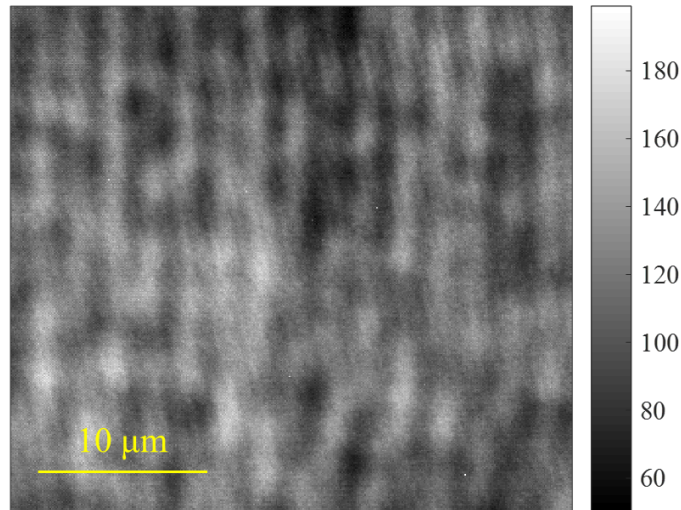
Figure 4.9 An observation for a flat silicon surface by the laser-based measurement system.

Besides the speckle noise, another disadvantage occurs when the laser source is used to measure the transparent surface. As mentioned in Chapter 1, there is an increasing trend of fabricating functional microstructures with the more traditional materials, such as polymers, metals and glasses. Especially, the microfluidics and some bio-inspired functional surfaces are mainly manufactured by the polymer materials. When it comes to the topography measurement of transparent structure, the multiple interference noise [108][109][110] is a significant factor for spatial background noise. Transparency or translucence is a physical characteristic for most of polymer materials, e.g. the amorphous thermoplastic polymer. As shown in Fig. 4.10, an incident beam (E_i) is partially reflected and partially transmitted at each interface of transparent structure. As a result, the reflectively multiple beams interfere with each other and the total reflected beam (E_r) is a coherent summation. The degree of constructive or destructive interference between multiple reflection depends on the difference in their phase, which is determined by the wavelength and angle of incident beam, the thickness and refractive index of transparent structure and the possible phase shifts that occur upon reflection. The practically spatial patterns resulting from the multiple interference and

optical path-length shifts can appear the visibly light and dark bands by laser and the colorful bands by LED source [109].
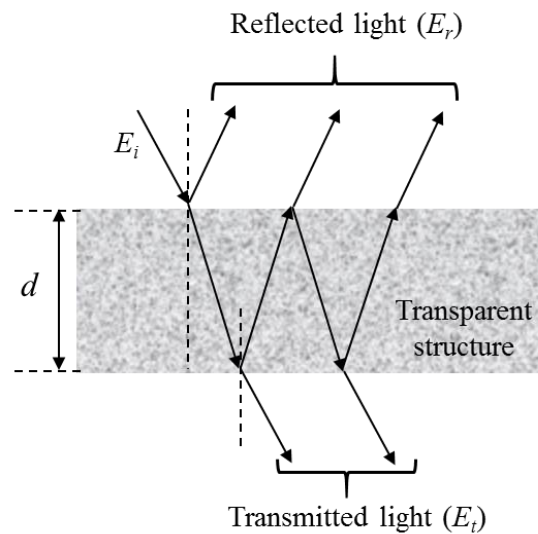
Figure 4.10 Multiple reflection on transparent material.

A flat surface on a transparent cyclic olefin copolymer (COC) sample with a thickness of several millimeters was irradiated by the developed laser-based measurement system, and Figure 4.11 shows the observation. From this figure, not only the random speckle noise can be observed, but the fringes (denoted in the red dashed box in Fig. 4.11) caused by multiple interference on the transparent structure can be found.
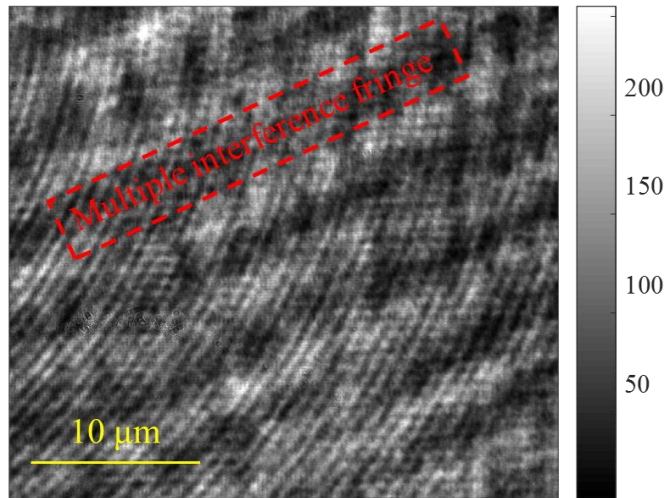
Figure 4.11 An observation for a flat surface on transparent cyclic olefin copolymer (COC) sample by the laser-based measurement system

4.4 A measurement system with low-coherence illumination

In order to reduce both the speckle noise and the multiple interference noise on the transparent structure, a new measurement system with low-coherence illumination was developed and introduced in this section.

Figure 4.12 is the design of the measurement system with low coherence illumination, which are achieved by a LED lighting and a bandpass filter. The light from a white LED lighting converges spontaneously in its focal plane, where an aperture is mounted to adjust the size of incident beam. Then, the incident beam passes through a bandpass filter and the generated low-coherence light goes through a collimating lens. After that, a plane-convex lens (lens 1, f = 200 mm) and two identical objective lenses (20x Plan Apo, NA = 0.42, Mitutoyo) are mounted. If the separation of lens 1 and objective lens is approximately equal to the sum of their focal lengths, the plane wave incidence will irradiate both the sample and reference. As the same with the laser-based setup, the shutter for switching from the infinite-corrected imaging system to interference system, an imaging lens, the CCD camera (see Tab. 4.2) and the PZT (see Tab. 4.3 and 4.4) are used to constitute the new measurement system.
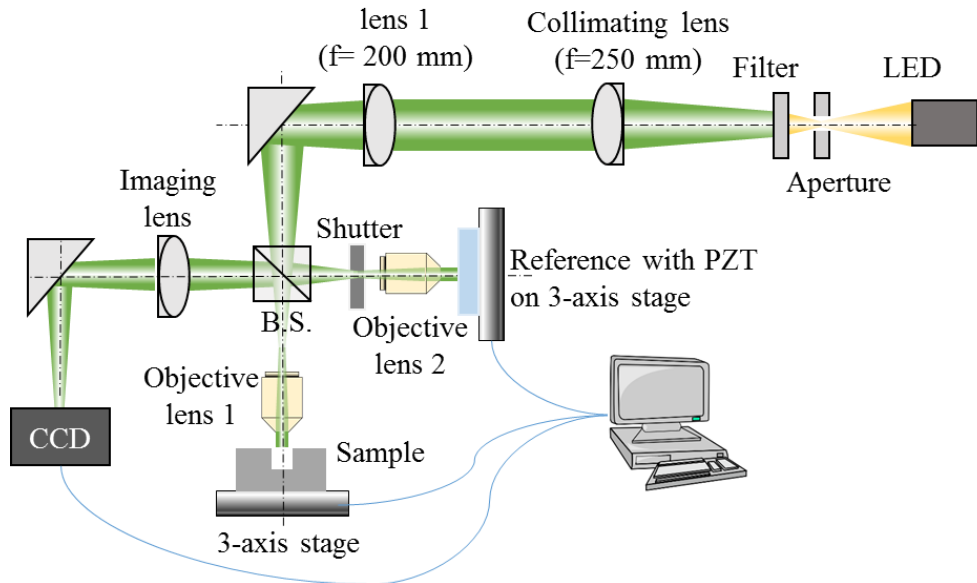
Figure 4.12 The design of the measurement system with low coherence illumination.

4.4.1 The white light source and the bandpass filter

In the new measurement system, the applied light source is a new type of white light LED, called hololight (HL05WW1FM-V, warm white LED lighting, Pi Photonics Inc.). There two main advantages by using hololight. As shown in Fig. 4.13(a), it is a schematic of the illumination for most LED sources with a diffuse propagation and an extremely small emitter size (point source). This illumination design can provide plane wave illumination for measurements, but the non-uniform irradiance is introduced because of the optical vignetting [111][112], which indicates the strong irradiance in the optical axis and the weak irradiance in the edge. In order to solve this problem, the applied hololight can produce the telecentric light [113][114][115] from a emitter area of 100 mm × 100 mm, as shown in Fig. 7(b). The beam from hololight converges spontaneously in its focal plane due to the directional characteristic, then a collimating lens is mounted to obtain the plane wave illumination with uniform irradiance, which can eliminate the adverse effect caused by optical vignetting in the follow-up data processing.
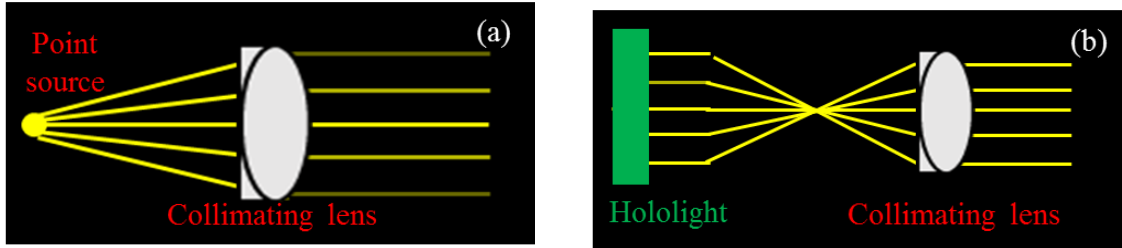
Figure 4.13 Schematics of illumination for (a) the LED point source with diffuse propagation and (b) hololight used in the measurement system

Another advantage by using hololight lies in the high power of irradiance. The optical signal from desired microgroove is one of important issue that must be considered in the experiments. Especially, because of the low reflection efficiency due to small refractive index of the polymer material, there is a high requirement for irradiance. The irradiance of hololight in its focal plane is several milliwatts level per square millimeter. Figure 4.14(a) shows an observation for a transparent cyclic olefin copolymer (COC) sample under 0.4 s exposure time by developed measurement system. As a contrast, the same sample was illuminated under the same exposure time by a LED-based measurement system (MCWHLP1, 41.3 μW/mm^2, Thorlabs), which was interfaced with the same optics of hololight. And the observation is shown in Fig 4.14 (b).
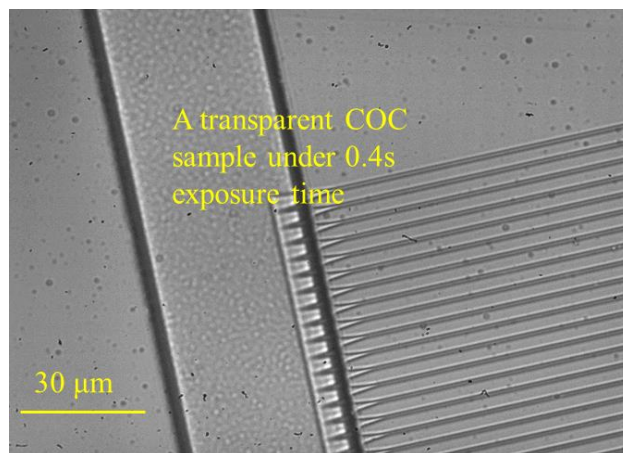
(a)
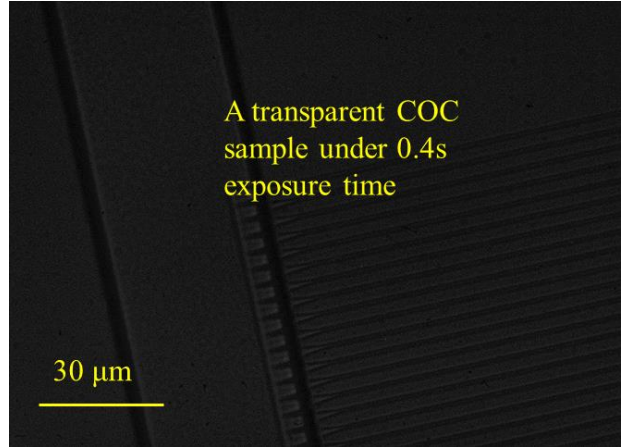
(b)

Figure 4.14 Observation of a transparent COC sample under same 0.4 s exposure time: (a) by hololight and (b) conventional LED source.

Figure 4.15 presents the spectrum of applied hololight, which is provided by the manufacture company. According to both the relative intensity of hololight and the diffraction limit of the measurement system, the bandpass filter can be selected. In order to eliminate the fringe caused by multiple interference on the transparent structure, the center wavelength (CWL) and the bandwidth of applied filter also should be optimally designed to ensure the coherence length is smaller than the thickness of sample to be detected. Table 4.6 lists the parameters of the applied filter, and the transmission are plotted in Fig 4.16, which are provided by the manufacture company.
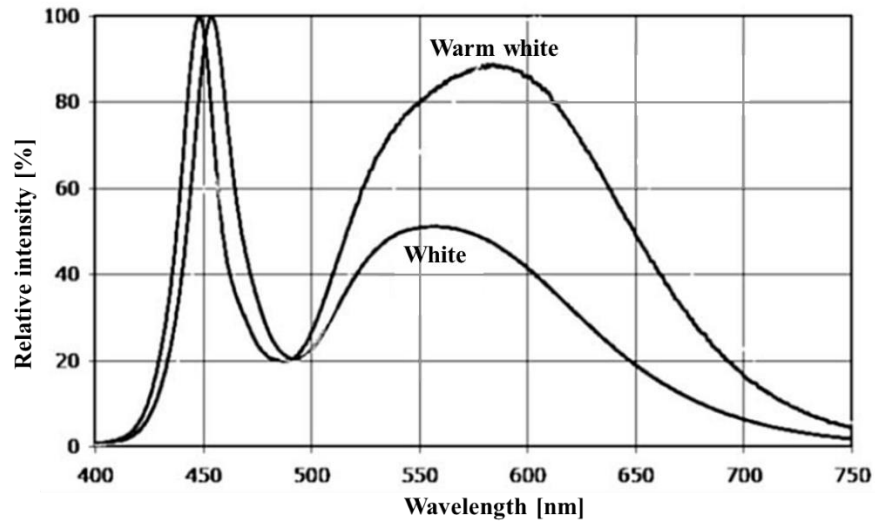
Figure 4.15 Spectrum of hololight, provided by Pi Photonics Inc.

Table 4.6 Parameters of applied bandpass filter

	Parameters
Manufacture company	Thorlabs
Series number	FLH532-10
CWL	532 nm
Bandwidth (FWHM)	10 nm
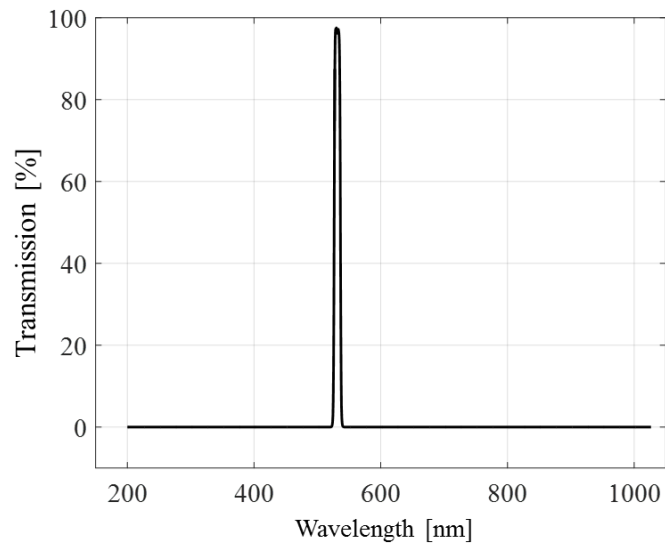
Figure 4.16 Transmission of applied bandpass filter, provided by Thorlabs.

4.4.2 Optical cage system

Another improvement of the measurement system with low-coherence illumination is the optical cage design, which uses four rigid steel rods to mount optical components along a common optical axis. The center-to-center rod spacing in our system is 30 mm. The optical cage system can provide the good robustness, overall solidity and optical coaxiality for measurements. A photography of the measurement system with low-coherence illumination is presented in Fig. 4.17.
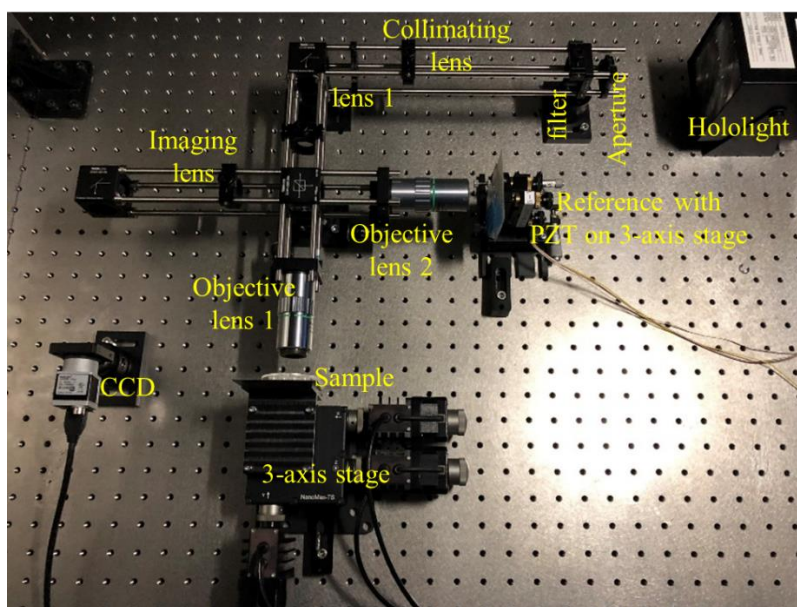
Figure 4.17 A photography of the measurement system with low-coherence illumination

A type of drop-in mount is used, for quick and easy insertion of Ø1" optical elements into the developed 30 mm cage system. As shown in Fig. 4.18, they are photographs of inserting the mount into a pre-assembled cage system (Fig. 4.18(a)), and removing the mount (Fig. 4.18(b)). As we can see, the drop-in mount allows for 360 ° rotation of optical elements within a 30 mm cage system. After inserting the mount into a cage system, turn the optic perpendicular to the optical axis and snap the mount onto adjacent cage rods before tightening the setscrew. The drop-in mount allows optical elements to be inserted or removed from an assembled cage system without affecting the alignment or assembly of the rest of the system,

which is crucial to obtain the visible interference fringes to be introduced in Chapter 5 and in dual-wavelength measurement system to be introduced in Chapter 6.

(a) Inserting optical elements

(b) Removing optical elements

Figure 4.18 photographs of (a) inserting the mount and (b) removing the mount in a cage system

In this setup based on the low-coherence illumination, the CWL of incident LED light is 532 nm and the numerical aperture of the objective lens is 0.42. Hence, the diffraction limit of this system is 772 nm, while the magnification power is 40.

4.4.3 Measurement by low-coherence illumination

The coherence length can be calculated by

$$L = \frac{\text{CWL}^2}{\text{FWHM}} \tag{4.1}$$

Under the hololight and the bandpass filter, the coherence length of the developed measurement system is 28 μm and far less than the coherence length of laser source (meters level). Using this measurement system with low coherence illumination to measure the same silicon sample with Fig. 4.9 and the same COC sample with Fig. 4.11, the results are presented in Fig. 4.19 and 4.20, respectively.
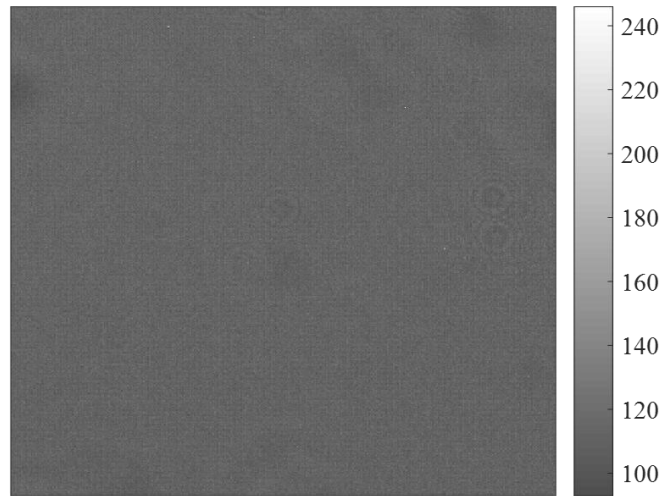
Figure 4.19 An observation for the same silicon surface as Fig. 4.9 by the developed setup with low-coherence illumination
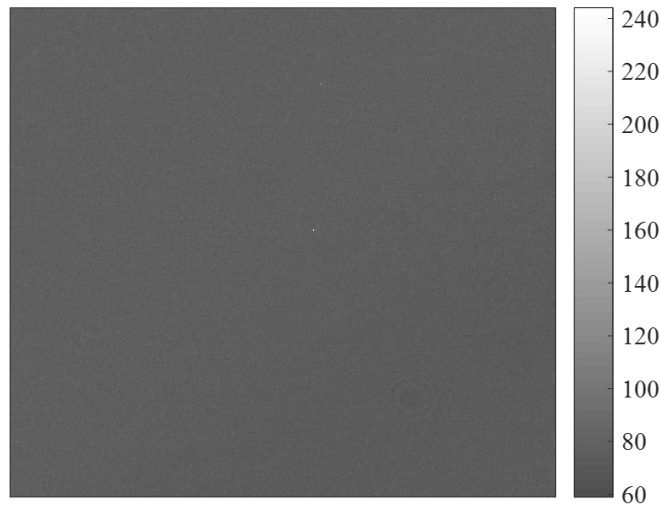
Figure 4.20 An observation for the same COC surface as Fig. 4.11 by the developed setup with low-coherence illumination

Obviously, from Figs 4.19 and 4.20, the spatial noise caused by the speckle noise and multiple interference disappeared by the low-coherence illumination. In order to quantitatively compare the spatial background noises by the measurement system based on low-coherence illumination and a laser-based system, we measured the spatial topography images from the same flat surface on a transparent COC sample by the two systems, respectively. The thickness of this COC sample is several millimeters and greatly larger than

the coherence length (28 μm) of the developed measurement system. The referenced laser-based system is interfaced with the same cage system of hololight. The Linnik interferometer and the four-step phase shift method are used to calculate the spatial height distribution. The spatial topography images (height maps) by the two measurement systems are presented in Fig. 4.21. The standard deviation of heights is reduced from 16 nm by laser source (Fig. 4.21(b)) to 2 nm by the low-coherence illumination (Fig. 4.21(a)). The experiment results show that, by eliminating both the speckle noise and multiple interference noise on transparent structure, the spatial uniformity and accuracy by the low-coherence illumination are substantially better than the laser source. Furthermore, with the developed measurement system based on low-coherence illumination, the standard deviation of heights from the flat surface on a transparent COC sample is 2 nm.
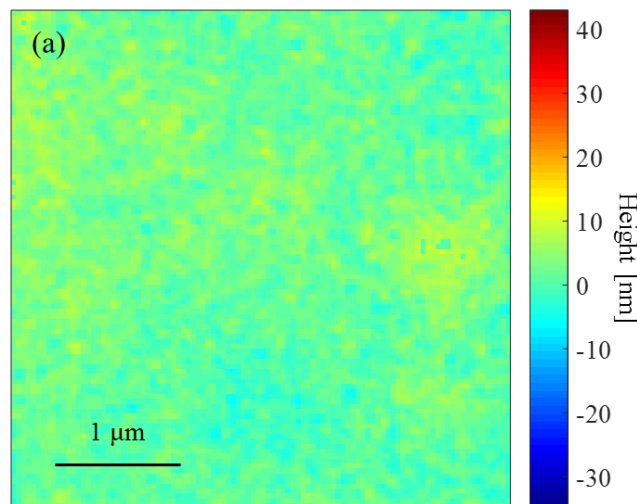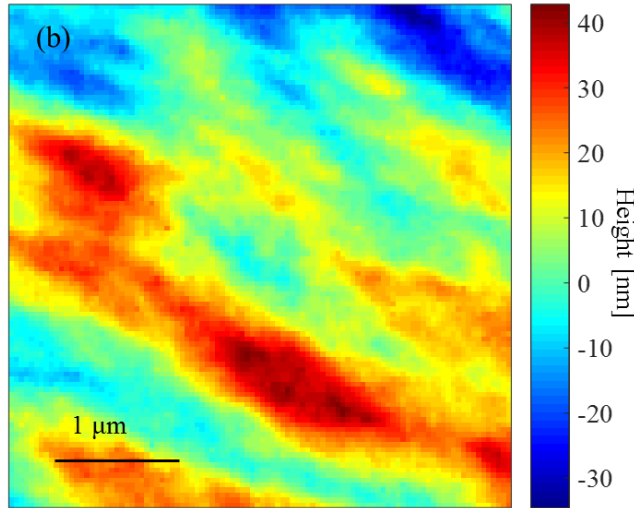
Figure 4.21 Spatial topography images by (a) the developed measurement system based on low-coherence illumination and (b) a laser-based system.

4.5 Sensitivity of the developed measurement system

In this section, the sensitivity of the developed measurement system based on low-coherence illumination (Fig. 4.17) is discussed through practical measurements. Using the developed setup and the four-step phase shift method, we imaged the height maps from a flat surface on a transparent COC sample repeatedly, to obtain a 28-frame stack. For each frame of one topography image, the evaluated field of view (FOV) is 4×4 μm^2. Figure 4.22 shows the temporal histogram of the heights at the same measurement point over the entire stack. The red dots denote the raw data, while the black line indicates the fitting profile by a Gaussian distribution, given by

$$f = a \exp\left(-\frac{(x-b)^2}{2c^2}\right) \tag{4.2}$$
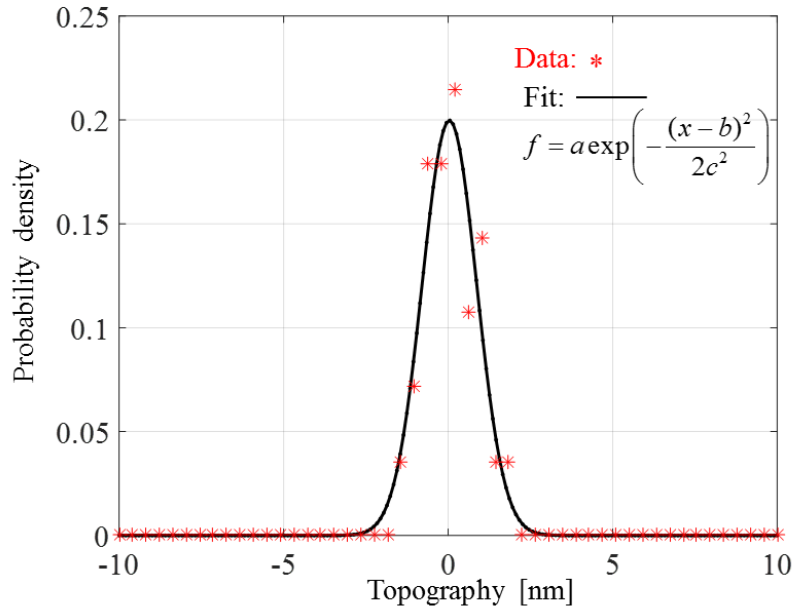
Figure 4.22 Temporal sensitivity of optical path-length measurement

With f of the probability density, x of the topography, a, b and c are the coefficients of the Gaussian distribution. Figure 4.23 depicts the spatial histogram of the heights over the entire FOV of one frame. And Table 4.7 lists the coefficients of the Gaussian distributions applied in temporal and spatial histograms. Both the temporal and spatial histograms basically coincide with the Gaussian distribution ($R^2 = 0.95$ and 0.99). The noise levels, 0.83 nm and 2.24 nm, represent the limit in optical path-length sensitivity across the entire FOV and between frames, respectively.

Table 4.7 Parameters of the fitting Gaussian distributions

	a [nm]	b [nm]	c [nm]	Goodness of Fit (R^2)
Temporal histogram	0.20	0.04	0.83	0.95
Spatial histogram	0.07	-0.08	2.24	0.99
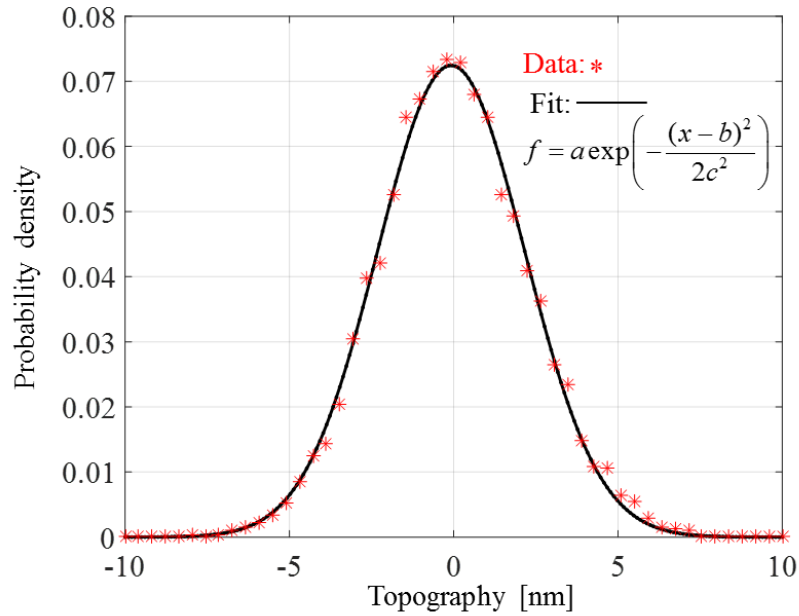
Figure 4.23 Spatial sensitivity of optical path-length measurement

4.6 Conclusions

In order to measure the three required far-field observations of the proposed FNRDM method, the measurement system was developed and introduced in this Chapter.

Firstly, according to the measurement requirements, the fundamental designs of the infinite corrected imaging system and the Linnik interferometer were presented, for obtaining the high magnification power and high lateral resolution.

Secondly, in order to achieve a plane wave incident illumination for the sample and reference, a design of the modified Linnik interferometer based on the optical path reversibility principle was proposed. A commercial shearing plate is used to verify the validity of this optical path design.

Thirdly, we developed a laser-based measurement system, which enables the measurements of required far-field observations. However, due to the high coherence of this system, the laser speckle and the multiple interference from a transparent structure lead to a great spatial background noise, which is adverse to depth measurement.

In order to solving the mentioned problem, a new setup based on low-coherence illumination was developed. The optical cage system was also applied in this new setup. By comparing the observations of same flat surfaces with a laser-based setup and the new setup based on low-coherence illumination, it is found that the spatial uniformity and accuracy of images by the low-coherence illumination are substantially better than the laser source. The diffraction limit, magnification power and coherence length of the setup based on low-coherence illumination are 772 nm, 40 and 28 μm, respectively.

Finally, we analyzed the sensitivity of the developed measurement system based on low-coherence illumination. The results suggest that this setup not only provides speckle-free images, but also allows for spatially sensitive optical path-length measurement (2.24 nm) and temporally sensitive optical path-length measurement (0.83nm).

Chapter 5. Experiment verification of FNRDM beyond the diffraction limit

In Chapter 4, a measurement system based on the low-coherence illumination and Linnik interferometry was developed to measure the required far-field observations of the proposed FNRDM method. In this chapter, the channels with a nominal width of 300 nm and a nominal depth of 110 nm on a transparent cyclic olefin copolymer (COC) surface were measured to verify the validity of the proposed FNRDM method. Not only a greatly improved accuracy over conventional interferometry, but also a possible evaluation of the individual differences for each channel which is not possible with scattertometry will be demonstrated.

5.1 A transparent microfluidic sample with functional channels

Figure 5.1 illustrates a schematic of a microfluidic sample (thermoplastic COC 5013L molded sample, transparent), which was fabricated by Technical University of Denmark. The thickness of sample is several millimeters and far larger than the coherence length (28 μm) of developed measurement system. On the surface of this microfluidic sample, there are two main areas: uniform surface (denoted as red dashed box in Fig. 5.1(a)) and functional nanochannels (denoted as yellow dashed box in Fig. 5.1(a)). The nanochannels are connected with a terminal microchannel by tapered inlets. Figure 5.1(b) depicts a schematic of cross-section of the functional nanochannels. The nominal width, depth and pitch of these periodic nanochannels are 300 nm, 110 nm and 4300 nm, respectively. Obviously, the nominal width is far less than the diffraction limit (772 nm) of the developed measurement system. Hence, this microfluidic sample is suitable for the experimental verification of proposed depth evaluation method and developed measurement system. Figure 5.2 shows an observation of the microfluidic sample by an optical microscopy.
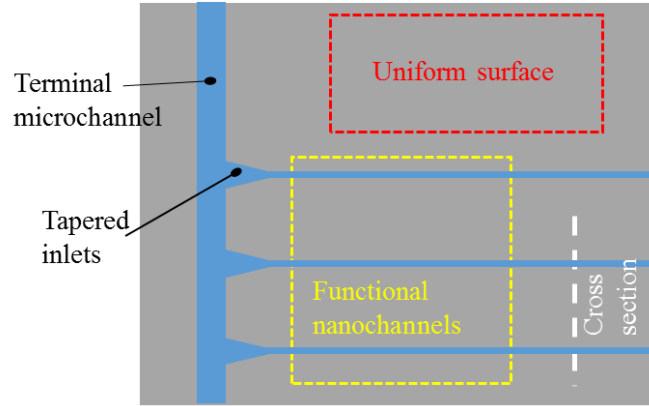
(a) Top view
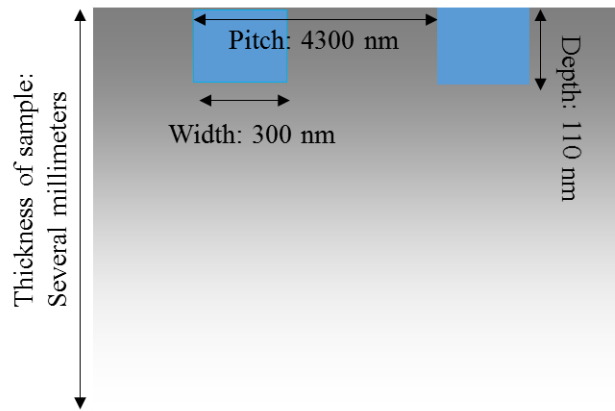
(b) Cross-section of functional nanochannels

Figure 5.1 Schematics of the transparent microfluidic sample: (a) top view and (b) cross-section.
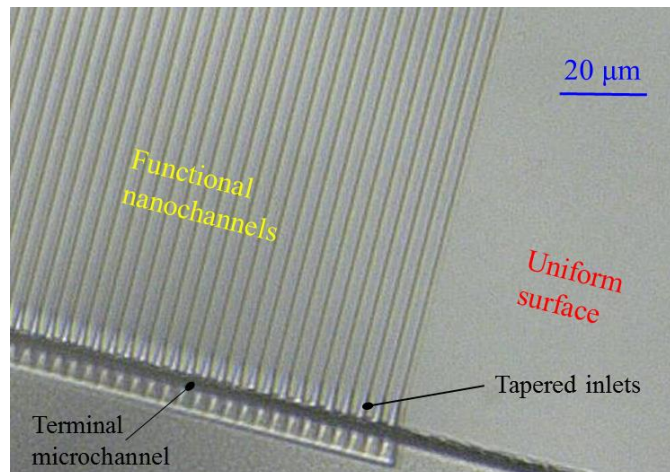
Figure 5.2 An observation of the transparent sample by an optical microscopy.

5.2 AFM measurement of the transparent microfluidic sample

In order to obtain the reliable reference data for verification, the transparent microfluidic sample has been measured by AFM. The applied Innova AFM [116][117][118], which delivers accurate, high-resolution imaging and a wide range of functionality for advanced research in physical, life and material sciences. The Innova AFM uses a stationary probe, and samples are scanned back and forth beneath the probe. Typically, the samples are attached to round metal disks (pucks) which are magnetically attached to the top of the scanner tube. The scanner moves the sample in the x, y and z direction, and the probe obtains information from the sample. All aspects of the electromechanical design of Innova AFM have been optimized, from the rigid microscope stage with a short mechanical loop and low thermal drift to the ultra-low noise electronics. The result is a unique combination of high-resolution performance and closed-loop positioning. The Innova AFM uses Bruker's proprietary ultra-low noise digital closed-loop scan linearization for accurate measurements in all dimensions, regardless of size, offset, speed, or rotation in air and liquid.

Before the measurement of the transparent microfluidic sample, a calibration of AFM was performed to ensure the accuracy. A standard artifact (VGRP-18M) is used as a general purpose sample of known feature sizes to calibrate the AFM scanners within a certain tolerance. The nominal pitch and depth of the standard artifact are 10 μm and 180 nm, respectively. Figure 5.3 shows a two-dimensional image of the standard artifact, and the height histograms before and after calibration. After calibration by using the standard artifact, the measurement accuracy of AFM scanner in Z direction is approximately 3 nm.
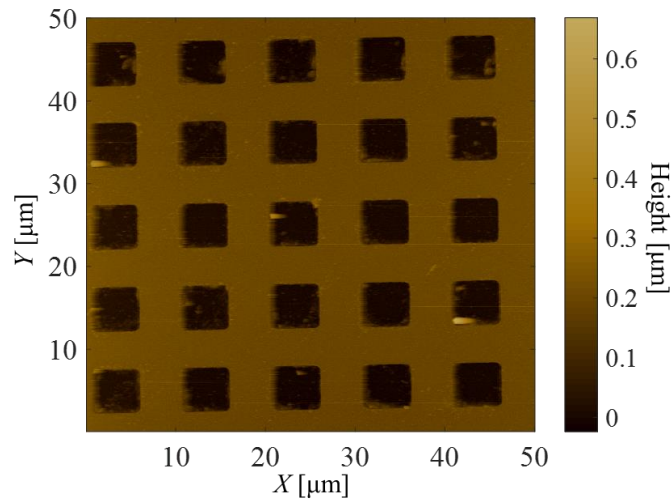
(a)
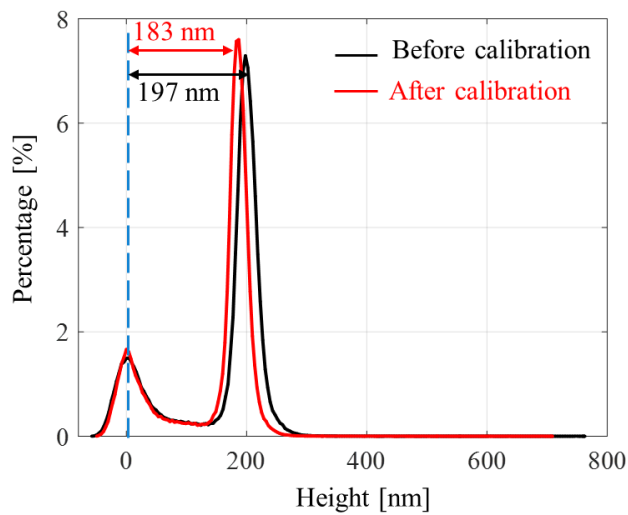
(b)

Figure 5.3 AFM calibration: (a) a two-dimensional image of standard artifact (VGRP-18M) and (b) height histograms before and after calibration.

The AFM measurement of the transparent microfluidic sample includes the following processes. Firstly, identify the location. In order to evaluate the same nanochannels between AFM measurement and the developed setup based on low-coherence illumination, a rough scanning of AFM measurement was implemented on the microfluidic sample. The samples per line, scan rate and scan range of rough scanning are 256, 1.0 Hz and $30 \times 30 \ \mu m^2$,

respectively. As shown in Fig. 5.4, both the functional nanochannels (bottom right region) and the uniform surface (upper right region) are clearly found, and the terminal microchannel (the thick dark line) is the key location mark. The evaluating area (dashed blue box), containing four nanochannels, has a distance of 11 μm to the terminal microchannel in X direction and is adjacent to the uniform surface in Y direction. The size of the evaluating area is $2 \times 16 \ \mu m^2$.
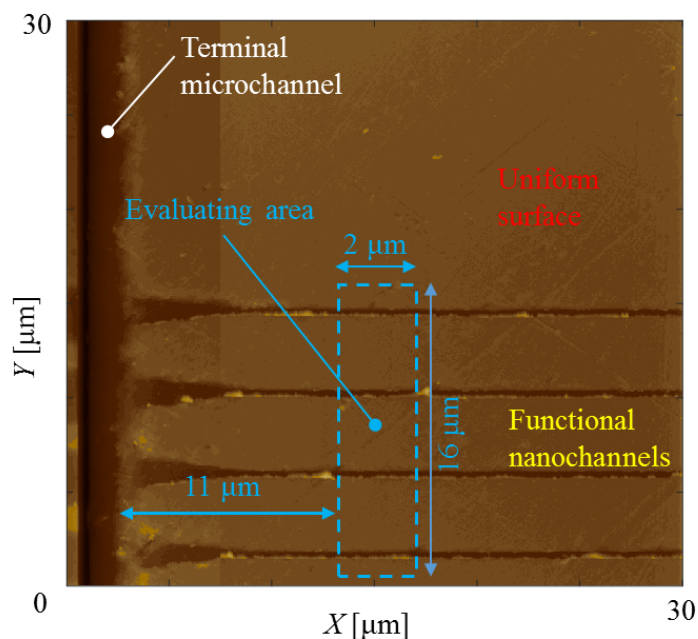
Figure 5.4 AFM measurement by a rough scanning process for location identification.

Then, a fine scanning process was carried out to obtain the topography in the evaluating area. The samples per line, scan rate and scan range of rough scanning are 1024, 0.1 Hz and $2 \times 16 \ \mu m^2$, respectively. Figure 5.5(a) plots the two-dimensional topography image of the evaluating area, while the corresponding height histogram is illustrated in Fig. 5.5(b). According the AFM measurement, the depth of nanochannels in the evaluating area on the transparent microfluidic sample is approximately 114 nm.
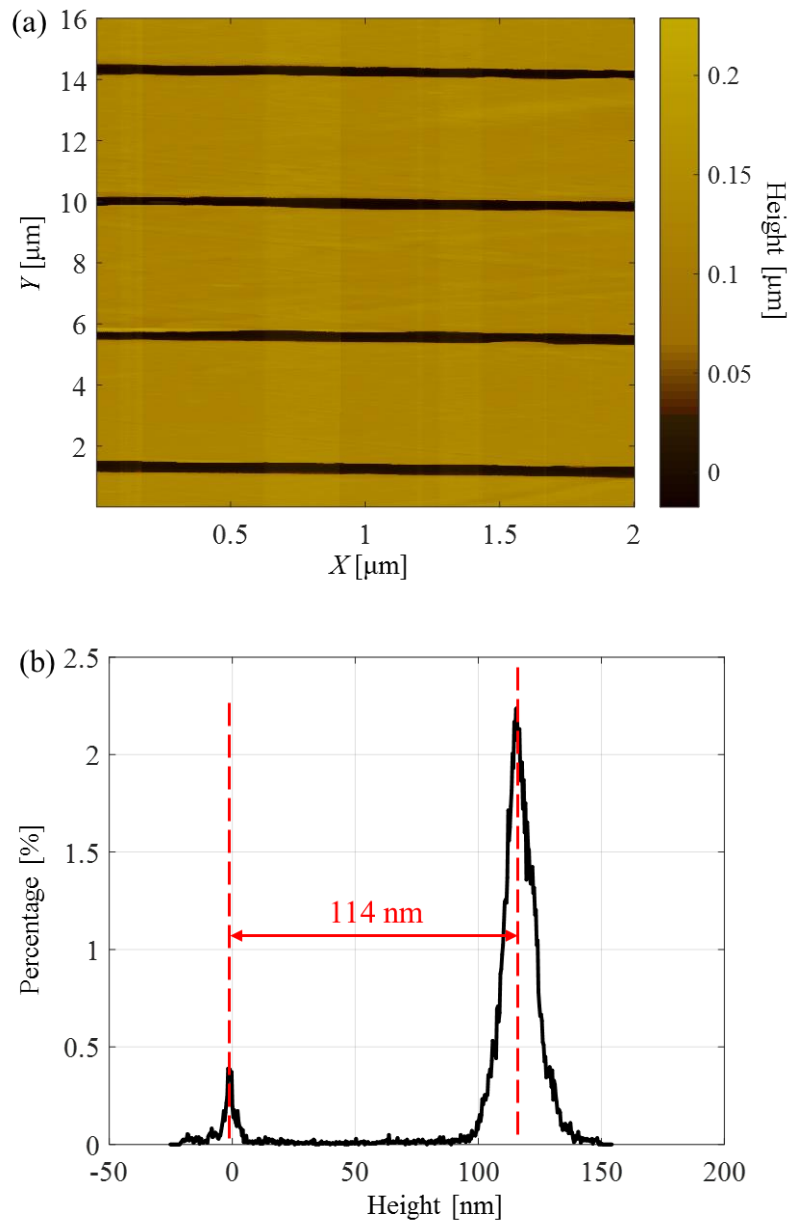
Figure 5.5 AFM measurement of the evaluating area by a fine scanning process: (a) a two-dimensional topography image and (b) a height histogram.

5.3 Measurement by the developed setup

In this section, the three far-field observations of the proposed FNRDM method, including the amplitude from the microgroove structure (A_f), phase difference between the top surface

and the bottom surface (θ_f), and the amplitude from a uniform surface without microgroove area (A_u), were measured by the developed system based on low-coherence illumination. The measurement processes are as followings.

5.3.1 Measurements for far-field amplitudes

Firstly, the same evaluation area with the fine scanning of AFM measurement is located. Turn off the shutter in the reference arm of the developed setup, then the imaging of the microfluidic sample was presented in Fig. 5.6 by the infinite corrected imaging system. The functional nanochannels (bottom right region), uniform surface (upper right region) and the terminal microchannel (the thick dark line) are clearly observed. Here, A_u of the proposed method can be regarded as the average amplitude of the measured uniform surface in Fig. 5.6, then the amplitude from the top surface (A_t) of the nanochannel is calculated by Eq. (2.30).
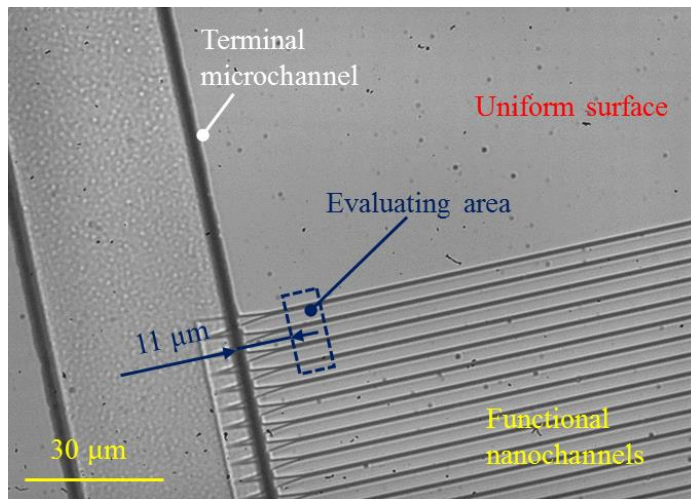
Figure 5.6 Raw observation of the transparent microfluidic sample by the infinite-corrected imaging system.

By using the marks of the terminal microchannel and the uniform surface, the data in the same evaluating area (blue dashed box in Fig. 5.6) with AFM measurement can be exported. After a rotation process by Matlab, the amplitude distribution in the evaluating area was shown in Fig. 5.7. The dark part and bright part indicate the bottom surface and the top

106

surface of the nanochannels, respectively. The amplitudes at the central positions of the four nanochannels denote the amplitudes (A_f) from the nanochannels.
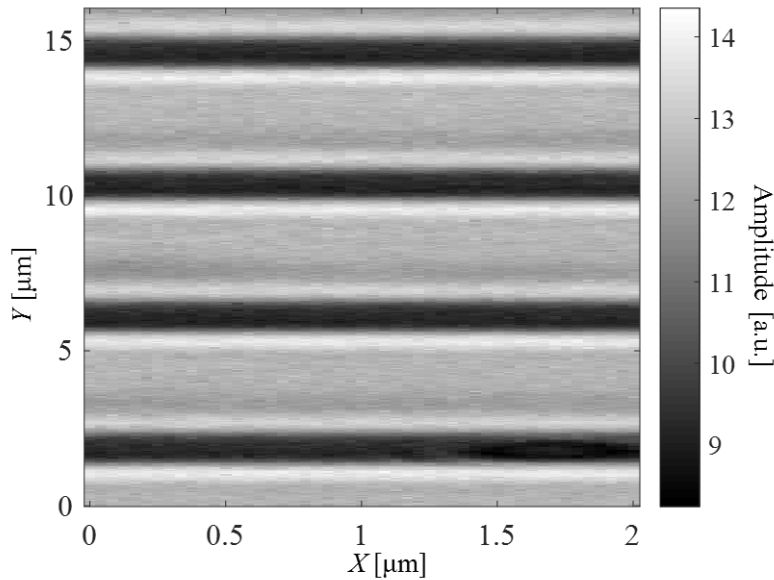
Figure 5.7 Amplitude distribution of the four nanochannels in the evaluating area.

5.3.2 Far-field phase measurement

Then, the shutter in the reference arm was turned on, to measure the far-field phase by the Linnik interferometer. Although the Linnik interferometer has the advantages of a high lateral resolution and magnification power, it is difficult to search for interference fringes in Linnik white light interferometry with an extremely short coherence length because of the optical path mismatch of two interference arms [119][120][121][122][123][124].

As we know, the visibility of interference fringes is affected by the amplitude ratio of two interferometric light, the size of light source (spatial coherence) and the monochromaticity of light source (temporal coherence). In order to get the visible interference fringes by the developed setup, some efforts were made: (1) an aperture was mounted in the focal plane of hololight to adjust the size of incident beam, as shown in Fig. 4.12 or 4.17. (2) The reference mirror was replaced by a flat surface made from the same material with sample (transparent thermoplastic COC 5013L), for obtaining the maximal amplitude ratio of two interferometric light.

107

Furthermore, the practical adjustments for reducing the optical path difference (OPD) in our experiments are introduced. Figure 5.8 illustrates a schematic of OPD in the developed Linnik white light interferometer. The length in measurement path (L_m) or reference path (L_r) includes the distances between the beamsplitter and objectives (L_1 or L_1') and between objectives and sample or reference (L_2 or L_2'). For obtaining the interference fringes, OPD should be minimized less than at least the coherence length of developed measurement system (28 μm). The adjustment processes are as followings.
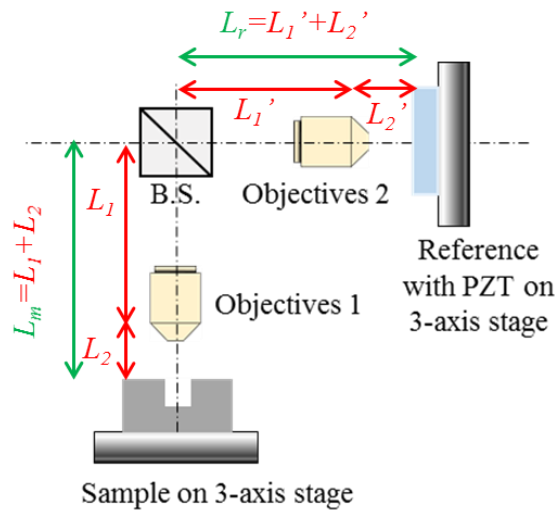
Figure 5.8 Schematic of OPD in a Linnik white light interferometer

(1) Roughly determine the positions of two objective lenses by the marks on the rods of caged system, to enable $L_1 \approx L_1$'.

(2) As mentioned, a flat surface made from COC was used as the reference. Besides the flat surface, there are some other features on this COC surface. By the visual observation of features from the measured sample and the reference, the in-focus positions in the measurement arm and reference arm are determined ($L_2 \approx L_2$').

(3) Provisionally increase the coherence length of the measurement system by changing the bandpass filter, to search the interference fringes under larger coherence lengths. Two more bandpass filters are used here: one has a CWL of 532 nm, a bandwidth of 4 nm and a coherence length of 71 μm, while another has a CWL of 532 nm, a bandwidth of 1 nm and a coherence length of 280 μm. When the interference fringes occur, we replaced the filter with

the original one with the coherence length of 28 μm. As shown in Fig. 5.9 (a), the blurred interference fringes (indicated in the dashed yellow box) are found by the developed measurement system. Besides the features from the measured sample (see Fig. 5.6), another microchannel (indicated in the red dashed box) occurs in the left side of FOV, which is the feature from the reference COC surface and is used to determine the in-focus position in the reference arm.

(4) Move the reference along optical axis to make the interference fringes more clear but features more blurred, which indicates a decrement of OPD, as shown in Fig. 5.9(b).

(5) Move the objectives 2 along optical axis to get the clear imaging of features from the reference again, as shown in Fig. 5.10(c). In the developed cage system, the two objectives are fixed on the adjustable mounts (SM1Z, Z-axis translation mount, Thorlabs) capable of moving the objectives along optical axis. The purpose of this process is to determine the position of objectives 2 accurately, making $L_1 = L_1'$ and $L_2 = L_2'$. The results are presented in Fig. 5.9(c).

(6) Adjust the angle of the reference to make the interference fringes wider, which is beneficial to the phase calculation. Simultaneously, the OPD should be minimized by the clear imaging of the features from the reference. Figure 5.9(d) illustrates the results.

(7) Finally, move the reference along observation plane to ensure that only flat surface of the reference is captured by CCD, as shown in Fig. 5.9(e).

(a)

(b)

clear

blurred

(c)

Clear

(d)

Wide and visible
interference fringes

(e)

interference fringes

without features from
the reference in FOV
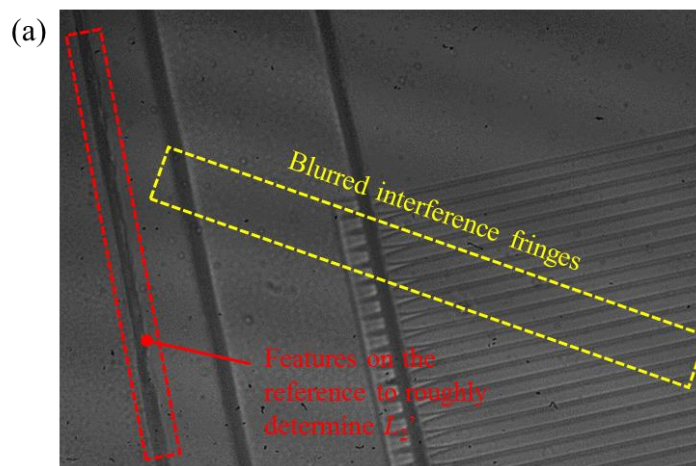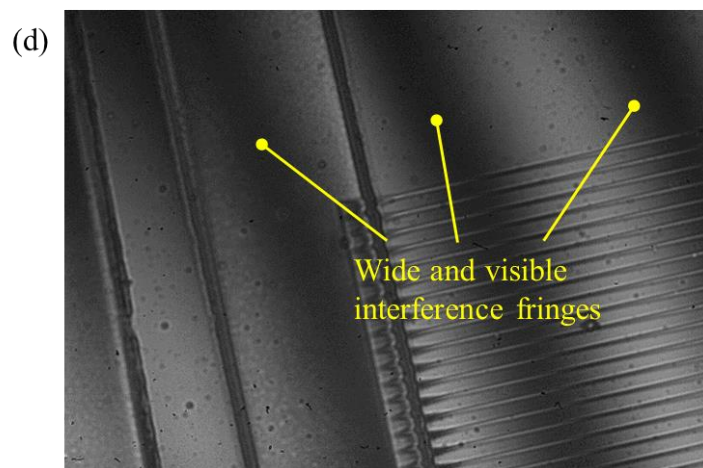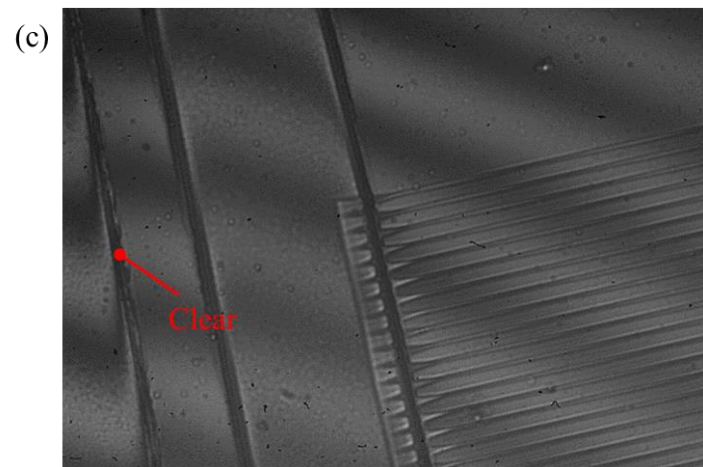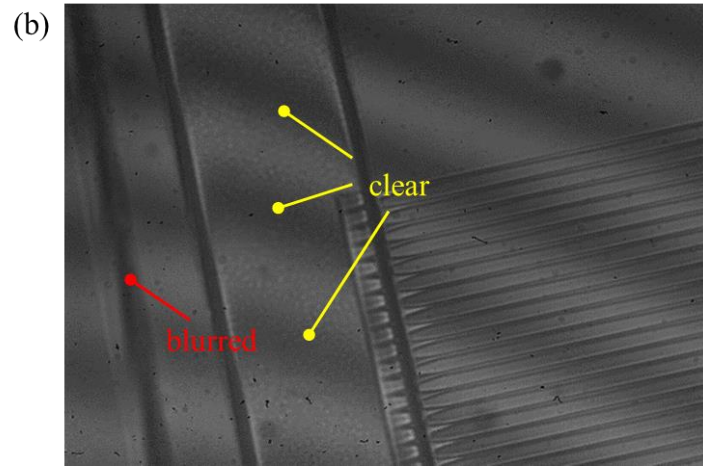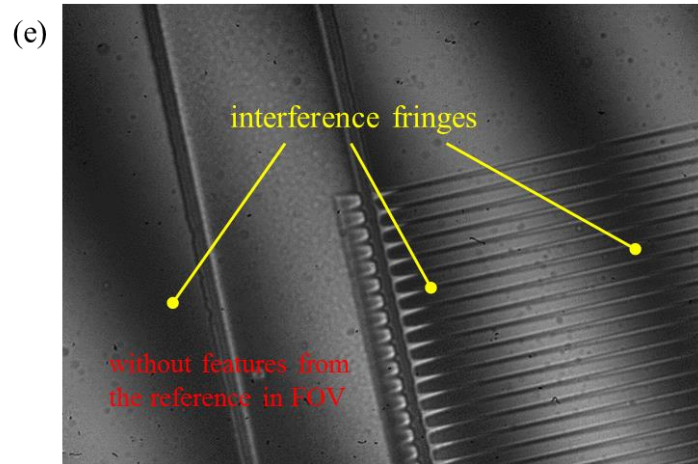
Figure 5.9 Observations during the adjustment processes for obtaining visible interference fringes in Linnik white light interferometry.

As shown in Fig. 5.10, the four interferograms with $\pi/2$ phase shifting, which are denoted as I_1, I_2, I_3, and I_4, are used to calculate the wrapped far-field phase distribution (φ) by four-step phase shift method. Figure 5.11 plots the calculated φ in the evaluating area, from which the alternate distribution of darkness and brightness reflecting the upper surface and bottom can be clearly observed. The far-field phase differences θ_f are obtained through subtracting the phases at the central position of the four nanochannels by the average phase of only top surface.
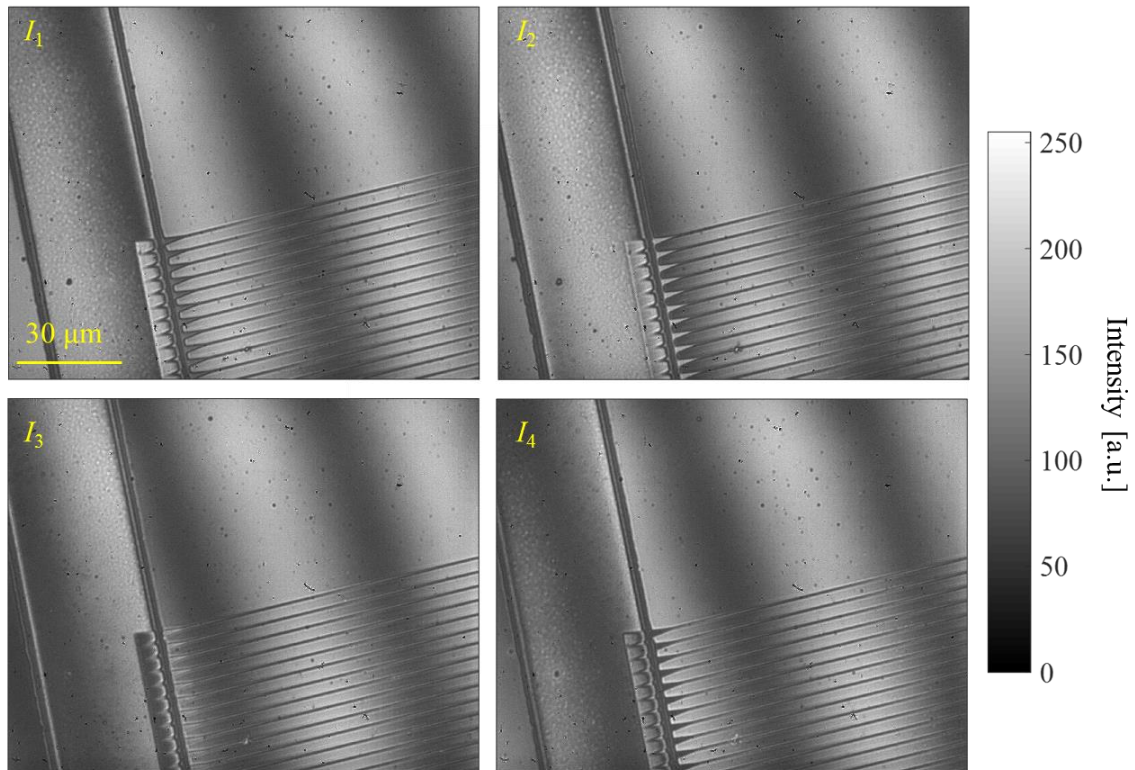
Figure 5.10 Four adjacent interferograms with π/2 phase shifting
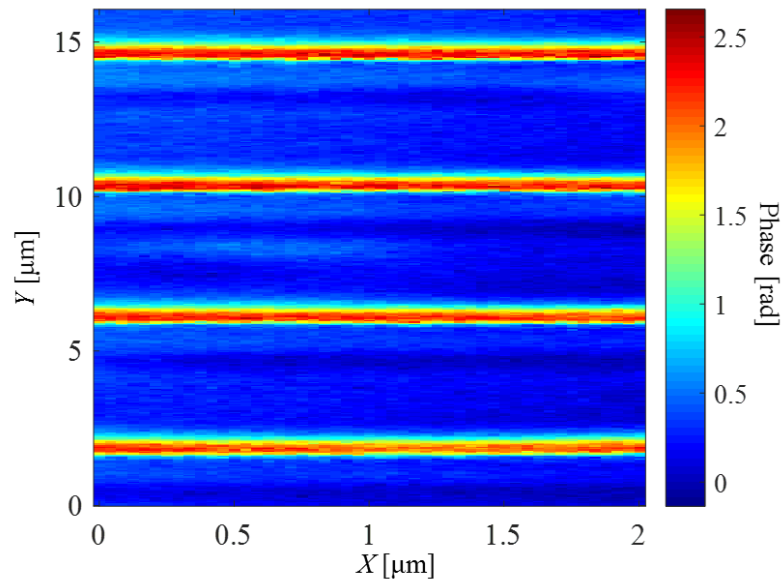
Figure 5.11 Far-filed phase distribution in the evaluating area.

5.4 Experiment results

5.4.1 Feasibility and superiority of FNRDM

According to the proposed FNRDM method, the measured amplitude from nanochannels (A_f), the amplitude from the top surface (A_u) and far-field phase difference (θ_f) in the evaluating area are substituted into Eq. (2.31) to calculate the near-field phase differences and corresponding depths. The k in Eq. (2.31) is 0 in this calculation process, because the nominal depth of the nanochannel (110 nm) is less than half of the applied wavelength (532 nm) of measurement system. As shown in Fig. 5.12, the calculated near-field phase difference and depth are 2.53 rad and 107 nm. The measured depths by the proposed FNRDM method are compared to the results by conventional interferometry using only θ_f. The overall quality of the two methods is assessed by computing the average depths of the nanochannels in the evaluating area. Table 5.1 summarizes the measured depths by the two methods and AFM measurement.
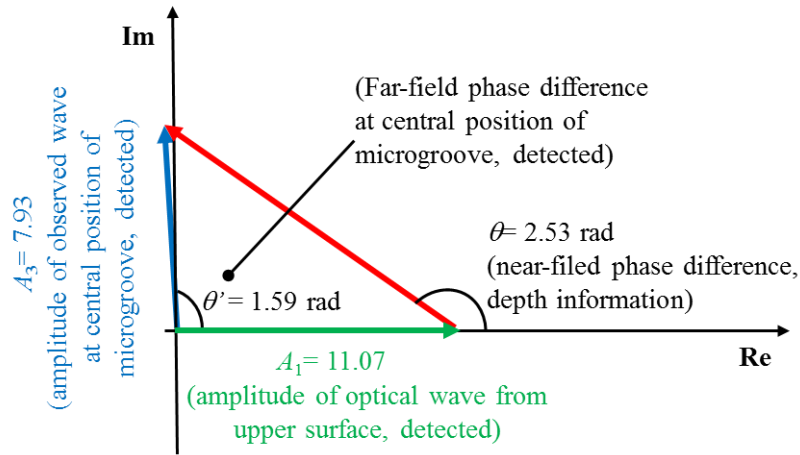
Figure 5.12 The depth calculation of measured nanochannels by the proposed method.

Table 5.1 Measured depths of the nanochannels in the evaluating area by three different methods

Methods	Measured depths in the evaluating area [nm]
Conventional interferometry using only θ_f	67
Proposed method	107
AFM	114

As shown in Tab. 5.1, the difference between the results by the proposed method and AFM measurement is 7 nm and far less than that by conventional interferometry (47 nm). It is clearly suggested that 300-nm-wide nanochannels, with width less than the diffraction limit (772 nm) of develop measurement system on a transparent COC surface, cannot be measured by conventional interferometry accurately but can be quantitatively evaluated with an accuracy of less than 10% by the proposed FNRDM method.

The quantitative discrepancy between the measured depths by using AFM and the proposed FNRDM method mainly results from the theoretical errors caused by the scattering light from the edge of nanochannels, which can attenuate the optical response from the bottom surface. Here, we simulated an identical nanochannel on a COC surface under the same conditions with the developed measurement system by the FDTD method. Table 5.2 lists the simulation parameters, while the measurement results are shown in Fig. 5.13. It is found that, compared to the theoretical depth (114 nm), a same decreasing trend in measured depth (110 nm) with experiment results (107 nm) is confirmed, which indicates that the scattering light from the edge of nanochannels is the main source of measurement accuracy in the experiment results.

Table 5.2 Parameters of simulating an identical nanochannel with the experiments

Parameters	
Wavelength of incident beam	532 nm
Grid size	5 nm (x) × 5 nm (z)
Simulation region	4 μm (width) × 2.5 μm (height)
Near-field recording plane	20 nm above the top surface of nanochannel
NA	0.42
Width of the nanochannel	300 nm
Depth of the nanochannel	114 nm
Material	COC 5013 ($n = 1.53$)
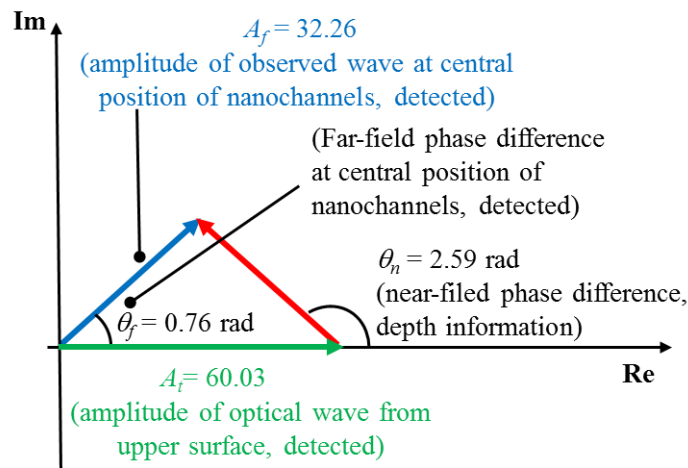
Methods	Measured depths [nm]
Conventional interferometry using θ_f	32
FRNDM	110

Figure 5.13 Simulation results of an identical nanochannel under the same conditions with the developed measurement system.

5.4.2 Individual difference evaluation by FNRDM

In this section, another experiment results were shown to demonstrate that the proposed FNRDM method enable the evaluation of individual differences for each nanochannel, which

115

is not possible with scattertometry. The evaluation of individual difference of the nanochannels in the evaluating area is carried out by calculating the depths in a same cross-section. As show in Fig. 5.14, in the evaluating area, the four nanochannels are named as nanochannels *A-D*, the yellow dashed line denotes the cross-section, and data points *a-d* denote the central positions of the nanochannels in this cross-section.
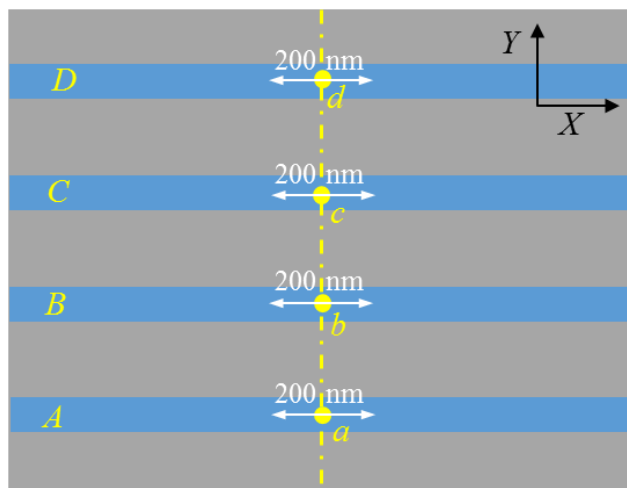
Figure 5.14 Schematic of the method for individual difference evaluation in the evaluating area

Considering the location error between AFM and the proposed method, the topography uniformity at the bottom of nanochannels within a small range and the repeatability of AFM measurement was analyzed further. Calculated from the data by AFM fine scanning (Fig. 5.6), the uniformity is evaluated by the standard deviation values (Std_u) of the measured depths along *X* direction within a 200-nm range (denoted as the white double-headed arrow in Fig. 5.14), the middle of which are data points *a-d*. Here, a 200-nm range is far larger than the estimated location error in the evaluating area between AFM measurement and the proposed method. And the repeatability is assessed by the standard deviation values (Std_r) of the measured depths at data points *a-d* through three repeated AFM measurements. Table 5.3 lists the evaluation results for the uniformity and repeatability of AFM measurement. Std_u is influenced by both the systematic error of AFM and the uniformity of the measured bottom topography, while Std_r reflects the systematic error of AFM measurement. It is found that

116

Std$_u$ and *Std$_r$* agree within a fraction of a nanometer, which is an indicator for a fine uniformity of depths at data points *a-d* with a 200-nm range.

Table 5.3 Evaluation for repeatability of AFM measurement and uniformity of bottom topography of nanochannels within a 200-nm range

Data points	*Std$_u$* [nm]	*Std$_r$* [nm]
a	1.2	1.4
b	1.7	2.0
c	1.8	1.5
d	1.5	1.6

Figure 5.15 presents the bar graph of measured depths at data-points *a-d* by repeated AFM measurements for nanochannels *A-D*. Then, following the processes introduced in Section 5.3, we measured the depths at the same data points *a-d* by the proposed method repeatedly. The results of seven repeated experiments are depicted in Fig. 5.16. The experiment results show that: (1) from Fig. 5.16, all the standard deviations of measured depths under seven experiments are approximately 2 nm, which is an indicator for the acceptable repeatability of the proposed method. (2) Through the comparison of Fig. 5.15 and 5.16, it is found that there is a uniformly increasing trend in depth variation from nanochannels *A* to *D* by both the proposed method and AFM measurement. It is indicated that the proposed method is feasible to evaluate the difference of each nanochannel, which cannot be achieved by scatterometry.
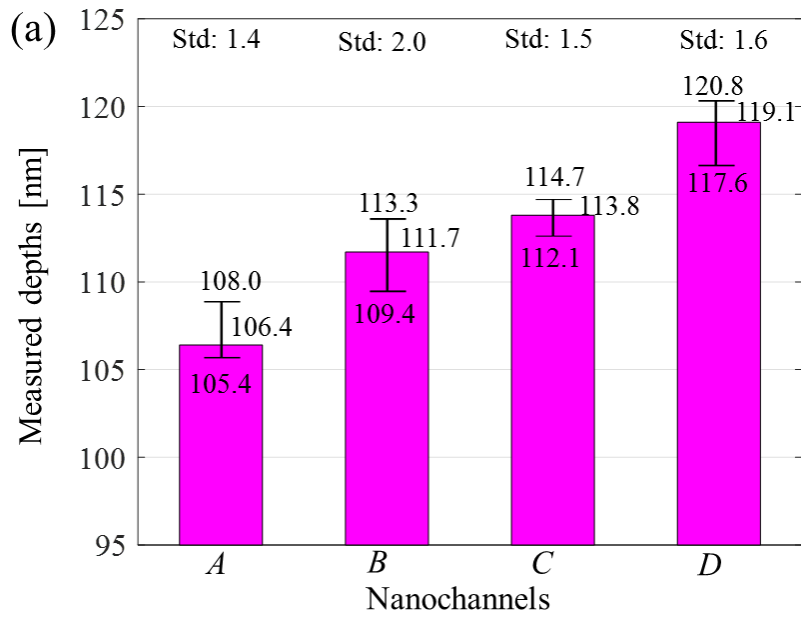
Figure 5.15 Measured depths at data-points a-d by repeated AFM measurements for nanochannels *A*-*D*
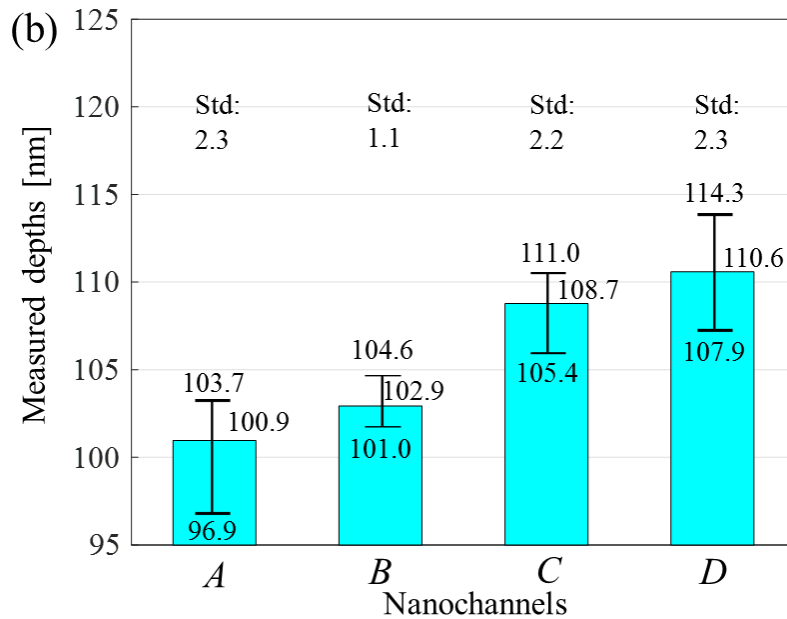
Figure 5.16 Measured depths at data-points a-d by the proposed method repeatedly for nanochannels *A*-*D*

5.5 Conclusions

In this chapter, the nanochannels on a microfluidic sample (transparent cyclic olefin copolymer (COC) material, nominal width = 300 nm, depth = 110 nm) were measured to verify the validity of the proposed FNRDM method.

Firstly, the transparent microfluidic sample was measured by a Innova AFM, to obtain the reliable data of depth information. Under a calibration error of 3 nm, the measured depth of the nanochannels by AFM measurement is 114 nm in a field of $2 \times 16 \ \mu m^2$.

Secondly, the measurement processes of the required parameters by the developed setup based on low-coherence illumination were presented. Especially, in order to get the visible interference fringes in a Linnik white light interferometer, the practical adjustments in our experiments were demonstrated.

There some experiment results: (1) the overall evaluation of measured depths of nanochannels in the same area are 67 nm by conventional interferometry, 107 nm by proposed method and 114 nm by AFM measurement, respectively. (2) The same trend in depth variation of different nanochannels between the proposed method and AFM was confirmed. (3) Seven repeated experiments by the proposed method were performed, and the standard deviation is approximately 2 nm. According to the experiment results, our method has the advantages of greatly improved accuracy over conventional interferometry and enables the individual difference evaluation of each nanochannel, which is not possible with scatterometry. It is demonstrated that the proposed FNRDM method and the developed measurement system can measure the depth of 300-nm-wide nanochannels beyond the diffraction limit (772 nm) with an accuracy of less than 10%.

Chapter 6. Phase unwrapping based on dual-wavelength interferometry

In Chapter 5, the nanochannels on a transparent cyclic olefin copolymer (COC) surface were measured to verify the validity of the proposed FNRDM method. Since the phase of light is 2π periodic, the depths of microstructures which are optically larger than half of the incident wavelength subject to phase measurement ambiguity. For example, with the developed measurement system with low-coherence illumination in Chapters 4 and 5, the maximum measurable depth is 266 nm. In order to solve the phase wrapped problem, a technique that combines the proposed FNRDM method and dual-wavelength interferometry was proposed to extend the phase measurement range and achieve the depth measurement for diffraction-limited and deep microgrooves with high accuracy. In this chapter, both the measurement principle and two experiments on a silicon sample and a transparent COC sample will be demonstrated.

6.1 Phase unwrapping

Phase unwrapping has been a research topic for more than two decades. Hundreds of papers have been published aimed at solving the phase wrapped problem. Many phase unwrapping algorithms have been suggested and implemented. The reason for such interest in phase unwrapping is due to many applications, such as terrain elevation estimation in synthetic aperture radar (SAR) [125][126][127], field mapping in magnetic resonance imaging (MRI) [128][129][130], wavefront distortion measurement in adaptive optics [131][132][133], and surface topography by optical interferometry.

As introduced in previous chapters, by the four-step phase shift interferometry, the phase can be calculated as

$$\varphi = \arctan \frac{I_4 - I_2}{I_1 - I_3} \tag{6.1}$$

Where I_1, I_2, I_3, and I_4 denote the intensities of the four interferograms with $\pi/2$ phase shifting. The algorithm used to recover φ leads to an expression involving the arctangent function. Arctangent has an inherent ambiguity, as multiples of 2π can be added to a given argument, and the arctangent will return the same result. The arctangent function has principal values in the range $-\pi$ to π if the signs of the numerators and denominators in Eq. (6.1) is taken into account. If the phase function exceeds this range, the phase values will be wrapped back down into this range. Formally, the phase unwrapping can be defined as given the wrapped phase $\varphi \in (-\pi, \pi]$, find the "true" value phase ψ, which is related to φ by

$$\varphi = \text{Wrap}(\psi) = \psi - 2\pi \times \text{Round}\left(\frac{\psi}{2\pi}\right) \tag{6.2}$$

Where "Wrap()" is the wrapping operator, "Round" means rounding off to the nearest integer. Although phase unwrapping is mathematically ill-posed in general, the practically true phase value at a certain point is not independent of its spatial or temporal information, which can provide the additional information to make unwrapping possible. The factors resulting in the phase wrapped problem include phase aliasing due to an insufficient sampling rate, phase noise, thermal noise of sensor electronics, and the topography of measured surface. In this PhD thesis, surface topography or depth measurement by optical interferometry is the main topic. Thus, the phase wrapped problem caused by surface topography will be demonstrated.

For a continuous surface, the phase continuity being measured can be expected. Under this condition, the unwrapped phase can be obtained by adding or subtracting 2π to the discontinuity of the measured phase. Assume a continuously slant surface with a height far larger than the incident wavelength, the phase wrapped problem occurs. Considering the one-dimensional phase unwrapping,

$$\begin{aligned}\Delta\psi_i &= \psi_i - \psi_{i-1} \\ \Delta\varphi_i &= \varphi_i - \varphi_{i-1}\end{aligned} \tag{6.3}$$

Where i denotes the measured pixel. For a continuous surface,

$$\left|\Delta\psi_i\right| < \pi \tag{6.4}$$

Then, at the discontinuity of the measured phase, we can get

$$\begin{cases} \psi_i = \varphi_i + 2\pi, \Delta\varphi_i < -\pi \\ \psi_i = \varphi_i - 2\pi, \Delta\varphi_i > \pi \end{cases} \tag{6.5}$$

Therefore, in the case of a continuous surface, the phase unwrapping can be easily achieved by making the phase difference between adjacent pixels less than π. However, for the discontinuous surface, the phase change between adjacent pixels may be larger than π and 2π ambiguity problem will ruin the result of the phase measurement. In other words, this unwrapping algorithm (Eq. (6.4)) cannot handle the case in which there is a large discontinuity on the sample, such as the deep step in the functional microstructures.

An example is given to illustrate the phase wrapped problem in our research. By the FDTD method, Figures 6.1, 6.2 and 6.3 plot the far-field intensity and phase distributions for three types of microgrooves, under the conditions of a 488-nm incident wavelength and a *NA* of 0.55. The widths of the three simulated microgrooves are all 1000 nm, while the depths are 60 nm, 304 nm and 548 nm, respectively. The depth difference is 244 nm, which is half of the wavelength. As the simulated depth increase, the far-field intensity at the opening position of the microgroove decreases. However, the far-filed phase distributions of the three types of microgrooves are almost the same, and the same phase difference between the top surface and bottom surface can be obtained, which reflects the different depth information.
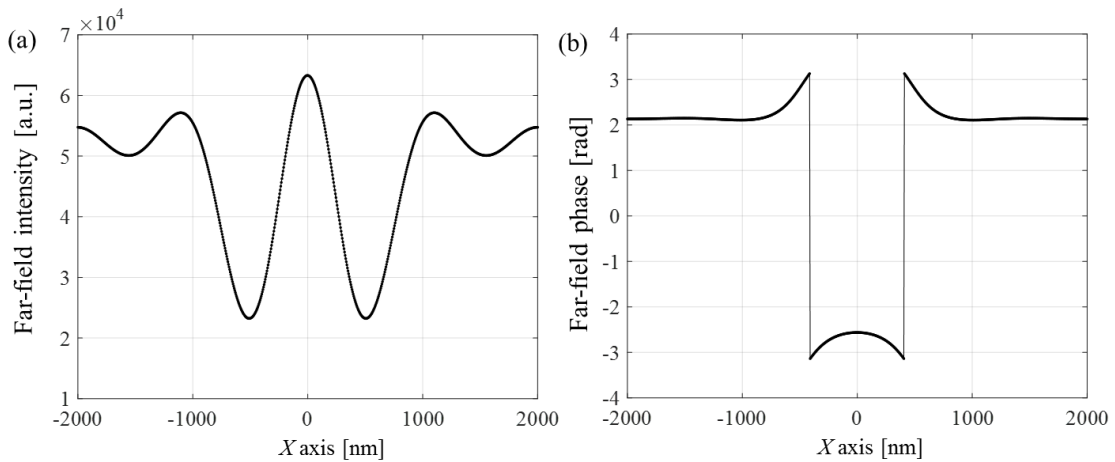
Figure 6.1 Far-field intensity and phase distribution of a 1000-nm-wide and 60-nm-deep microgroove
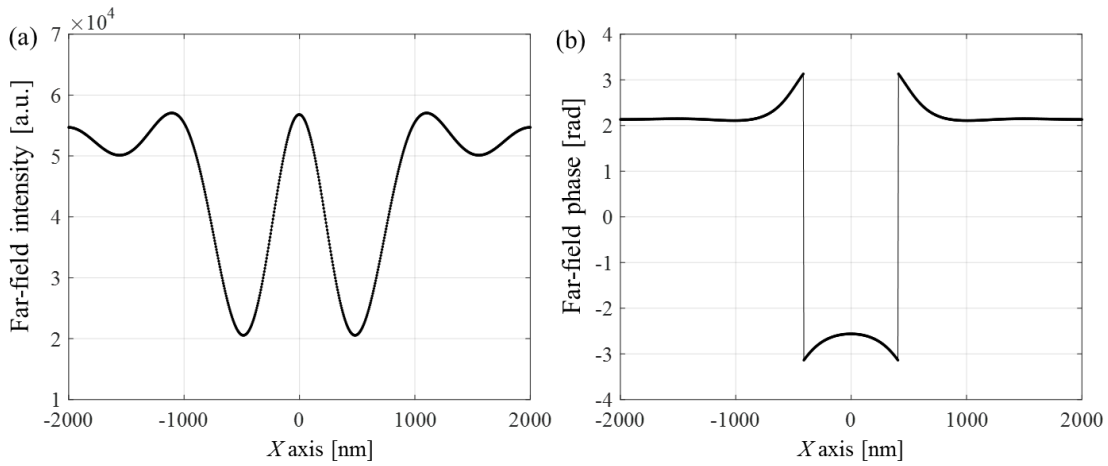
Figure 6.2 Far-field intensity and phase distribution of a 1000-nm-wide and 304-nm-deep microgroove
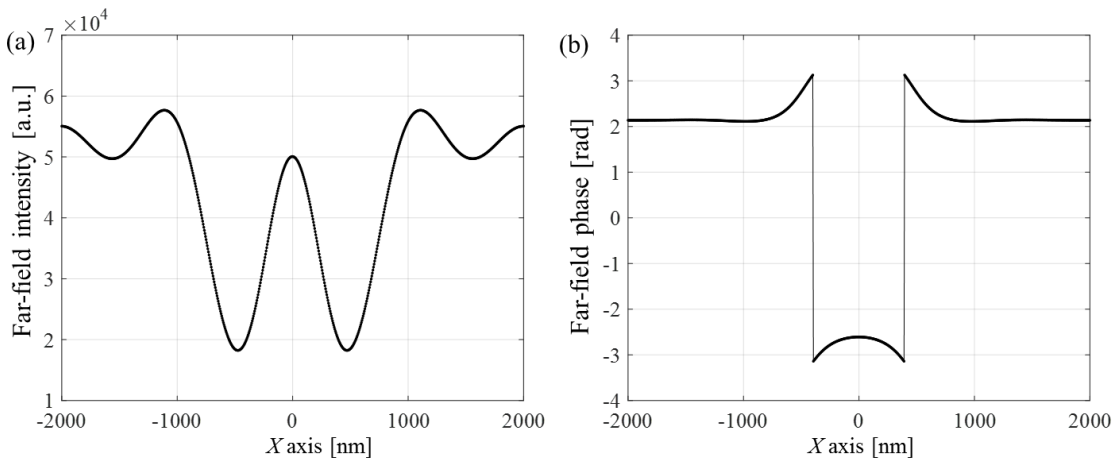
Figure 6.3 Far-field intensity and phase distribution of a 1000-nm-wide and 548-nm-deep microgroove

6.2 Dual-wavelength interferometry

To address the phase wrapped problem caused by the discontinuity of surface topography, the dual-wavelength interferometry is proposed in which an unambiguous phase map with extended measurement range beyond the step height can be obtained by using incident beams with two separate wavelengths [134][135][136][137][138][139][140].

6.2.1 Fundamental measurement principle

For simplicity, only the 1D phase calculation algorithm will be shown here, since the 2D phase calculation is basically the same as that of the 1D case. By doing separate phase measurements for λ_a and λ_b, two sets of phase data are obtained: φ_{1a}, φ_{2a}, φ_{2a}, … φ_{na} for λ_a and φ_{1b}, φ_{2b}, φ_{2b}, … φ_{nb} for λ_b, where n is the total number of pixel elements in the CCD camera.

Assuming the reflected beam from measured surface travels through the air (the refractive index = 1), then the optical path difference (OPD) on an arbitrary pixel i can be given

$$\text{OPD}_i = \begin{cases} \left(\dfrac{\varphi_{ia}}{2\pi} + p\right)\lambda_a \\ \left(\dfrac{\varphi_{ib}}{2\pi} + q\right)\lambda_b \end{cases}, i = 1,2,3...n \tag{6.6}$$

where p and q are order numbers for λ_a and λ_b on pixel number i. Similarly, one can write equations for the next pixel ($i+1$):

$$\text{OPD}_{i+1} = \begin{cases} \left(\dfrac{\varphi_{(i+1)a}}{2\pi} + p'\right)\lambda_a \\ \left(\dfrac{\varphi_{(i+1)b}}{2\pi} + q'\right)\lambda_b \end{cases}, i = 1,2,3...n \tag{6.7}$$

Again, p' and q' are order numbers for λ_a and λ_b on pixel number ($i+1$). There is one more unknown than the equations we have, if we want to solve for the absolute OPD at every pixel. Since we are interested in relative OPDs rather than absolute OPDs, let us write the expressions for the difference of OPDs between adjacent pixels:

$$2\pi \times \Delta\text{OPD}_{i+1} = \begin{cases} \left[\Delta\varphi_{(i+1)a} + 2\pi\left(p'-p\right)\right]\lambda_a \\ \left[\Delta\varphi_{(i+1)b} + 2\pi\left(q'-q\right)\right]\lambda_b \end{cases} \tag{6.8}$$

Where

$$\begin{aligned} \Delta\text{OPD}_{i+1} &= \text{OPD}_{i+1} - \text{OPD}_i \\ \Delta\varphi_{(i+1)a} &= \varphi_{(i+1)a} - \varphi_{ia} \\ \Delta\varphi_{(i+1)b} &= \varphi_{(i+1)b} - \varphi_{ib} \end{aligned} \tag{6.9}$$

Here, we have three unknowns, i.e., ΔOPD_{i+1}, $(p'-p)$ and $(q'-q)$. One more assumption is given, which is that the difference of order numbers between any adjacent pixels is the same for both λ_a and λ_b, $(p' - p) = (q' - q)$. Then, Eq. (6.8) can be written as

$$\Delta OPD_{i+1} = \frac{\Delta\varphi_{(i+1)b} - \Delta\varphi_{(i+1)a}}{2\pi} \times \frac{\lambda_a \lambda_b}{\lambda_a - \lambda_b} \tag{6.10}$$

Rewriting Eq. (6.10), we can get

$$\Delta OPD_{i+1} = \begin{cases} \dfrac{\Delta\varphi_{(i+1)b} - \Delta\varphi_{(i+1)a}}{2\pi} \lambda_{eq}, \lambda_a > \lambda_b \\[3mm] \dfrac{\Delta\varphi_{(i+1)a} - \Delta\varphi_{(i+1)b}}{2\pi} \lambda_{eq}, \lambda_a < \lambda_b \end{cases}, \quad \lambda_{eq} = \left| \frac{\lambda_a \lambda_b}{\lambda_a - \lambda_b} \right| \tag{6.11}$$

Where λ_{eq} is an equivalent wavelength in the dual-wavelength interferometry. If the assumption mentioned above is true, the difference of OPD between any adjacent pixels can be obtained using Eq. (6.11). Then, simply by adding all the $\Delta OPDs$ together, the OPD distribution across the detector array can be reconstructed. Note, the fundamental assumption for the single-wavelength PSI is that the $\Delta OPDs$ between any adjacent pixels are less than $\lambda/2$. In the case of dual-wavelength PSI, the $\Delta OPDs$ between any adjacent pixels must be less than $\lambda_{eq}/2$. This means that, if the test were performed using a single-wavelength (wavelength $= \lambda_{eq}$) light source, the phase difference between any adjacent pixels would be $< \pi$ and no 2π ambiguity problem would occur. Under the assumption that $[(p' - p) - (q' - q)]$ may be equal to +1 or -1 instead of 0 depending on the relative position between detector elements and the fringe pattern imaged on the detector array. If $[(p' - p) - (q' - q)]$ is not equal to 0, Eq. (6.11) would give a wrong value of ΔOPD_{i+1} such that its absolute value would always be larger than $\lambda_{eq}/2$ and appear to violate the fundamental assumption. These discontinuities can be checked and removed by a method introduced in the case of continuous surface (Eq. (6.5)).

Considering the microgroove or microhole structure in this research, as introduced in previous chapters, the depth is proportional to the reflected phase difference (θ) between the top surface and the bottom surface, given by

$$depth = \frac{\lambda}{2} \times \left(\frac{\theta}{2\pi} + k \right) \tag{6.12}$$

Using Eq. 6(11) to achieve phase unwrapping, we can get

$$depth = \begin{cases} \dfrac{\theta_b - \theta_a}{4\pi} \lambda_{eq}, \lambda_a > \lambda_b \\ \dfrac{\theta_a - \theta_b}{4\pi} \lambda_{eq}, \lambda_a < \lambda_b \end{cases} \tag{6.13}$$

Where θ_a and θ_b denote the phase difference between the top surface and the bottom surface by λ_a and λ_b, respectively.

6.2.2 Simulation analysis of a combination of FNRDM and dual-wavelength interferometry

In this section, a combination of the proposed FNRDM method and dual-wavelength interferometry was analyzed through a FDTD simulation, to demonstrate the feasibility of this technology in measuring the diffraction-limited and deep microgrooves.

A silicon microgroove, 400-nm-wide and 300-nm-deep, was simulated under the conditions of Table 6.1. Both the applied incident wavelengths are larger than twice the depth of the microgroove, which indicates the phase wrapping problem by using each wavelength in single-wavelength phase shift interferometry. By the four-step phase shift method, Figure 6.4(a) plots the far-field phase distribution under the incident wavelength of 532 nm, while the results by 520-nm incident wavelength are shown in Fig. 6.4(b). The phase differences between the top surface and bottom surface are 0.41 rad and 0.51 rad, respectively. According to the algorithm of dual-wavelength interferometry (Eq. (6.13)), we can calculate the depth as 193 nm. The results show that the conventional dual-wavelength phase shift interferometry cannot evaluate the depth of a diffraction-limited and deep microgroove.

Table 6.1 Basic simulation settings for the analysis of a combination of the proposed FNRDM method and dual-wavelength interferometry

Parameters	
Dual wavelengths	532 nm and 520 nm
Grid size	5 nm (x) × 5 nm (z)
Simulation region	4 μm (width) × 2.5 μm (height)
Near-field recording plane	20 nm above the top surface of microgroove
NA	0.55
The diffraction limit	590 nm ($\lambda = 532$ nm)
	578 nm ($\lambda = 520$ nm)
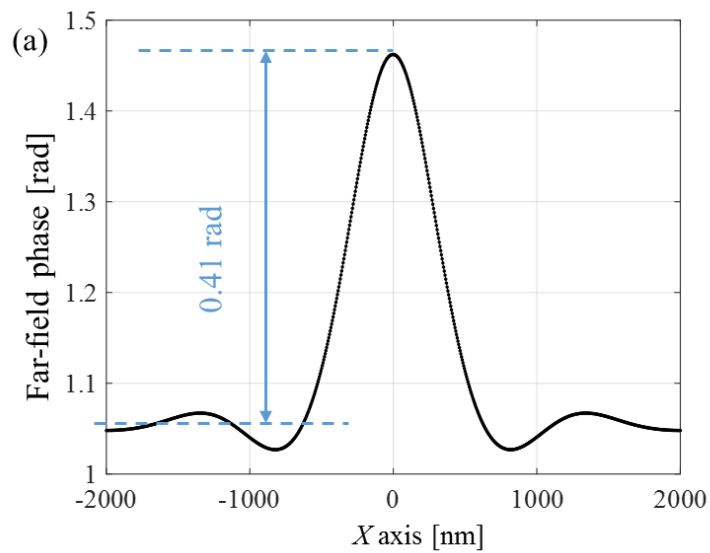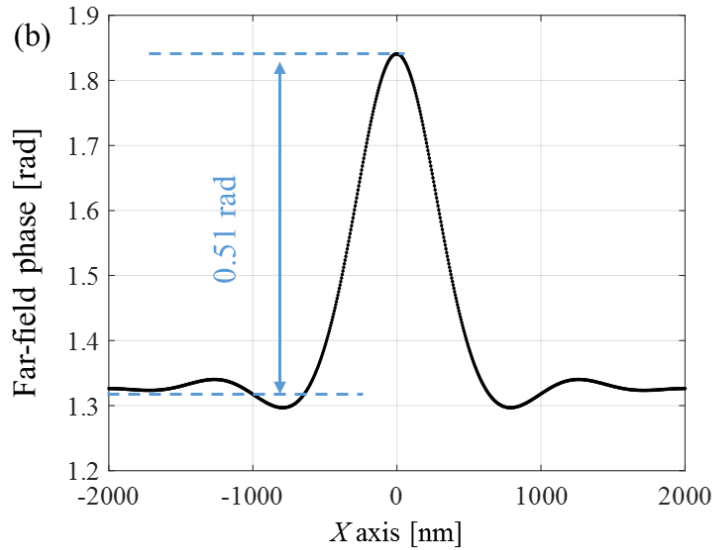
Figure 6.4 Far-field phase distributions under the incident wavelength of (a) 532 nm and (b) 520 nm.

Then, apply the proposed FNRDM method to each results, and calculate the corresponding near-field phase difference (θ_n). Figure 6.5 presents the depth calculation by FNRDM under the incident wavelength of 532 nm (Fig. 6.5(a)) and 520 nm (Fig. 6.5(b)), respectively. The near-field phase differences (θ_n), 0.80 rad for $\lambda = 532$ nm and 0.96 rad for $\lambda = 520$ nm, can be substituted into Eq. (6.13) to obtain the depth as 297 nm.
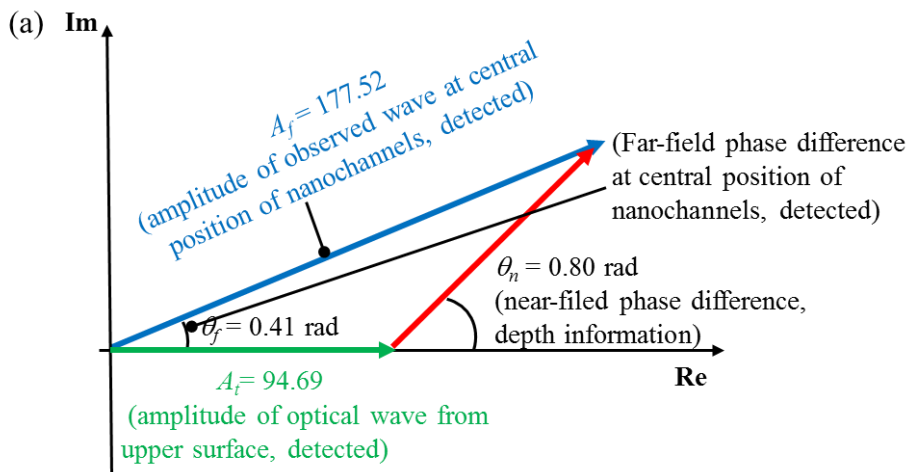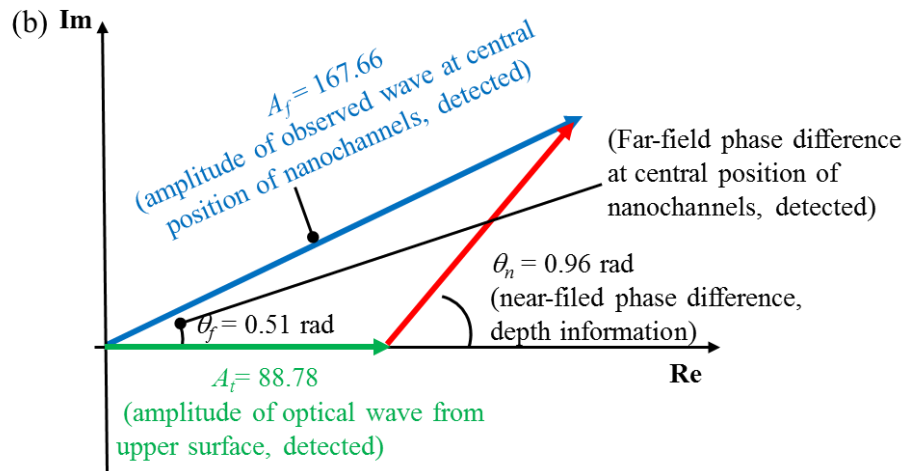
Figure 6.5 Depth calculation by the proposed method under the incident wavelength of (a) 532 nm and (b) 520 nm.

Obviously, under the mentioned conditions, the error of depth measurement is decreased from 36% by the conventional dual-wavelength phase shift interferometry to 1% by a combination of the proposed FNRDM method and dual-wavelength interferometry. The simulation results suggest that the combination of the proposed FNRDM method and dual-wavelength interferometry can accurately evaluate the depth of a diffraction-limited and deep microgroove, without the phase ambiguity problem.

6.2.3 Noise-immune dual-wavelength interferometry

Although the conventional dual-wavelength interferometry can extend the depth measurement range, the downside of the conventional dual-wavelength interferometry is that its noise has been magnified significantly when compared to that in a single-wavelength phase map [141][142][143]. As we can see from Eq. (6.13), the magnified noise comes from two sources: (1) the subtraction process between the phases obtained by separately sing-wavelength illumination; (2) a magnification factor of λ_{eq}/λ_1 or λ_{eq}/λ_2.

To solve this problem, we presented a new algorithm of the dual-wavelength interferometry, called noise-immune dual-wavelength interferometry. In this new algorithm, the integer k of the phase wrapped problem can be determined by the phases obtained from

129

the separately sing-wavelength illumination. Because the depth to be measured is the same, we can get

$$\frac{(\theta_a + 2\pi k_a)\lambda_a}{4\pi} = \frac{\theta_{eq}\lambda_{eq}}{4\pi}$$
$$\theta_{eq} = \theta_b - \theta_a \qquad (6.14)$$
$$\lambda_{eq} = \frac{\lambda_a \lambda_b}{\lambda_a - \lambda_b}$$

Where k_a is the integer of the phase wrapped problem under the incident wavelength of λ_a. Then, k_a can be solved as

$$k_a = \text{Round}(\frac{\lambda_b \theta_b - \lambda_a \theta_a}{2\pi(\lambda_a - \lambda_b)}) \qquad (6.15)$$

Where "Round" means rounding off to the nearest integer. Hence, using k_a and the phase information by a single wavelength of λ_a, the depth can be calculated by

$$depth = \frac{\lambda_a}{2} \times \left(\frac{\theta_a}{2\pi} + k_a \right) \qquad (6.16)$$

Similarly, as shown in Eq. (6.17), the depth can be measured by using k_b and the and the phase information by a single wavelength of λ_b.

$$depth = \frac{\lambda_b}{2} \times \left(\frac{\theta_b}{2\pi} + k_b \right)$$
$$k_b = \text{Round}(\frac{\lambda_a \theta_a - \lambda_b \theta_b}{2\pi(\lambda_b - \lambda_a)}) \qquad (6.17)$$

The simulation analysis in last section was performed without considering the practically environmental noise condition. Here, a statistical analysis adding Gaussian noise with sigma $2\sigma = 3\%$ to the observed intensity distributions (A_f, A_u and the interferograms used for calculating the far-filed phase) of the simulation results in last section is performed. As the same with that introduced in Section 3.4.2, the analysis processes are as followings: (1) for the separately sing-wavelength illumination, add the Gaussian noise with sigma $2\sigma = 3\%$ to each of the interferograms in the four-step phase shift method, and calculate the correspondingly maximal phase errors under the two wavelengths. Then consider the worst

situations by using ±3% noise to the observed amplitudes from the microgroove and the uniform surface (A_f and A_u) combined with plus or minus the maximal error of far-field phase difference (θ_f). By the proposed FNRDM method, the near-filed phase differences (θ_n) under the worst situations are obtained for the two wavelengths, respectively. (2) Both the conventional dual-wavelength interferometry and the noise-immune dual-wavelength interferometry are applied to the near-filed phase differences. When calculating the integer k in Eq. (6.16) or (6.17) by the noise-immune method, the average value of the near-field phase differences under all the worst situations are used.

Figure 6.6 shows the measured depths for a 400-nm-wide and 300-nm-deep microgroove, with the NA of 0.55, under the Gaussian noise (sigma $2\sigma = 3\%$), by conventional dual-wavelength interferometry and the noise-immune dual-wavelength interferometry. It is found that, although the average values of measured depths by the two methods are extrmely close to the simulated depth (300 nm), the noise level of standard deviation is 97.6 nm by conventional dual-wavelength interferometry while it is less than 2 nm by the proposed noise-immune dual-wavelength interferometry. Hence, by the proposed noise-immune algorithm, the noise level of standare deviation can be reduced to that of a single wavelength phase map. At the production site, the combination of FNRDM and the noise-immune dual-wavelength interferometry is a feasible technology to achieve the depth measurement of the diffraction-limited and deep microgroove with high accuracy, without the phase ambiguity problem.
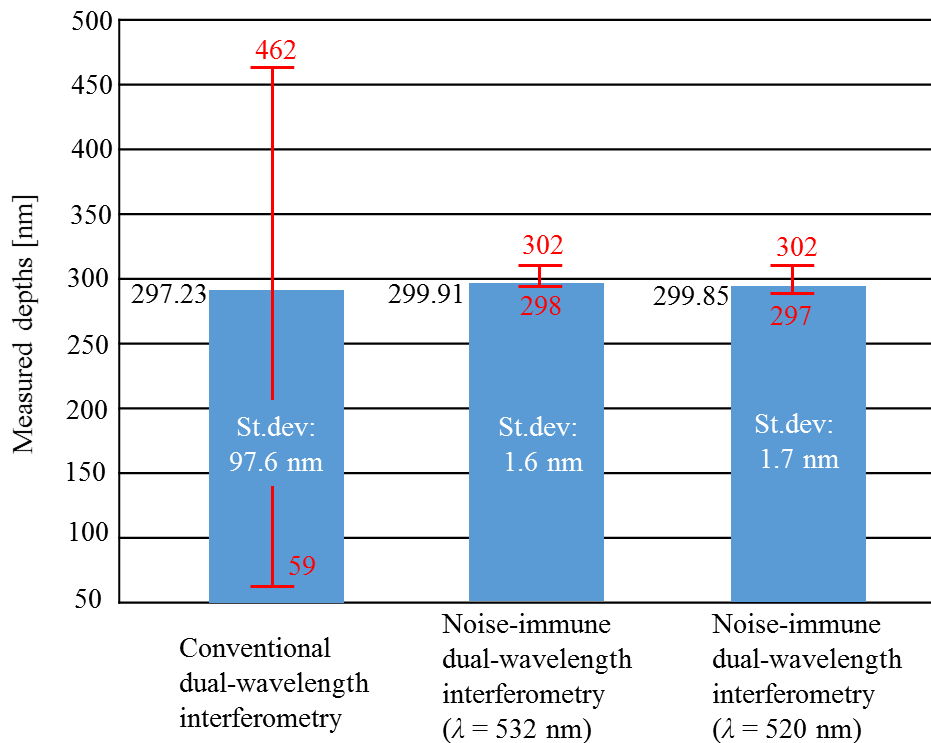
Figure 6.6 Measured depths for a 400-nm-wide and 300-nm-deep microgroove, with the NA of 0.55, under the Gaussian noise (sigma $2\sigma = 3\%$), by conventional dual-wavelength interferometry and the noise-immune dual-wavelength interferometry

6.3 Experiments of measuring the grating structure on a silicon surface

In order to verify the feasibility of the combination of FNRDM and the noise-immune dual-wavelength interferometry, two experiments were performed. In this section, a silicon grating structure was measured by the proposed method. Another experiments about the grating on a COC surface will be demonstrated in Section 6.4.

6.3.1 A silicon sample with the grating structure

Figure 6.7 illustrates a schematic of the standard silicon sample (mold, stamper, DTM-2-1 fabricated by Kyodo International Incorporation). This standard sample has beared nanoimprinting, the first tests of the imprint and other related experiments. On the surface of this silicon sample, there are two main areas: the uniform surface and the grating area. As

shown in Fig. 6.8, it is a photography of commercial DTM-2-1 with cross-section scanning electron microscopy (SEM) measurement, which is provided by Kyodo International Incorporation. For the grating structure on this standard silicon sample, the nominal width, depth, and pitch are 1, 1, and 2 μm, respectively.
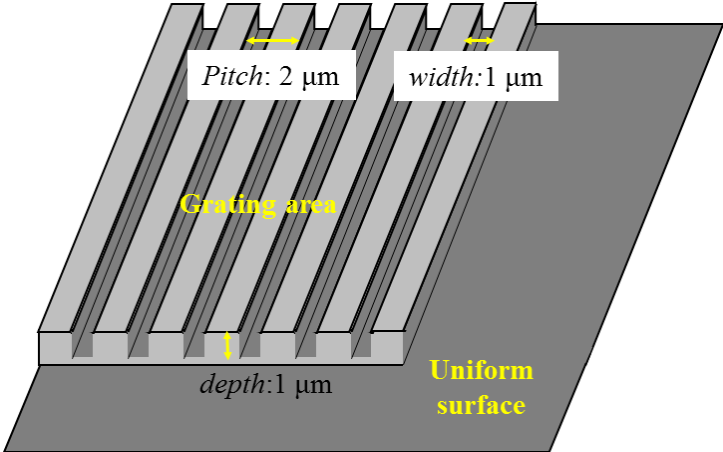
Figure 6.7 Schematic of the standard silicon sample to be measured.
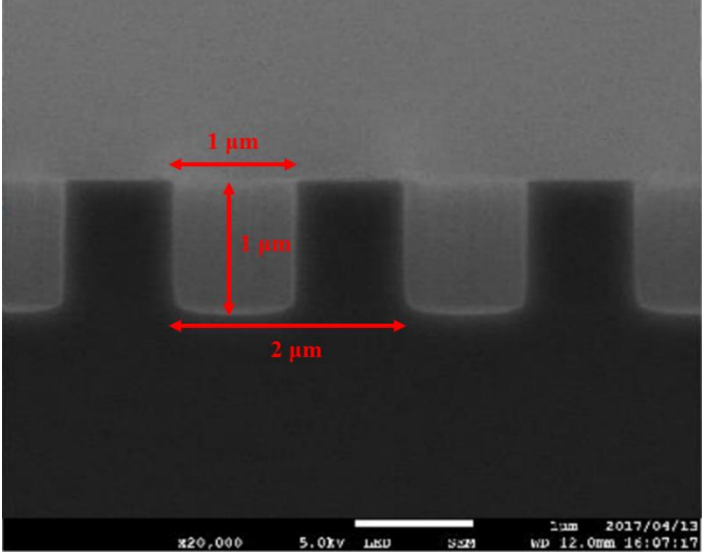
Figure 6.8 Cross-section SEM measurement for commercial DTM-2-1 sample provided by Kyodo International Incorporation.

Several optical methods using commercial equipment have been used to inspect the depth of the microgrooves on this standard silicon sample. The first method is white light

interferometer (Newview 700s, Zygo Corporation). Figure 6.9 presents the measurement results of the grating area of this standard silicon sample with the magnification power of 50x and the lateral resolution of 292 nm. Although the pitch is clearly obtained (2 μm, denoted in Fig. 6.9(b)), the depth information cannot be accurately measured.
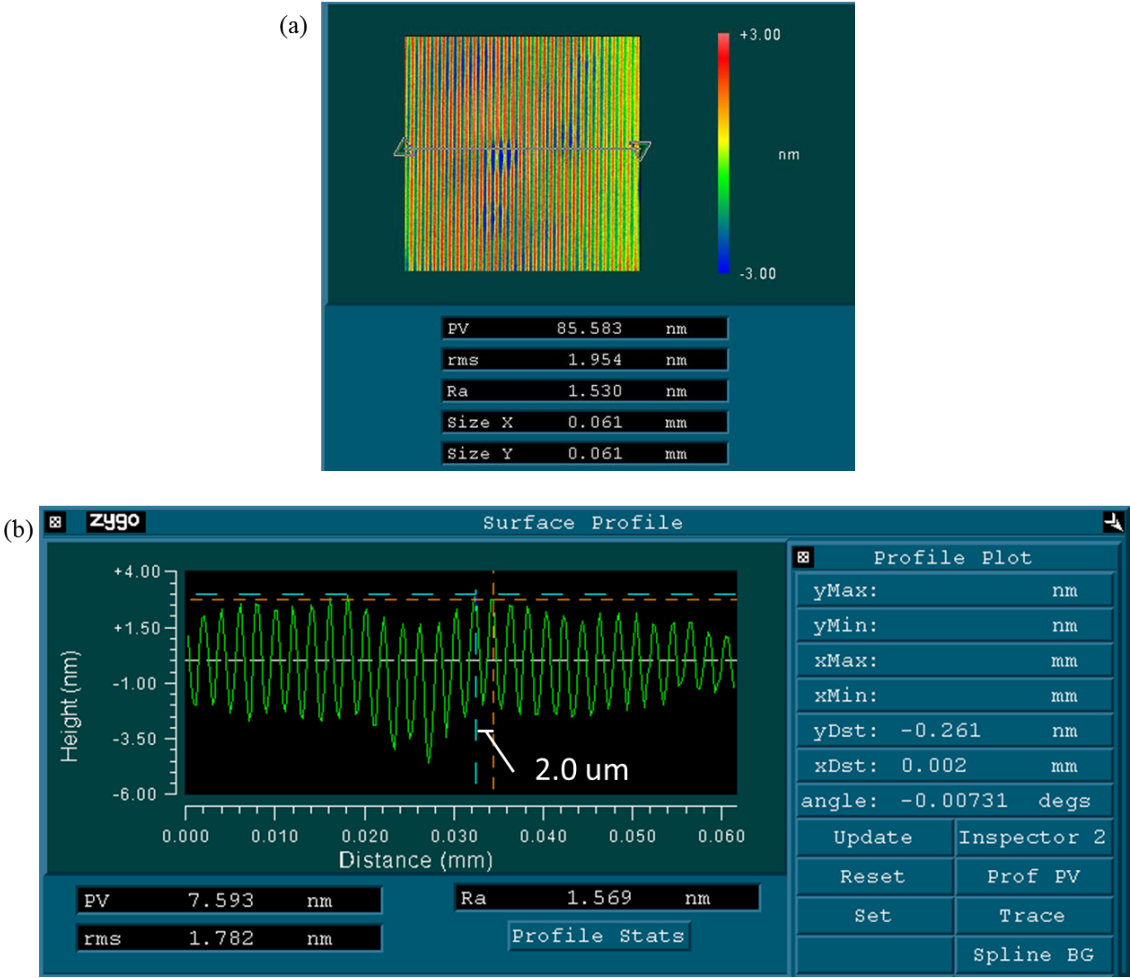
Figure 6.9 Measurement results of the grating area of standard silicon sample by a white light interferometer (Newview 700s, Zygo Corporation): (a) a surface topography and (b) a cross-section profile.

Another optical method is laser confocal microscope. A commercial laser confocal microscope (VK-X1000, $\lambda = 404$ nm, $NA = 0.95$, the lateral resolution = 93 nm, one of the latest high lateral resolution optical microscope, Keyence Corporation) was also used to inspect the depths of the grating area on this standard silicon sample. Figure 6.10 presents

134

the measurement results: (a) a surface topography and (b) a same cross-section profile by two repeated measurements. The depth of this measured grating area is approximately 800 nm and far less than the nominal size of 1000 nm. Furthermore, the two measurement results of a same cross-section profile are not in a good agreement. Especially, for the bottom surface of the grating structure, the topography difference between the two measurement is approximately 100 nm. Hence, even by the commercial laser confocal microscope with high lateral resolution, the depth information of this standard silicon sample cannot be measured.
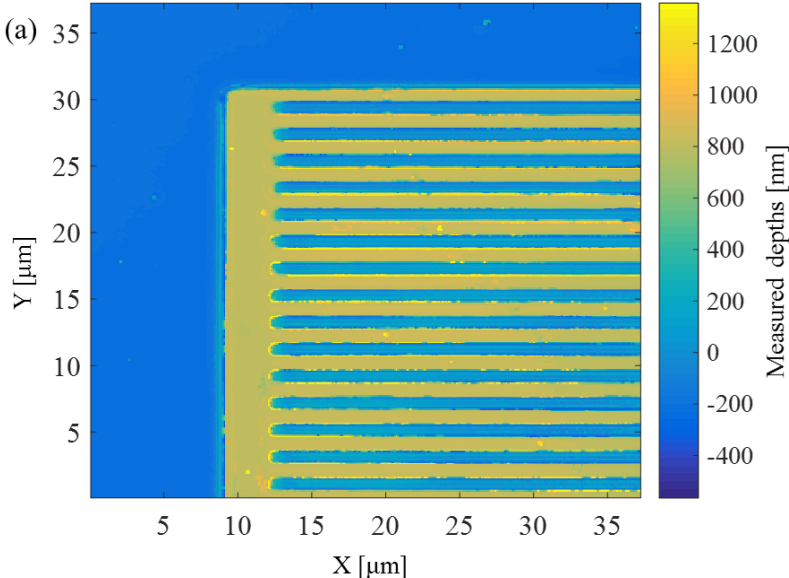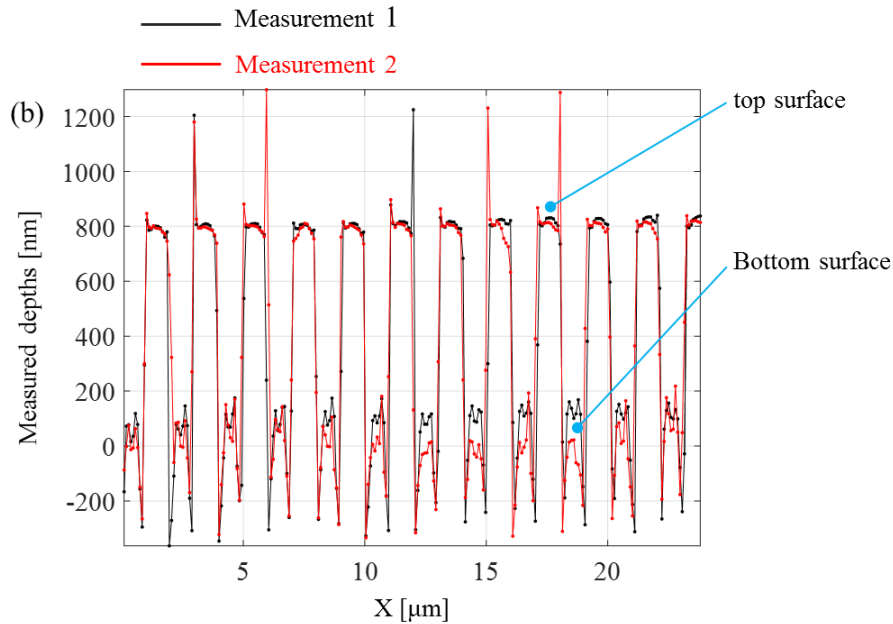
Figure 6.10 Measurement results of the grating area on the standard silicon sample by a commercial laser confocal microscope (VK-X1000, the lateral resolution = 93 nm, Keyence Corporation): (a) a surface topography and (b) a same cross-section profile by two repeated measurements.

Therefore, even by the commercial optical instruments with high later resolution, e.g. the white light interferometer and the laser confocal microscopy, it is still difficult to measure the depth information of this 1-µm-wide silicon grating structure with a pitch of 2 µm and an aspect-ratio of 1.

6.3.2 AFM measurement of the silicon grating structure

In order to obtain the reliable reference data for verification, the silicon grating structure has also been measured by AFM (Innova with ultra-low noise, high-resolution performance and closed-loop positioning), which was introduced in Section 5.2. After the calibration introduced in Section 5.2, The AFM measurement of the silicon grating structure includes the following processes. Firstly, identify the location. In order to evaluate the same grating area between AFM measurement and the proposed method, a rough scanning of AFM measurement was implemented on the standard silicon sample. The samples per line, scan

136

rate and scan range of rough scanning are 512, 1.0 Hz and 50 × 50 μm², respectively. As shown in Fig. 6.11, both the grating area (tope left region) and the uniform surface (the rest) are clearly found, and the two perpendicular boundaries are the key location mark. The evaluating area (dashed blue box), a grating area with four microgrooves, has a same distance of 8 μm to each of the boundaries. The size of the evaluating area is 8 × 4 μm².
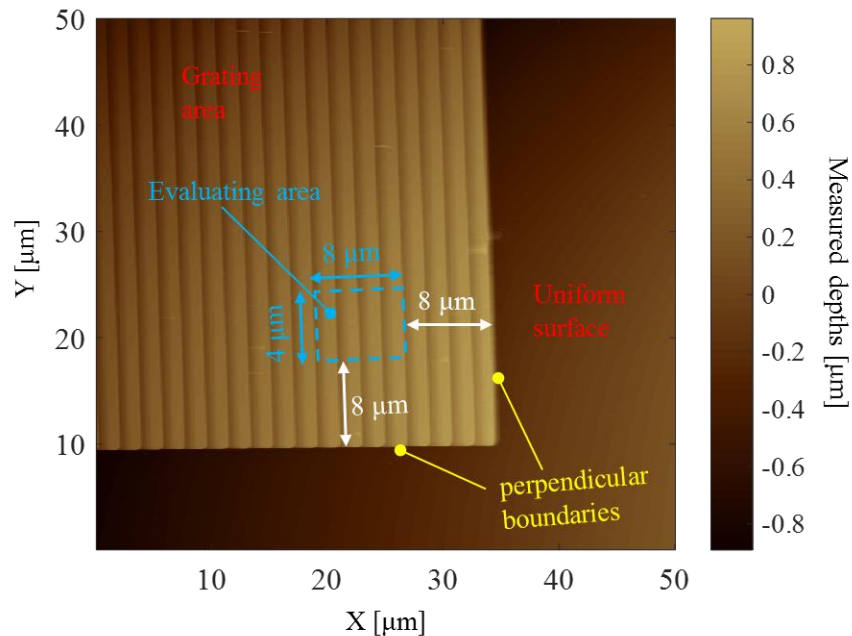
Figure 6.11 AFM measurement of the standard silicon sample by a rough scanning process for location identification.

Then, a fine scanning process was carried out to obtain the topography in the evaluating area of the silicon sample. The samples per line, scan rate and scan range of rough scanning are 1024, 0.1 Hz and 8 × 4 μm², respectively. Figure 6.12(a) plots the two-dimensional topography image of the evaluating area, while the corresponding height histogram is illustrated in Fig. 6.12(b). According the AFM measurement, the depth of nanochannels in the evaluating area on the transparent microfluidic sample is 1021 nm.
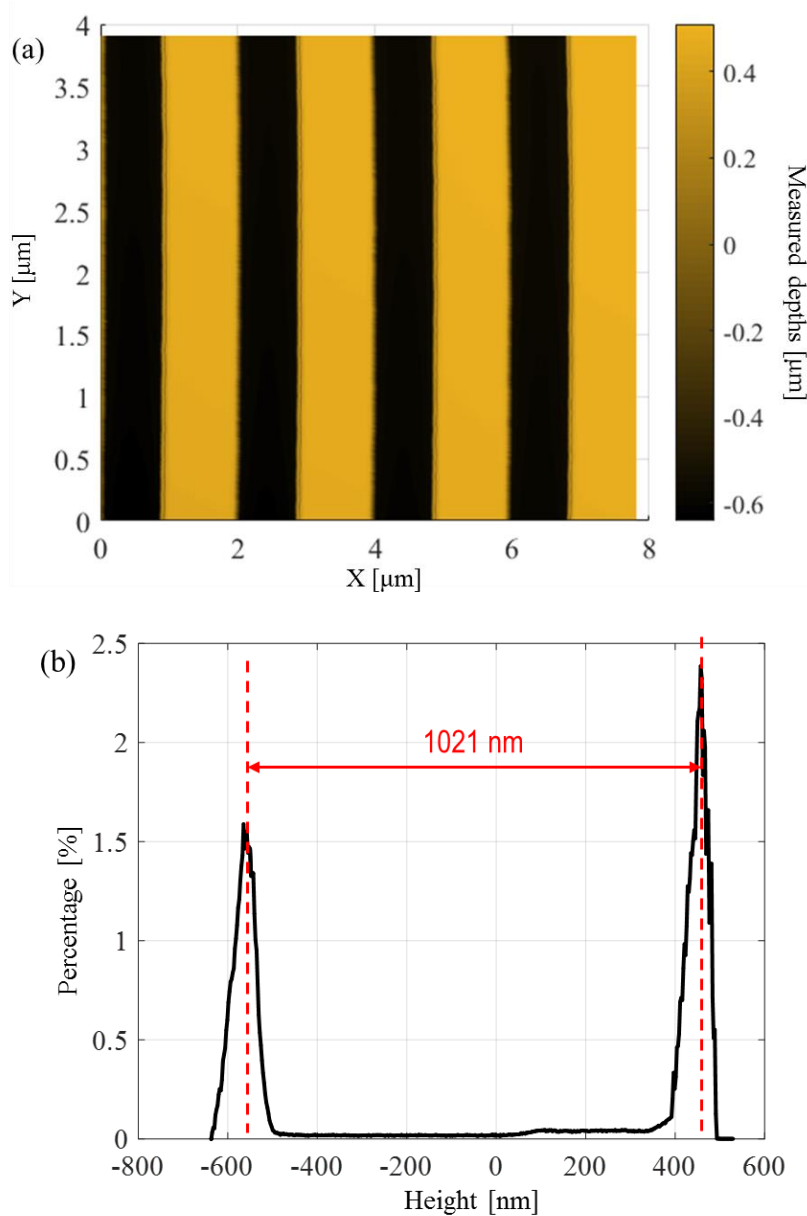
Figure 6.12 AFM measurement in the evaluating area of the silicon sample by a fine scanning process: (a) a two-dimensional topography image and (b) a height histogram.

6.3.3 Dual-wavelength incident unit of experiment setup

Based on the developed setup with low-coherence illumination and Linnik interferometry, introduced in Chapter 4, a dual-wavelength incident unit was added to achieve the illumination with two separated wavelengths. The schematic of this dual-wavelength

interferometer is shown in Fig. 6.13. The incident wavelength is controlled by the applied bandpass filter, which can be switched through the drop-in mount and the optical caged system.
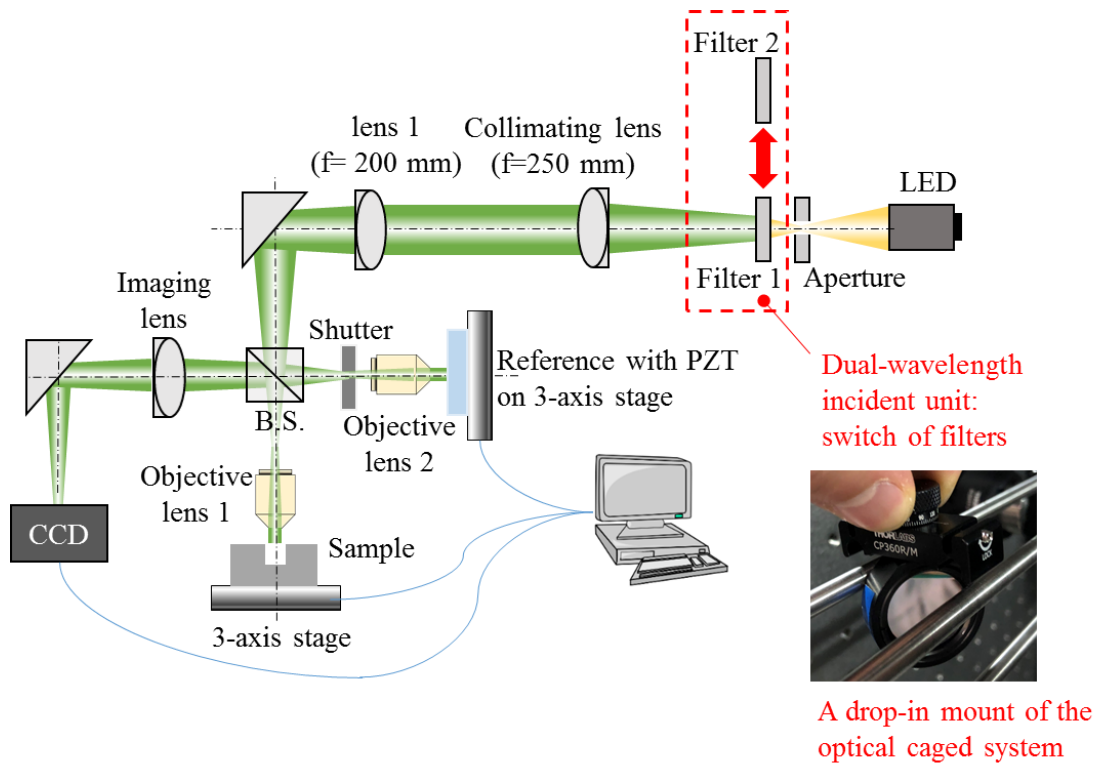
Figure 6.13 A dual-wavelength incident unit of the developed setup based on low-coherence illumination and Linnik interferometry

The two applied wavelengths should be carefully selected. Figure 6.14 show the observed interferograms of the standard silicon sample under different wavelengths. The top left area is the grating area, while the rest is the uniform surface. By the incident wavelength of 532 nm or 520 nm, the interference fringes on both the grating area and the uniform surface can be clearly observed, shown in Fig. 6.14(a) and (b). However, with the illumination of $\lambda = 450$ nm, the interference fringes are found only on the uniform surface, shown in Fig. 6.14(c). That results from the scattering light generated by the grating structure. As the applied wavelength becomes smaller, the intensity of the scattering light becomes stronger while the reflected intensity becomes weaker. In the grating area, by the illumination of $\lambda = 450$ nm,

the intensity ratio between measurement path and reference path become worse than that by $\lambda = 532$ nm or $\lambda = 520$ nm. Furthermore, due to a larger contribution of the scattering light in the measurement path, the optical path difference with the reference path might be increased. Besides the problem of the visible interference fringes in the grating area, we should also consider the optical responses from structures and the imaging aberrations from the same objectives under different wavelengths. Hence, two numerically similar wavelengths are suitable for our experiments: one (FLH532-10, Thorlabs) has the CWL of 532 nm and the bandwidth of 10 nm, another (FLH520-10, Thorlabs) has the CWL of 520 nm and the bandwidth of 10 nm.
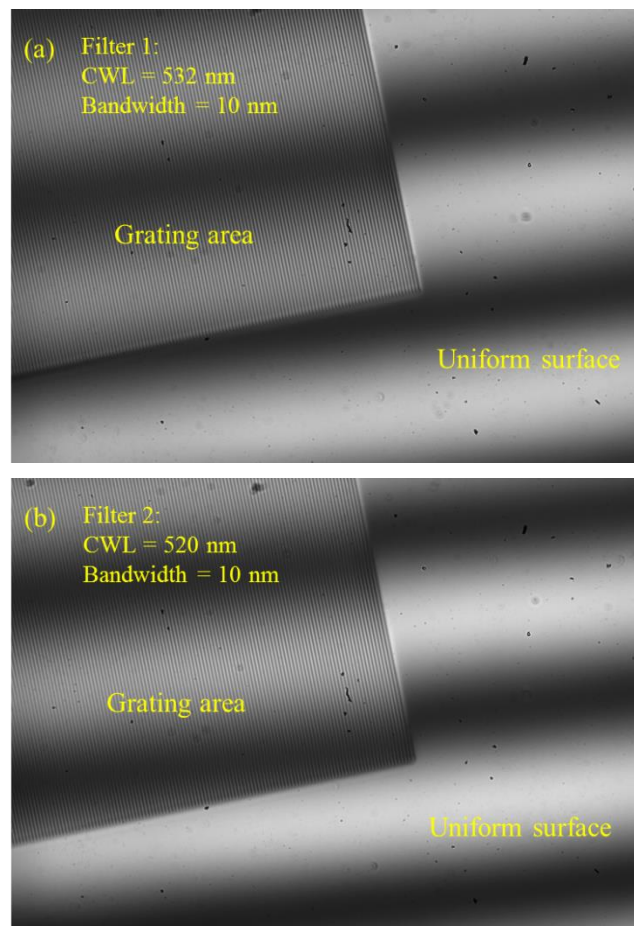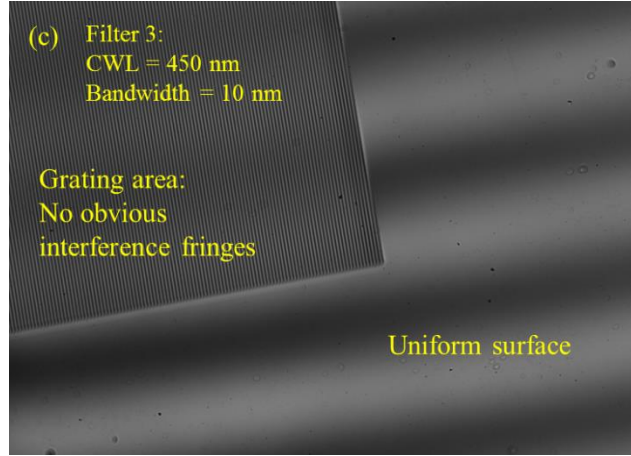
Figure 6.14 The observed interferograms of the standard silicon sample under (a) $\lambda = 532$ **nm, (b)** $\lambda = 520$ **nm and (c)** $\lambda = 450$ **nm.**

Considering the diffraction limit of the measurement system and the purpose of verifying the feasibility of the combination of FNRDM and the noise-immune dual-wavelength interferometry, two identical objectives (10x Plan Apo, *NA* = 0.28, Mitutoyo) are applied in the Linnik interferometry to measure the standard silicon sample. Table 6.2 summaries the parameters of the dual-wavelength setup when measuring the silicon sample. Hence, the width of the microgrooves in the silicon grating area is less than the diffraction limit with each of incident wavelength.

Table 6.2 parameters of the dual-wavelength setup when measuring the silicon sample

Filters	FLH532-10	FLH520-10
CWL	532 nm	520 nm
Bandwidth	10 nm	10 nm
Coherence length	28 μm	27 μm
The diffraction limit	1159 nm	1132 nm
Magnification	20x	20x

6.3.4 Measurement process of the silicon grating structure by the proposed method

Similar to measuring the microfluidic sample in Chapter 5, the measurement process of this silicon sample are as followings.

(1) Locate the same evaluation area with the fine scanning of AFM measurement. Figure 6.15 shows the images under the two separated wavelengths. The grating area (top left region), uniform surface (the rest) and the two perpendicular boundaries are clearly observed. The amplitude from the uniform surface (A_u) of FNRDM can be regarded as the average amplitude of the measured uniform surface. Then, the amplitude from the top surface (A_t) of the microgrooves is calculated by Eq. (2.30) for each wavelength.
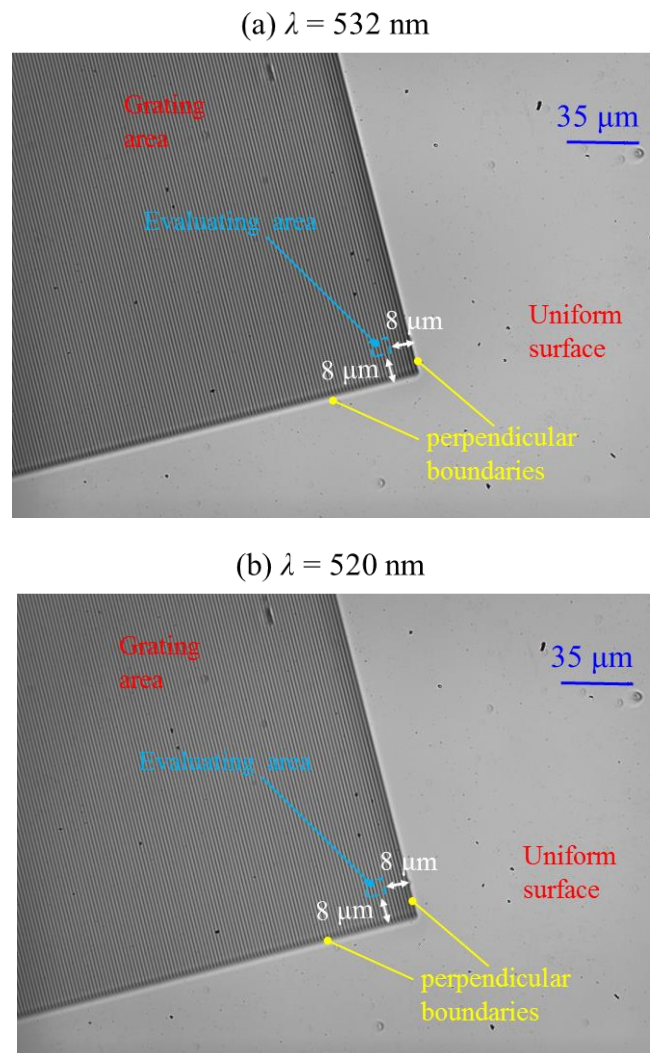
(a) $\lambda = 532$ nm

(b) $\lambda = 520$ nm

Figure 6.15 The observed images of the silicon sample by the developed setup with (a) $\lambda = 532$ nm and (b) $\lambda = 520$ nm.

(2) By using the two perpendicular boundaries, the data in the same evaluating area with AFM measurement can be exported for each observed images in Fig. 6.15. After a rotation process by Matlab, the amplitude distributions in the evaluating area was shown in Fig. 6.16. The dark part and bright part indicate the bottom surface and the top surface of the microgrooves, respectively. For each incident wavelength, the amplitudes at the central positions of the four microgrooves denote the A_f in the proposed FNRDM method.
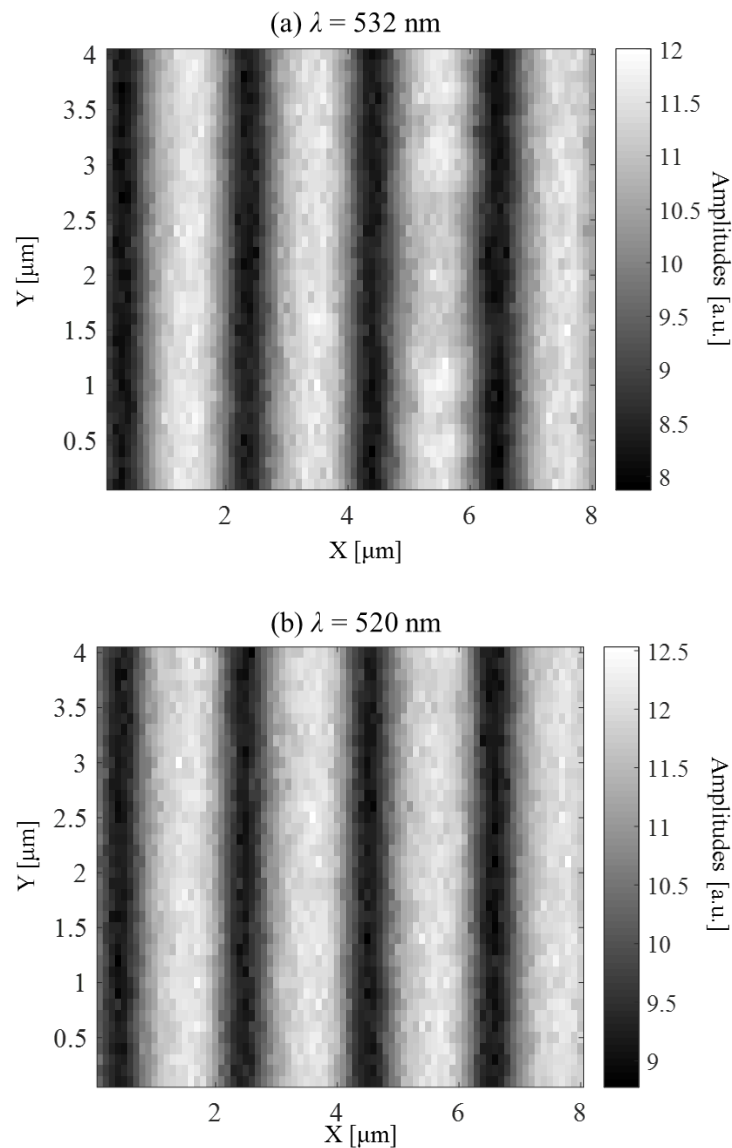
Figure 6.16 Amplitude distributions of the four microgrooves in the evaluating area with (a) $\lambda = 532$ nm and (b) $\lambda = 520$ nm.

(3) For each incident wavelength, the four-step phase shift method was used to obtain the corresponding far-field phase distribution. As shown in Fig. 6.17, under each incident wavelength, the four interferograms with $\pi/2$ phase shifting are used to calculate the wrapped far-field phase distribution (φ). Figure 6.18 plots the calculated φ in the evaluating area, from which the alternate distribution of darkness and brightness reflecting the upper surface and bottom can be clearly observed. The far-field phase differences θ_f are obtained through subtracting the phases at the central position of the four microgrooves by the average phase of only top surface.
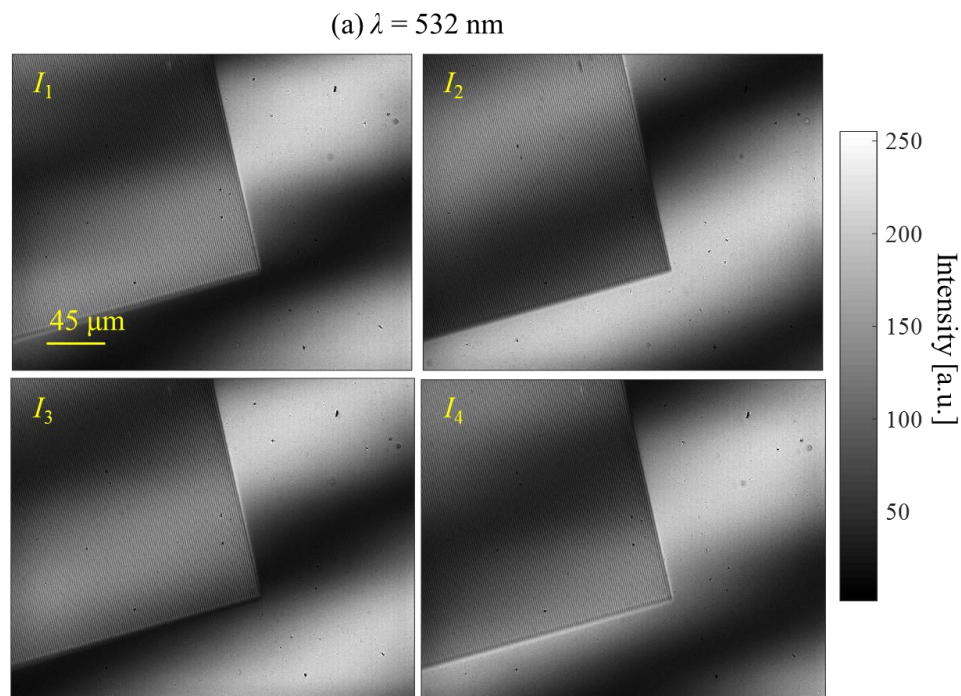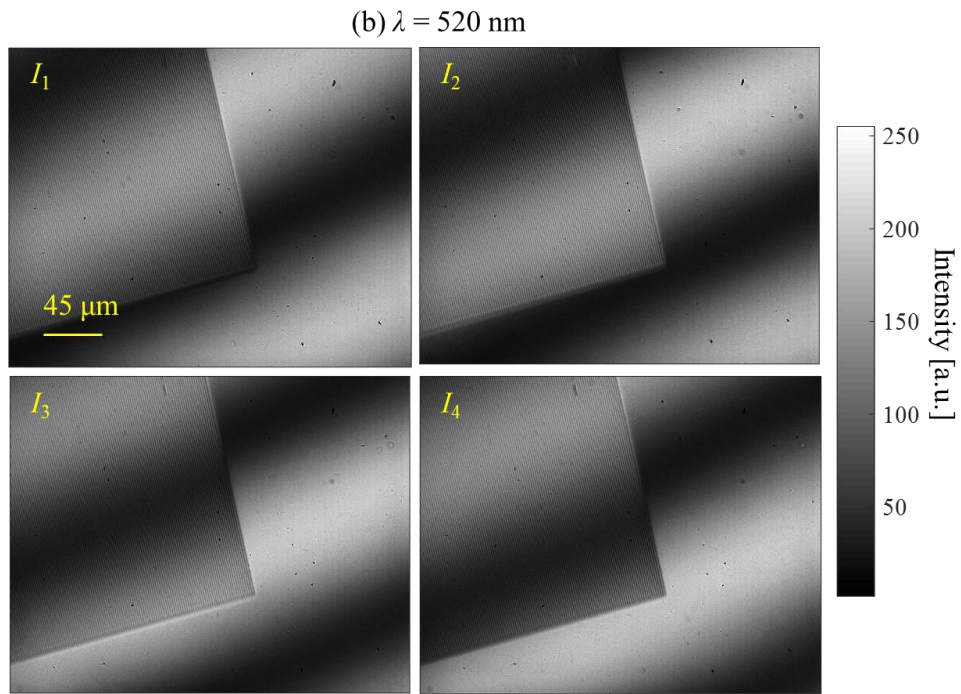
(a) $\lambda = 532$ nm

Figure 6.17 Four adjacent interferograms with π/2 phase shifting for the silicon sample with (a) λ = 532 nm and (b) λ = 520 nm.
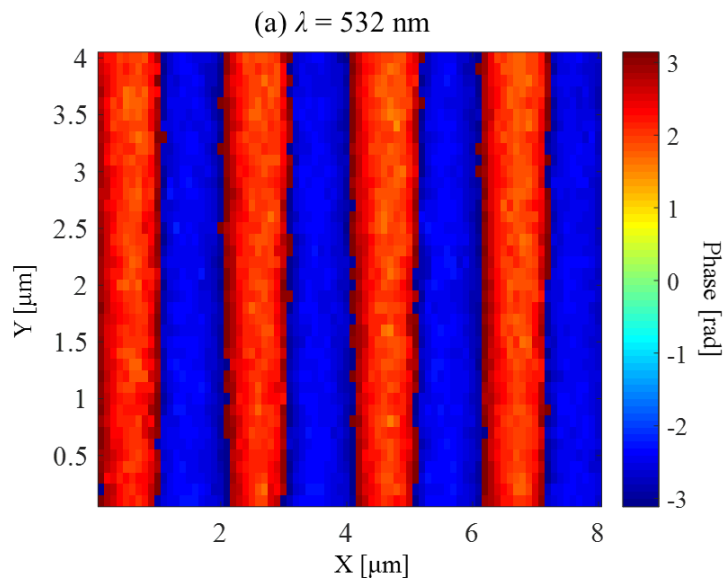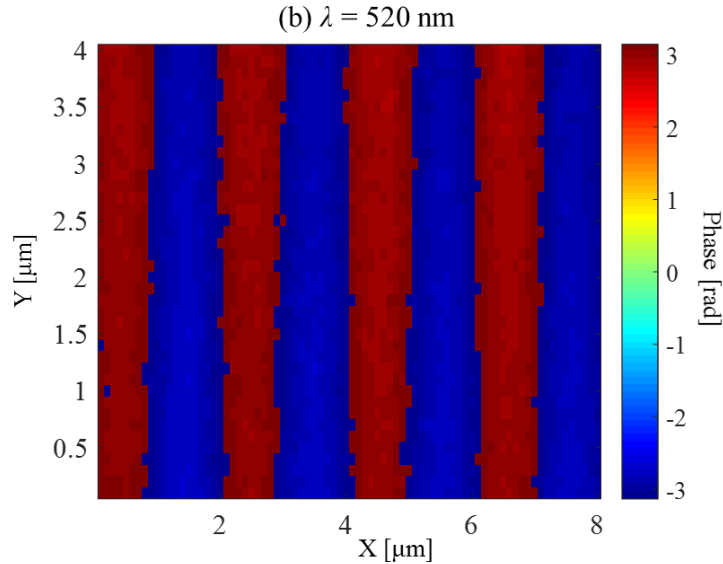
Figure 6.18 Far-field phase distributions of the four microgrooves in the evaluating area with (a) λ = 532 nm and (b) λ = 520 nm.

6.3.5 Measurement results of the silicon grating structure by the proposed method

According to the proposed FNRDM method, the measured amplitude from microgrooves (A_f), the amplitude from the top surface (A_u) and far-field phase difference (θ_f) in the evaluating area are substituted into Eq. (2.31) to calculate the near-field phase differences and corresponding depths, for each incident wavelength.

Firstly, using the algorithm of conventional dual-wavelength interferometry (Eq. (6.13)), the near-field phase difference (θ_n) calculated by the proposed FNRDM method and the far-filed phase difference (θ_f) directly obtained from the phase shift method are substituted into the calculation of phase unwrapping. Figure 6.19(a) presents the depth histogram by conventional interferometry using only θ_f and conventional dual-wavelength interferometry, while the results by FNRDM and conventional dual-wavelength interferometry are shown in Fig. 6.19(b). Because the depth measured by AFM is 1021 nm, the differences of the average depths of the two results and AFM results are 270 nm and 48 nm, respectively. Although a great improvement of the average depth by FNRDM and conventional dual-wavelength interferometry can be verified, when compared to conventional dual-wavelength phase shift

146

method. However, the noises of the standard deviation in the two results are still hundreds of nanometers level.
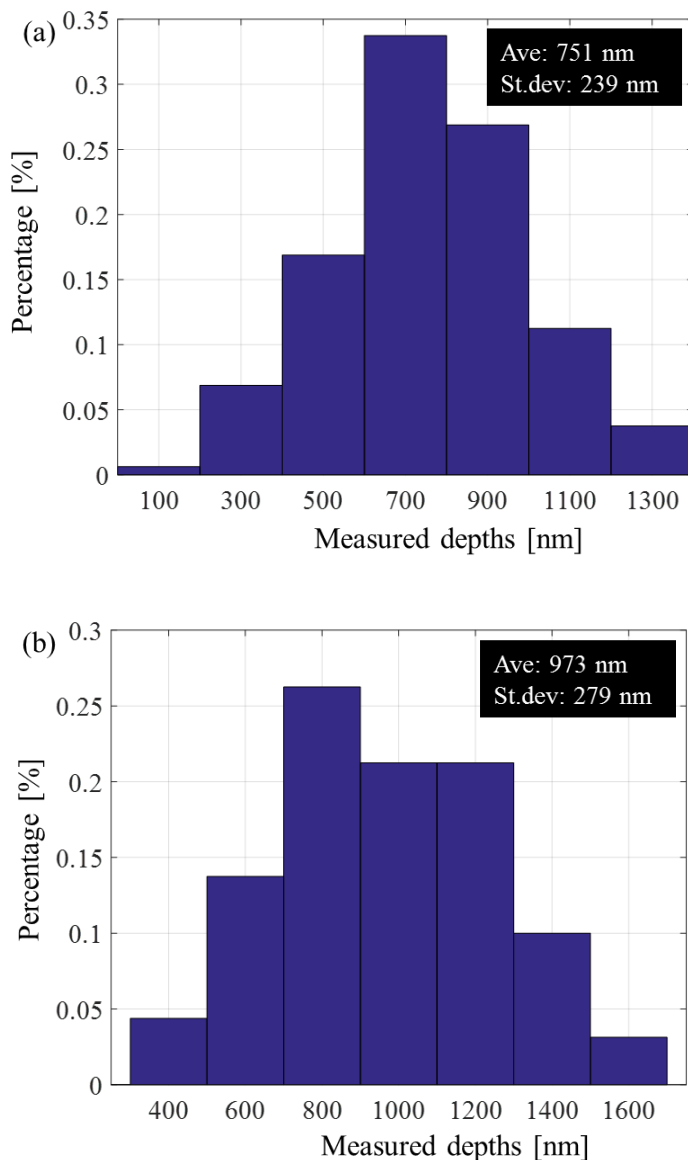
Figure 6.19 Depth histograms in the evaluating area by (a) conventional dual-wavelength phase shift method and (b) a combination of FNRDM and conventional dual-wavelength interferometry

Then, using the algorithm of noise-immune dual-wavelength interferometry (Eqs. (6.15) and (6.16)) to achieve the phase wrapping problem. Table 6.3 lists the average values of the

near-field phase difference (θ_n) calculated by the proposed FNRDM method and the far-filed phase difference (θ_f) directly obtained from the phase shift method. And calculated by Eq. (6.15), the integer of the phase wrapped problem for each incident wavelength are shown in the Table 6.4. The values in the bracket are directly calculated to obtain the closest integer for phase unwrapping process. Hence, by the algorithm of noise-immune dual-wavelength interferometry, the integers are 2 with far-filed phase difference (θ_f) and 3 with near-field phase difference (θ_n) by the proposed FNRDM method, respectively.

Table 6.3 Average values of measured far-field phase differences and calculated near-field phase differences for each incident wavelength

	FLH532-10	FLH520-10
Average value of θ_f	5.18 rad	5.58 rad
Average value of θ_n	4.73 rad	5.26 rad

Table 6.4 Integers calculated by noise-immune algorithm using far-field and near-field phase differences

	k_{532}	k_{520}
Using average value of θ_f	2 (1.99)	2 (1.99)
Using average value of θ_n	3 (2.90)	3 (2.90)

Finally, using Eq. (6.16) to obtain the unwrapped phase difference. With the phase information under $\lambda = 532$ nm, Figure 6.20(a) presents the depth histogram by conventional interferometry using only θ_f and the noise-immune dual-wavelength interferometry, while the results by FNRDM and the noise-immune dual-wavelength interferometry are shown in Fig. 6.20(b). Correspondingly, the two results using the phase information under $\lambda = 520$ nm are illustrated in Fig. 6.21. It is found that, using the algorithm of noise-immune dual-wavelength interferometry, the noise levels of standard deviations in the four results are all less than 5 nm, which is a dramatic improvement than that by conventional dual-wavelength interferometry (hundreds of nanometers level). Furthermore, by conventional interferometry using only θ_f, shown in Figs. 6.20(a) and 6.21(a), the differences between the average depths

and AFM results are 270 nm for λ = 532 nm and 253 nm for λ = 520 nm. While by the proposed FNRDM method, shown in Figs. 6.20(b) and 6.21(b), the differences are both 23 nm for the two incident wavelengths. Because the integers calculated by noise-immune algorithm are different using far-field and near-field phase differences, as shown in Table 6.4.
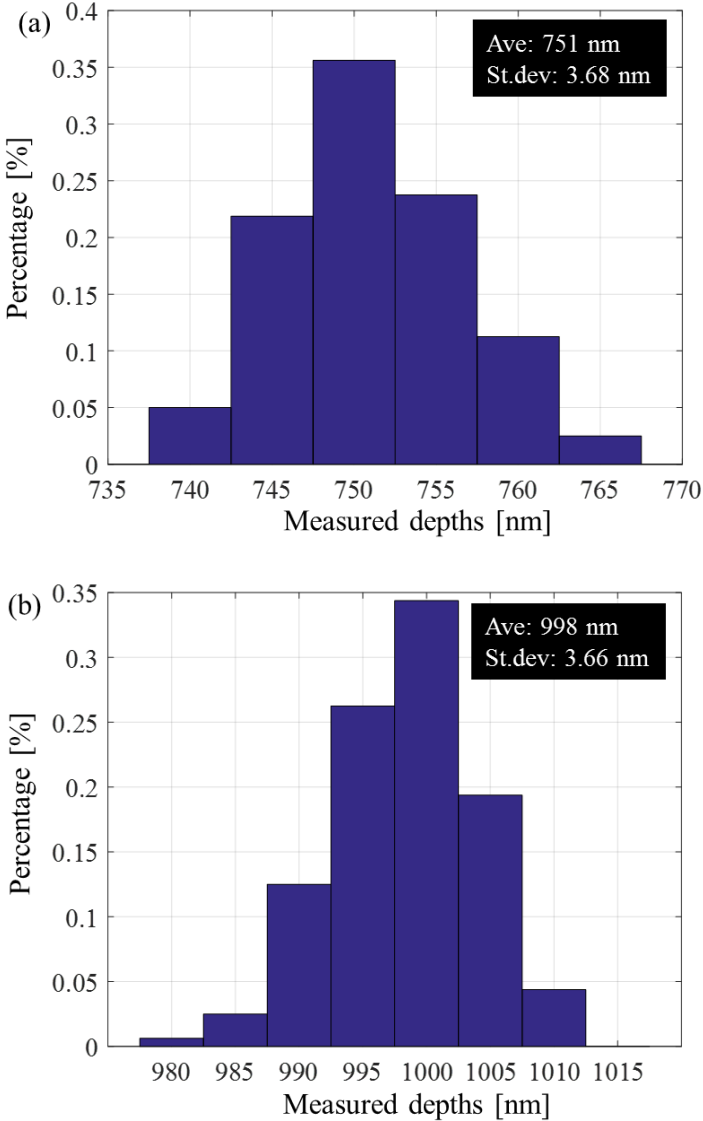
Figure 6.20 Depth histograms in the evaluating area, using the phase information under λ **= 532 nm, by (a) the conventional interferometry using only** θ_f **and the noise-immune dual-wavelength interferometry and (b) a combination of FNRDM and the noise-immune dual-wavelength interferometry.**
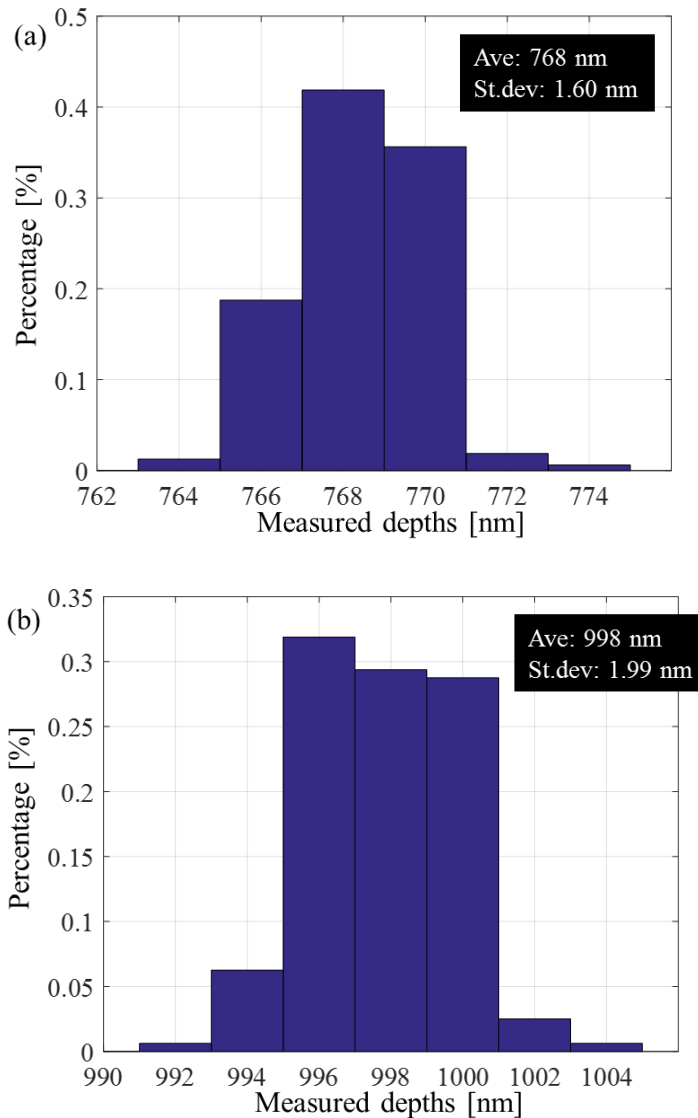
Figure 6.21 Depth histograms in the evaluating area, using the phase information under λ = 520 nm, by (a) the conventional interferometry using only θ_f and the noise-immune dual-wavelength interferometry and (b) a combination of FNRDM and the noise-immune dual-wavelength interferometry.

The depth histograms in Figs. 6.19, 6.20 and 6.21 can be summarized in Fig. 6.22. Only using both the proposed FNRDM method and the noise-immune dual-wavelength interferometry, both the difference between the average depth and AFM results and the noise level of the standard deviation are less than 5%, indicated as the results by methods *E* and *F*

in Fig. 6.22. It is clearly suggested that the 1000-nm-wide microgrooves, having an aspect-ratio of 1, with width less than the diffraction limit (1159 nm and 1132 nm) of develop measurement system on a silicon surface, cannot be measured by the commercial white light interferometer and the laser confocal microscopy, but can be quantitatively evaluated with an accuracy of less than 5% by the combination of the proposed FNRDM method and noise-immune dual-wavelength interferometry.

A: conventional dual-wavelength phase shift method
B: a combination of FNRDM and conventional dual-wavelength interferometry
C: conventional interferometry and noise-immune dual-wavelength interferometry (λ = 532 nm)
D: conventional interferometry and noise-immune dual-wavelength interferometry (λ = 520 nm)
E: FNRDM and noise-immune dual-wavelength interferometry (λ = 532 nm)
F: FNRDM and noise-immune dual-wavelength interferometry (λ = 520 nm)

Figure 6.22 Summarization of the measured depths of the microgrooves on the silicon surface by different methods

6.4 Experiments of measuring the grating structure on a COC surface

151

Another experiment of measuring the grating structure on a COC surface was also performed to verify the feasibility of the combination of FNRDM and the noise-immune dual-wavelength interferometry.

6.4.1 A COC sample with grating structure

This COC sample with the grating structure was also fabricated and provided by Technical University of Denmark. The nominal width, depth and pitch of the grating structure are 700 nm, 380 nm and 1400 nm, respectively. Besides the COC sample to be measured, the reference data measured by AFM was also provided by Technical University of Denmark. The applied AFM is Icon AFM (high-resolution performance and closed-loop positioning), whose temperature-compensating position sensors render noise levels in the sub-angstroms range for the Z-axis, and angstroms in XY axis. Figure 6.23 is an imaging of the grating structures on this COC sample under an optical microscopy. As we can see, on the surface, there are various of grating structures, and the red box denotes the evaluating area.
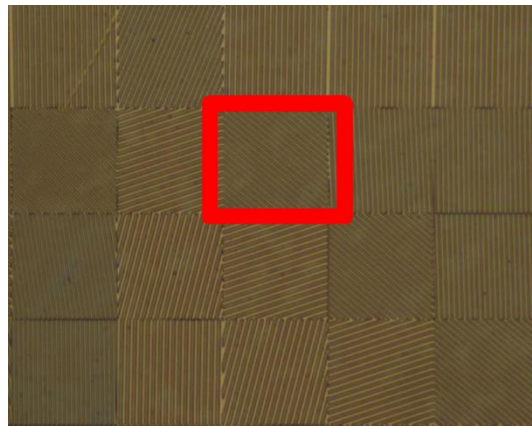
Figure 6.23 An imaging of the grating structures on this COC sample under an optical microscopy

Considering both the measurement accuracy and measurement time, four locations with a same image dimension of $3 \times 3 \ \mu m^2$ in the evaluating area are measured by Icon AFM. Figure 6.24(a) plots the two-dimensional topography image for one location. Here, two methods are used to calculate the depth information. One is histograms, which is presented in Fig. 6.24(b). The measured depth is 387 nm. Another is the analysis of cursors value. As shown in Fig.

6.24(c), the green and red cursors denote the top surface while the blue cursors indicate the bottom surface. The measured depths are 381 nm and 388 nm, respectively.
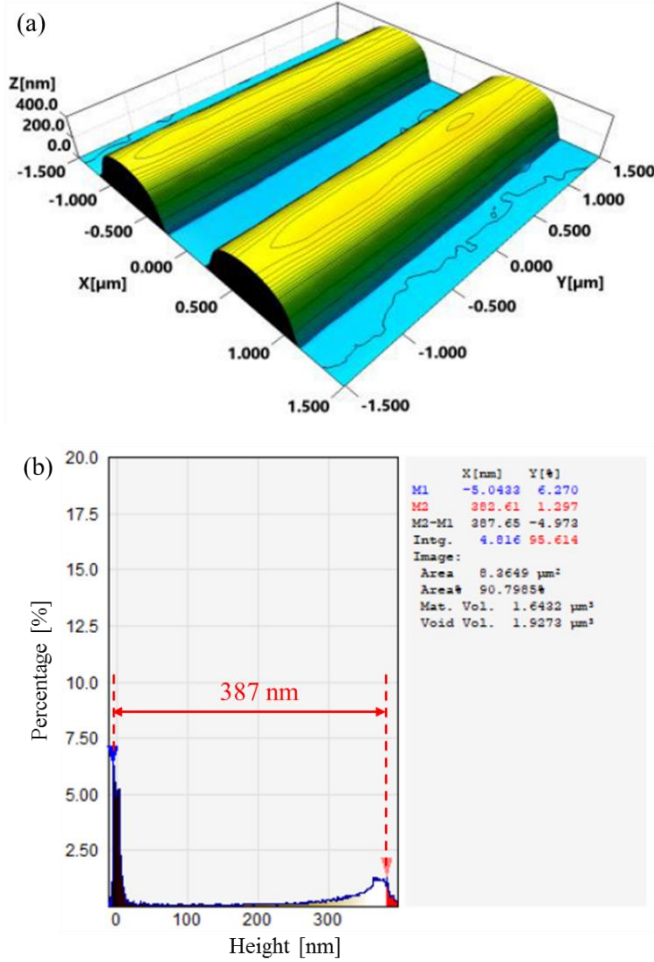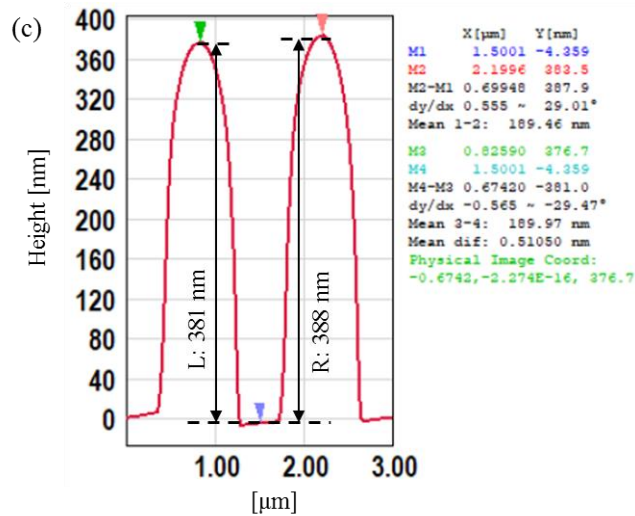
Figure 6.24 An example of AFM measurement of the grating in the evaluating area on the COC surface: (a) two-dimensional topography image, (b) the topography histogram and (c) the analysis of cursors value.

The measured depths for all the four locations are summarized in Table 6.5. It is found that, by the two methods, the average value and the standard deviation are both 389 nm and 5 nm. The results suggest a good uniformity of the surface topography in the evaluating area. Hence, the measured depth of the investigated grating on the COC surface is 389 nm by Icon AFM.

Table 6.5 The measured depths for all the four locations by AFM

	Depths by histogram [nm]	Depths by cursor values [nm]	
		L	R
Location 1	396	396	396
Location 2	385	387	391
Location 3	387	381	390
Location 4	387	381	388
Average	389	389	
St.dev	5	5	
Cov	1%	1%	
Max	396	396	
Min	385	381	

6.4.2 Measurement process of the COC sample by the proposed method

When measuring the grating on this COC surface, the experiment setup is almost the same with that used in measuring the silicon sample, introduced in Section 6.3. But the applied objectives are different. Considering a higher resolving power of the developed setup, two identical objectives (20x Plan Apo, $NA = 0.42$, Mitutoyo) are exploited to measure the COC sample. Table 6.6 summaries the parameters of the dual-wavelength setup when measuring the grating on this COC sample. Hence, the width (700 nm) of the microgrooves in the COC sample is less than the diffraction limit with each of incident wavelength.

Table 6.6 Parameters of the dual-wavelength setup when measuring the COC sample.

Filters	FLH532-10	FLH520-10
CWL	532 nm	520 nm
Bandwidth	10 nm	10 nm
Coherence length	28 μm	27 μm
The diffraction limit	772 nm	755 nm
Magnification	40x	40x

Similar to measuring the grating structure on the silicon surface in Section 6.3, the measurement process of this COC sample are as followings.

(1) On the surface of this COC sample, the grating area and the uniform surface are not coterminous, unlike the microfluidic sample in Chapter 5 or the silicon sample in Section 6.3. Therefore, the separated images for the two regions are measured. With $\lambda = 532$ nm, Figure 6.25 (a) shows the image of the grating area, while the image of the uniform surface is presented in Fig. 6.25(b). The red box in Fig. 6.25(a) denotes the same evaluating area with AFM measurement. Correspondingly, the two images under $\lambda = 520$ nm are illustrated in Fig. 6.26. The amplitude from the uniform surface (A_u) of FNRDM can be regarded as the average amplitude of the measured uniform surface. Then, the amplitude from the top surface (A_t) of the microgrooves is calculated by Eq. (2.30) for each wavelength.
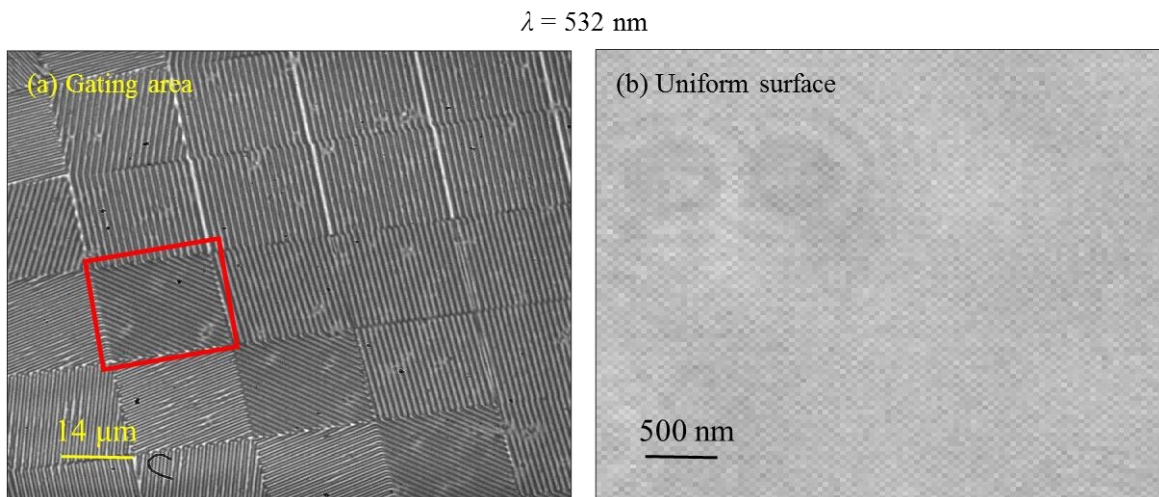
$$\lambda = 532 \text{ nm}$$

Figure 6.25 Images under the incident wavelength of 532 nm of (a) the grating area and (b) the uniform surface on the COC sample.
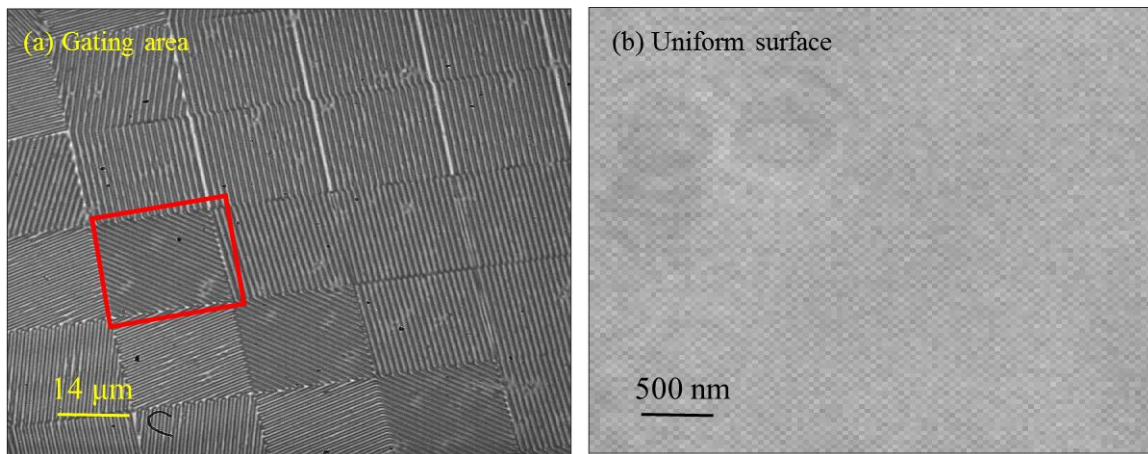
Figure 6.26 Images under the incident wavelength of 520 nm of (a) the grating area and (b) the uniform surface on the COC sample.

(2) After a rotation process by Matlab, the amplitude distributions of the grating in the evaluating area was shown in Fig. 6.27. The image dimension is 2 μm in X direction and 5 μm in Y direction. The dark part and bright part indicate the bottom surface and the top surface of the microgrooves, respectively. For each incident wavelength, the amplitudes at the central positions of the four microgrooves denote the A_f in the proposed FNRDM method.
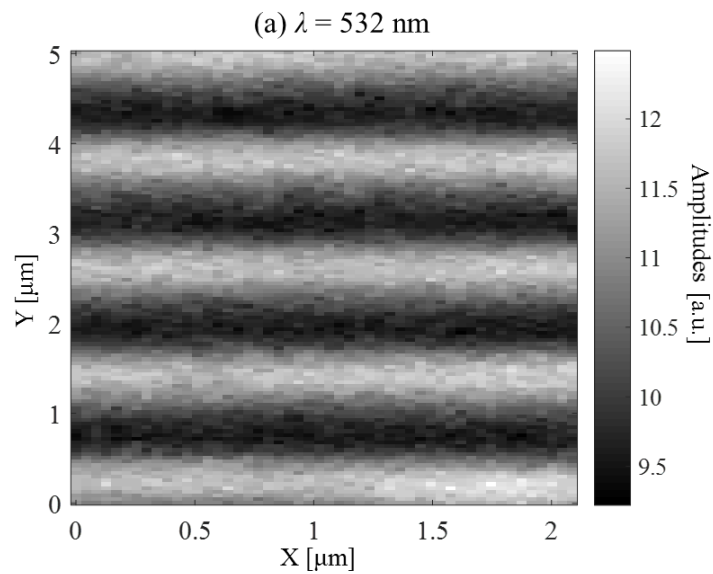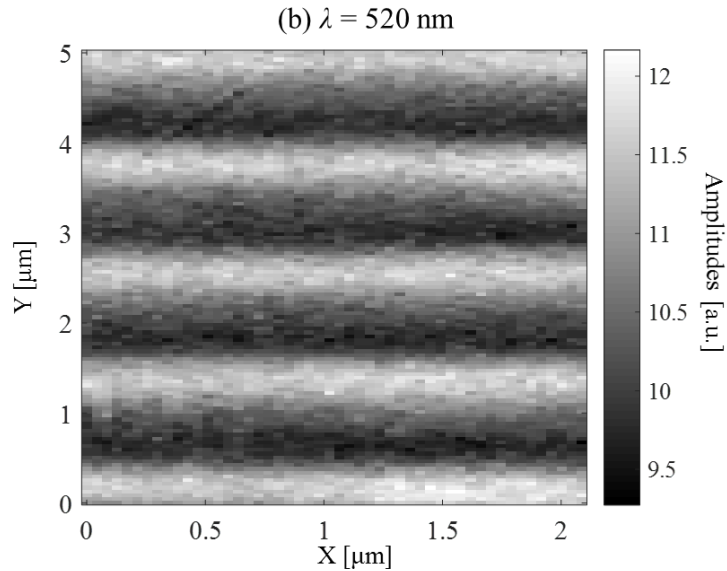
(b) $\lambda = 520$ nm

Figure 6.27 Amplitude distributions of the grating in the evaluating area on the COC surface with (a) $\lambda = 532$ nm and (b) $\lambda = 520$ nm.

(3) For each incident wavelength, the four-step phase shift method was used to obtain the corresponding far-field phase distribution. As shown in Fig. 6.28, under each incident wavelength, the four interferograms with $\pi/2$ phase shifting are used to calculate the wrapped far-field phase distribution (φ). Figure 6.29 plots the calculated φ of the grating in the evaluating area, from which the alternate distribution of darkness and brightness reflecting the upper surface and bottom can be clearly observed. The far-field phase differences θ_f are obtained through subtracting the phases at the central position of the four microgrooves by the average phase of only top surface.
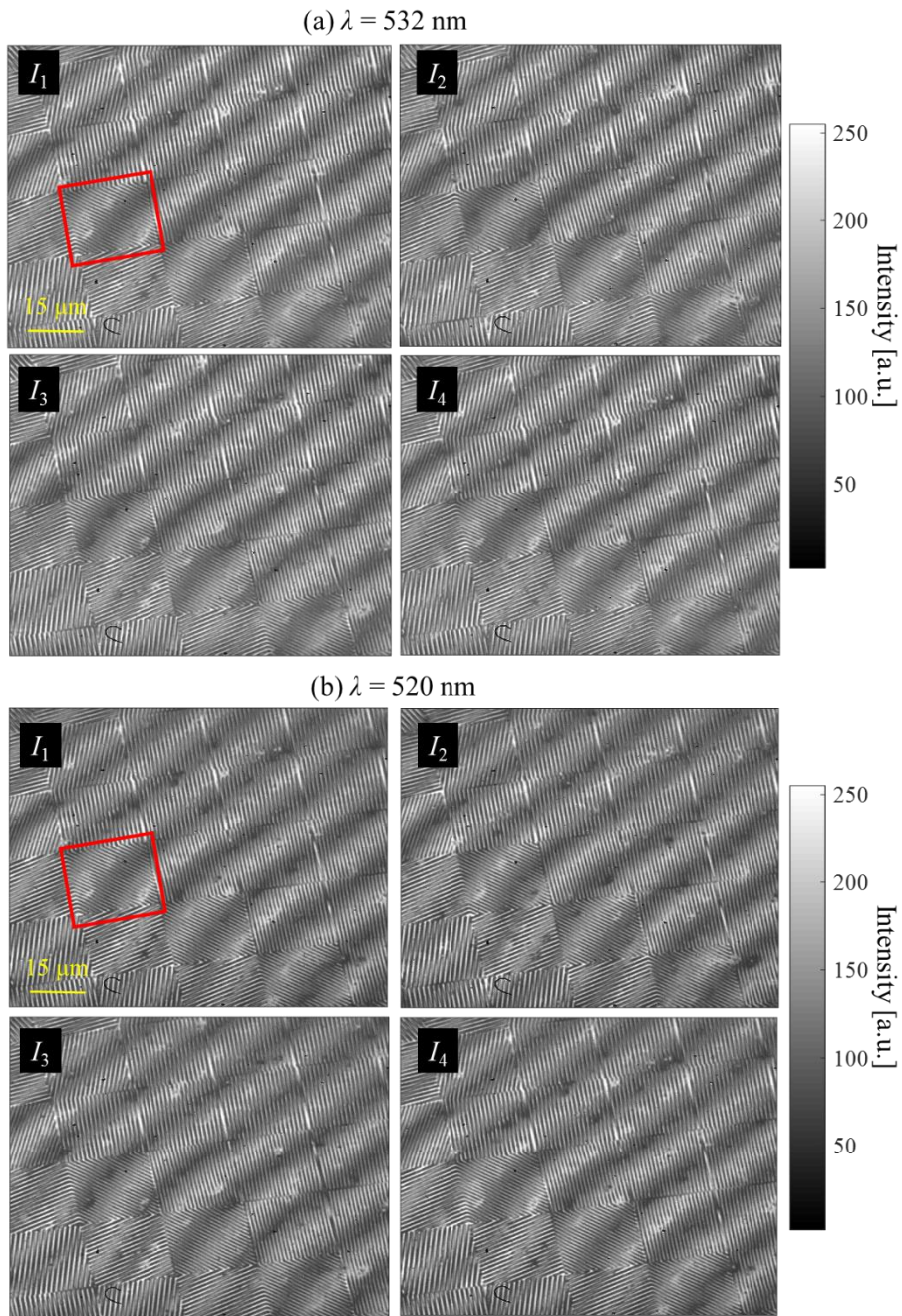
Figure 6.28 Four adjacent interferograms with π/2 phase shifting for the COC sample with (a) λ = 532 nm and (b) λ = 520 nm.
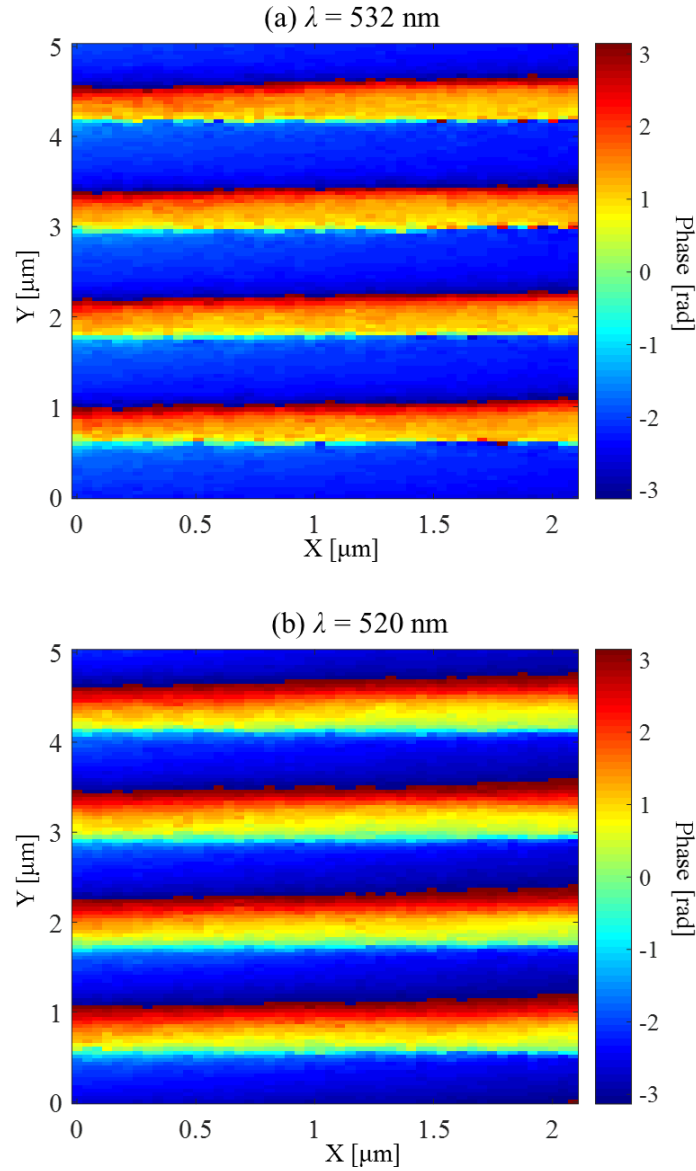
Figure 6.29 Far-field phase distributions of the grating in the evaluating area on the COC surface with (a) λ = 532 nm and (b) λ = 520 nm.

6.4.3 Measurement results of the grating on the COC surface by the proposed method

According to the proposed FNRDM method, the measured amplitude from microgrooves (A_f), the amplitude from the top surface (A_u) and far-field phase difference (θ_f) in the evaluating area are substituted into Eq. (2.31) to calculate the near-field phase differences and corresponding depths, for each incident wavelength.

Table 6.7 lists the average values of the near-field phase difference (θ_n) calculated by the proposed FNRDM method and the far-filed phase difference (θ_f) directly obtained from the phase shift method. And calculated by Eq. (6.15), the integer of the phase wrapped problem for each incident wavelength are shown in the Table 6.8. By the algorithm of noise-immune dual-wavelength interferometry, the integers are 0 with far-filed phase difference (θ_f) and 1 with near-field phase difference (θ_n), respectively.

Table 6.7 Average values of measured far-field phase differences and calculated near-field phase differences for each incident wavelength

	FLH532-10	FLH520-10
Average value of θ_f	3.67 rad	3.82 rad
Average value of θ_n	2.82 rad	2.71 rad

Table 6.8 Integers calculated by noise-immune algorithm using far-field and near-field phase differences

	k_{532}	k_{520}
Using average value of θ_f	0 (0.45)	0 (0.45)
Using average value of θ_n	1 (1.23)	1 (1.23)

The measured depths by different methods are summarized in Fig. 6.30. As shown in Table 6.5, the depth of the grating in the evaluating area is 389 nm by AFM measurement. When using the combination of FNRDM and the noise-immune dual-wavelength interferometry, the measured depth has an average residual of 4 nm with a standard deviation of 5.5 nm for $\lambda = 532$ nm (Results by Method E), and for $\lambda = 520$ nm, the average residual and the standard deviation are 17 nm and 7.41 nm (Results by Method F). Compared to other results, a dramatic accuracy improvement by Methods E and F can be verified from Fig. 6.30. Hence, the experiment results suggested that the 700-nm-wide microgrooves, having an aspect-ration over 0.5, with width less than the diffraction limit (772 nm and 755 nm) of develop measurement system on a COC surface, can be quantitatively evaluated with an

accuracy of less than 10% by the combination of the proposed FNRDM method and noise-immune dual-wavelength interferometry.
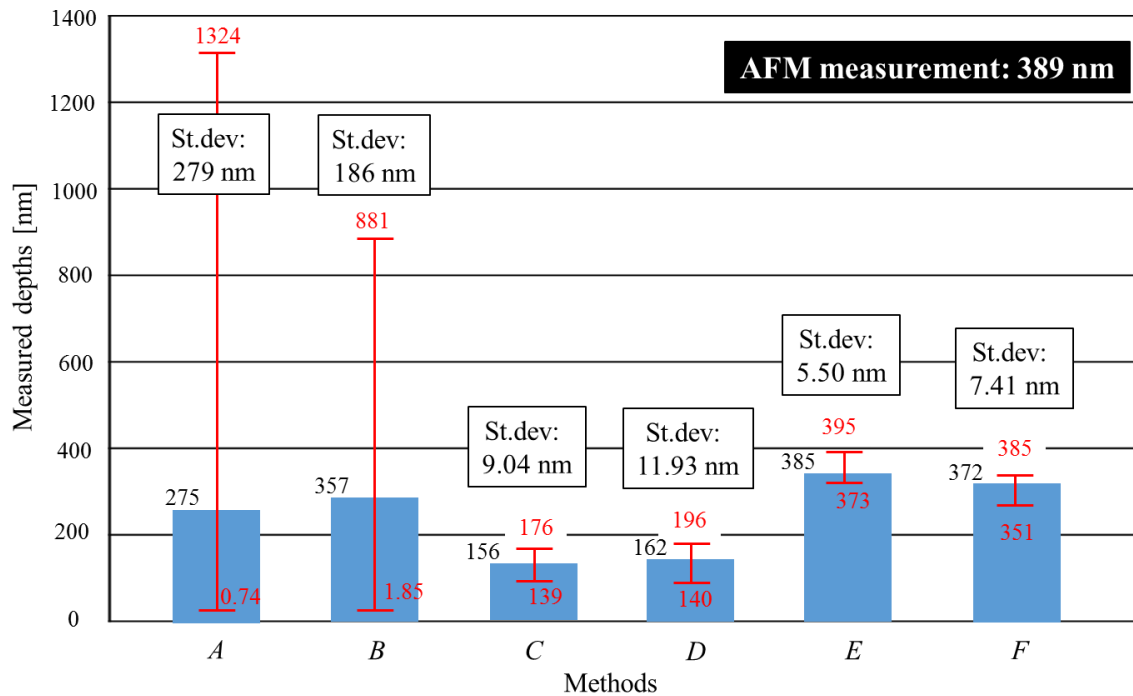
A: conventional dual-wavelength phase shift method
B: a combination of FNRDM and conventional dual-wavelength interferometry
C: conventional interferometry and noise-immune dual-wavelength interferometry ($\lambda = 532$ nm)
D: conventional interferometry and noise-immune dual-wavelength interferometry ($\lambda = 520$ nm)
E: FNRDM and noise-immune dual-wavelength interferometry ($\lambda = 532$ nm)
F: FNRDM and noise-immune dual-wavelength interferometry ($\lambda = 520$ nm)

Figure 6.30 Summarization of the measured depths of the grating in the evaluating area on the COC surface by different methods

6.5 Conclusions

Since the phase of light is 2π periodic, the depths of microstructures which are optically larger than half of the incident wavelength subject to phase measurement ambiguity. In order to achieve the depth measurement of the diffraction-limited and deep microstructures, a combination of FNRDM and dual-wavelength interferometry was proposed in this chapter.

Although the conventional dual-wavelength interferometry is capable of extending the depth measurement range, the downside of conventional dual-wavelength interferometry is

that its noise has been magnified significantly when compared to that in a single-wavelength phase map. In order to solve this problem, the noise-immune dual-wavelength interferometry was proposed. The two phase unwrapping methods are used in a case of a 400-nm-wide and 300-nm-deep microgroove, under the Gaussian noise (sigma $2\sigma = 3\%$), by the FDTD simulation. The simulation results showed that the noise level of the standare deviation is decreased from 97.6 nm by the conventionla dual-wavelength interferometry to less than 2 nm by the proposed noise-immune dual-wavelength interferometry.

In order to verify the feasibility of the combination of FNRDM and the noise-immune dual-wavelength interferometry, two experiments were performed. The first experiment is measuring the grating structure (nominal width = 1000 nm, an aspect-ratio of 1, pitch = 2000 nm) on a slicon surface, the depth of which cannot be accurately measured by the commercial white light interferometer and the laser confocal microscopy. The Innova AFM was used to measure the silicon sample, providing a reliable reference data for verification. Then, the grating structure on this silicon sample was measured by the developed setup with a dual-wavelength interferometer unit ($\lambda = 532$ nm and 520 nm). The experiment results indicated that the 1000-nm-wide microgrooves, having an aspect-ratio of 1, with width less than the diffraction limit (1159 nm and 1132 nm) of develop measurement system on a silicon surface, can be quantitatively evaluated with an accuracy of less than 5% by the combination of the proposed FNRDM method and the noise-immune dual-wavelength interferometry.

The second experiment is measuring the grating structure (nominal width = 700 nm, depth = 380 nm, pitch = 1400 nm) on a transparent COC surface. The Icon AFM was used to measure the COC sample, providing a reliable reference data for verification. The experiment results demonstrated that the 700-nm-wide microgrooves, having an aspect-ratio over 0.5, with width less than the diffraction limit (772 nm and 755 nm) of develop measurement system on transparent polymer surface, can be quantitatively evaluated with an accuracy of less than 10% by the combination of the proposed FNRDM method and the noise-immune dual-wavelength interferometry.

Therefore, considering the two experiment results, it is suggested that using the proposed method of a combination of the proposed FNRDM method and the noise-immune dual-

wavelength interferometry enables the quantitative depth evaluation of the diffraction-limited and deep microgrooves, on both silicon surface and the transparent polymer surface, with an accuracy of less than 10%, without the phase ambiguity problem. The combination also has a potential of measuring the depth of diffraction-limited and steep microgrooves with high accuracy.

Chapter 7. Numerical analysis of a novel droplet-based phase unwrapping method

In order to achieve the phase unwrapping, a novel method using a Fluorinert droplet was proposed in this section. This method includes the generation and combination of two phase maps under an air condition and a droplet condition. When the two phase maps are combined, the measured depths are equivalent to those measured by a longer wavelength based on the refractive index difference. In this method, a one-shot interferometry based on the Fourier Transform method and a Fluorinert liquid which evaporates rapidly were presented. A numerical analysis based on Rigorous Coupled-Wave Analysis (RCWA) was performed to demonstrate the feasibility of the novel phase unwrapping method in both the diffraction-free and the diffraction-limited microgrooves. The proposed method enables the phase unwrapping by using only single-wavelength illumination and requires significantly less computational work than other least-squares integration technologies.

7.1 Proposal of a novel phase unwrapping method using a Fluorinert droplet

7.1.1 Measurement principle

As shown in Fig. 7.1, it is a schematic of the proposed phase unwrapping method. This method includes the generation and combination of two phase maps under an air condition and a droplet condition. The air condition means there is only the air between the microgrooves to be measured and the optical measurement system. While the droplet condition denotes a stable and volatile liquid is inserted into the microgrooves during the measurement process. In optics, optical path length (OPL) is the product of the geometric length of the path followed by light through a given system, and the refractive index of the medium through which it propagates. Hence, in the air condition, the phase difference (θ_g) between the bottom surface and the top surface is given by

$$\theta_g = \frac{4\pi h n_g}{\lambda} \tag{7.1}$$

Where h, n_g and λ are the depth of the microgroove, the refractive index of the air and the wavelength of the incident beam.

<p align="center">(a) Air condition   (b) Droplet condition</p>
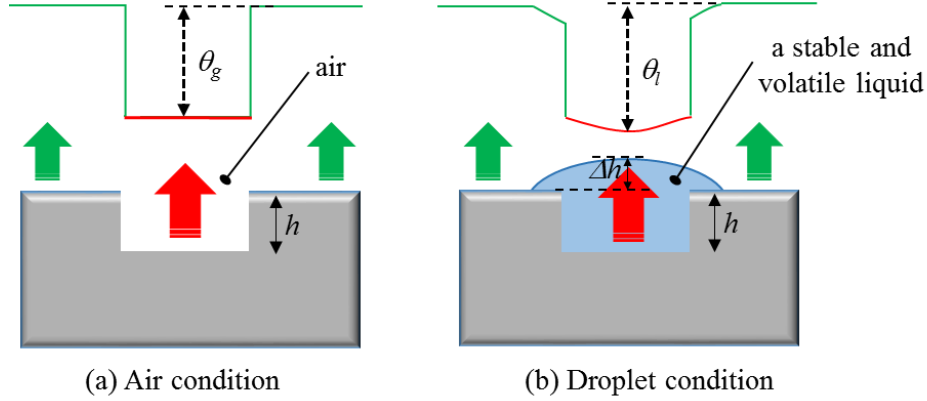
Figure 7.1 Schematic of the proposed phase unwrapping method: (a) air condition and (b) droplet condition

When the same microgroove is dripped with a droplet, assume that the droplet contacts the whole surface, including the bottom of the microgroove. Then, the phase difference (θ_l) under the droplet condition is given by

$$\theta_l = \frac{4\pi(h + \Delta h)n_l}{\lambda} \tag{7.2}$$

Where Δh and n_l are the distance between the gas-liquid interface and the top surface of the microgroove, and the refractive index of the liquid. Subtracting Eq. (7.2) with Eq. (7.1), we can obtain

$$\begin{aligned}
\Delta\theta &= \frac{4\pi h \Delta n}{\lambda} + C \\
\Delta\theta &= \theta_l - \theta_g \\
\Delta n &= \Delta n_l - \Delta n_g \\
C &= \frac{4\pi \Delta h \Delta n}{\lambda}
\end{aligned} \tag{7.3}$$

Where $\Delta\theta$ and Δn are the differences of the phase differences and the refractive indexes between the droplet condition and the air condition, respectively. C is a phase factor caused

by Δh and Δn. In the practical measurement, Δh can be directly observed by an auxiliary horizontal imaging system with high speed camera, thus C can be regarded as a known parameter. The depth to be measured is calculated as

$$h = \frac{\Delta\theta - C}{4\pi}\lambda_{eq}, \lambda_{eq} = \frac{\lambda}{\Delta n} \qquad (7.4)$$

If the refractive index of the inserted droplet (n_l) is close to that of the air ($n_g = 1$), the depth measurement range can be extended with a magnification factor of $1/\Delta n$. The measured depth is equivalent to that measured by a longer wavelength based on the refractive index difference.

7.1.2 A Fluorinert liquid

In this research, a Fluorinert liquid (liquid of perfluorocarbon, C_6F_{14}; namely, 3M Fluorinert FC-72) is considered as the inserted liquid [144]. The Fluorinert liquid FC-72 is a clear, colorless, fully-fluorinated liquid. Like other Fluorinert electronic liquids, FC-72 is thermally and chemically stable, compatible with sensitive materials, nonflammable, practically nontoxic and leaves essentially no residue upon evaporation. This unique combination of properties makes Fluorinert liquid FC-72 ideal as a contact liquid probe in our application. Table 7.1 lists some parameters of Fluorinert liquid FC-72.

Table 7.1 Some parameters of Fluorinert liquid FC-72

Liquid	Boiling Point	Liquid Density	Kinematic Viscosity	Surface energy	Refractive Index
FC-72	56 ℃	1680 kg/m^3	0.38 cSt	12 mJ/m^2	1.251

Furthermore, the low surface energy of Fluorinert liquid FC-72 is another great property when using it as the inserted liquid to measure the microgroove. The measurement principle of Section 7.1.1 is based on the assumption that the droplet can contact the whole surface, including the bottom of the microgroove. Hence, the wetting ability of the applied liquid should be considered. Fluorinert liquid FC-72, whose surface energy ($\gamma = 12$ mJ/m^2) is the lowest known, has never been observed to bead up or even roll off on any surface [145]. No natural or man-made surface has been reported to repel liquids of extremely low surface

tension or energy (i.e., $\gamma < 15$ mJ/m^2). Therefore, Fluorinert liquid FC-72 completely wet the existing materials. In our previous work [146][147], the contact angle between a bare silicon wafer and Fluorinert liquid FC-72 is 6 °. Although, it is known that surface hydrophobicity is enhanced by surface roughness. According to according to the Wenzel model [148], the contact angle (β') at a rough surface is

$$\cos \beta' = r \cos \beta \qquad (7.5)$$

Where β is the contact angle of the droplet on a flat surface with same material. r is a roughness factor, defined as the ratio of the actual area of the solid surface to the geometric projected area. In the case of the microgroove structure, there is an extremely large contact area between the solid surface and liquid surface, then the roughness factor r is very small and close to 1 [149]. Considering the superior wetting ability of Fluorinert liquid FC-72 and the small roughness factor of the microgroove structure synthetically, the droplet enables a contact with the whole surface, including the bottom of the microgroove.

7.2 One-shot interferometry based on the Fourier Transform method

7.2.1 Principle and algorithm

Due to the dynamic property of liquid, the phase map under the droplet condition requires a high temporal resolution. Especially, since Fluorinert liquid FC-72 evaporates completely within a few seconds, the phase map under the droplet condition cannot be obtained by the phase shift method, in which multiple recordings are required for retrieving a single phase map. In this section, one-shot interferometry based on the Fourier transform method [150] is introduced to obtain the phase information with high temporal resolution.

One-shot interferometry based on the Fourier transform method is one of the spatial carrier interferometry [151][152][153][154], in which carrier fringes are introduced by tilting the reference mirror, as shown in Fig. 7.2. For a given sample, the intensity distribution ($g(x)$) under the spatial carrier interferometry across either the x or the y axis has the form of

$$g(x) = I_s(x) + I_r(x) + 2\sqrt{I_s(x)I_r(x)} \cos[2\pi f_0 x + \varphi(x)] \qquad (7.6)$$
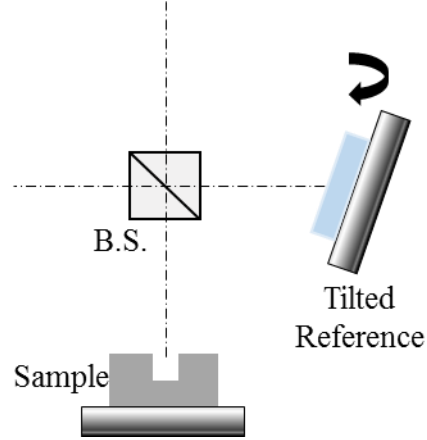
Figure 7.2 Schematic of spatial carrier interferometry

Where $I_s(x)$ and $I_r(x)$ are the intensity distributions from the sample and the reference, respectively. $\varphi(x)$ is the phase distribution to be measured. f_0 is the frequency of spatial carrier fringes. By using Euler's formula, Eq. (7.6) can be rewritten as

$$g(x) = a(x) + b(x)\exp(2\pi i f_0 x) + b^*(x)\exp(-2\pi i f_0 x)$$
$$a(x) = I_s(x) + I_r(x) \tag{7.7}$$
$$b(x) = \sqrt{I_s(x)I_r(x)}\,\exp\left[i\varphi(x)\right]$$

Where $*$ denotes a complex conjugate.

Then, the Fourier transform of Eq. (7.7) with respect to x is given by

$$G(f) = A(f) + B(f - f_0) + B^*(f - f_0) \tag{7.8}$$

Where the capital letters denote the Fourier spectrum and f is the spatial frequency in the x direction. Because the spatial variations of $I_s(x)$, $I_r(x)$ and $\varphi(x)$ are slow compared with the spatial frequency f_0, the Fourier spectrum in Eq. (7.8) are separated by the carrier frequency f_0, as a schematic shown in Fig 7.3(a). Either of the two spectrums by the carrier fringes, $B(f-f_0)$ or $B^*(f+f_0)$, can be exploited for post processing. Take $B(f-f_0)$ as an example. $B(f-f_0)$ can be translated by f_0 toward the origin of the Fourier spectrum to obtain $B(f)$, as depicted in Fig. 3(b). Simultaneously, the unwanted background variation $a(x)$ is filtered out.
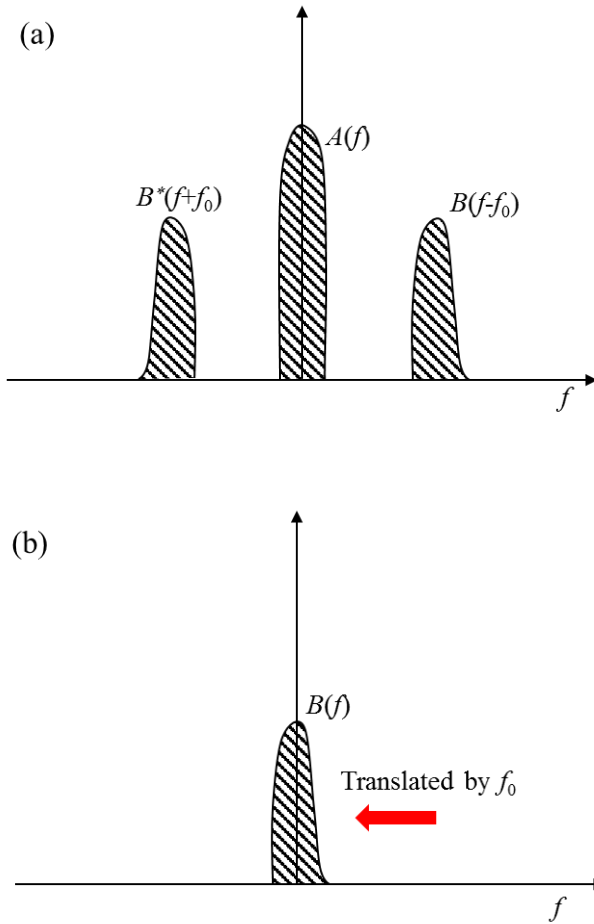
Figure 7.3 Schematic of one-shot interferometry based on the Fourier transform method: (a) the separated components in the Fourier spectrum under the spatial carrier interferometry and (b) translating the selected spectrum to the origin.

Next, the inverse Fourier transform of $B(f)$ is calculated with respect to f, then $b(x)$ is obtained. Finally, using a complex logarithm, we can get

$$\log[b(x)] = \log\left[\sqrt{I_s(x)I_r(x)}\right] + i\varphi(x) \tag{7.9}$$

Therefore, the phase $\varphi(x)$ to be measured can be obtained from the imaginary part of Eq. (7.9), completely separated from the unwanted amplitude variation in the real part.

7.2.2 RCWA simulation of one-shot interferometry based on the Fourier transform method

Similar to the FDTD method, the Rigorous Coupled Wave Analysis (RCWA) method is a semi-analytical method in computational electromagnetics, typically applied to solve scattering from periodic dielectric structures [155][156][157]. The FDTD method is based on Yee Cell, thus the theoretical errors occur in the case of oblique incidence. However, the oblique incidence is required to get the spatial carrier fringes by one-shot interferometry based on the Fourier transform method. In order to ensure the accuracy of numerical analysis, the simulation based on the RCWA method were performed in this chapter.

Figure 7.4 shows a schematic of the models of RCWA simulation to analyze the feasibility of one-shot interferometry based on the Fourier transform method. Figure 7.4(a) denotes the sample model of a 1000-nm-wide and 140-nm-deep microgroove to be irradiated by vertically incident light, while the reference model of a flat surface is illuminated by 45° tilted light source in Fig. 7.4(b). The parameters of this RCWA simulation are listed in Table 7.2.
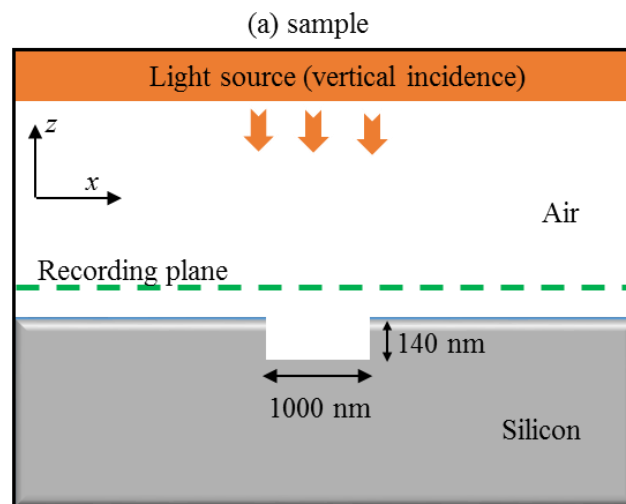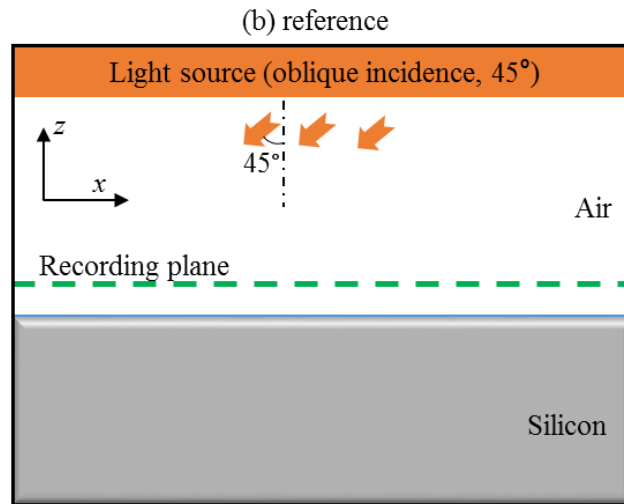
(a) sample

Figure 7.4 Models of RCWA simulation to analyze the feasibility of one-shot interferometry based on the Fourier transform method: (a) the sample model and (b) the reference model

Table 7.2 Parameters of RCWA simulation to analyze the feasibility of one-shot interferometry based on the Fourier transform method

Parameters	
Wavelength of incident beam	488 nm
Grid size	10 nm (x) × 10 nm (z)
Simulation region	10 μm (width) × 2 μm (height)
Near-field recording plane	20 nm above the top surface of microgroove
NA	0.55

Figure 7.5 plots the interferogram generated by the reflected lights from the two models, while the Fourier transform of this interferogram is presented in Fig. 7.6. It is found that the components in the Fourier spectrum are separated by the carrier frequency f_0, which is 1.44 lines/μm under the mentioned simulation conditions.
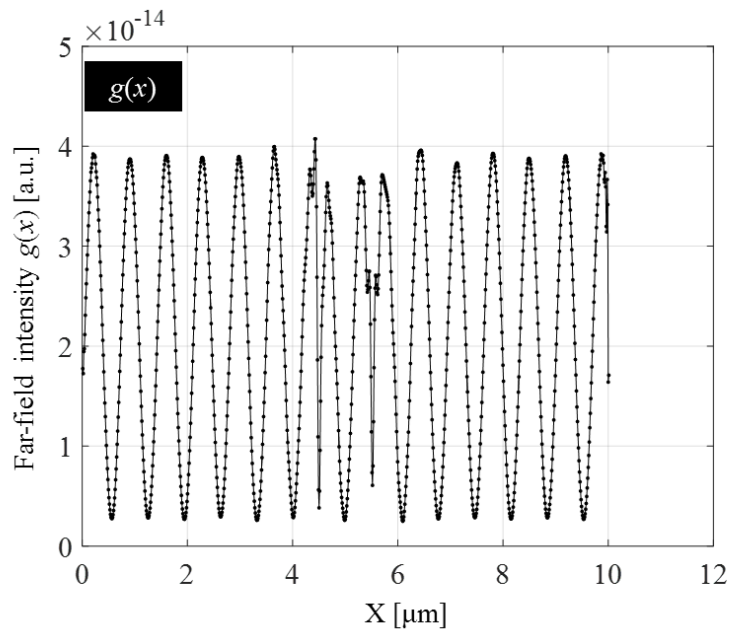
Figure 7.5 The interferogram generated by the reflected lights from the two models in Fig. 7.4.
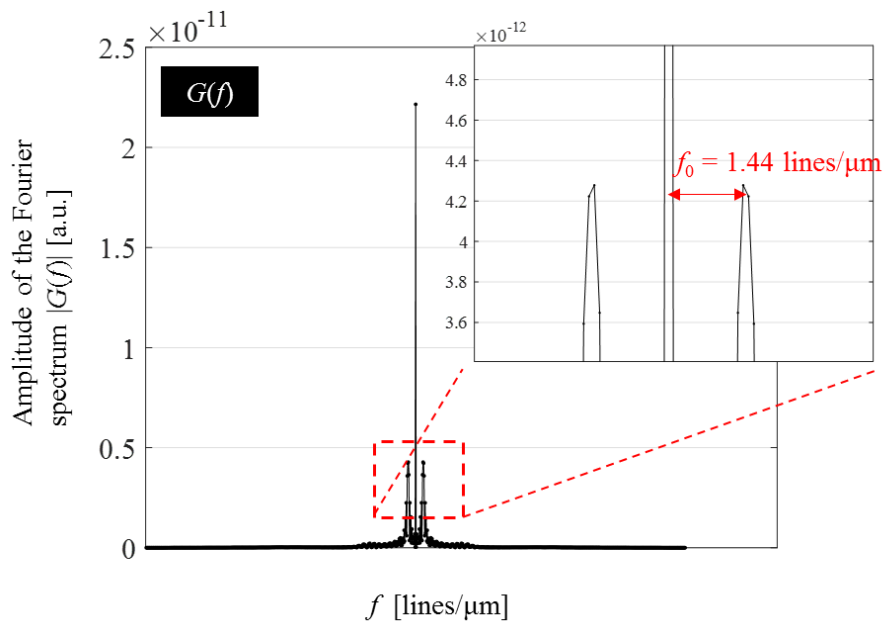
Figure 7.6 The Fourier transform of the interferogram in Fig. 7.5.

Then, one spectral sideband was selected and translated with $f_0 = 1.44$ lines/μm to the origin, as shown in Fig. 7.7.
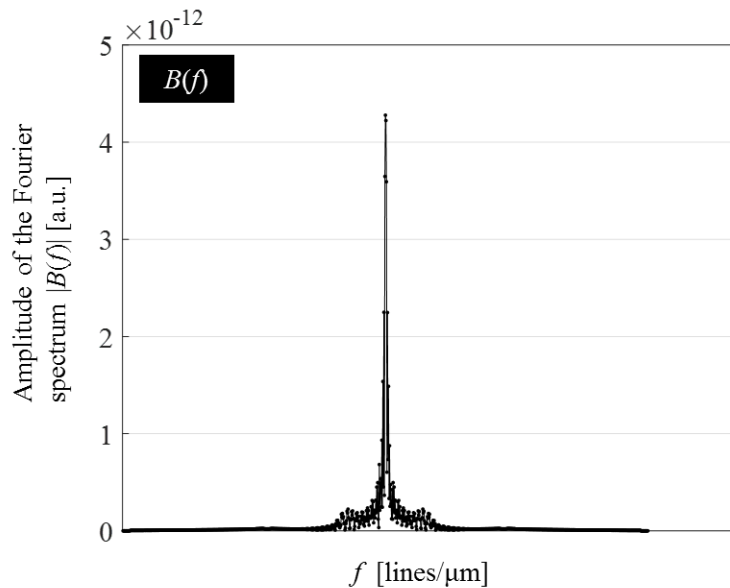
Figure 7.7 The Fourier spectrum of one selected sideband with a shift of f_0, B(f).

By calculating the inverse Fourier transform of Fig. 7.7, $b(x)$ is obtained. Then the complex logarithm of $b(x)$ is computed based on Eq. (7.9). The phase information can be obtained from the imaginary part, shown in Fig. 7.8. The phase difference between the top surface and the bottom surface at the central position of the microgroove is -2.60 rad.
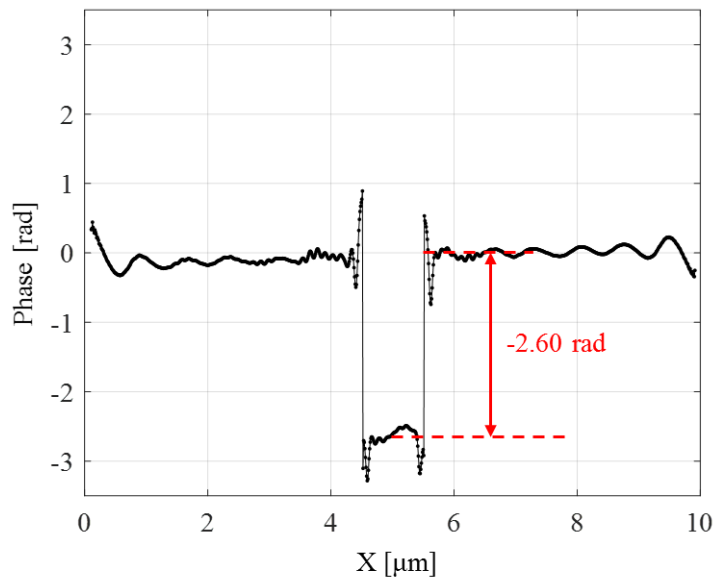
Figure 7.8 The phase map calculated by one-shot interferometry based on the Fourier transform method

As a contrast, the phase map of the same sample directly obtained by RCWA simulation is plotted in Fig. 7.9, from which the phase difference is -2.56 rad. The consistency between the two far-field phase differences (Figs 7.8 and 7.9) can be observed, which indicates the feasibility of one-shot interferometry based on the Fourier transform method. This method permits the retrieval of a full-field phase image from a single spatial interferogram. Compared with the phase shift method, one-shot interferometry based on the Fourier transform method has an extremely high temporal resolution, which is only limited in frame acquisition rate of the recording device in the practical measurement. Hence, the one-shot interferometry based on the Fourier transform method can be used to calculate the phase map under the droplet condition.
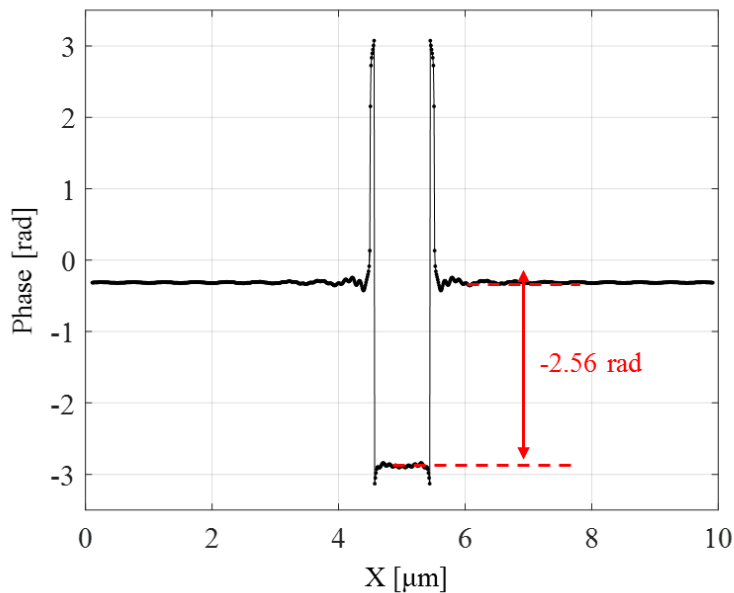
Figure 7.9 The phase map of the same sample directly obtained by RCWA simulation

7.3 Numerical analysis of the proposed phase unwrapping method

In this section, the numerical analysis of the proposed phase unwrapping method was performed to demonstrate its validity by a combination of the RCWA simulation and the Matlab process. Considering the applicability for practical measurement, an envisioned experimental setup to realize the proposed concept is shown in Fig. 7.10. The phase

measurement unit, indicated as the red dashed box, is the same with the measurement system based on low coherence illumination, introduced in the previous chapters. An auxiliary horizontal imaging system with high speed camera, denoted as the blue dashed box, is developed to observe the evaporation of Fluorinert liquid FC-72 and determine the distance between the gas-liquid interface and the top surface of the microgroove (Δh). In this horizontal imaging system, the light from a high power LED source is collimated by a convex-plane lens, then focused by an objective into the sample. The scattering light from the droplet can be collected by the high speed camera.
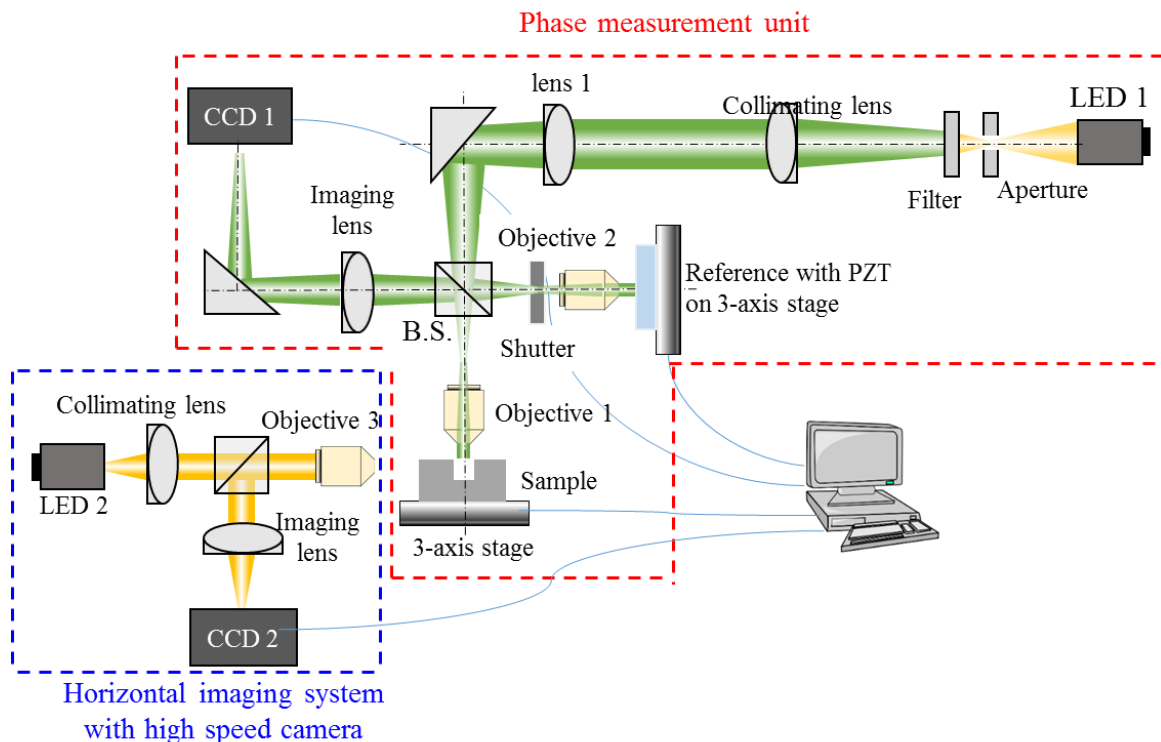
Figure 7.10 Schematic of the measurement system for the droplet-based phase unwrapping method with an auxiliary horizontal imaging system with high speed camera.

7.3.1 For diffraction-free microgrooves

Firstly, the validity of the proposed phase unwrapping method was analyzed in the case of diffraction-free microgrooves. Figure 7.11 shows the model of RCWA simulation for an

air condition and a droplet condition, respectively. Δh at the central position of the microgroove is set as 10 nm, and the refractive index of Fluorinert liquid FC-72 is 1.251. The reference model for generating spatial carrier fringes is the same with Fig. 7.4(b), using the obliquely incident beam with a tilted angle of 45°. Other parameters used for RCWA simulation and far-field imaging are listed in Table 7.3. Hence, the width (1000 nm) of the microgroove is larger than the diffraction limit (541 nm), and the depth (300 nm) to be measured is larger than half of incident wavelength (488 nm), which results in a phase ambiguity problem.
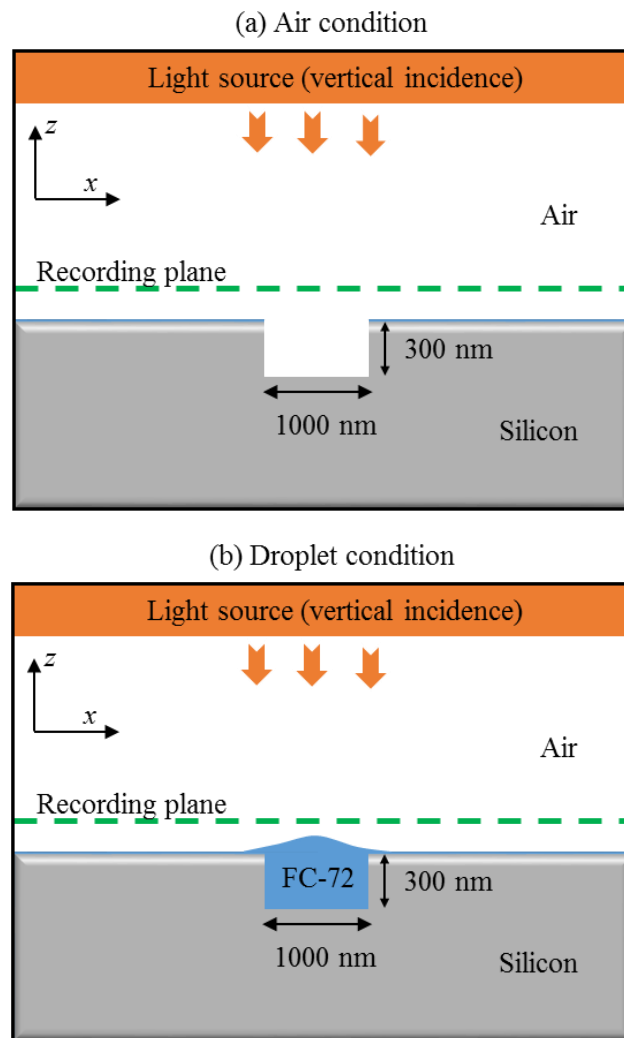
Figure 7.11 Models of RCWA simulation to analyze the feasibility of the proposed phase unwrapping method: (a) the air condition and (b) the droplet condition

Table 7.3 Other parameters used for RCWA simulation and far-field imaging in the case of diffraction-free microgroove

Parameters	
Wavelength of incident beam	488 nm
Grid size	5 nm (x) × 5 nm (z)
Simulation region	20 μm (width) × 2 μm (height)
Near-field recording plane	20 nm above the top surface of microgroove
NA	0.55

Figures 7.12 and 7.13 show the calculation processes for the phase maps by one-shot interferometry based on the Fourier transform method under the air condition and the droplet condition, respectively. In Fig. 7.12 or Fig. 7.13, (a) denotes the single interferogram ($g(x)$), (b) plots the Fourier spectrum ($G(f)$) of the interferogram, (c) shows the Fourier spectrum ($B(f)$) of one selected sideband with a shift of f_0, and (d) presents the calculated phase map. The phase differences between the top surface and the bottom surface at the central position of the microgroove are 1.25 rad for the air condition, and 3.15 rad for the droplet condition, respectively.
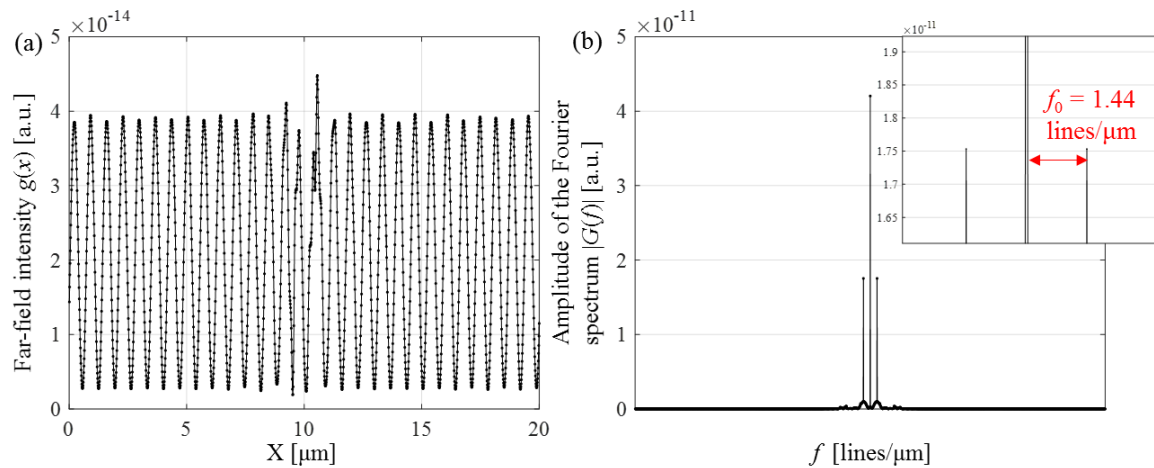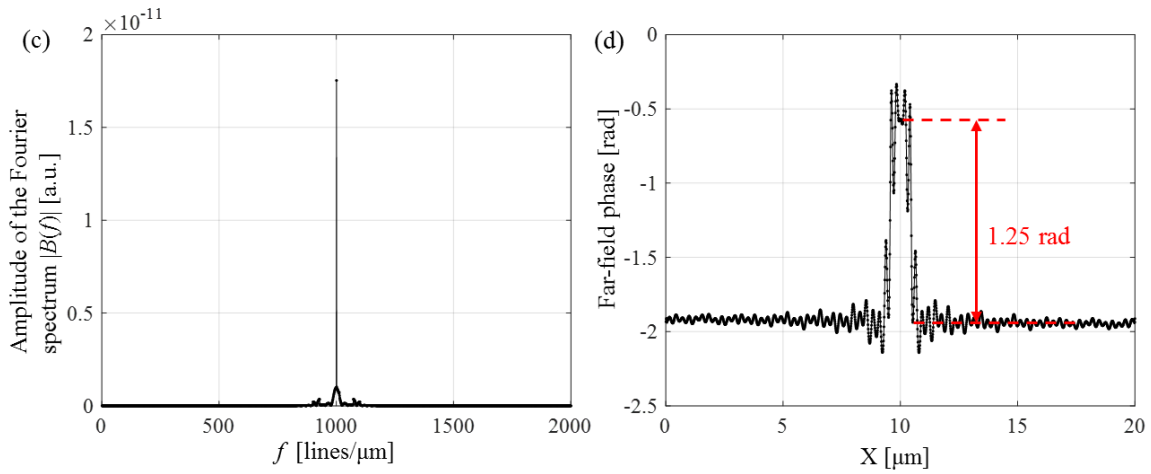
Figure 7.12 Calculation processes for the phase maps by one-shot interferometry based on the Fourier transform method under the air condition: (a) the single interferogram $g(x)$, (b) the Fourier spectrum $G(f)$ of the interferogram, (c) the Fourier spectrum $B(f)$ of one selected sideband with a shift of f_0, and (d) the calculated phase map.
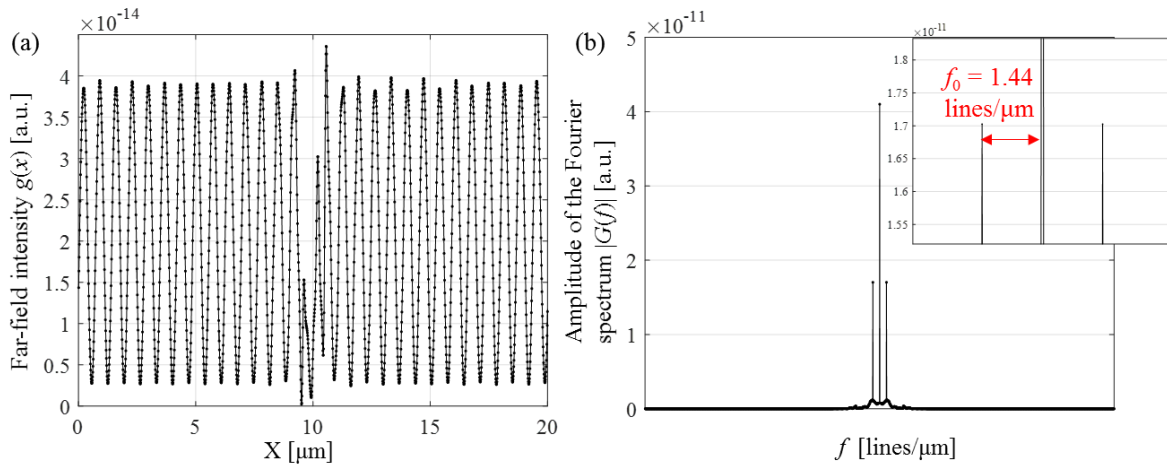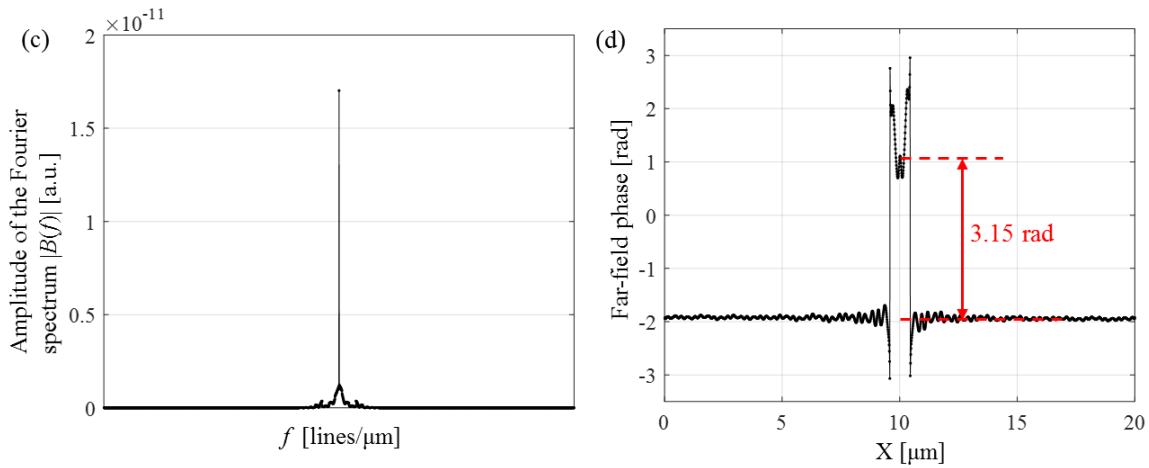
Figure 7.13 Calculation processes for the phase maps by one-shot interferometry based on the Fourier transform method under the droplet condition: (a) the single interferogram $g(x)$, (b) the Fourier spectrum $G(f)$ of the interferogram, (c) the Fourier spectrum $B(f)$ of one selected sideband with a shift of f_0, and (d) the calculated phase map.

Substituting the measured two phase differences into Eq. (7.4), the depth is calculated as 284 nm by the proposed phase unwrapping method using a Fluorinert droplet. The simulation results suggest that by the proposed droplet-based phase unwrapping method the depth of a 1000-nm-wide and 300-nm-deep microgroove can be measured, without the phase ambiguity problem, with an accuracy of 16 nm (5%), using the wavelength of 488 nm.

7.3.2 For diffraction-limited microgrooves

Then, in this section, the applicability of the droplet-based phase unwrapping method combined with FNRDM is discussed when measuring the diffraction-limited and high-aspect-ratio microgrooves. The width and depth of the simulated microgroove are both 300 nm, and other settings are the same with the parameters of analyzing the diffraction-free microgroove in last section. Hence, the width (400 nm) of the microgroove is smaller the diffraction limit (541 nm), and the depth (300 nm) to be measured is larger than half of incident wavelength (488 nm), which results in a phase ambiguity problem.

Under the air condition, Figures 7.14(a) shows the calculated far-field phase map by one-shot interferometry based on the Fourier transform method, while the calculation process for

computing the near-field phase difference by FNRDM is depicted in Fig. 14(b). The far-field phase difference ($\theta_{f,\,a}$) at the central position of the microgroove is 0.41 rad, while the near-filed difference ($\theta_{n,\,a}$) calculated by FNRDM is 1.05 rad.
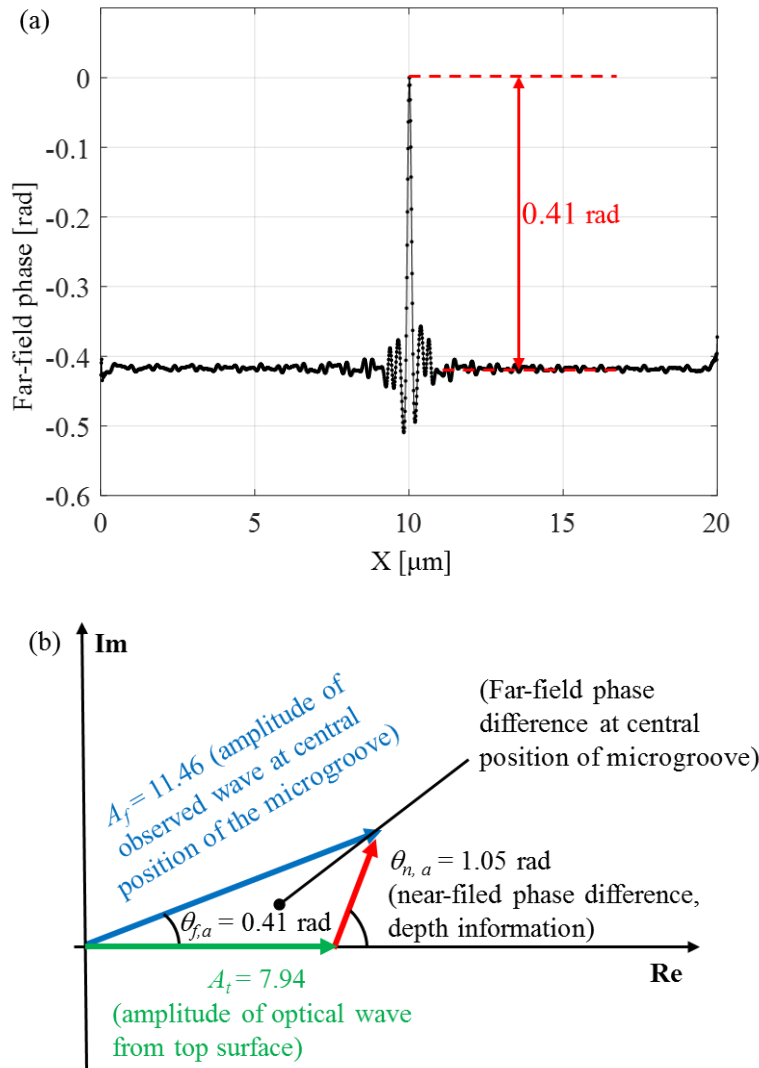
Figure 7.14 The calculation process under the air condition: (a) the calculated far-field phase map by one-shot interferometry based on the Fourier transform method, and (b) the calculation process for computing the near-field phase difference by FNRDM.

In the case of the droplet condition, when calculating the near-field phase difference by FNRDM, the contributions reflected from the gas-liquid interface should be considered, as shown in Fig. 15. Because the difference of the incident intensities between the top surface

of the microgroove and the gas-liquid interface is negligible, the ratio of the reflected intensities between the two surfaces is determined by the refractive indexes of the air, the liquid and the microgroove. Hence, and the amplitude from the top surface ($A_{t, l}$) under the droplet condition is giving by

$$A_{t,l} = \frac{A_u[\int_{\frac{w}{2}}^{+\infty} asf(x)dx + \int_0^{\frac{w}{2}} effe \times asf(x)dx]}{\int_{-\infty}^{+\infty} asf(x)dx}$$

$$effe = \frac{r_{al}}{r_{as}}$$

$$r_{al} = \frac{n_a - n_l}{n_a + n_l}$$

$$r_{as} = \frac{n_a - n_s}{n_a + n_s}$$

(7.10)

Where n_a, n_l and n_s are the refractive indexes of the air, the liquid and the microgroove, respectively. r_{al} and r_{as} are the amplitude reflection coefficient from the gas-liquid interface and the top surface of the microgroove, respectively. $effe$ denotes the ratio of the two amplitude reflection coefficients.

Far-field imaging system
gas-liquid interface
air
liquid

⬆: Optical wave from the top surface
⬆: Optical wave from the bottom surface
⬆: Optical wave from the gas-liquid interface
⬆: Far-filed observed optical wave
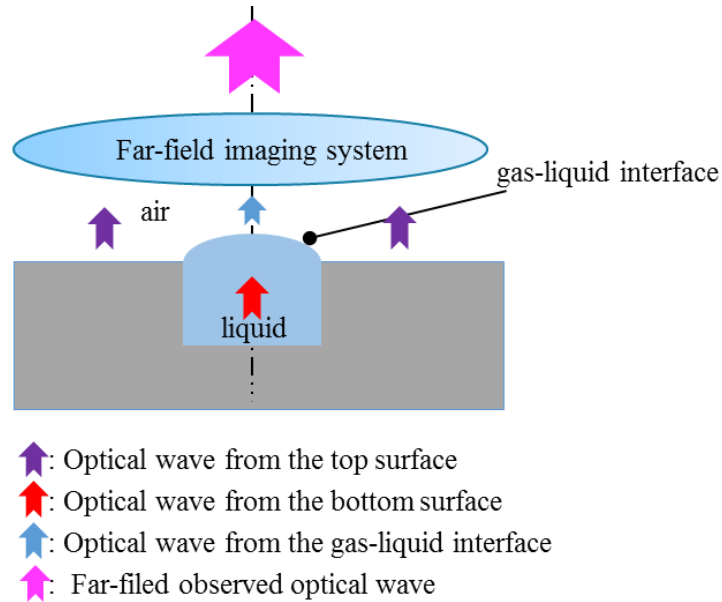
Figure 7.15 Contributions reflected from the gas-liquid interface under the droplet condition

Therefore, under the droplet condition, Figures 7.16(a) shows the calculated far-field phase map by one-shot interferometry based on the Fourier transform method, while the calculation process for computing the near-field phase difference by FNRDM is depicted in Fig. 16(b). The far-field phase difference ($\theta_{f,\ l}$) at the central position of the microgroove is 2.07 rad, while the near-filed difference ($\theta_{n,\ l}$) calculated by FNRDM is 2.90 rad.
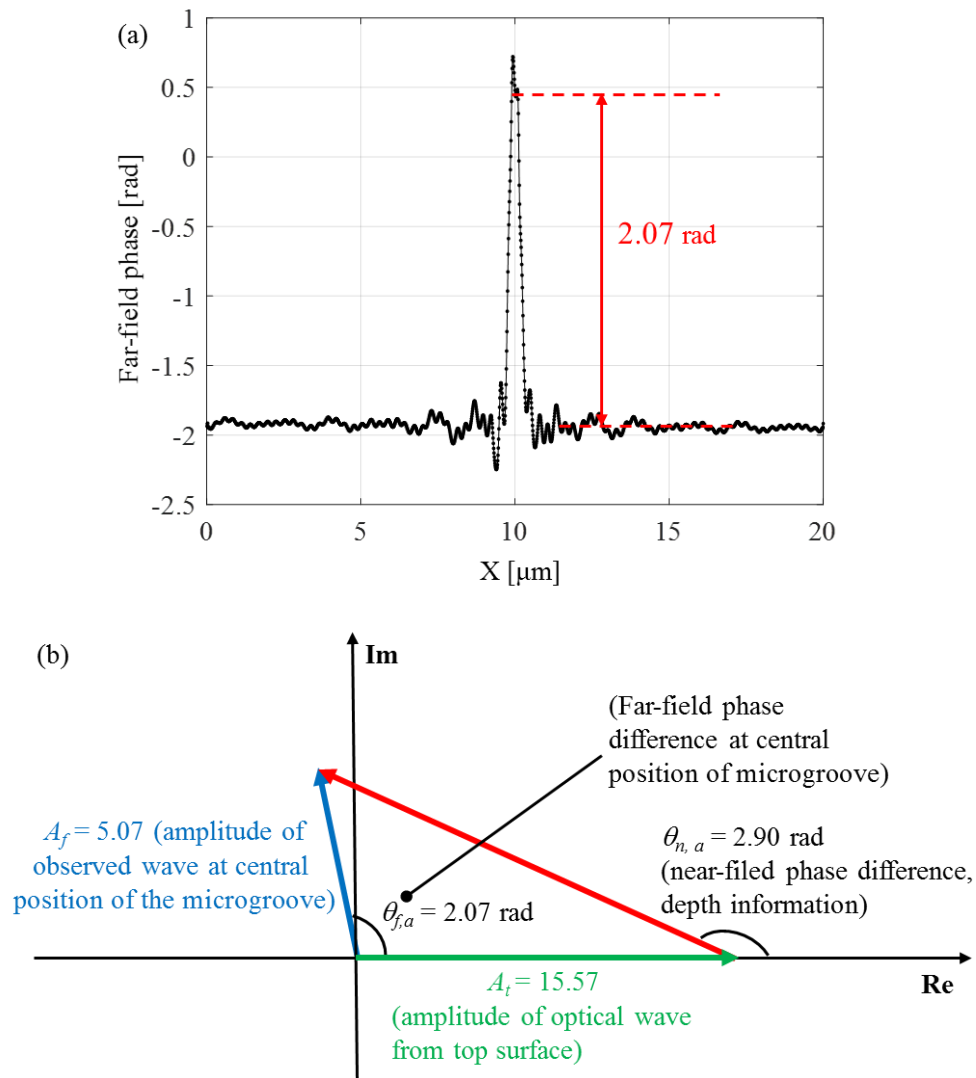
Figure 7.16 The calculation process under the droplet condition: (a) the calculated far-field phase map by one-shot interferometry based on the Fourier transform method, and (b) the calculation process for computing the near-field phase difference by FNRDM.

Substituting the measured two near-field phase differences into Eq. (7.4), the depth is calculated as 276 nm. The simulation results suggest that by the proposed droplet-based phase unwrapping method and the FNRDM method, the depth of a 300-nm-wide and 300-nm-deep microgroove can be quantitatively evaluated with an accuracy of 24 nm (8%), without the phase ambiguity problem, beyond the diffraction limit of 540 nm, using numerical aperture of 0.55 and the wavelength of 488 nm.

7.4 Conclusions

In this chapter, a novel method using a Fluorinert droplet was proposed to achieve the phase unwrapping when measuring the depths of steep microgrooves. This method includes the generation and combination of two phase maps under an air condition and a droplet condition. When the two phase maps are combined, the measured depths are equivalent to those measured by a longer wavelength based on the refractive index difference.

The applied liquid in this method is Fluorinert liquid FC-72, which is clear, colorless and fully-fluorinated. Like other Fluorinert electronic liquids, FC-72 is thermally and chemically stable, compatible with sensitive materials, nonflammable, practically nontoxic and leaves essentially no residue upon evaporation. Furthermore, the low surface energy of Fluorinert liquid FC-72 make it possible to contact with the whole surface, including the bottom of the microgroove. This unique combination of properties makes Fluorinert liquid FC-72 ideal as a contact liquid probe in our application.

In order to obtain the phase map under the droplet condition, one-shot interferometry based on the Fourier Transform method was used. Due to the dynamic property of liquid, the phase map under the droplet condition cannot be obtained by the phase shift method, in which multiple recordings are required for retrieving a single phase map. A numerical analysis based on the RCWA simulation was performed to demonstrate the validity of one-shot interferometry based on the Fourier Transform method.

Finally, the numerical analysis for both the diffraction-free and diffraction-limited microgrooves was implemented to verify the applicability of the droplet-based phase unwrapping method. In the case of the diffraction-free microgrooves, the simulation results

show that the droplet-based phase unwrapping method enables the depth evaluation of a 1000-nm-wide microgroove with an accuracy of 16 nm (5%), without the phase ambiguity problem, using the wavelength of 488 nm. In the case of the diffraction-limited microgrooves, the FNRDM was combined to calculate the near-field phase difference. The simulation results suggest that by the droplet-based phase unwrapping method and the FNRDM method, the depth of a 300-nm-wide microgroove, with an aspect-ratio of 1, can be quantitatively evaluated with an accuracy of 24 nm (8%), without the phase ambiguity problem, beyond the diffraction limit of 540 nm, using numerical aperture of 0.55 and the wavelength of 488 nm.

The proposed droplet-based method enables the phase unwrapping by using only single-wavelength illumination, has a high temporal resolution and requires significantly less computational work than other least-squares integration technologies.

Chapter 8. Numerical analysis of the practical applicability of FNRDM

In this chapter, a feasibility study for the practical applicability of FNRDM will be demonstrated. The practical applicabilities to be investigated include versatile microgrooves with different internal conditions, grating structure and microhole structure. The simulations based on the FDTD method are performed to demonstrate the validity of measuring the mentioned diffraction-limited microstructures by FNRDM.

8.1 Depth measurement of diffraction-limited microgrooves with versatile conditions

At the production site, the internal shape of the fine microgroove is not necessarily the ideal design shape, but there are the unknown deviations of the practically manufactured microgrooves. Therefore, in this section, the simulation analysis for the robustness of the proposed FNRDM method was implemented for versatile microgrooves.

Table 8.1 lists the basic parameters of the FDTD simulation and the settings for optical imaging system. Figure 8.1 shows the schematic of typical seven examples of microgrooves: two tapered structures (Fig. 8.1(b) and (c)), micro-roughness surfaces on the bottom (Fig. 8.1(d)) and on the wall (Fig. 8.1(e)), different materials (SiO$_2$; refractive index $n = 1.4631$) constituting the bottom substrate (Fig. 8.1(f)), a SiO$_2$ coating on the top surface (Fig. 8.1(g)), and the structure made from PMMA material (Fig. 8.1(h)). The width and depth of the standard microgroove are 200 nm and 300 nm (an aspect ratio = 1.5).

Table 8.1 Basic simulation settings for the verification of FNRDM

Parameters	
Wavelength of incident beam	488 nm
Grid size	5 nm (x) × 5 nm (z)
Simulation region	4 μm (width) × 2.5 μm (height)
Near-field recording plane	20 nm above the top surface of microgroove
NA	0.55
The diffraction limit	540 nm

(a) Standard microgroove
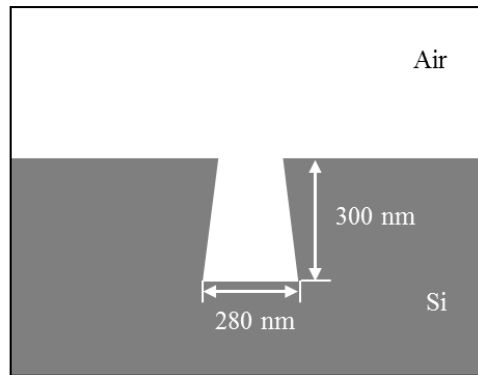
(b) Tapered structure 1
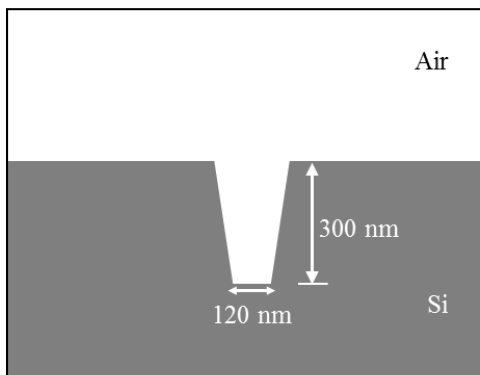
(c) Tapered structure 2
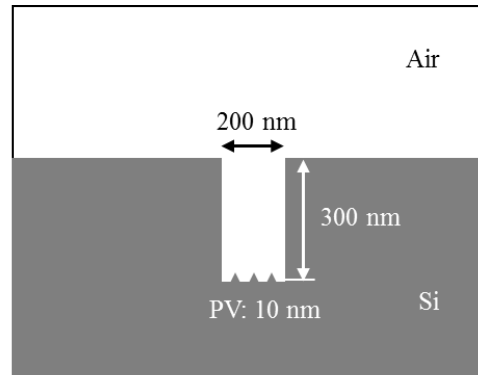
(d) Micro roughness on the bottom

(f) Micro roughness on the wall

(e) Different material constituting the bottom

(g) SiO2 coating on the top surface

(h) PMMA material
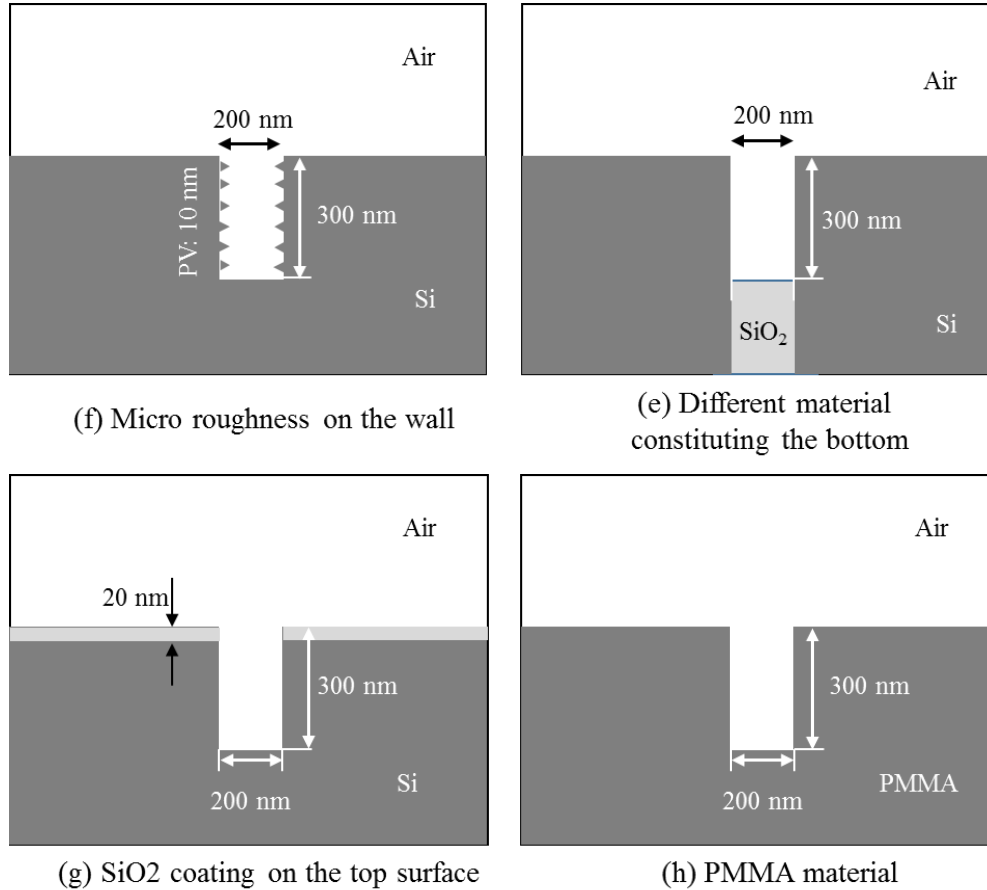
Figure 8.1 Schematic of typical examples of microgrooves: (a) a standard microgroove; (b) and (c) two tapered structures; (d) micro-roughness surfaces on the bottom surface; (e) micro-roughness surfaces on the wall; (f) different materials (SiO₂; refractive index *n* = 1.4631) constituting the bottom substrate; (g) a 20-nm-thick SiO₂ coating on the top surface and (h) the fine microgroove made from PMMA material (refractive index *n* = 1.49).

Table 8.2 shows the measurement results for the examined structures in the Fig. 8.1. It is found that the observed far-field amplitude from the microgroove (A_f) changes depending on the internal situations of the examined structures. However, for all those structures, the measured depths by the proposed FNRDM method have an accuracy of less than 10% error without being affected by the differences of such internal situations. These results suggest that we do not need a priori know about the reflection efficiency from the bottom surface of microgrooves, but can solve it as an unknown information, which is one of the important

measurement characteristics of the proposed FNRDM method. Therefore, even if there is a change in the amplitude of the optical wave from the bottom due to such differences of internal situations, as long as it is radiated to the far-field, FNRDM has the potential to evaluate the depth.

Table 8.2 The measurement results for the examined structures in the Fig. 8.1.

Types	(a)	(b)	(c)	(d)	(e)	(f)	(g)	(h)
Measured depths by conventional method using only θ_f [nm]	8.9	8.9	6.6	8.5	6.2	0.7	7.4	7.8
Observed far-field amplitude from the microgroove (A_f) [a.u.]	150.5	146.9	149.5	152.7	134.4	149.5	168.6	40.2
Calculated far-field phase difference by 4-step phase shift method (θ_f) [rad]	0.23	0.23	0.17	0.22	0.16	0.02	0.19	0.20
Calculated far-field amplitude from the top surface (A_t) [a.u.]	149.3	149.3	149.3	149.3	149.3	149.3	145.5	44.4
Measured depths by FNRDM [nm]	308	312	308	305	321	302	283	327

8.2 Depth measurement of diffraction-limited grating structures

Grating structures constituted by periodic microgrooves are widely applied in the semiconductor industry and diffraction gratings of optical elements. In order to extend the application of the proposed FNRDM method into the diffraction-limited grating structures, a further analysis was performed in this section. As shown in Fig. 8.2(b), when measuring the

grating structures by FNRDM, the contributions for the target microgroove (denoted by red dashed box) from the neighbouring microgrooves (denoted by green dashed boxes) should be considered. In the case of a single microgroove structure, the amplitude from the top surface (A_t) is calculated by Eq. (2.30), and the integral interval (blue diagonal box) is from half of the width to infinite due to the evaluation location of the central position of the microgroove, indicated in Fig. 8.2(a). Analogically, for the grating structures, the integral interval is decreased according to the pitch of the grating structure, and the amplitude from the top surface ($A_{t,g}$) is giving by

$$A_{t,g} = \frac{A_u \times \left(\int_{-\infty}^{+\infty} asf(x)dx - \int_{-w/2}^{+w/2} asf(x)dx - 2\sum_{n=1}^{+\infty} \int_{-w/2+pn}^{w/2+pn} asf(x)dx \right)}{\int_{-\infty}^{+\infty} asf(x)dx} \tag{8.1}$$
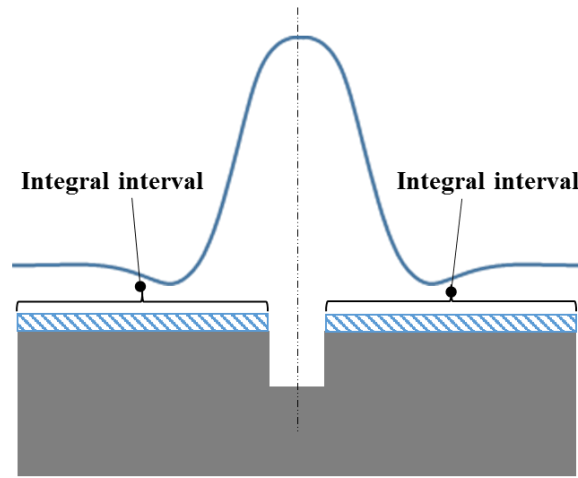
(a) A single microgroove structure
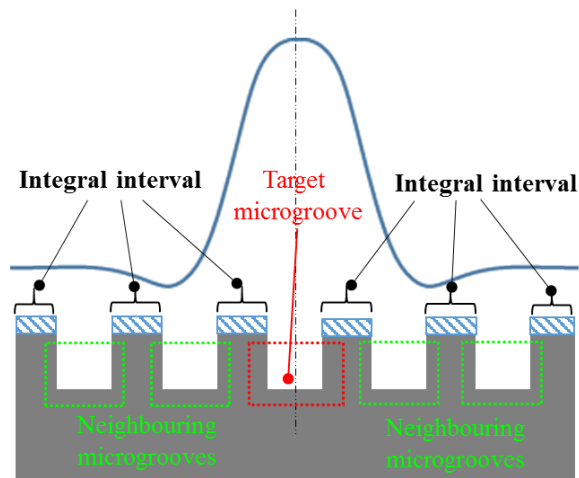
(b) A grating structure

Figure 8.2 Amplitude reflected from the top surface: (a) a single microgroove structure and (b) a grating structure.

Where w and p are the width of microgrooves and the pitch of grating. In the consideration of the practical application, the different grating structures with a same unit of 200-nm-wide and 100-nm-deep microgroove but different pitches are simulated. Figure 8.3 plots an example of the near-field amplitude distribution reflected from a 600-nm-pitch grating. And the fundamental simulation parameters are the same with Tab. 8.1 (NA = 0.55, diffraction limit = 540 nm). Figure 8.4 plots the amplitude spread function using imaging objective with numerical aperture of 0.55 and the wavelength of 488 nm in the simulation region.
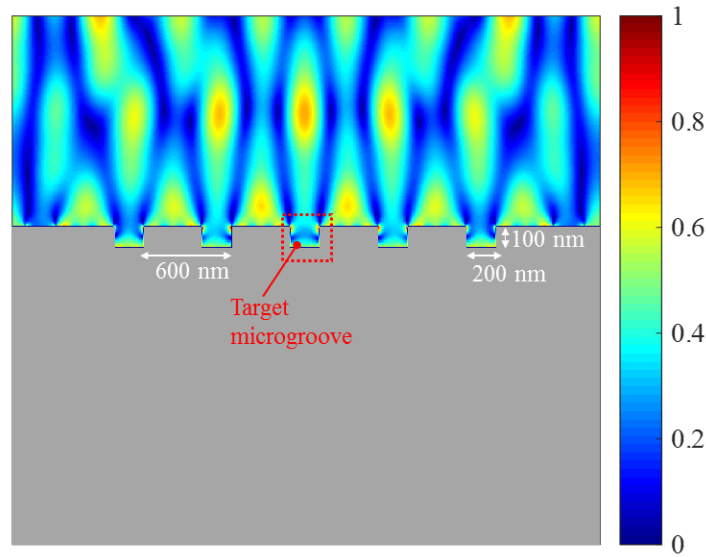
Figure 8.3 An example of the near-field amplitude distribution reflected from a grating structure (width = 200 nm, depth = 100 nm, pitch = 600 nm).
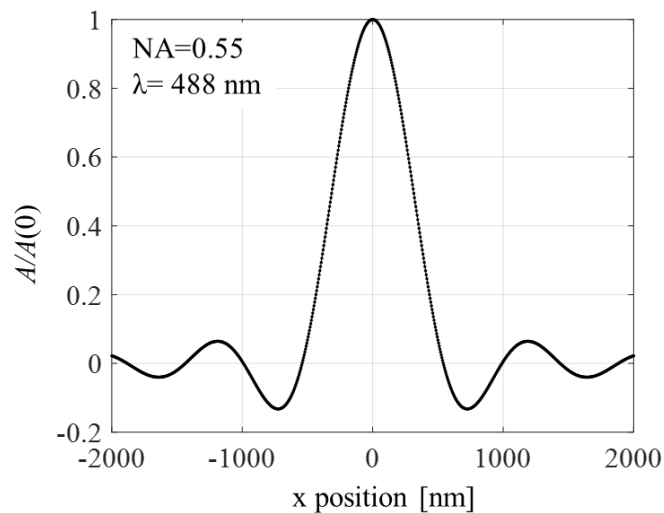
Figure 8.4 The amplitude spread function under the simulation settings.

Firstly, as the number of microgrooves increase, the measured depths by using two methods of computing the top surface reflection (A_t and $A_{t,\,g}$) were compared for 300-nm-pitch and 1000-nm-pitch. The results are plotted in Fig. 8.5. As the number of microgrooves increase, almost constant measurement errors between the two methods can be observed for 300-nm-pitch, and the measured depths by the two methods are almost the same for 1000-

nm-pitch. It is indicated that the influence for the top surface reflection in the grating structure mainly comes from the adjacent microgrooves, and is greatly affected by the pitch.
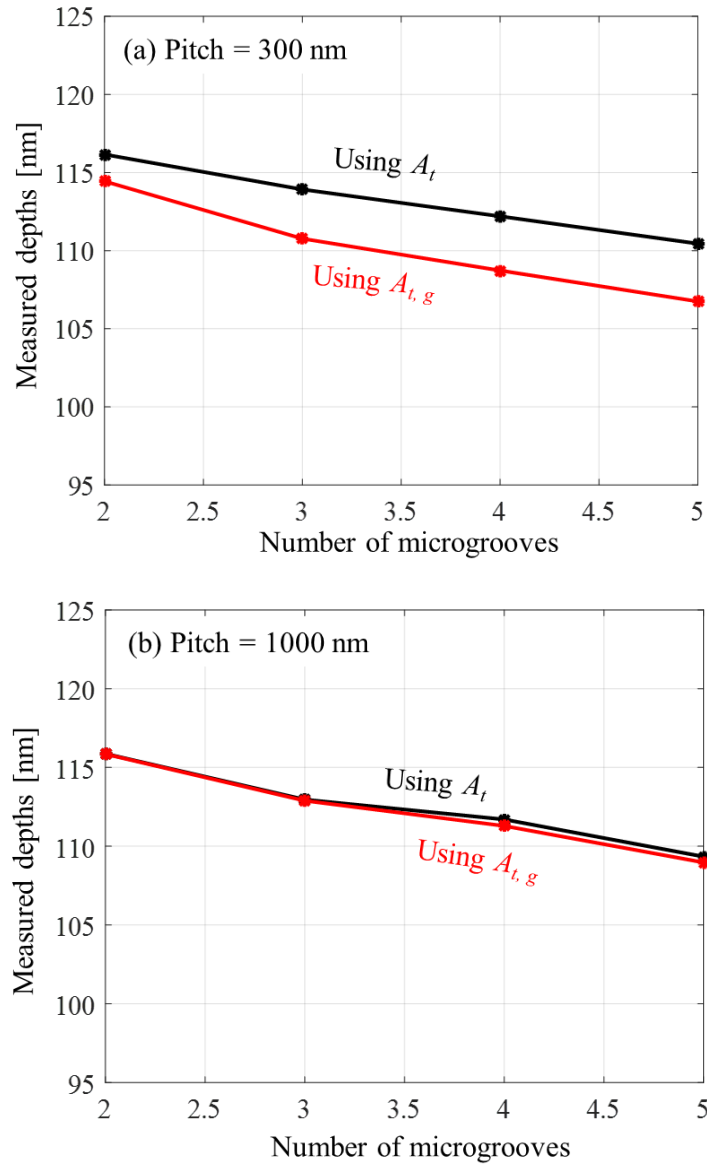
Figure 8.5 Measured depths by using A_t and $A_{t,g}$ as the number of microgrooves increase.

Then, in order to further analyze the influence of the pitch, the measured depths using A_t and $A_{t,g}$ are compared according to pitch variation. The simulated pitches vary from 300 nm to 1000 nm. There are some interesting results: (a) the average error for all the simulated gratings is 10 nm, while the accuracy of the measured depth from a single 200-nm-wide and

100-nm-deep microgroove is 8 nm (see Fig. 3.8). Thus, the proposed FNRDM method is feasible to quantitatively evaluate the diffraction-limited grating structures with high accuracy, as the results of an equally single microgroove. The discrepancy of the measured depths between a single microgroove and a grating structure can be explained by the scattering light from the neighbouring microgrooves. (b) When the simulated pitch exceeds the diffraction limit (540 nm), the measurement accuracies between the two calculation methods are almost the same. Because the amplitude ratio in the amplitude spread function (Fig 8.4) is rather small when there is a far distance to the central position, then $A_{t,g}$ is approximately equal to A_t. In other words, when the pitch of the grating structure is much larger than the diffraction limit of applied imaging system, each microgroove of the grating can be regarded as an isolated element, and the depth can be quantitatively evaluated as the case of an equally single microgroove.
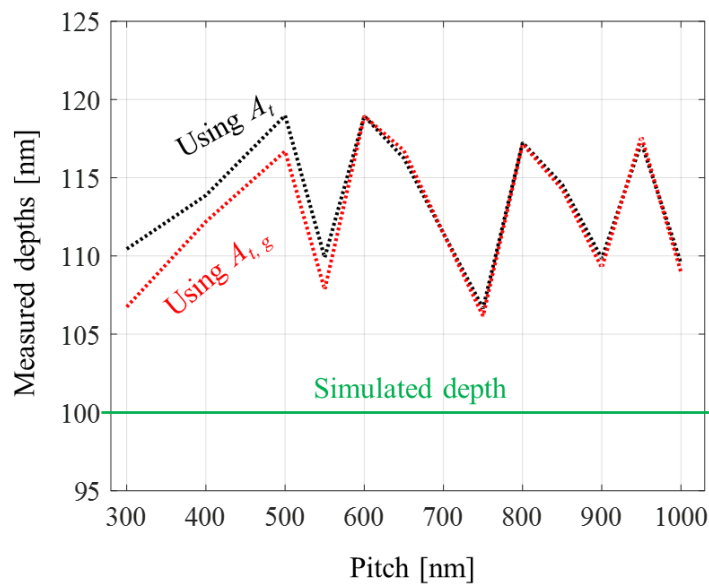
Figure 8.6 Measured depths by using A_t and $A_{t,g}$.

8.3 Depth measurement of diffraction-limited microholes

Microhole and nanohole structures have been used for a variety of applications, such as the superlenses produced by a metal nanohole array [158], the structured photovoltaic devices used to improve carrier extraction and light absorption [159], and photonic crystal

waveguides [21]. A microgroove structure has a rectangular opening which is long but narrow, while a microhole structure has a circular opening. In this section, the feasibility of the proposed FNRDM method in evaluating the diffraction-limited microhole was analyzed. Considering the shape differences of the openings between microgroove and microhole, the influence of two types of polarization was further discussed: (a) linear polarization and (b) circular polarization.

8.3.1 Circular polarization [63]

Each state of polarization can be split into two linearly polarized orthogonal components, in which one is oriented in the x direction and one in the y direction. If both components have equal amplitudes and the phase shift of the y component relative to the x component is $\pi/2$ or $-\pi/2$, the light is circularly polarized. When the phase shift is $-\pi/2$, the two orthogonal waves can be represented as

$$\begin{cases} E_x(z,t) = \vec{i}E_0 \cos(kz - wt) \\ E_y(z,t) = \vec{j}E_0 \sin(kz - wt) \end{cases} \tag{8.2}$$

Then the consequent circularly polarized wave is

$$E = E_0 \left[\vec{i} \cos(kz - wt) + \vec{j} \cos(kz - wt) \right] \tag{8.3}$$

Although the scalar amplitude (E_0) is a constant, the direction of E is time-varying. Figure 8.7 depicts what is happening at an arbitrary point z_0 on the axis. At $t = 0$, E lies along the reference axis in Fig. 8.7(a), and $E_x = iE_0\cos(kz_0)$ and $E_y = iE_0\sin(kz_0)$. At a later time, $t = kz_0/w$, $E_x = iE_0$, $E_y = 0$, and E is along the x-axis. Assuming $kz_0 = \pi/4$, Figure 8.7(b) plots the directions of E in different t. The resultant electric field vector E is rotating clockwise at an angular frequency of w, as seen by an observer toward whom the wave is moving (i.e., looking back at the source). Such a wave is so-called right-circularly polarized light. Similarly, in the case of left circular polarization with a phase shift of $\pi/2$, the amplitude is unaffected but E rotates counterclockwise.
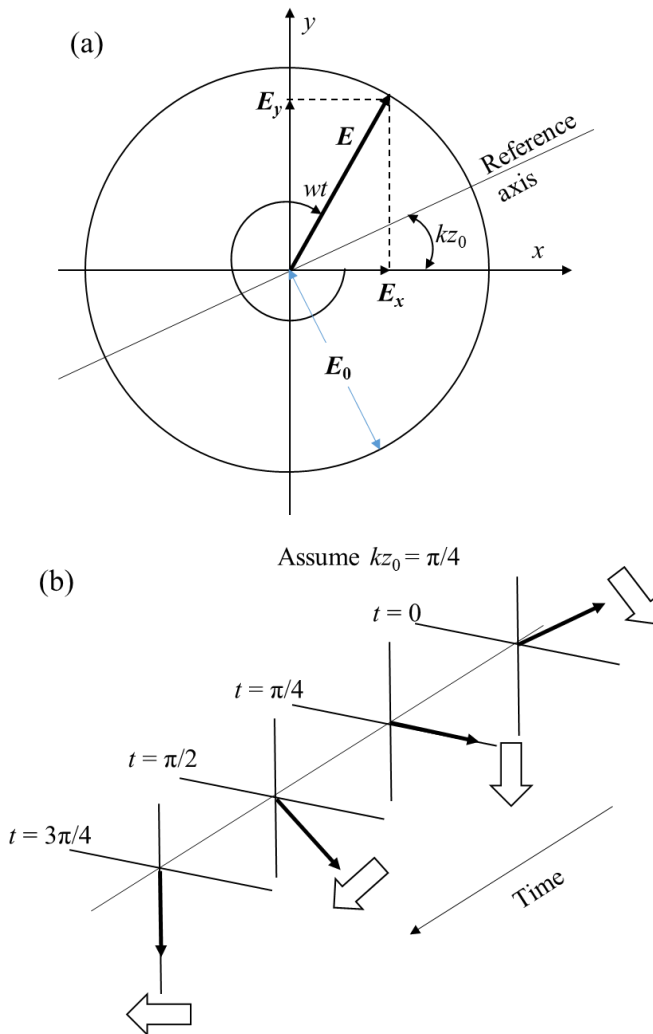
Figure 8.7 Rotation of the electric vector in a right-circular wave. Note that the rotation rate is ω and $kz_0 = \pi/4$.

8.3.2 Simulation analysis

Figure 8.8 is the three-dimensional simulation model by the FDTD method, and the parameters used in this simulation are listed in Tab. 8.3. The diameter and the depth of the microhole are 200 nm and 300 nm, respectively. In order to reduce the storage memory and the simulation time, the simulation region is 2-μm-long, 2-μm-wide and 3-μm-high with the grid size of $10 \times 10 \times 10$ nm^3. The optical imaging system has a *NA* of 0.95, and the diffraction limit is 313 nm. Two types of polarization are analyzed: (a) linear polarization: the

polarization direction of incident electric wave is along *x* axis; and (b) left circular polarization.
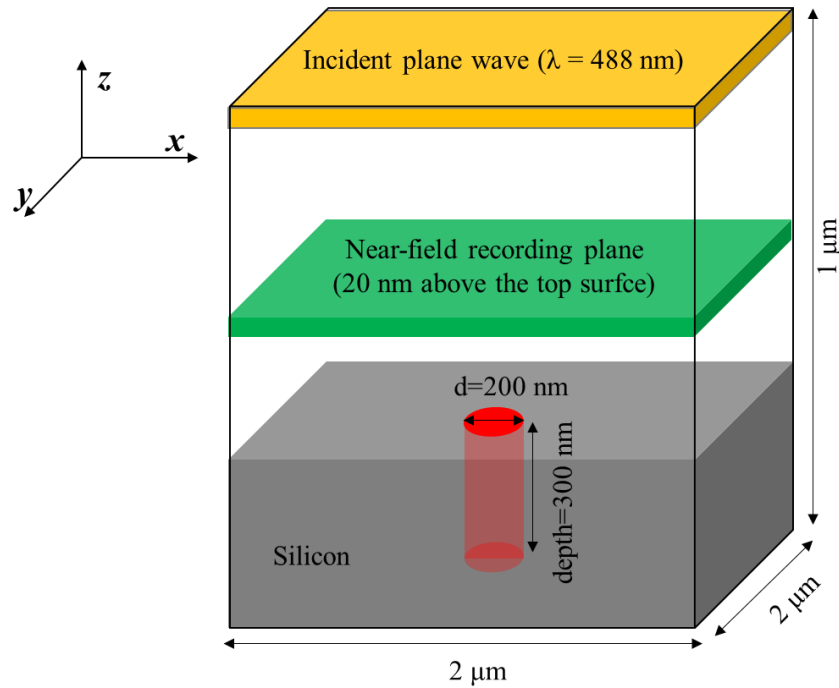
Figure 8.8 Schematic of a three-dimensional simulation model of microhole structure by the FDTD method.

Table 8.3 Basic simulation parameters for analyzing the microhole structure.

Parameters	
Wavelength of incident beam	488 nm
Grid size	10 nm (*x*) × 10 nm (*y*) × 10 nm (*z*)
Simulation region	2 μm (length) × 2 μm (width) × 1 μm (height)
Near-field recording plane	20 nm above the top surface of microgroove
NA	0.95
The diffraction limit	313 nm

Figure 8.9 shows the near-field amplitude distribution reflected from the microhole structure by linearly polarized incident beam (Fig. 8.9(a)) and circularly polarized incident beam (Fig. 8.9(b)). Compared to the results by the linear polarization, the imaging of the

opening of the microhole is much close to a circle by circular polarization, which is an indicator of the superior performance in two-dimensional imaging of microhole structure by an illumination with circular polarization.
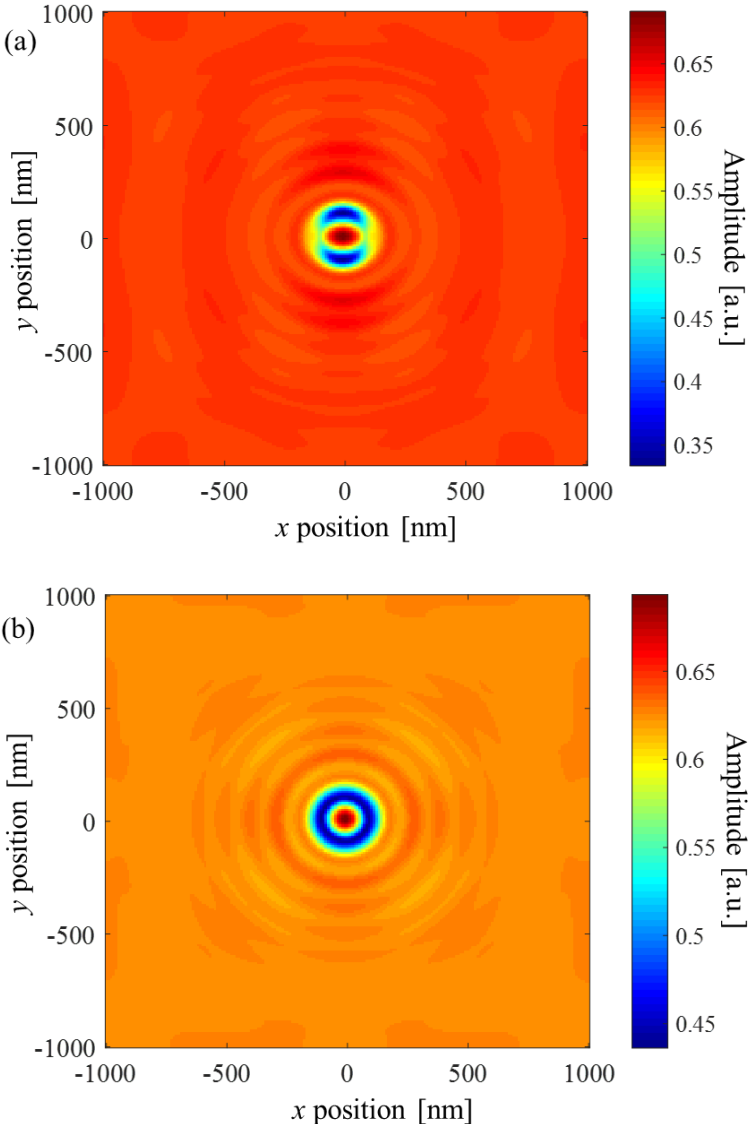
Figure 8.9 The near-field amplitude distribution reflected from the microhole structure by (a) linearly polarized incident beam and (b) circularly polarized incident beam

Then, the simulations of 4-step phase shift were performed to obtain the phase information of the microhole structure. Figure 8.10 is the far-field phase distribution by linearly polarized incident beam, while the results by circular polarization are plotted in Fig. 8.11. Similar to

the results of amplitude distribution in Fig. 8.9, the phase deviations exist between the two orthogonal cross-sections by linear polarization (Fig. 8.10(b)), while the two phase distributions coincide well with each other in the case of circular polarization (Fig. 8.11(b)). However, by the proposed FNRDM method, we also evaluate the depths of the diffraction-limited microhole by an effective depth at the central position of microgroove, rather than the depth distribution along the overall opening positions. Hence, the accuracies by using phase difference at the central position of microhole under the two types of polarization should be discussed further.
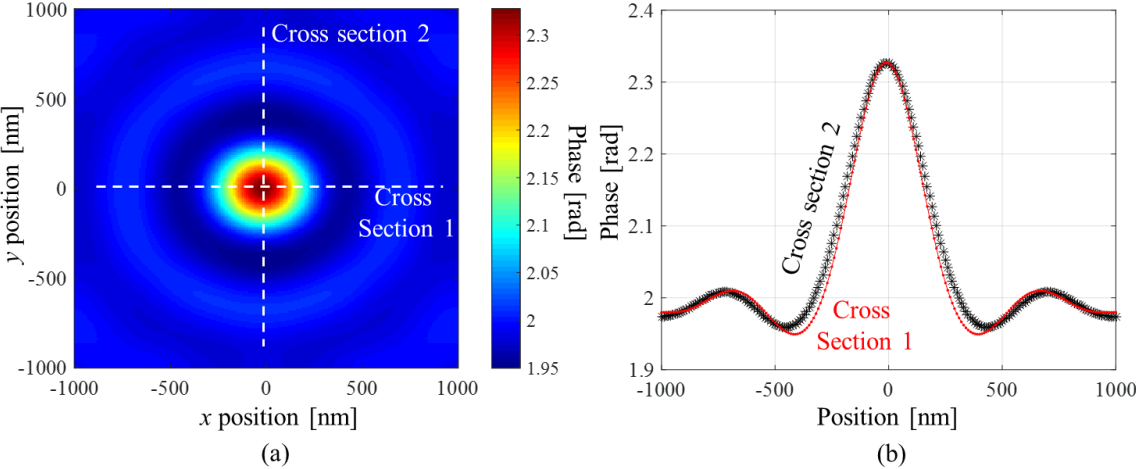
Figure 8.10 The far-field phase distribution reflected from the microhole structure by linearly polarized incident beam.
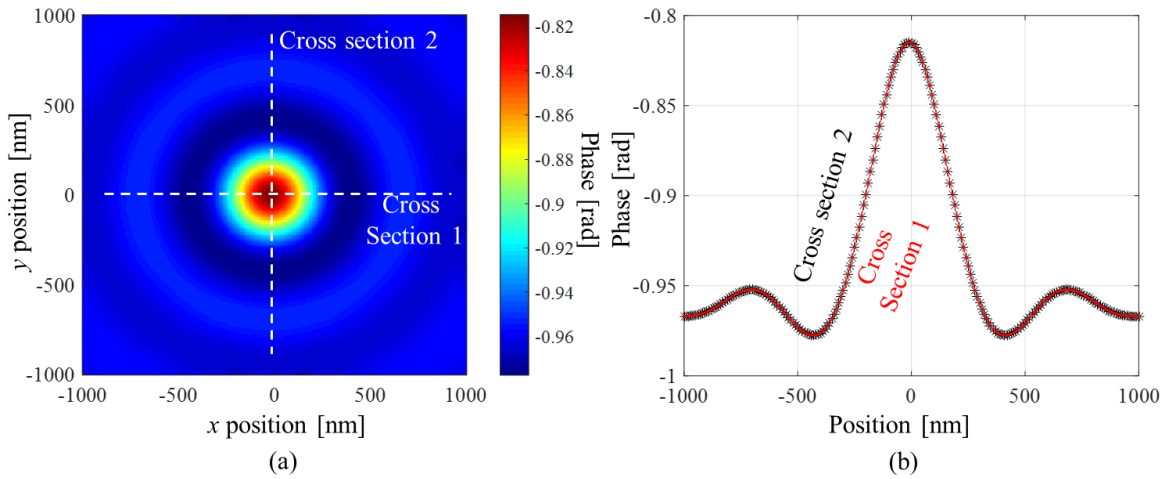
Figure 8.11 The far-field phase distribution reflected from the microhole structure by circularly polarized incident beam.

The measured depths using the phase difference at the central position of microhole are listed in Table 8.4. Using only the far-field phase differences by the two types of polarization, the depth of the microhole with a diameter of 200 nm cannot be quantitatively evaluated, when the diffraction limit of optical imaging system is 313 nm. By the proposed FNRDM method, the measurement errors are 10 nm and 30 nm under linear polarization and circular polarization, respectively. Hence, by the proposed FNRDM method, the measured depth of the diffraction limited microhole has a higher accuracy when the linear polarization applied.

Table 8.4 measured depths at the central position of the diffraction-limited microhole

	Under linear polarization	Under circular polarization
Measured depths using far-field phase by conventional method [nm]	13	6
Measured depths by FNRDM [nm]	290	270

The improved accuracy by linear polarization can be explained by the influence of scattering light. It is assumed that, under the same irradiation, the phase information under circular polarization suffers more influence from the edges of the microhole. In order to prove

this assumption, another simulation for the same microhole (diameter = 200 nm, depth = 300 nm) was performed by Matlab. The steps are as followings: (a) the near-field complex distributions are generated without scattering light. According to Eq. (8.2), the complex electric fields under circular polarization in the simulation can be given

$$
\begin{cases}
E_x = E_0 \exp(\alpha) \\
E_y = E_0 \exp(\alpha + \dfrac{\pi}{2})
\end{cases}
\tag{8.4}
$$

Considering the reflectivity difference and optical path difference between the top surface and the bottom surface, E_0 and α are set in the Table 8.5. d is the diameter of the microhole, and the applied wavelength is 488 nm. With these settings, the near-field intensity distribution under circular polarization is shown in the Fig. 8.12(a). (b) Then, by the optical imaging theory and the four-step phase shift method, the far-field phase distribution can be obtained, depicted in Fig. 8.12(b). The applied numerical aperture is 0.95, which is the same with aforementioned FDTD simulation analysis. (c) Following the steps (a) and (b), the near-field intensity distribution and far-field phase distribution without scattering light under linearly polarization are plotted in Fig. 8.13. It is found that the far-field phase differences at the central position of the microhole are both 0.45 rad under the two types of polarization without the scattering light, which indicates that the scattering light in case of the circular polarization leads to a larger measurement error of depth evaluation.

Table 8.5 Parameters of E_0 and α to generate the near-field distribution under circular polarization without scattering light by Matlab.

	E_0	α
Top surface	$\sqrt{\dfrac{1}{2}}$	$\dfrac{\pi}{4}$
Bottom surface	$\sqrt{\dfrac{2}{5}}$	$\dfrac{\pi}{4} + \dfrac{4\pi d}{\lambda}$
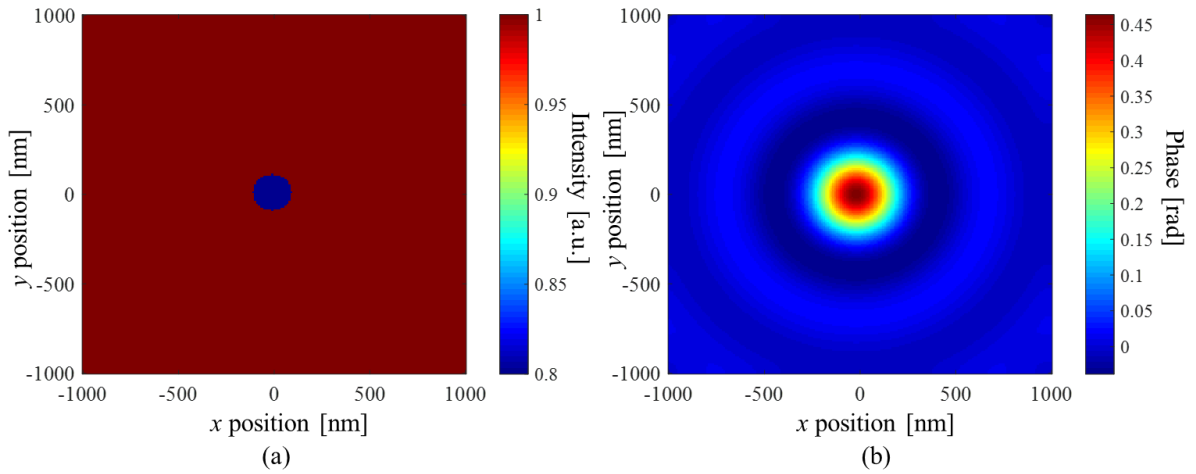
Figure 8.12 The generated distribution under circular polarization without scattering light: (a) near-field intensity distribution and (b) far-field phase distribution.
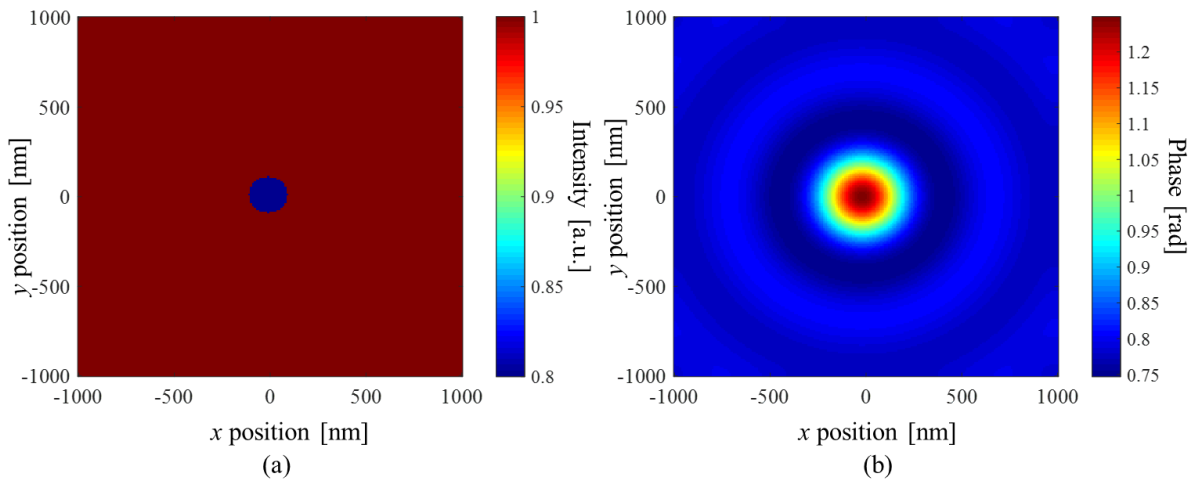
Figure 8.13 The generated distribution under linear polarization without scattering light: (a) near-field intensity distribution and (b) far-field phase distribution.

When measuring the diffraction-limited microhole structure, using circularly polarized illumination can enhance the roundness of the imaging of the circular opening. However, because of the influence of the scattering light, the measured depth by the proposed FNRDM method has a smaller error under linear polarization. The simulation results suggest that, under linear polarization, the proposed FNRDM method can evaluate the depth of a

microhole with 200-nm in diameter and 300-nm in depth, with an accuracy of 10 nm (3%), beyond the diffraction limit of 313 nm.

8.4 Conclusions

In this chapter, we discussed the practical applicability of the proposed FNRDM method based on the FDTD simulations. Firstly, considering the production site, the versatile microgrooves with different conditions were analyzed to verify the robustness of the proposed FNRDM method, including tapered structure, micro roughness, coating condition and PMMA material. The results show that, for all simulated structures, the measured depths by FNRDM have an accuracy of less than 10% error without being affected by the differences of internal situations. Hence, as long as the optical wave from the bottom surface is radiated to the far-field, FNRDM has the potential to evaluate the depth. One of the important measurement characteristics of FNRDM is that we do not need a priori know about the reflection efficiency from the bottom surface of microgrooves, which can be solved as an unknown information.

Then, the feasibility of measuring diffraction-limited grating structure by FRDNM was analyzed. According to the pitch of grating structure, a modified equation for calculating the amplitude of the top surface was proposed, with which the depth of diffraction-limited grating structure can be quantitatively evaluated with an accuracy of approximately 10%. Furthermore, it is found that when the pitch of the grating structure is much larger than the diffraction limit of applied imaging system, each microgroove of the grating can be regarded as an isolated element, and the depth can be measured as the case of an equally single microgroove.

Finally, considering the shape differences of the openings between microgroove and microhole, the influence of two types of polarization was further discussed in the case of diffraction-limited microhole structure: linear polarization and circular polarization. Although using circular polarization can achieve the imaging of the opening of microhole with a better circular symmetry, the measured depth under the linear polarization has a higher accuracy. The simulation results suggest that, under linear polarization, the proposed

FNRDM method can evaluate the depth of a microhole with 200-nm in diameter and 300-nm in depth, with an accuracy of 10 nm (3%), beyond the diffraction limit of 313 nm.

The results indicate that the proposed FNRDM method not only can be applied to depth measurement of fine microgrooves, but also has a potential to evaluate the depth of kinds of diffraction-limited microstructures.

Chapter 9. Conclusions and future work

In this chapter, the work of this thesis is summarized and the important conclusions of each chapter are illustrated. Then, based on the investigation of this thesis, the future work is presented.

9.1 Conclusions

The main goal of the research in this thesis was to develop a novel optical depth measurement method, which (1) enables the quantitative evaluation of the diffraction-limited microgrooves, having an aspect-ratio of 1, on different materials, with an accuracy of 10%, (2) is capable of the individual difference evaluation of each microgroove, which is not possible with scatterometry, and (3) has a depth measurement range optically greater than half of the incident wavelength, without the phase ambiguity problem. In order to achieve this target, the FNRDM method and two phase unwrapping methods were presented, and a measurement system based on the low-coherence illumination was also developed. Not only the numerical analysis but also the experiments were implemented to demonstrate the feasibility of the proposed method. The conclusions of each chapter can be summarized as followings.

Chapter 1 provided an introduction to the functional microstructures concerning the functional properties, the miniaturization trend and the applications. Especially, on the surface of these functional microstructures, the microgroove is one of the essential micro-shape component and acts as the key functional element. The great demand for and the miniaturization trend of functional microstructures are driving the need of depth measurement in micro and nano scale with high accuracy. Then, an overview of the current approaches used in depth measurement was given, including stylus profilometry, SPM, cross-section SEM, optical metrologies. Optical interferometry is a promising method due to its high throughput, noninvasiveness, feasibility in individual difference evaluation, high axial resolution and the potential of in-process measurement. However, when the width of

microgrooves is fewer than the diffraction limit, optical interferometry cannot be exploited owing to the significant errors of the measured depths. These all motivated the developments made within the course of this work.

Chapter 2 gave a brief introduction about the theory of diffraction, Fourier Optics and near-field optics, to develop an understanding of the way optical systems process light to form images. Then, by the FDTD method, the near-field and far-field optical waves reflected from microgrooves were numerically analyzed. It is found that, for the diffraction-limited microgroove, the depth information can be accurately measured using the near-field phase difference. According to optical imaging theory, the forming mechanism of far-field optical waves from the diffraction-limited microgrooves was discussed, which clearly explains the inaccuracy of depth measurement of the diffraction-limited microgrooves by the conventional optical interferometry based on phase change. In order to solve this problem, a novel optical depth measurement method, called FNRDM, was proposed. FNRDM connects the depth information of diffraction-limited microgrooves with the near-field phase difference, which can be calculated from practical far-field optical observations rather than directly measured by specialized equipment, i.e., near-field scanning optical microscopy.

Chapter 3 presents the theoretical analysis based on the FDTD method to demonstrate the validity of FNRDM and discuss the detectable depth and the applicability under noise condition, when measuring the diffraction-limited microgrooves. There are some results: (1) the depth of a fine 200-nm-wide and 300-nm-deep microgroove can be measured by FNRDM, with an accuracy of 8 nm (3%) beyond the diffraction limit of 540 nm. (2) When the scattering light from the edges of microgrooves becomes the dominating contribution of the synthetically observed optical wave, FNRDM cannot be applied to evaluate the depth. It is found that, by FNRDM, the measurable aspect-ratios are 5 for the 200-nm-wide microgroove, 3 for the 100-nm-wide microgroove and 1 for 50-nm-wide microgroove, beyond the diffraction limit, by using the wavelength of 488 nm. (3) Under the noise condition, although the accuracy of depth measurement is greatly influenced by numerical aperture, both a 200-nm-wide microgroove with an aspect ratio of 1.5 and a 100-nm-wide microgroove with an aspect ratio of 2 can be quantitatively evaluated with less than 10% error by using imaging

objective with numerical aperture of 0.95 and the wavelength of 488 nm (the Rayleigh criterion = 313 nm).

Chapter 4 focused on the development of the measurement system. A measurement system based on low-coherence illumination was developed to inspect the required far-field observations of the proposed FNRDM method. Besides the feature of low-coherence illumination, the designs of this measurement system also include an infinite corrected imaging system, a Linnik interferometer, an incident plane wave unit and an optical cage system. By comparing the height maps of a same flat surface on transparent polymer by a laser-based setup and the developed system based on low-coherence illumination, it is found that the spatial uniformity and accuracy of images by the low-coherence illumination are substantially better than the laser source. Finally, we analyzed the sensitivity of the developed measurement system based on low-coherence illumination. The measurement results suggest that this setup not only provides speckle-free images, but also allows for spatially sensitive optical path-length measurement (2.24 nm) and temporally sensitive optical path-length measurement (0.83nm).

Chapter 5 describes an experiment to verify the validity of the proposed FNRDM method. The nanochannels on a microfluidic sample (COC, nominal width = 300 nm, depth = 110 nm) were measured to verify the validity of the proposed FNRDM method. Both a AFM and the developed measurement system were used to measure this sample. There some experiment results: (1) the overall evaluation of measured depths of nanochannels in the same area are 67 nm by conventional interferometry, 107 nm by the proposed method and 114 nm by AFM measurement, respectively. (2) The same trend in depth variation of different nanochannels between the proposed method and AFM was confirmed. (3) The repeated experiments by the proposed method were performed, and the standard deviation is approximately 2 nm. According to the experiment results, our method has the advantages of greatly improved accuracy over conventional interferometry and enables the individual difference evaluation of each nanochannel, which is not possible with scatterometry. It is demonstrated that the proposed FNRDM method and the developed measurement system can

measure the depth of 300-nm-wide nanochannels beyond the diffraction limit (772 nm) with an accuracy of less than 10%.

Chapter 6 presented a noise-immune dual-wavelength interferometry to solve the phase ambiguity problem when the depth of microgroove is optically larger than half of the incident wavelength. The noise-immune dual-wavelength interferometry not only extends the depth measurement range, but also reduces the noise level to that in a single-wavelength phase map. Then, the measurement system based on the low-cohernece illumination was combined with a dual-wavelength interferometer unit (λ = 532 nm and 520 nm) to meet the requirements of practical measurements. Two experiments of measuring the gratings on different materials were performed. The experiment results showed that: (1) the 1000-nm-wide microgrooves, having an aspect-ratio of 1, with width less than the diffraction limit (1159 nm and 1132 nm) of develop measurement system on a silicon surface, can be quantitatively evaluated with an accuracy of less than 5% by the combination of the proposed FNRDM method and the noise-immune dual-wavelength interferometry. (2) The 700-nm-wide microgrooves, having an aspect-ratio over 0.5, with width less than the diffraction limit (772 nm and 755 nm) of develop measurement system on transparent polymer surface, can be quantitatively evaluated with an accuracy of less than 10% by the combination of the proposed FNRDM method and the noise-immune dual-wavelength interferometry. The combination also has a potential of measuring the depth of diffraction-limited and steep microgrooves with high accuracy.

Chapter 7 proposed a novel method using a Fluorinert droplet to achieve the phase unwrapping. This method includes the generation and combination of two phase maps under an air condition and a droplet condition. When the two phase maps are combined, the measured depths are equivalent to those measured by a longer wavelength based on the refractive index difference. In order to achieve the droplet-based phase unwrapping method, a one-shot interferometry based on the Fourier Transform method, an auxiliary horizontal observation setup with high speed camera and a Fluorinert liquid with unique properties were presented. Based on the RCWA simulation, the numerical analysis for both the diffraction-free and diffraction-limited microgrooves was performed to verify the applicability of the droplet-based phase unwrapping method. In the case of the diffraction-free microgrooves,

the simulation results show that the droplet-based phase unwrapping method enables the depth evaluation of a 1000-nm-wide and 300-nm-deep microgroove with an accuracy of 16 nm (5%), without the phase ambiguity problem, using the wavelength of 488 nm. In the case of the diffraction-limited microgrooves, the FNRDM was combined to calculate the near-field phase difference. The simulation results suggest that by the droplet-based phase unwrapping method and the FNRDM method, the depth of a 300-nm-wide microgroove, with an aspect-ratio of 1, can be quantitatively evaluated with an accuracy of 24 nm (8%), without the phase ambiguity problem, beyond the diffraction limit of 540 nm, using numerical aperture of 0.55 and the wavelength of 488 nm. The proposed method enables the phase unwrapping by using only single-wavelength illumination, has a high temporal resolution and requires significantly less computational work than other least-squares integration technologies.

Chapter 8 discussed the practical applicability of FNRDM. The practical applicabilities to be investigated include versatile microgrooves with different internal conditions, grating structure and microhole structure. The simulation results by the FDTD method suggested: (1) Considering the production site, the internal shapes of versatile microgrooves were analyzed. The results suggest that as long as the optical wave from the bottom surface is radiated to the far-field, FNRDM has the potential to evaluate the depth information. (2) When using FNRDM to measure the depth of grating structure, a modified equation for calculating the amplitude of the top surface was proposed to ensure the measurement accuracy. Furthermore, it is found that when the pitch of the grating structure is much larger than the diffraction limit of applied imaging system, each microgroove of the grating can be regarded as an isolated element, and the depth can be measured as the case of an equally single microgroove. (3) When measuring microhole structure by FNRDM using linear polarization, the depth of a microhole with 200-nm in diameter and 300-nm in depth can be quantitatively evaluated, with an accuracy of 10 nm (3%), beyond the diffraction limit of 313 nm. All the results indicated that the proposed FNRDM method not only can be applied to depth measurement of fine microgrooves, but also has a potential to evaluate the depth of kinds of diffraction-limited microstructures.

The contribution of this Ph.D. thesis can be summarized as followings:

(a) Optical depth-measurement of diffraction-limited microstructures. As summarized in Chapter 1, it is difficult to obtain the depth information of diffraction-limited microstructures by optical methods based on phase change. The proposed FNRDM uses only far-field observations and achieves the depth-measurement accuracy less than 10%, which fills a gap in this research field. According to the experiment results from Chapter 5, our technology has the advantages of greatly improved accuracy over conventional interferometry and enables the individual difference evaluation of each nanochannel, which is not possible with scatterometry. It is demonstrated that the proposed FNRDM method and the developed measurement system can measure the depth of 300-nm-wide nanochannels beyond the diffraction limit (772 nm) with an accuracy of 8%.

(b) Optical depth-measurement of steep microstructures. When using optical depth-measurement methods based on phase change, the measured depth optically greater than half of the incident wavelength subjects to the phase measurement ambiguity. In this thesis, two solutions were provided: noise-immune dual-wavelength interferometry and droplet-based phase unwrapping method. The combination of FNRDM and the two solutions enables the depth evaluation of diffraction-limited and steep microstructures with high accuracy. The experiment results from Chapter 6 showed that: by the combination of the proposed FNRDM method and the noise-immune dual-wavelength interferometry, (1) the 1000-nm-wide microgrooves, having an aspect-ratio of 1, with width less than the diffraction limit (1159 nm and 1132 nm) of develop measurement system on a silicon surface, can be quantitatively evaluated with an accuracy of less than 5%; (2) the 700-nm-wide microgrooves, having an aspect-ratio over 0.5, with width less than the diffraction limit (772 nm and 755 nm) of develop measurement system on transparent polymer surface, can be quantitatively evaluated with an accuracy of less than 10%.

(c) Providing a reference for the development of optical depth-measurement system, especially inspecting the transparent microstructures. Measurement systems were developed to demonstrate the feasibility of the proposed method, including the plane wave incident unit in Linnik interferometry, the low-coherence illumination, optical cage system and dual-

wavelength unit. The developed measurement system not only provides speckle-free images, but also allows for nanometer scale accuracy in optical path-length measurement. Furthermore, the topography of transparent microstructures can be measured by the developed system with extremely low spatial noise. Hence, the design and development of optical depth-measurement system in this thesis provides useful information and experience in related fields, such as optical interferometry, topography measurement of transparent material and low-coherence illumination.

(d) A progress to some industrial fields and related research fields. Due to the clear merits of optical metrology and a dependence of only far-field observations, the proposed method has a high potential of in-process measurement. Hence, the work in this thesis has the potential to impact various industries where high-precision-microstructure mass production is crucial, such as semiconductors and microsystem techniques. Furthermore, our work brings a progress to optically three-dimensional imaging and motivates the studies in bio-inspired functional surfaces, precision engineering, medical and biochemical applications, etc.

However, the proposed FRNDM method is theoretically limited by the influence of the scattering light from the edges. When the scattering light from the edges of microgrooves becomes the dominating contribution of the synthetically observed optical wave on far-field plane, FNRDM cannot be applied to evaluate the depth. The analysis based on FDTD simulations suggested, by FNRDM, the measurable aspect-ratios are 5 for the 200-nm-wide microgroove, 3 for the 100-nm-wide microgroove and 1 for 50-nm-wide microgroove, beyond the diffraction limit, by using the wavelength of 488 nm. A method to weaken the scattering light needs to be investigated further and is our important future work.

9.2 Future work

Based on the measurements and analysis described in this thesis, the valuable future work is illustrated in the following contexts.

(1) Achieve the depth distribution along the overall opening positions of the diffraction-limited microgrooves, then reconstruct the 3D imaging with high resolution and accuracy. In

the proposed FNRDM method, we evaluated the depths of diffraction-limited microgroove by an effective depth at the central position of microgroove, rather than the depth distribution along the overall opening positions. There are two limiting factors: one is the theoretical error caused by the scattering light from the edges of microgrooves when measuring the depth distribution. Another is the requirement of measuring the far-filed parameters with high later resolution in practical experiments. In order to solve the problems, a method to weaken the scattering light needs to be investigated further, and Structured Illumination Microscopy (SIM) also can be considered to improve the lateral resolution of practical intensity images and phase maps.

(2) The numerical analysis was performed to discuss the detectable depth, the influence of the internal shapes and microhole structure when using the proposed FNRDM method. However, due to a lack of such samples, the manufacture of which is still difficult, the experimental investigation has not been implemented in this thesis. Hence, the practical measurements are required to further verify some of the simulation results.

(3) During the measurement processes by the developed setup based on the low-coherence illumination, the most difficult part lies in adjusting the visible interference fringes. Although the practical adjustments for reducing the OPD in our experiments were introduced in Section 5.3.2. In order to determine the best foci of the reference and the test sample, a new unit using the astigmatic method and quadrant photodiode detector can be supplemented into the measurement system.

(4) The droplet-based phase unwrapping method should be experimentally verified. The concept of the design of the auxiliary horizontal observation setup was proposed, however, it is still difficult to capture the weak scattering light of the droplet, let alone with a high evaporation speed. A light source with high power, a camera with high sampling rate and a heat-absorbing filter can be used to optimize the horizontal observation setup. The silicon and COC sample, used in Chapter 6, are the optional samples for verifying this droplet-based phase unwrapping method. Furthermore, the research based on the liquid probe is a valuable topic. There are two main reasons: (a) due to the multiple interference of thin film, the sensitivity can be enhanced when observing the microstructures by inserting a liquid probe

[146][147]. (b) When there is liquid layer between the microgroove and the imaging system, the scattering light from the edges of microgrooves might be decreased.

(5) Extending the measured objects from a fine microgroove, a microhole, grating structure and some microgrooves with different internal shapes, to an arbitrary microstructure, the opening of which is fewer than the diffraction limit. In order to achieve this target, the contribution of the amplitude from the top surface needs to be investigated, including the topography and material.

References

[1] CJ Evans and JB Bryan. "Structured", "Textured" or "Engineered" Surfaces. CIRP Annals - Manufacturing Technology 48(2): 541-556 (1999).

[2] K Autumn, YA Liang, ST Hsieh, et al. Adhesive Force of a Single Gecko Foot-Hair. Nature 405: 681-685 (2000).

[3] C Greiner, A del Campo and E Arzt. Adhesion of bioinspired micropatterned durfaces: effects of pillar radius, aspect ratio, and preload. Langmuir 23: 3495-3502 (2007).

[4] A Malshe, K Rajurkar, A Samant, et al. Bio-inspired functional surfaces for advanced applications. CIRP Annals - Manufacturing Technology 62: 607-628 (2013).

[5] M Lanzetta, MR Cutkosky. Shape Deposition manufacturing of biologically inspired hierarchical microstructures. CIRP Annals - Manufacturing Technology 57: 231-234 (2008).

[6] GN Levy, R Schindel, JP Kruth. Rapid manufacturing and rapid tooling with layer manufacturing (LM) technologies, state of the art and future perspectives. CIRP Annals - Manufacturing Technology 52: 589-609 (2003).

[7] RN Wenzel. Resistance of solid surfaces to wetting by water. American Dyestuff Reporter 25: 598-601 (1936).

[8] Z Yoshimitsu, A Nakajima, T Watanabe and K Hashimoto. Effects of surface structure on the hydrophobicity and sliding behavior of water droplets. Langmuir 18: 5818-5822 (2002).

[9] GY Bae, J Jang, YG Jeong, WS Lyoo, BG Min. Superhydrophobic PLA fabrics prepared by UV photo-grafting of hydrophobic silica particles possessing vinyl groups. Journal of Colloid and Interface Science 344: 584-587 (2010).

[10] X Zhang, F Shi, J Niu, Y Jiang, Z Wang. Superhydrophobic surfaces: from structural control to functional application. Journal of Materials Chemistry 18: 621-633 (2008).

[11] J Ou, B Perot, JP Rothstein. Laminar drag reduction in microchannels using ultrahydrophobic surfaces. Physics of Fluids 16: 4635-4643 (2004).

[12] VA Lifton, S Simon, RE Frahm. Reserve battery architecture based on superhydrophobic nanostructured surfaces. Bell Labs Technical Journal 10: 81-85 (2005).

[13] SJ Wilson, MC Hutley. The optical properties of 'Moth Eye' antireflection surfaces. Optica Acta 29(7): 993-1009 (1982).

[14] HK Raut, VA Ganesh, AS Nair, S Ramakrishna. Anti-reflective Coatings: A Critical In-depth Review. Energy & Environmental Science 4: 3779 (2011).

[15] RH Siddique, G Gomard, H Hölscher. The role of random nanostructures for the omnidirectional antireflection properties of the glasswing butterfly. Nature Communications 6: 6909 (2015).

[16] H Kikuta, Y Ohira, and K Iwata. Achromatic quarter-wave plates using the dispersion of form birefringence. Applied Optics 36(7): 1566-1572 (1997).

[17] E Popov, AL Fehrembach, Y Brule, et al. Two-dimensional grating for narrow-band filtering with large angular tolerances. Optics Express 24(13): 14974-14985 (2016).

[18] H Kikuta, H Toyota and W Yu. Optical elements with subwavelength structured surfaces. Optical Review 10(2): 63-73 (2003).

[19] RD Schaller, VM Agranovich, VI Klimov. High-efficiency carrier multiplication through direct photogeneration of multi-excitons via virtual single-exciton states. Nature Physics 1: 189-194 (2005).

[20] NM Gabor, Z Zhong, K Bosnick, et al. Extremely efficient multiple electron-hole pair generation in carbon nanotube photodiodes. Science 325: 1367-1371 (2009).

[21] KQ Peng, X Wang, L Li, et al. High-performance silicon nanohole solar vells. American Chemical Society 132(20): 6872-6873 (2009).

[22] BJ Kirby. Micro- and nanoscale fluid mechanics: transport in microfluidic devices. Cambridge University Press (2010).

[23] AJ Demello. Control and detection of chemical reactions in microfluidic systems. Nature 442: 394-402 (2006).

[24] KE Herold, A Rasooly. Lab-on-a-Chip Technology: Fabrication and Microfluidics. Caister Academic Press. ISBN: 978-1-904455-46-2 (2009).

[25] I Fernandez, A Laura Palmarelli, X Liang, et al. Fabrication of fluidic devices with 30nm nanochannels by direct imprinting. Journal of Vacuum Science & Technology B 29: 06F801 (2011).

[26] J Bico, U Thiele, D Quere. Wetting of textured surfaces. Colloids and Surfaces A 206 (1-3): 41-46 (2002).

[27] N Taniguchi. Current status in, and future trends of, ultraprecision machining and ultrafine materials processing. CIRP Annals - Manufacturing Technology 32(2): 573-582 (1983).

[28] SK Tanu, DS Victor, SN Wan, et al. Fabrication of a gecko-like hierarchical fibril array using a bonded porous alumina template. Journal of Micromechanics and Microengineering: N75-N81 (2007).

[29] L Alting, F Kimura, HN Hansen, G Bisacco. Micro Engineering. CIRP Annals - Manufacturing Technology 52(2): 635-657 (2003).

[30] HN Hansen, RJ Hocken and G Tosello. Replication of micro and nano surface geometries. CIRP Annals - Manufacturing Technology 60: 695-714 (2011).

[31] YL Ho, A Portela, Y Lee, E Maeda, H Tabata, JJ Delaunay. Hollow plasmonic U-cavites with high-aspect-ratio nanofins sustaining strong optical vortices for light trapping and sensing. Advanced Optical Materials 2(6): 522-528 (2014).

[32] M Ajay, B Salil, R Kamlakar and H Han. Bio-inspired textures for functional applications. CIRP Annals - Manufacturing Technology 67: 627-650 (2018).

[33] HN Hansen, K Carneiro, H Haitjema and LD Chiffre. Dimensional micro and nano metrology. CIRP Annals - Manufacturing Technology 55: 721-743 (2006).

[34] Y Liu, J Shigley, K Hurwit. Iridescent color of a shell of the mollusk pinctada margaritifera caused by diffraction. Optics Express 4: 177-182 (1999).

[35] D Content and P Arsenovic. Grating groove metrology and efficiency predictions from the soft x-ray to the far infrared. Proc. SPIE 4485: 405-416 (2002).

[36] Hansma P, Elings V, Marti O, Bracker C. Scanning Tunneling Microscopy and Atomic Force Microscopy: Application to Biology and Technology. Science 242: 209-216 (1988).

[37] Cuenat A. Scanning Probe and Particle Beam Microscopy. Fundamental Principles of Engineering Nanometrology: 205-239 (2014).

[38] Rai-Choudhury P. Handbook of Microlithography, Micromachining, and Microfabrication. Volume 1: Microlithography, SPIE Press (1997).

[39] LA Firstein, A Noz. Cross-sectional imaging in SEM: signal formation mechanism and CD measurements. Proc. SPIE 1464, Integrated Circuit Metrology, Inspection, and Process Control V: 81-88 (1991).

[40] J Garnaes, PE Hansen, N Agersnap, et al. Profiles of a high-aspect-ratio grating determined by spectroscopic scatterometry and atomic-force microscopy. Applied Optics 45(14): 3201-3211 (2006).

[41] JS Madsen, LH Thamdrup, I Czolkos et al. In-line characterization of nanostructured mass-produced polymer components using scatterometry. J. Micromech. Microeng. 27: 085004 (2017).

[42] CJ Raymond, MR Mumane, SL Prins, et al. Multiparameter grating metrology using optical scatterometry. Journal of Vacuum Science & Technology B: Microelectronics and Nanometer Structures Processing, Measurement, and Phenomena 15, 361 (1997).

[43] CJ Raymond, MR Mumane, S Sohail, et al. Metrology of subwavelength photoresist gratings using optical scatterometry. Journal of Vacuum Science & Technology B 13(4): 1484-1495 (1995).

[44] RH Webb. Confocal optical microscopy. Reports on Progress in Physics 59: 427-471 (1996).

[45] P Hutzler, R Fischbach, W Heller, et al. Tissue localization of phenolic compounds in plants by confocal laser scanning microscopy. Journal of Experimental Botany, 49(323): 953-965 (1998)

[46] R Rezakhaniha, A Agianniotis, JTC Schrauwen, et al. Experimental investigation of collagen waviness and orientation in the arterial adventitia using confocal laser scanning microscopy. Biomechanics and Modeling in Mechanobiology 11(3-4): 461-473 (2012).

[47] PE Hanninen, SW Hell, J Salo and E Soini. Two-photon excitation 4Pi confocal microscope: Enhanced axial resolution microscope for biological research. Appl. Phys. Lett. 66 (13): 1698-1700 (1995).

[48] S Hell and EHK Stelzer. Fundamental improvement of resolution with a 4Pi-confocal fluorescence microscope using two-photon excitation. Optics Communications 93: 277-282 (1992).

[49] Peter de Groot. Principles of interference microscopy for the measurement of surface topography. Advances in Optics and Photonics 7: 1-65 (2015).

[50] M Takeda. Spatial-carrier fringe-pattern analysis and its applications to precision interferometry and profilometry: An overview. Industrial Metrology 1(2) 79-99 (1990).

[51] H Mori, Y Otani, T Yoshizawa. Local sampling phase shifting technique for precise surface profile measurement. Journal of the Japan Society for Precision Engineering 64(6): 856-860 (1998).

[52] K Kitagawa, T Tsuboi, H Sugihara, et al. Development of multi-wavelength single-shot interferometry and its practical application. Journal of the Japan Society for Precision Engineering 78(2): 112-116 (2012).

[53] M Takeda, H Ina, and S Kobayashi. Fourier-transform method of fringe-pattern analysis for computer-based topography and interferometry. Journal of the Optical Society of America 72(1): 156-160 (1982).

[54] T Kuwahara, Y Otani, T Yoshizawa. Profile Measurement using Abramson Interferometer by One-Step Phase Shifting Method. Journal of the Japan Society for Precision Engineering 64(9): 1380-1384 (1998).

[55] Y Otani, E Oda, O Ido, et al. Surface Profile Measurement by Optical Heterodyne Interferometry using Acousto-Optic Modulator. Journal of the Japan Society for Precision Engineering 61(8): 1097-1100 (1995).

[56] M Takeda, H Ina. Topometry and Interferometry by Use of a FFT AIgorithm for Fringe Pattern Analysis. Journal of the Japan Society for Precision Engineering 10(6): 476-480 (1981).

[57] M Takeda. Fourier- transform technique for fringe pattern analysis and its applications. Journal of the Japan Society for Precision Engineering 62(6): 579-583 (1993).

[58] T Naito, M Sugiyama, H Ogawa, K Kitagawa, K Suzuki. Single-shot Interferometry of Film-covered Objects. Journal of the Japan Society for Precision Engineering 75(11): 1315-1322 (2009).

[59] H Ogawa, KI Shimoyama, M Fukunaga, et al. Simultaneous Measurement of Film Thickness and Surface Profile of Film-Covered Objects by Using White-Light Interferometry. Transactions of the Society of Instrument and Control Engineers 43(2): 71-77 (2007).

[60] Y Mizutani, T Higuchi, T Iwata, et al. Time-Resolved Oblique Incident Interferometry for Vibration Analysis of an Ultrasonic Motor. International Journal of Automation Technology 11(5): 800-805 (2017).

[61] S Takahashi, C Jin, S Ye, M Michihata and K Takamasu. Theoretical analyses of in-process depth measurements of fine microgrooves based on near-field optical response. Annals of Cirp 66: 503-506 (2017).

[62] S Ye, S Takahashi, M Michihata and K Takamasu. Modified Linnik microscopic interferometry for quantitative depth evaluation of diffraction-limited microgroove. Meas. Sci. Technol 29: 054011 (2018).

[63] Eugene Hecht. Optics (Fourth Edition). Higher Education Express.

[64] Max Born and Emil Wolf. Principles of Optics: Electromagnetic Theory of Propagation, Interference and Diffraction of Light (Fourth Edition). Pergamon Express.

[65] WHA Fincham and MH Freeman. Optics (Ninth Edition). ISBN: 0-407-93422-7 (1980).

[66] Joseph W Goodman. Introduction to Fourier Optics (Third Edition). ISBN: 0-9747077-2-4 (2005).

[67] G Christian and D Alain. Near-field optics theories. Reports on Progress in Physics 59: 657-699 (1996).

[68] Dieter W Pohl and Daniel Courjon. Near Field Optics. ISBN: 978-94-010-4873-6.

[69] RC Dunn. Near-Field Scanning Optical Microscopy. Chem. Rev. 99 (10): 2891–2928 (1999).

[70] A Harootunian, E Betzig, M Isaacson, and A Lewis. Super-resolution fluorescence near-field scanning optical microscopy. Appl. Phys. Lett. 49: 674-676 (1986).

[71] Y Inouye and S Kawata. Near-field scanning optical microscope with a metallic probe tip. Optics Letters 19(3): 159-161 (1994).

[72] Dennis M Sullivan. Electromagnetic simulation using the FDTD method (Second Edition). ISBN: 978-1-118-45939-3 (2013).

[73] A Didari, MP Menguc. Analysis of near-field radiation transfer within nano-gaps using FDTD method. Journal of Quantitative Spectroscopy & Radiative Transfer 146: 214-226 (2014).

[74] Z Zeng, Y Liu, J Wei. Recent advances in surface-enhanced raman spectroscopy (SERS): Finite-difference time-domain (FDTD) method for SERS and sensing applications. Trends in Analytical Chemistry 75: 162-173 (2016).

[75] Yee Kane. Numerical solution of initial boundary value problems involving Maxwell's equations in isotropic media. IEEE Transactions on Antennas and Propagation 14(3): 302-307 (1966).

[76] A Taflove, SC Hagness. Computational electrodynamics: the finite-difference time domain method. Boston, MA: Artech House (2005).

[77] JA Roden and SD Gedney. Convolution PML (CPML): An efficient FDTD implementation of the CFS–PML for arbitrary media. Microwave and Optical Technology Letters 27(5): 334-339 (2000).

[78] SD Gedney. An Anisotropic PML Absorbing Media for the FDTD Simulation of Fields in Lossy and Dispersive Media. Electromagnetics 16(4): 399-415 (1996).

[79] M Fleischer, A Weber-Bargioni, MVP Altoe, et al. Gold Nanocone Near-Field Scanning Optical Microscopy Probes. ACS Nano 5(4): 2570-2579 (2011).

[80] A Andrea and E Nader. Cloaked Near-Field Scanning Optical Microscope Tip for Noninvasive Near-Field Imaging. Phys. Rev. Lett. 105: 263906 (2010).

[81] B Filiberto, T Simone, P Francesco, and V Lucio. Cloaking apertureless near-field scanning optical microscopy tips. Optics Letters 36(2): 211-213 (2011).

[82] J Tisler, T Oeckinghaus, RJ Stohr, R Kolesov, et al. Single Defect Center Scanning Near-Field Optical Microscopy on Graphene. Nano Lett., 13 (7): 3152-3156 (2013).

[83] R Sakuma, S Ye, M Michihata, K Takamasu and S Takahashi. Non-destructive optical depth inspection of sub-diffraction limit fine holes - construction of a low noise optical model based on the FDTD Method. 2017 JSPE Autumn Meeting; 179-180 (2017).

[84] VB Johannes, JF Hans and S Cornelis. Linear approximation for measurement errors in phase shifting interferometry. Applied Optics, 30(19); 2718-2729 (1991).

[85] A Chiayu and CW James. Effect of piezoelectric transducer nonlinearity on phase shift interferometry. Applied Optics 26(16): 1112-1116 (1987).

[86] L Guanming and Y Toyohiko. Generalized phase-shifting interferometry. J. Opt. Soc. Am. A 8(5): 822-827 (1991).

[87] I Yamaguchi and T Zhang. Phase-shifting digital holography. Optics Letters 22(16): 1268-1270 (1997).

[88] T Zhao, T Mauger, and G Li. Optimization of wavefront-coded infinity-corrected microscope systems with extended depth of field. Biomedical Optics Express 4(8): 1464-1471 (2013).

[89] SH Williams, A Hilger, N Kardjilov, I Manke, M Strobl, PA Douissard, T Martin, H Riesemeier and J Banhart. Detection system for microimaging with neutrons. Journal of Instrumentation 7 (2012).

[90] SRP Pavani, R Piestun. Microparticles using a photon-limited double-helix response system. Optics Express 16(26): 22048-22057 (2008).

[91] AD Kersey, MJ Marrone, MA Davis. Polarisation-insensitive fibre optic Michelson interferometer. Electronics Letters 27(6): 518-520 (1991).

[92] PG Kwiat, WA Vareka, CK Hong, H Nathel, and RY Chiao. Correlated two-photon interference in a dual-beam Michelson interferometer. Phys. Rev. A 41: 2910-2913 (1990).

[93] JV Knuuttila, PT Tikka, and MM Salomaa. Scanning Michelson interferometer for imaging surface acoustic wave fields. Optics Letters 25(9): 613-615 (2000).

[94] B Bharat, CW James, and LK Chris. Measurement of surface topography of magnetic tapes by Mirau interferometry. Applied Optics 24(10): 1489-1497 (1985).

[95] J Albero, S Bargiel, N Passilly, P Dannberg, M Stumpf, UD Zeitner, C Rousselot, K Gastinger and C Gorecki. Micromachined array-type Mirau interferometer for parallel inspection of MEMS. Journal of Micromechanics and Microengineering 21(6): 065005 (2011).

[96] A Tulsi, S Vishal, SM Dalip, and S Chandra. High-resolution full-field optical coherence microscopy using a Mirau interferometer for the quantitative imaging of biological cells. Applied Optics 50(34): 6343-6351 (2011).

[97] X Hu, S Deng, W Wang, and X Hu. Long-working-distance Linnik microscopic interferometry for measuring the surface profile of microstructures. J. Vac. Sci. Technol. B 27: 1403-1407 (2008).

[98] J Niehues, P Lehmann, W Xie. Low coherent Linnik interferometer optimized for use in nano-measuring machines. Meas. Sci. Technol. 23: 125002 (2012).

[99] A Dubois, L Vabre, AC Boccara, E Beaurepaire. High-resolution full-field optical coherence tomography with a Linnik microscope. Applied Optics 41(4): 805-812 (2002).

[100] P Andreas and S Johannes. Interferometers and its implications for evaluation procedures. Applied Optics 40(34): 6223-6228 (2001).

[101] R Dandliker, R Thalmann, and D Prongue. Two-wavelength laser interferometry using superheterodyne detection. Optics Letters 13(5): 339-341 (1988).

[102] Norman Bobroff. Residual errors in laser interferometry from air turbulence and nonlinearity. Applied Optics 26(13): 2676-2682 (1987).

[103] T Suzuki, K Fujikura, T Higashiyama, and K Takata. DNA Staining for Fluorescence and Laser Confocal Microscopy. The Journal of Histochemistry & Cytochemistry 45(1): 49-53 (1997).

[104] B Sun, W Xie, G Yi, D Chen, Y Zhou, J Cheng. Microminiaturized immunoassays using quantum dots as fluorescent label by laser confocal scanning fluorescence detection. Journal of Immunological Methods 249(1-2): 85-89 (2001).

[105] Y Tamaki, M Araie, E Kawamoto, S Eguchi and H Fujii. Noncontact, two-dimensional measurement of retinal microcirculation using laser speckle phenomenon. Investigative Ophthalmology & Visual Science 35: 3825-3834 (1994).

[106] Z Wang, L Millet, M Mir, H Ding, et al. Spatial light interference microscopy (SLIM) Optics Express 19(2): 1016-1026 (2011).

[107] M Shimizu, H Sawano, H Yoshioka and H Shinno. Surface texture assessment of ultra-precision machined parts based on laser speckle pattern analysis. Precision Engineering 38: 1-8 (2014).

[108] SW Kim and GH Kim. Thickness-profile measurement of transparent thin-film layers by white-light scanning interferometry. Appl. Opt. 38(28): 5968-5973 (1999).

[109] DG Stavenga. Thin film and multilayer optics cause structural colors of many insects and birds. Materilas Today: Proceedings 1S: 109-121 (2014).

[110] MA Kats, R Blanchard, S Ramanathan, et al. Thin-Film Interference in Lossy, Ultra-Thin Layers. Optics and Photonics News 25(1): 40-47 (2014).

[111] W Yu, Y Chung, and J Soh. Vignetting Distortion Correction Method for High Quality Digital Imaging. Proceedings of the 17th International Conference on Pattern Recognition (2004).

[112] B Alessandro, P Filippo and G Alessandro. Vignetting correction by exploiting an optical microscopy image sequence. 33rd Annual International Conference of the IEEE EMBS, Boston (2011).

[113] R Wartmann. Double-sided telecentric measurement objective. U.S. patent, 5708532A (1998).

[114] SG Ronald, JF Victor. Raster following telecentric illumination scanning system for enhancing light throughout in light valve projection systems. U.S. patent, US5450219A (1993).

[115] T Andrew, N Joseph and O Mark. A method to correct for stray light in telecentric optical-CT imaging of radiochromic dosimeters. Institute of Physics and Engineering in Medicine 56(14): 4433-4451 (2011).

[116] W Yang, X Liu, W Lu, N Yu, L Chen. A Novel White Light Interference Based AFM Head. Journal of Lightwave Technology 35(16): 3604-3610 (2017).

[117] S Yang, C Li, C Wang, Z Jiang. A sub-50 nm three-step height sample for AFM calibration. Measurement Science and Technology 25(12): 125004 (2014).

[118] A Sikora and L Bednarz. The implementation and the performance analysis of the multi-channel software-based lock-in amplifier for the stiffness mapping with atomic force

microscope (AFM). Bulletin of the Polish Academy of Sciences: Technical Sciences 60(1): 83-88 (2012).

[119] A Pfortner and J Schwider. Dispersion error in white-light Linnik interferometers and its implications for evaluation procedures. Appl. Opt. 40: 6223-6228 (2001).

[120] DK Cohen, JD Ayres, and ER Cochran. Apparatus and method for automatically focusing an interference microscope. U.S. patent, US5122648 (1992).

[121] RW Swinford, DJ Aziz, BW Guenther and PR Unruh. Automated minimization of optical path difference and reference mirror focus in white-light interference microscope objective. U.S. patent, US6552806 (2003).

[122] LL Deck. Method and apparatus for automated focusing of an interferometric optical system. U.S. patent, US5208451 (1993).

[123] LL Deck and H Chakmakjian. Method and apparatus for automatically and simultaneously determining best focus and orientation of objects to be measured by broad-band interferometric means. U.S. patent, US5784164 (1998).

[124] J Dong, R Lu, Y Li, K Wu. Automated determination of best focus and minimization of optical path difference in Linnik white light interferometry. Applied Optics 50(30): 5861-5871 (2011).

[125] R Bamler and P Hartl. Synthetic aperture radar interferometry. Inverse problems 14: R1-R54 (1998).

[126] AZ Howard, MG Richard. Topographic mapping from interferometric synthetic aperture radar observations. Journal of Geophysical Research 91(B5): 4993-4999 (1986).

[127] E Rodriguez and JM Martin. Theory and design of interferometric synthetic aperture radars. IEE Proceedings F (Radar and Signal Processing) 139(2): 147-159 (1992).

[128] S Chavez, QS Xiang, L An. Understanding Phase Maps in MRI: A New Cutline Phase Unwrapping Method. IEEE Transactions on Medical Imaging 21(8): 966-977 (2002).

[129] William Scott Hoge. A Subspace Identification Extension to the Phase Correlation Method. IEEE Transactions on Medical Imaging 22(2): 277-280 (2003).

[130] H Mark and R Dov. A new two-dimensional phase unwrapping algorithm for MRI images. Magnetic Resonance in Medicine 24: 177-181 (1992).

[131] DL Fried. Adaptive optics wave function reconstruction and phase unwrapping when branch points are present. Optics Communications 200(1-6): 43-72 (2001).

[132] BD Jose, K Vladimir, A Jaakko, and E Karen. Absolute phase estimation: adaptive local denoising and global unwrapping. Applied Optics 47(29): 5358-5369 (2008).

[133] M Schwertner, MJ Booth, and T Wilson. Characterizing specimen induced aberrations for high NA adaptive optical microscopy. Optics Express 12(26): 6540-6552 (2004).

[134] YY Cheng and JC Wyant. Two-wavelength phase shifting interferometry. Applied Optics 23(24): 4539-4543 (1984).

[135] R Guo, W Zhang, R Liu, C Duan, F Wang. Phase unwrapping in dual-wavelength digital holographic microscopy with total variation regularization. Optics Express 43(14): 3449-3452 (2018).

[136] Katherine Creath. Step height measurement using two-wavelength phase-shifting interferometry. Applied Optics 26(14): 2810-2816 (1987).

[137] K Jonas, C Tristan, M Frederic, C Florian, E Yves, C Etienne, M Pierre, and D Christian. Real-time dual-wavelength digital holographic microscopy with a single hologram acquisition. Optics Express 15(12): 7231-7242 (2007).

[138] AD Kersey and A Dandridge. Dual-Wavelength Approach to Interferometric Sensing. Proc. SPIE 0798, Fiber Optic Sensors II, doi: 10.1117/12.941102 (1987).

[139] W Zhang, X Lu, L Fei, H Zhao, H Wang, L Zhong. Simultaneous phase-shifting dual-wavelength interferometry based on two-step demodulation algorithm. Optics Letters 39(18): 5375-5378 (2014).

[140] AD Kersey and TA Berkoff. Dual wavelength fibre interferometer with wavelength selection via fibre Bragg grating elements. Electronics Letters 28(13): 1215-1216 (1992).

[141] J Gass, A Dakoff, and MK Kim. Phase imaging without 2p ambiguity by multi-wavelength digital holography. Optics Letters 28(13): 1141-1143 (2003).

[142] A Khmaladze, RL Matz, C Zhang, T Wang, et al. Dual-wavelength linear regression phase unwrapping in three-dimensional microscopic images of cancer cells. Optics Letters 36(6): 912-914 (2011).

[143] J Xiong, L Zhong, S Liu, X Qiu, Y Zhou, J Tian, et al. Improved phase retrieval method of dual-wavelength interferometry based on a shorter synthetic-wavelength. Optics Express 25(7): 7181-7191 (2017).

[144] 3M, Fluorinert™ Electronic LiquidFC-72 https://www.3m.com/3M/en_US/company-us/all-3m-products/~/3M-Fluorinert-Electronic-Liquid-FC-72/?N=5002385+3290667393&rt=rud.

[145] T Liu and CJ Kim. Turning a surface superrepellent even to completely wetting liquids. Science 346(6213): 1096-1100 (2014).

[146] S Asai, K Tachibana, M Michihata, K Takamasu, S Takahashi. Measurement of fine particulate defects with autonomous search and split multi-probe Analysis of behavior of liquid probe by using CFD. 2017 JSPE Spring Meeting (2017).

[147] K Tachibana, S Asai, M Michihata, K Takamasu, S Takahashi. Optical Detection of Fine Particulate Defects with Autonomous Search-and-split Liquid Probe -Characteristics analysis of optical detection. 16th International Conference on Precision Engineering, A307-8210 (2016).

[148] RN Wenzel. Resistance of solid surfaces to wetting by water. Industrial & Engineering Chemistry 28(8): 988-994 (1936).

[149] Z Yoshimitsu, A Nakajima, T Watanabe and K Hashimoto. Effects of Surface Structure on the Hydrophobicity and Sliding Behavior of Water Droplets. Langmuir 18: 5818-5822 (2002).

[150] M Takeda, H Ina and S Kobayashi. Fourier-transform method of fringe-pattern analysis for computer-based topography and interferometry. Journal of the Optical Society of America 72(1): 156-160 (1982).

[151] S Toyooka and M Tominaga. Spatial fringe scanning for optical phase measurement. Optics Communications 51(2): 68-70 (1984).

[152] KH Womack. Interferometric Phase Measurement Using Spatial Synchronous Detection. Optical Engineering 23(4): 234391 (1984).

[153] M Takeda . Spatial-carrier fringe-pattern analysis and its applications to precision interferometry and profilometry: An overview. Industrial Metrology 1(2): 79-99 (1990).

[154] Bradley T Kimbrough. Pixelated mask spatial carrier phase shifting interferometry algorithms and associated errors. Applied Optics 45(19): 4554-4562 (2006).

[155] T Schuster, J Ruoff, N Kerwien, S Rafler, W Osten. Normal vector method for convergence improvement using the RCWA for crossed gratings. Journal of the Optical Society of America A 24(9): 2880-2890 (2007).

[156] JJ Hench and Z Strakos. The RCWA method - a case study with open questions and perspectives of algebraic computations. Electronic Transactions on Numerical Analysis 31: 331-357 (2008).

[157] P Gotz, T Schuster, K Frenner, S Rafler, W Osten. Normal vector method for the RCWA with automated vector field generation. Optics Express 16(22): 17295-17301 (2008).

[158] FM Huang, TS Kao, VA Fedotov, Y Chen. Nanohole Array as a Lens. Nano Lett. 8(8): 2469-2472 (2008).

[159] E Johlin, A Al-Obeidi, G Nogay, et al. Nanohole Structuring for Improved Performance of Hydrogenated Amorphous Silicon Photovoltaics. ACS Appl. Mater. Interfaces 8 (24): 15169-15176 (2016).

Appendix A Codes used in the simulation

A-1 Numerical analysis of the feasibility of FNRDM

```
%% parameter setting
NA = 0.55;
wavelength = 488*10^(-9);
unit = 5*10^(-9);      % Corresponding to the grid size of FDTD simulation
unit_sum = 801;        % Corresponding to the simulation region of FDTD simulation
ex_unit_sum = 801;  % Corresponding to the expected region of far-filed imaging


%% reading the data of FDTD simulation
samp_file_nameA = 'ari_m1_f2_ex.dat';   % data of the microgroove model
samp_file_nameB = 'nasi_m1_f2_ex.dat';  % data of the air model
[samp2D_real_imag_dataA,
samp2D_real_imag_headA]=A131215importfile2D(samp_file_nameA);
[samp2D_real_imag_dataB,
samp2D_real_imag_headB]=A131215importfile2D(samp_file_nameB);


%% get the reflective component
samp2D_real_imag_dataC = samp2D_real_imag_dataA-samp2D_real_imag_dataB;
column=size(samp2D_real_imag_dataC,2);
samp2D_real_dataC=samp2D_real_imag_dataC(:,1:2:column);
samp2D_imag_dataC=samp2D_real_imag_dataC(:,2:2:column);
samp2D_complex_dataC1=samp2D_real_dataC + samp2D_imag_dataC * i;


%% read the data at the required position in near-field
samp2D_complex_dataC=samp2D_complex_dataC1(:,305);
samp2D_intensity_dataC=samp2D_real_dataC.^2+samp2D_imag_dataC.^2;
```

```matlab
samp2D_amplitude_dataC=samp2D_intensity_dataC. ^ (1/2);
samp2D_phase_dataC=angle(samp2D_complex_dataC);

%% plot the near-filed data
x_axis=unit:unit:unit_sum*unit;
nearfield_amp = samp2D_amplitude_dataC (: , 305)';
figure ()
plot (x_axis, nearfield_amp, 'k.-')
nearfield_Pha=samp2D_phase_dataC';
figure ();
plot (x_axis, nearfield_Pha, 'k.-')

%% far-field imaging
samp_compamp_ex=zeros(ex_unit_sum,1);
unit_part=(ex_unit_sum-unit_sum-1)/2;
samp_compamp_ex(unit_part+1: unit_part+unit_sum)
=samp2D_complex_dataC(1:unit_sum);
[image_compamp, airyAMP_forFFT, FFTed_airyAMP_forFFT]
= opticsimaging (wavelength, NA, samp_compamp_ex, unit, ex_unit_sum);
image_compamp_real=real(image_compamp);
image_compamp_imag=imag(image_compamp);
image_amp=abs(image_compamp);
image_phase=angle(image_compamp);
image_int=image_amp . ^2;

%% plot the far-filed data
x_axis1=unit:unit:ex_unit_sum*unit;
farfield_amp=image_amp';
figure ()
```

```
plot (x_axis1, farfield_amp, 'k.-')
farfield_Pha=image_phase';
figure ();
plot (x_axis1, farfield_Pha, 'k.-')

%% FNRDM
amp_top=149.3;     % amplitude of top surface reflection
pha_uniform=2.14;  % phase of top surface
farfield_middle_amp=farfield_amp((ex_unit_sum+1)/2);
farfield_middle_pha=farfield_Pha((ex_unit_sum+1)/2)-pha_uniform;
nearfield_cal_amp=(farfield_middle_amp^2+amp_reflect^2-
2*farfield_middle_amp*amp_reflect*cos(farfield_middle_pha))^(1/2);
if farfield_middle_amp*cos(farfield_middle_pha)<amp_reflect && farfield_middle_pha>0
  theta=abs(asin(farfield_middle_amp*sin(farfield_middle_pha)/nearfield_cal_amp));
  theta1=pi-theta;
  else if farfield_middle_amp*cos(farfield_middle_pha)>amp_reflect &&
farfield_middle_pha>0
  theta1=abs(asin(farfield_middle_amp*sin(farfield_middle_pha)/nearfield_cal_amp));
    else if farfield_middle_amp*cos(farfield_middle_pha)<amp_reflect &&
farfield_middle_pha<0
    theta=-abs(asin(farfield_middle_amp*sin(farfield_middle_pha)/nearfield_cal_amp));
    theta1=-(pi-theta);
    else
  theta1=-abs(asin(farfield_middle_amp*sin(farfield_middle_pha)/nearfield_cal_amp));
    end
  end
end
h=wavelength*theta1/4/pi;   % theta1 is the calculated near-field phase.
```

```
% %define function A131215importfile2D
function [samp2D_real_imag_data, samp2D_real_imag_head]
=A131215importfile2D(fileToRead1)
DELIMITER = '';
HEADERLINES = 4;
newData1 = importdata(fileToRead1, DELIMITER, HEADERLINES);
samp2D_real_imag_data=newData1.data;
samp2D_real_imag_head=newData1.textdata;


% %define function opticsimaging
function [image_compamp, airyAMP_forFFT, FFTed_airyAMP_forFFT]
=opticsimaging(wavelength, NA, samp_compamp, unit, unit_sum)
k=2*pi/wavelength;
const=k*NA*unit;
airy_amplitude= zeros(unit_sum, 1);
airy_amplitudeinverse= zeros(unit_sum, 1);
for ii = 1:unit_sum;
    airy_amplitude(ii) = ( 2 * besselj(1, const*(ii-0.5)) / (const*(ii-0.5)) );
    airy_amplitudeinverse(unit_sum+1-ii)=airy_amplitude(ii);
end
airyAMP_forFFT=airy_amplitudeinverse+airy_amplitude;
FFTed_airyAMP_forFFT=fft(airyAMP_forFFT);
image_compamp=(ifft(((fft(samp_compamp)).*FFTed_airyAMP_forFFT));
end


%% calculate top surface reflection
NA = 0.55;
wavelength = 488;
unit=5;   % Corresponding to the grid size of FDTD simulation
```

```matlab
k=2*pi/wavelength;
const=k*NA*unit;
unit_sum=801;    Corresponding to the simulation region of FDTD simulation
airy_amplitude= zeros(unit_sum, 1);
for ii = 1:unit_sum;
    airy_amplitude(ii) = ( 2 * besselj(1, const*(ii-0.5)) / (const*(ii-0.5)) );
end
airy_amplitude1=airy_amplitude;
for i=1:20   % half of the width of microgroove
    airy_amplitude1(i)=0;
end
sum_amplitude_0=sum(airy_amplitude);
sum_amplitude_1=sum(airy_amplitude1);
amp_top =sum(airy_amplitude1)*229.2/sum_amplitude_0;
```

A-2 Applicability of FNRDM under practical noise conditions

```matlab
%% read the data
cd='F:\research\for graduation\code\chapter2\nqdm\noise\w200d300' ;
a=dir(cd);
for i=1:1:4
pathA=strcat(cd,'\sampleshift\',(num2str(i*122)),'\NA0.55 sabun','\parameter.mat');
j=load(pathA);
compA=j.image_compamp;
A(i,:)=compA;
pathB=('F:\research\for graduation\code\chapter2\nqdm\noise\w200d300\parameter.mat');
k=load(pathB);
compB=k.image_compamp;
B(i,:)=compB;
```

```matlab
compC=compA+compB;
image_amp(i,:)=abs(compC);
image_int(i,:)=image_amp(i,:).^2;
end

%% 4-step phase shift
I1=image_int(1,:);
I2=image_int(2,:);
I3=image_int(3,:);
I4=image_int(4,:);
phase_no_noise=atan2((I4-I2),(I1-I3));
%% plot the interferograms
x=-2000:5:2000;
figure()
plot(x,I1,'k-')
grid on
set(gca,'fontsize',15,'fontname','Times New roman')
figure()
plot(x,I2,'k-')
grid on
set(gca,'fontsize',15,'fontname','Times New roman')
figure()
plot(x,I3,'k-')
grid on
set(gca,'fontsize',15,'fontname','Times New roman')
figure()
plot(x,I4,'k-')
grid on
set(gca,'fontsize',15,'fontname','Times New roman')
```

```matlab
%% adding the noise 2sigma = 3%
I1_noise=I1+I1.*normrnd(0,0.015,1,801);
I2_noise=I2+I2.*normrnd(0,0.015,1,801);
I3_noise=I3+I3.*normrnd(0,0.015,1,801);
I4_noise=I4+I4.*normrnd(0,0.015,1,801);
phase_noise=atan2((I4_noise-I2_noise),(I1_noise-I3_noise));
figure()
plot(x,phase_noise,'r.-')
hold on
plot(x,phase_no_noise,'k.-')
grid on
set(gca,'fontsize',15,'fontname','Times New roman')

%% calculate the maximal error under noise condition
phase_error=phase_noise-phase_no_noise;
phase_error_max=max(abs(phase_error'));
phase_error_std=std(phase_error');
```

Appendix B Codes used in the experiments

B-1 Calculating the data of A_f AND A_u

```
%% data reading
unit = 1.67/40;                 % 1.67 is pixel size of CCD, 40 is magnification power
xc1 = 0: unit:3839* unit;       % 3840 is the pixel number along X-axis
yc1=0: unit:2747* unit;         % 2748 is the pixel number along Y-axis
I11 = imread ('Image__2018-08-28__16-38-24.tiff');   % reading the raw data
AA1=int16(I11);


%% plot the image
Figure ()
imagesc(xc1, yc1,AA1);
set (gca,'fontsize',15,'fontname','Times New roman')
colormap(gray)


%% rotating the image
tan_theta = (1037-841) / (925-21);
theta=-atan(tan_theta) *180/pi;
AA1_ro= imrotate (AA1, theta, 'bilinear','crop');
Figure ()
imagesc(AA1_ro);
set (gca,'fontsize',15,'fontname','Times New roman')
colormap(gray)
%
x_applied=0: unit: 50* unit;    % 50 is the pixel number in the evaluating area along X-axis
y_applied=0: unit:500* unit;    % 500 is the pixel number in the evaluating area along X-axis
AA1_col=AA1_ro (1551:2050,1481:1530);
```

AA1_col_am=sqrt(double(AA1_col));   % amplitude

Figure ()

imagesc (x_applied, y_applied, AA1_col_am);

set(gca,'YDir','normal')

colormap(gray)

set (gca,'fontsize',16,'fontname','Times New roman')

axis tight

%% selecting uniform area of the sample

AA1_flat=double (AA1_ro (961:1410,3146:3595));

%% plot the uniform area

Figure ()

imagesc(AA1_flat);

set (gca,'fontsize',15,'fontname','Times New roman')

set (gca,'ytick', [], 'yticklabel', [])

set (gca,'xtick', [], 'xticklabel', [])

colormap(gray)

axis tight

axis image

%% calculating A_u

am_flat=mean(mean(AA1_flat));

std_flat=std (AA1_flat (:))/256;

am_flat1=sqrt(am_flat);

save (parameter1.mat.mat',' AA1_col)

B-2 Calculating the phase distribution by 4-step phase shift method

%% data reading

```
k=1;
i=1;
for i=1:4;
 N1=sprintf('%s%d.tiff','Basler acA3800-14um (21952933)_20180828_163951887_000',i);
 II=imread(N1);
 A{i}=int16(II);
 va=i;
end
AA1=A{va-3};
AA2=A{va-2};
AA3=A{va-1};
AA4=A{va};
xc1=0: unit:3839* unit;     % 3840 is the pixel number along X-axis
yc1=0: unit:2747* unit;     % 2748 is the pixel number along Y-axis

%% plot the interferograms
Figure ()
imagesc (xc1, yc1, AA1);
set (gca,'ytick', [],'yticklabel', [])
set (gca,'xtick', [],'xticklabel', [])
colormap(gray)
set (gca,'fontsize',15,'fontname','Times New roman')

figure ()
imagesc (xc1, yc1, AA2);
set (gca,'ytick', [],'yticklabel', [])
set (gca,'xtick', [],'xticklabel', [])
colormap(gray)
set (gca,'fontsize',15,'fontname','Times New roman')
```

```matlab
figure ()
imagesc (xc1, yc1, AA3);
set (gca,'ytick', [],'yticklabel', [])
set (gca,'xtick', [],'xticklabel', [])
colormap(gray)
set (gca,'fontsize',15,'fontname','Times New roman')


figure ()
imagesc (xc1, yc1, AA4);
set (gca,'ytick', [],'yticklabel', [])
set (gca,'xtick', [],'xticklabel', [])
colormap(gray)
set (gca,'fontsize',15,'fontname','Times New roman')


%% rotating the images
tan_theta = (1037-841) / (925-21);
theta=-atan(tan_theta) *180/pi;
AA1_ro=imrotate (AA1, theta, 'bilinear','crop');
AA2_ro=imrotate (AA2, theta, 'bilinear','crop');
AA3_ro=imrotate (AA3, theta, 'bilinear','crop');
AA4_ro=imrotate (AA4, theta, 'bilinear','crop');
A1=AA1_ro;
A2=AA2_ro;
A3=AA3_ro;
A4=AA4_ro;


%% phase shift method
S1=atan2(double((A4-A2)), double((A1-A3)));
Figure ()
```

```
imagesc(S1);
colormap(jet)
set (gca,'fontsize',15,'fontname','Times New roman')
axis tight
axis image


%% Selecting the evaluating area
x_applied=0: unit:50* unit;      % 50 is the pixel number in the evaluating area along X-axis
y_applied=0: unit:500*unit;    % 500 is the pixel number in the evaluating area along X-axis
figure ()
imagesc(x_applied, y_applied,S1(1551:2050,1481:1530));
set(gca,'YDir','normal')
colormap(jet)
set (gca,'fontsize',16,'fontname','Times New roman')
S1_unwrap=S1(1551:2050,1481:1530);
S1_save=S1_unwrap;
save ('parameter1-4.mat','S1_save')
```

B-3 Data processing by FNRDM

```
%% loading amplitude distribution
load('F:\research\experiment\data2018\180828\int\parameter1.mat');
int=double(AA1_col);
farfield_amp=sqrt(int);
unit=1.64/40;
x_applied=0: unit:50*unit;
y_applied=0: unit:500*unit;
figure ()
imagesc (x_applied,y_applied,farfield _amp)
```

```matlab
set (gca,'YDir','normal')
colormap (gray)
set (gca,'fontsize',16,'fontname','Times New roman')
axis tight

%% loading phase distribtuion
load('F:\research\experiment\data2018\180828\pha\parameter2-5.mat');
phase=S1_save;
figure ()
imagesc(x_applied,y_applied,phase)
set(gca,'YDir','normal')
set (gca,'ytick', [],'yticklabel', [])
set (gca,'xtick', [],'xticklabel', [])
colormap(jet)
set (gca,'fontsize',16,'fontname','Times New roman')

% % locate the central position of the microgrooves
farfield_amp_gr=[farfield_amp(44,:);farfield_amp(147,:);farfield_amp(248,:);farfield_amp(
350,:);farfield_amp(451,:)];
phase_upper=[phase(71:110,:);phase(171:210,:);phase(271:310,:);phase(381:420,:)];
phase_upper_mean= mean(phase_upper(:));
phase_bottom=[phase(44,:);phase(147,:);phase(248,:);phase(349,:);phase(451,:)];
phase_difference=phase_bottom-phase_upper_mean;

% % calculated At by using Au
a1=11.0705;

%% FNRDM
for i=1:5
```

```
  for j=1:50
 if (farfield_amp_gr(i,j).^2+a1^2-2*farfield_amp_gr(i,j).*a1.*cos(phase_difference(i,j))) >0
   nearfield_cal_amp(i,j) = (farfield_amp_gr(i,j).^2+a1.^2-
2*farfield_amp_gr(i,j).*a1.*cos(phase_difference(i,j))).^(1/2);
  else
    nearfield_cal_amp(i,j)=0;
end
end
end


for i=1:5
for j=1:50
  if phase_difference(i,j)<0 && farfield_amp_gr(i,j)*cos(phase_difference(i,j))>a1
    theta1(i, j) = -abs(asin(farfield_amp_gr(i,j)*
                 sin(phase_difference(i,j))/nearfield_cal_amp(i,j)));
    else if phase_difference(i,j)<0 && farfield_amp_gr(i,j)*cos(phase_difference(i,j))<a1
    theta (i, j) = -abs(asin(farfield_amp_gr(i,j)*
                 sin(phase_difference(i,j))/nearfield_cal_amp(i,j)));
    theta1(i,j) = -(pi+theta(i,j));
      else if phase_difference(i,j)>0 && farfield_amp_gr(i,j)*cos(phase_difference(i,j))>a1
theta1(i,j)=abs(asin(farfield_amp_gr(i,j)*sin(phase_difference(i,j))/nearfield_cal_amp(i,j)));
        else
 theta(i, j)=abs(asin(farfield_amp_gr(i,j)*sin(phase_difference(i,j))/nearfield_cal_amp(i,j)));
 theta1(i,j)=(pi-theta(i,j));
end
end
end
end
end
```

```
h_con=532*phase_difference/4/pi;     % 532 is the wavelength
h_wrapped=532*theta1/4/pi;
h_con_ave=mean(h_con);
h_wrapped_ave=mean(h_wrapped);
```

Achievements

1. Journal

[1-1] **<u>Shiwei Ye</u>**, Satoru Takahashi, Masaki Michihata, Kiyoshi Takamasu, Hans Nørgaard Hansen, Matteo Calaon. Quantitative depth evaluation of microgrooves on polymer material beyond the diffraction limit. Precision Engineering, 59: 56-65 (2019).

[1-2] **<u>Shiwei Ye</u>**, Satoru Takahashi, Masaki Michihata, Kiyoshi Takamasu. Modified Linnik microscopic interferometry for quantitative depth evaluation of diffraction-limited microgroove. Meas. Sci. Technol, 29: 054011 (2018).

[1-3] Satoru Takahashi, Chengshuo Jin, **<u>Shiwei Ye</u>**, Masaki Michihata, Kiyoshi Takamasu. Theoretical analyses of in-process depth measurements of fine microgrooves based on near-field optical response. CIRP Annals - Manufacturing Technology, 66: 503-506 (2017).

2. International conference

[2-1] **<u>Shiwei Ye</u>**, Masaki Michihata, Kiyoshi Takamasu, Satoru Takahashi. Optical depth measurement of the diffraction-limited microgrooves with a noise-immune dual-wavelength interferometer. International Symposium on Measurement Technology and Intelligent Instruments 2019, Niigata, Japan. (Manuscript Submitted, Oral)

[2-2] **<u>Shiwei Ye</u>**, Masaki Michihata, Kiyoshi Takamasu, Satoru Takahashi. Improvement of quantitative depth evaluation for diffraction-limited microgroove using LED light source. IMEKO 2018, Belfast, UK, 2018/09 (Oral).

[2-3] **<u>Shiwei Ye</u>**, Masaki Michihata, Kiyoshi Takamasu, Satoru Takahashi. Quantitative depth evaluation method of diffraction limited microgrooves based on near-field optical response. SIFYS 2018, Shanghai, China, 2018/05 (Oral).

[2-4] **<u>Shiwei Ye</u>**, Masaki Michihata, Kiyoshi Takamasu, Satoru Takahashi. Linnike microscopic interferometry for depth measurement of diffraction limited micro-groove

structure on the semiconductor surface. International Symposium on Optomechatronic Technology 2017, Taiwan, 2017/11 (Oral & Poster).

[2-5] **Shiwei Ye**, Masaki Michihata, Kiyoshi Takamasu, Satoru Takahashi. Experimental verification of a novel in-process depth measurements of diffraction limited micro-groove based on near-field optical response. International Symposium on Measurement Technology and Intelligent Instruments 2017, Xi'an, China, 2017/09 (Oral).

3. Domestic conference

[3-1] **Shiwei Ye**, Masaki Michihata, Kiyoshi Takamasu, Satoru Takahashi. Non-Destructive Optical Depth Inspection of Sub-Diffraction Limit Fine Holes (The Sixth Report) - a novel phase unwrapping method using a Fluorinert droplet. 2019 JSPE Autumn Meeting, Hamamatsu, Japan, 2019/09 (Manuscript submitted, Oral)

[3-2] **Shiwei Ye**, Masaki Michihata, Kiyoshi Takamasu, Satoru Takahashi. Non-Destructive Optical Depth Inspection of Sub-Diffraction Limit Fine Holes (The fifth report) - Experiment verification based on modified Linnike microscopic interferometry. 2018 JSPE Spring Meeting, Tokyo, Japan, 2018/03 (Oral).

[3-3] Ryoko Sakuma, **Shiwei Ye**, Masaki Michihata, Kiyoshi Takamasu, Satoru Takahashi. Non-destructive optical depth inspection of sub-diffraction limit fine holes - construction of a low noise optical model based on the FDTD Method. 2017 JSPE Autumn Meeting, Osaka, Japan, 2017/09.

4.Awards

[4-1] Constructing High-Level Universities Under Fund of China Scholarship Council, 2016/09 – 2019/09.

[4-2] Grants for Researchers Attending International Conferences by The NEC C&C Foundation, Japan, 2017.

[4-3] International Exchange Grant Project by Marubun Research Promotion Foundation, Japan, 2018.

Acknowledges

It is a pleasure to thank the people who have contributed each in their own way in the work that has led to this thesis.

First of all, I would like to thank my supervisor Prof. Takahashi. During those three years, his support and dedication to my project are really a great help. His enthusiasm for precision engineering and rigorous attitude towards research convinced me to continue the scientific research and conduct my own Ph.D. project. I always benefited a lot from the discussion with him. In addition to research work, he encouraged me to take a Japanese course, which helps me to lead a better life in Japan. I learned many and many things from Prof. Takahashi during my stay at University of Tokyo, and my experiences in Tokyo and Japan will last a lifetime. Again, thank you for your supervision and support for all of these years.

I would like to thank Prof. Michihata for giving me precious suggestions and providing his valuable guidance during my Ph.D. studying period.

I would like to thank Prof. Takamasu and Prof. Matsumoto for giving me constructive suggestions during the middle-term conference and introducing many interesting researches and knowledge during the excursion period.

I would like to thank Prof. Hansen and Dr. Calaon from Technical University of Denmark for providing the valuable samples and giving some suggestions to my research.

I would like to thank my committee members, Prof. Shimura, Prof. Toshiyoshi and Prof. Higurashi for providing their insightful comments and suggestions for my Ph.D. thesis.

I would like to thank my colleagues at Takahashi Laboratory. Mr. Kume is willing to share things with me in English and helped me to revise the spelling of Japanese. Mr. Masui gave me a lot of suggestions on developing an optical system and told me many interesting things about Japanese culture. Dr. Kong gave me lots of useful suggestions on my research. Mr. Zhao helped me to have a deep knowledge of optics. Mr. Hayashi Masahiro helped me a lot when complicated Japanese required. I would also like to thank other colleagues in our laboratory, Mr. Chu, Mr. Jin, Mr. Matsumoto, Mr. Kobayashi, Mr. Furuya, Mr. Yukei, Mr. Tachibana, Mr. Hayashi Kohei, Mr. Suzuki, Mr. Ono and Mr. Fujiwara. I would never forget

the days with you, research work, open campus and travels to areas around Tokyo, etc. It is really a valuable treasure in my life.

I would also like to thank my previous supervisors Prof. Yang and Prof. Peng from University of Xiamen for opening the world of scientific research and recommended me to University of Tokyo for doctoral study.

I would especially like to thank my parents for unconditionally supporting me to finish my Ph.D. program. I know how difficult to raise a willful and paranoid boy like me. Thank you for your giving and love for so many years.